SAND2012-7659
Unlimited Release
September 2012

Resposive Nanocomposites

Timothy J. Boyle,[a]
Thu Q. Doan,[a] Daniel T. Yonemoto,[a] Sarah M. Hoppe,[a] Chris Apblett,[b] Gregory von White II,[b] Nelson S. Bell,[b] PK Muthiah,[c] Wolfgang Sigmund,[c]

John Shelnutt,[a]
Kathleen E. Martin,[a] Yongming Tian, Yujiang Song, Eulalia Perreira,

C. Jeffrey Brinker,[a]
Bryan Kaehr,[a] Lauren Zarzar[d], Joanna Aizenberg[d],

Timothy N. Lambert,[b]
Carlos A. Chavez,[b] Nelson S. Bell,[b] Cody M. Washburn,[b] Michael T. Brumbach,[b] Todd M. Alam,[b] David R. Wheeler,[b] Claudia C. Luhrs,[e] Stephen Wakeland, Jeffrey R. Potts,[f] Prof. Rodney S. Ruoff,[f]

Gary S. Grest,[b]
Dong Meng,[g] and Sanat K. Kumary,[g] J. Matthew D. Lane,[b] Jagannathan T. Kalathi.[g]

[a] Advanced Materials Laboratory, Sandia National Laboratories, 1001 University Boulevard, SE, Albuquerque, New Mexico 87106
[b] Sandia National Laboratories, Albuquerque, New Mexico 87185, USA
[c] Department of Materials Science and Engineering, University of Florida, Gainesville, Florida 32611-6400, USA
[d] Department of Chemistry and Chemical Biology, Harvard University, Cambridge, Massachusetts 02138, USA
[e] Department of Mechanical Engineering, University of New Mexico, Albuquerque, New Mexico, 87131
[f] Department of Mechanical Engineering, University of Texas at Austin, Austin, Texas
[g] Department of Chemical Engineering, Columbia University, New York, NY 10027

Prepared by
Sandia National Laboratories
Albuquerque, New Mexico 87185 and Livermore, California 94550

Sandia National Laboratories is a multi-program laboratory managed and operated by Sandia Corporation, a wholly owned subsidiary of Lockheed Martin Corporation, for the U.S. Department of Energy's National Nuclear Security Administration under contract DE-AC04-94AL85000.

Approved for public release; further dissemination unlimited.

Sandia National Laboratories

Issued by Sandia National Laboratories, operated for the United States Department of Energy by Sandia Corporation.

NOTICE: This report was prepared as an account of work sponsored by an agency of the United States Government. Neither the United States Government, nor any agency thereof, nor any of their employees, nor any of their contractors, subcontractors, or their employees, make any warranty, express or implied, or assume any legal liability or responsibility for the accuracy, completeness, or usefulness of any information, apparatus, product, or process disclosed, or represent that its use would not infringe privately owned rights. Reference herein to any specific commercial product, process, or service by trade name, trademark, manufacturer, or otherwise, does not necessarily constitute or imply its endorsement, recommendation, or favoring by the United States Government, any agency thereof, or any of their contractors or subcontractors. The views and opinions expressed herein do not necessarily state or reflect those of the United States Government, any agency thereof, or any of their contractors.

Printed in the United States of America. This report has been reproduced directly from the best available copy.

Available to DOE and DOE contractors from
U.S. Department of Energy
Office of Scientific and Technical Information
P.O. Box 62
Oak Ridge, TN 37831

Telephone: (865) 576-8401
Facsimile: (865) 576-5728
E-Mail: reports@adonis.osti.gov
Online ordering: http://www.osti.gov/bridge

Available to the public from
U.S. Department of Commerce
National Technical Information Service
5285 Port Royal Rd.
Springfield, VA 22161

Telephone: (800) 553-6847
Facsimile: (703) 605-6900
E-Mail: orders@ntis.fedworld.gov
Online order: http://www.ntis.gov/help/ordermethods.asp?loc=7-4-0#online

SAND2012-7659
Unlimited Release
September 2012

Resposive Nanocomposites

Timothy J. Boyle,[a]
Thu Q. Doan,[a] Daniel T. Yonemoto,[a] Sarah M. Hoppe,[a] Chris Apblett,[b] Gregory von White II,[b] Nelson S. Bell,[b] PK Muthiah,[c] Wolfgang Sigmund,[c]

John Shelnutt,[a]
Kathleen E. Martin,[a] Yongming Tian, Yujiang Song, Eulalia Perreira,

C. Jeffrey Brinker,[a]
Bryan Kaehr,[a] Lauren Zarzar[d], Joanna Aizenberg[d],

Timothy N. Lambert,[b]
Carlos A. Chavez,[b] Nelson S. Bell,[b] Cody M. Washburn,[b] Michael T. Brumbach,[b] Todd M. Alam,[b] David R. Wheeler,[b] Claudia C. Luhrs,[e] Stephen Wakeland, Jeffrey R. Potts,[f] Prof. Rodney S. Ruoff,[f]

Gary S. Grest,[b]
Dong Meng,[g] and Sanat K. Kumary,[g] J. Matthew D. Lane,[b] Jagannathan T. Kalathi.[g]

[a] Advanced Materials Laboratory, Sandia National Laboratories, 1001 University Boulevard, SE, Albuquerque, New Mexico 87106
[b] Sandia National Laboratories, Albuquerque, New Mexico 87185, USA
[c] Department of Materials Science and Engineering, University of Florida, Gainesville, Florida 32611-6400, USA
[d] Department of Chemistry and Chemical Biology, Harvard University, Cambridge, Massachusetts 02138, USA
[e] Department of Mechanical Engineering, University of New Mexico, Albuquerque, New Mexico, 87131
[f] Department of Mechanical Engineering, University of Texas at Austin, Austin, Texas
[g] Department of Chemical Engineering, Columbia University, New York, NY 10027

Sandia National Laboratories
P.O. Box 5800
Albuquerque, New Mexico 87185-MSXXXX

ABSTRACT

The design of materials that respond to changing environmental conditions is a leading-edge materials area that will impact fundamental scientific and mission areas of Sandia. For this project, the responsive materials of interest were nanocomposites, which have come to the forefront of study since very low load levels (< 5 %) of the filler can have a dramatic impact on the matrices final properties. The production of Responsive Nanocomposites required the development of fundamental concepts and data to understand the nature and theory of nanomaterials interaction with polymeric materials. . Our initial response stimuli will focus on temperature or hydration since these are two of the major issues identified by our industrial

(Goodyear, Exxon and Intel) partners. The project was initiated by building on SNL's expertise in the synthesis of size- and shape-controlled nanomaterials of varied compositions and functionalizations (Boyle, Lambert, Shelnutt), nanocomposite self-assembly (Brinker), and computational modeling of nanocomposites (Grest) aided by several key university professors, students and industrial partners with expertise in nanocomposite testing. Obviously, a multi-discipline approach was undertaken to investigate the cross-over understanding required to make the quantum leaps necessary to realize the goal of this project. Therefore, several areas of research were undertaken: (i) Electrospinning (ii) Photoresponsive Thin Films, (iii) Soft-templating and (iv) Actuate Polymers. Together a model for nanocomposite mixtures that possess 'active' or 'applied' responses to temperature or hydration environmental changes were undertaken with several novel advancements produced.

EXECUTIVE SUMMARY

The design of materials that respond to changing environmental conditions is a leading-edge materials area that will impact fundamental scientific and mission areas of Sandia. For this project, the responsive materials of interest were nanocomposites. Nanocomposites have come to the forefront of study since very low load levels (< 5 %) of the filler can have a dramatic impact on the matrices final properties. This is due to the increased interfacial interaction of the 1D nanomaterials with the polymeric matrix. As we develop these *Responsive Nanocomposites* we expect to impact a wide number of research areas, including energy security and weapons. For example, polymeric materials in gasket seals would adapt to differing temperatures and humidity such that they maintain an optimal degree of functionality regardless of climate variations.

The production of *Responsive Nanocomposites* requires the development of fundamental concepts and data to understand the nature and theory of nanomaterials interaction with polymeric materials. The diverse nature of the project requires a multi-discipline approach to investigate the cross-over understanding required to make the quantum leaps necessary to realize the goal of this project. This pre-competitive study was designed to foster additional sponsors as progress is realized; however, without investment in the basic knowledge base, this project cannot proceed.

1. Nanoparticle synthesis. A variety of metal, semi-conductor, and ceramic nanomaterials are being synthesized to include in the responsive polymer matrix to allow for surface changes of the material. Several production routes are being investigated to include these nanomaterials with an emphasis on (i) electrospinning, (ii) soft templating and photocatalytic nanostructuring, and (iii) interfacial assembly.

2. Computational Modeling. Large-scale atomistic molecular dynamics simulations were carried out to determine the structure of functionalized nanoparticles in solution and to resolve the interactions between them. Simulations were also used to investigate the effect of nanoparticles on the flow and processibility of polymer nanocomposites.

Functionalization. Current efforts are focused on discovering what effect the existing materials interactions with the polymer matrices have and refining their functionalization.

Responsive Materials.
(i) Electrospinning: This approach focused on using electrospinning (i.e., the application of a charge to a drop of solution forming a Taylor cone to generate a mat of materials) to generate responsive polymeric/nanometal composites. The change at the surface, by the exposure or concealment of the nanometal components, will result in adaptive surface changes based on environmental conditions. This was analyzed by contact angle measurements.

(ii) ***Photoresponsive Thin Film***. This approach focused on using evaporation driven self-assembly to prepare graphene-ceramic nanocomposite films. The mechanism of self-assembly was studied. The films were shown to be responsive to light, which could be used to generate current or to induce the photoreduction of silver ions thereby forming a ternary silver-ceramic-graphene composite.

(iii) *Soft-templating.* Using insitu generated templates a variety of controlled shaped and sized nanomaterials of Cu^o, Pt^o, and Au^o were synthesized. The morphology of the Cu^o nanomaterials was found to be dependent on precursor anion and time. The Pt nandentrites formed displayed enhanced mobility in organic field-effect transistors (OFET) by lowering the Pt nanodendrites lower the threshold voltage and reduced (intrinsic) charged defect densities. Size control of the gold triangles is obtained by the choice of photocatalyst concentration with smaller nanoplates observed for higher concentrations of photocatalyst and capping agent.

(iv) Actuate Polymers

(a) Surfaces of hydrogel-driven actuating polymer structures. Routes to generate composite surfaces based on active control over passive 'cilia-like' structures were explored. 3D micro-scale hydrogel 'muscles' were integrated with polymer posts by *in situ* synthesis of environmentally responsive hydrogels using multiphoton lithography. Further, methods to pattern catalytic regions within engineered 3D microenvironments were developed and demonstrated to power micro-pumps and fluidics autonomously, based on environmental cues.

(b) Interfacial Assembly of Nanoparticle (NP)/Polymer Monolayers. Within the NINE program we extended the burgeoning work on ordered NP monolayer fabrication in three substantive respects. First, by assembly of hydrophobic gold NPs *on a fluid water interface* from toluene containing poly(methylmethacrylate) (PMMA), solvent evaporation concentrates the thinning film in NPs and PMMA, leading to *large scale* NP self-assembly and solidification into an ordered NP/polymer nanocomposite monolayer with physical dimensions of up to 10 cm^2. Second, we demonstrated that the NP/PMMA monolayer can be transferred to arbitrary substrates and remains stable as a free-standing membrane suspended over cm-sized holes. Third, the PMMA serves as a photoresist enabling two modes of electron beam (e-beam) NP patterning. Lower e-beam doses direct differential NP solubility serving as a positive resist, while at higher e-beam doses the PMMA serves as a negative resist resulting in sub-micrometer patterns with edge roughness comparable to that of the NP diameter (~5-nm). In combination these extensions contribute to the ability to integrate NP arrays into robust micro- and macro-scale devices. Additionally this approach represents a new means to attain very highly loaded yet flexible particle/polymer nanocmposites, which have eluded most synthetic efforts to date. Extending this concept to various responsive polymers has the potential to create large area smart surfaces.

As a fundamental incursion into this nascent field, this effort included collaborations with numerous academic and industrial partners. By combing diverse talents, we allowed unique experimental and modeling investigations of a wide scope of nanoparticle-polymer composites, including, for example, metals and electrospun polyvinylpyrrolidone, graphene-titania — whose self-assembling films are photoresponsive — and alkylsilane-coated silica nanoparticles with organic molecules such as squalene (model elastomer). Industrial collaborators, such as Goodyear™, Exxon/Mobil™, and Intel™ were involved as consultants with an eye toward potential customers as the project progressed.

Contents

Executive Summary 5
CHAPTER 1 9
CHAPTER 2 15
CHAPTER 3 45
CHAPTER 4 49
CHAPTER 5 59
CHAPTER 6 103
CHAPTER 7 157
Distribution 160

CHAPTER 1
Overview

The development of environmentally *Responsive Nanocomposites* will yield materials with increased robustness and stability. To produce these materials requires that the surface interaction between functionalized nanoparticles and the matrix be controlled. This proposal attacks this pre-competitive, general problem by invoking a multi-disciplinary approach employing predictive computational models and experimental verification based on a series of well-controlled complex nanomaterials dispersed in a variety of elastomeric or soft materials. In order to accomplish this, it is critical that the proper chemical species and length of the functional groups on the nanoparticle be determined as well as the surface coverage density. A model for nanocomposite mixtures that possess 'active' or 'applied' responses to temperature or hydration environmental changes will be developed. Our initial response stimuli will focus on temperature and/or reactivity of water, since these are two of the major issues identified to be of interest by our industrial (Goodyear, Exxon and Intel) partners. The project furthered Sandia's expertise in the synthesis of tailored-nanomaterials of varied compositions and functionalizations (Boyle, Lambert, Shelnutt), nanocomposite self-assembly (Brinker), and computational modeling of nanocomposites (Grest) aided by several key university (Clemson, Columbia, Wisconsin, Cornell, Florida, Harvard, Harvey Mudd, New Mexico, Northwestern, Texas, Washington) professors, students and industrial partners (GoodYear, ExxonMobil, Intel) with expertise in nanocomposite testing. The production of *Responsive Nanocomposites* required the development of fundamental concepts and data to understand the nature and theory of nanomaterials interaction with polymeric materials. The diverse nature of the project required a multi-discipline approach to investigate the cross-over understanding required to make the quantum leaps necessary to realize the goal of this project. This pre-competitive study fostered additional sponsors as progress was realized, but without investment in the basic knowledge base, this project would not have been successful.

The goal of this project was to develop environmentally *Responsive Nanocomposites* that are much more robust and stable than traditional nanocomposites but can adapt to new environmental situations. Together this team attempted to generate **a model for nanocomposite mixtures that possess 'active' or 'applied' responses to temperature or hydration environmental changes**. To achieve this goal, the project had three distinct parts: (1) computational modeling, (2) nanomaterial synthesis, and (3) responsive nanocomposite materials synthesis and testing. These are discussed briefly below and in more detail in the following chapters.

1. Nanomaterial synthesis. A variety of metal, semi-conductor, and ceramic nanomaterials were synthesized to be added to a responsive polymer matrix. As the polymer changed in the presence of the stimuli, the nanometallic particulates would be hidden or obfuscated, which would alter the surface properties of the nanocomposite. Several production routes were investigated to include these nanomaterials with an emphasis on (i) electrospinning, (ii) soft templating and photocatalytic nanostructuring, and (iii) interfacial assembly. For each *Responsive Nanocomposite* system developed, nanomaterials were required. Therefore numerous routes to a variety of nanomaterials (metals, semi-conductors, and ceramics) were developed. For the

externally generated nanomaterials an initial emphasis has focused on large-scale production of high aspect ratio nanoceramic wires. In particular, we have focused on the TiO_2 ceramic materials. Several routes have been developed to produce morphologically varied nanowires using solvothermal, solution precipitation, and the newly developed hybrid routes. The latter method allows for extremely large-scale production of very thin (>10 nm) but very long (< 0.5 mm) TiO_2 wires. In addition, a number of spinel $M_xCo_{3-x}O_4$ (where M = Mn, Fe, Ni, Cu) and x = 0-1) nanoparticles were prepared using low temperature solution precipitation methods. These could be applied in a magneto-responsive system. Further, standard nanoparticles of Au^o, Ag^o, Cu^o, Ge^o, and CdE, have been synthesized. These 1- D nanomaterials were employed mainly in the electrospinning efforts (see below). For 2-D materials, in addition to preparing graphene using published procedures the synthesis of graphene nanosheets from graphite oxide with UNM (Prof. C. Luhrs) using aerosol-through-plasma approach was realized and a patent application filed. This approach aerosolized graphite oxide and passes it through a plasma where it is rapidly heated - causing a reduction of the material along with thermal volume expansion, which is being characterized. In addition, the Ruoff group at University of Texas investigated the effect of graphene on the properties of polymeric matrices.

In situ photocatalytic growth of metal nanoparticles in soft templates (CTAB assemblies) has produced a variety of copper nanoparticles, nanowires, and nano-triangles using copper acetate or sulfate and ascorbic acid as the electron donor. Small platinum nanodendrites were also prepare using CTAB micelles for incorporation into regio-regular poly-3-hexylthiophene (P3HT) films of organic field effect transistors (OFETs) for enhancement of polymer conductivity. The hole mobility increases by a factor of 9 for OFETs containing the Pt nanodendrites even for low particle loading (0. 3 wt%). Surprisingly, nanostructure charging is absent in the films, and they exhibit lowered threshold voltage and reduced (intrinsic) charged defect densities. These properties may be altered by metal nanostructures serving as bridging conductors in the polymer or by altering the P3HT polycrystalline structure in some way.

2. Computational Modeling. Large-scale atomistic molecular dynamics simulations to determine the structure of functionalized nanoparticles in solution and to resolve the interactions between them was undertaken. For the first simulation, silica nanoparticles of diameter 5, 10 and 20 nm coated with polyethylene oxide oligomers in water were studied to develop and test effective methodologies for extracting forces between nanoparticles. For short oligomer coatings and coverages greater than 1 chain/nm^2 we determined the forces between functionalized nanoparticles which are being used in large-scale coarse-grained models of suspension flow and assembly. For longer oligomers (up to 100 repeat units) and lower coverages we found that the nanoparticles are not uniformly covered even at levels that are five times higher than what can be obtained experimentally. In this case, the interactions between the nanoparticles are very anisotropic and depend strongly on their relative orientation. At the highest experimental coverage of 0.2 chains/nm^2 the silica nanoparticle is exposed which can lead to nanoparticles sticking together and ultimately phase separating. In the second simulation, the effect of varying the chain length of the matrix polymer was investigated. We modeled 5 nm diameter amorphous silica physisorbed with $Si(OH)_3(CH_2)_{10}CH_3$ alkylsilanes in decane, $C_{24}H_{50}$ and $C_{48}H_{98}$ and squalene. It was determined that as the chain length increased the extent of the coating decreased. This is consistent with theoretical expectations that the longer melt chains act as a

poor solvent for the functionalized chains, which in turn can lead to phase separation at higher concentration.

To address the relation between miscibility of end grafted polymer nanoparticles and the chain length of the grafted chain and the melt, a coarse-grained simulation of highly entangled polymer nanoparticles in a polymer matrix was carried out. Using a new primitive path analysis developed by us, we studied how the chains grafted to a nanoparticle become entangled with the polymer matrix. Simulations were then used to delineate the forces between two polymer-grafted nanoparticles in a polymer melt, the associated potential of mean force, and the molecular origins of these forces. To study the effect of nanoparticles on the processability of polymer nanocomposites, we carried out non-equilibrium molecular dynamics simulations to determine the dependence of the shear viscosity on nanoparticle size and interaction strength. Our simulations allow us to systematically organize the viscosity data of filled polymer melts over a broad range of systems studied, thus providing a strong basis from which to predict the flow behavior of this commercially important class of materials.

3. Responsive Materials.

(i) Electrospinning: A number of electropsinning setups have been put in place : (i) SNL/AML (2 inert atmosphere and 1 benchtop), Bldg 823/Rm1043 (1 benchtop), Harvey Mudd College (HMC, 1 benchtop). A senior thesis project on arranging nanofibers on a rotating plastic pipe proved to be successful by the HMC students. The results of this study were detailed in a report available at HMC. In addition, several ES setups are in place at University of Florida with our collaborator Prof Sigmund. Initial efforts have focused on developing the ability to electropsin polymeric materials followed by inclusion of the nanomaterials discussed above with an emphasis on Au^o nanorods and CdE nanomaterials. The preliminary data indicate that loading of these nanoparticles will have to be kept low to minimize viscosity effects that prohibit electrospinning. Attempts to develop methods to spin-on and spin-off the polymer have been studied at HMC. This work is not represented in this report but a thesis is available upon request. It appears an electrostatic charge may assist in removing the electrospun nanocomposites once produced. A series of 'Tin(II) amide/alkoxide coordination compounds for production of Sn-based nanowires for lithium ion battery anode materials' were published as part of the no polymer aspect of this project. Further, work on the use of metal carboxylates also proved to generate wire like morphologies and will result in a paper. Several interesting results on the 'Thermally Tunable Wettability of Blended vs. Crosslinked Poly(N-isopropylacrylamide) Electrospun Fiber Mats' was jointly published on some responsive polymers and led to a patent application. The Au^o nanorods were introduced into these materials and are being characterized.
(ii) Forcespinning. The recently acquired forcespining equipment (collaboration with N. Bell (SNL)) has led to an alternative approach of generating the desired nanocomposites. While attempts are preliminary, it appears, several systems have the potential to directly form ceramic wires that can incorporate the nanoparticles of interest. More work is being conducted to verify and extend the latest efforts.

(ii) *Photoresponsive Thin Film* assemblies were developed. It was shown that thin films generated by the self-assembly of TiO_2-reduced graphene oxide (RGO) are photoconductive. Upon photo-reduction with UV light, the resulting solution after setting yielded thin films of material at the liquid-air surface. These films have been characterized using a variety of

analytical techniques and found to be < 100 nm thick. They were collected and deposited on inter-digitated electrodes (IDE) to study their photo-responsive nature. Data shows that upon photoexcitation, a drop in resistance (~ 200 kΩ decrease) is observed when using IDE. Photoexcitation in air, followed by immersion in silver salt solutions leads to the formation of silver nanoparticles on the surface of the graphene film.

(iii) Soft-templating. In an effort to produce new metal shapes in polymers, the use of an ABC type triblock terpolymer as a structure-directing agent for inorganic materials was investigated. Due to the unique bicontinuous morphologies that can be achieved through this block terpolymer, we expect that these hybrid organic/inorganic materials will be responsive to various temperature stimuli. The particular triblock terpolymer synthesized was polyisoprene-*b*-polystyrene-*b*-poly ethylene oxide (PI-*b*-PS-*b*-PEO). Neat films of this polymer cast from chloroform displayed alternating gyroid morphologies as determined by TEM and SAXS. It was established that this triblock terpolymer successfully structure directs aluminosilicate sol into various, well-ordered morphologies, including the bicontinuous alternating gyroid structure. The polymer material was used to investigate the capability to structure direct metal materials. Using a phase transfer technique an aqueous platinum precursor was incorporated into an organic phase containing the block terpolymer. Oxygen plasma was subsequently used to remove the organic polymer while simultaneously reducing the platinum species.

(4) Actuate Polymers (a) Surfaces of hydrogel-driven actuating polymer structures. High-aspect-ratio polymer structures (posts and platelets - prepared via a two-step replication process from a reusable, lithographically-etched silicon wafer, to a PDMS mold, and finally into the desired polymer) can be embedded in topographically patterned, responsive hydrogel films, such that actuation direction can be controlled. The volume-phase transition of the hydrogel works as a "muscle" to drive the actuation of the passive polymer surface structures when the hydrogel chemical composition (demonstrated humidity, pH, and temperature response) is altered. Such actuating surfaces can be envisioned to have unique and tunable responsive properties. Further development of responsiveness, including sensitivity to redox state, light, or electric field is being pursued on newly formed nanoscale structures. *(b) Interfacial Assembly of Nanoparticle (NP)/Polymer Monolayers*. Our work has extended to free-standing, patternable NP/polymer monolayer arrays formed by evaporation induced self-assembly at a fluid interface using polymethylmethacrylate (PMMA) to conjugated polymers and poly-N-isopropylacrylamide (poly-NIPAM), which could be useful matrices to impart optical-, temperature- or pH-sensitive responsiveness. We are also investigating NP/polymer assembly on water drops whose shape and contact angle are optically patterned on hydrophobic surfaces by 'gray-scale' lithography. The water droplet shape can be predicted through finite element techniques and engineer patterns of 3D corrugation of interfacial NP/polymer arrays during drying, which transfers the array to the substrate surface. For the first time, in situ, grazing incidence, small angle X-ray scattering was used to follow NP/polymer self-assembly on an evaporating water droplet. Additionally. it was demonstrated that apoly-NIPAM interfacial film forms at the water interface, which is the critical step for development of temperature and pH responsive NP/polymer arrays.

Summary

One of the main challenges of this research was the development of the design principles that will allow the rational fabrication of arbitrary responsive structures with the required properties. To address this challenge, fundamental studies of self-assembly in nanostructures and materials that enable actuation through rationalizing and modeling designs were conducted. Theoretical descriptions of the hydrogel-actuated nanofibers have been developed with extensive characterization tools that will be looped into the design process facilitating the required changes and alternative architectures. This project employed a multidisciplinary research group consisting of national laboratory and university personnel that are developing a fundamental science concerning responsive nanocomposites. It is expected that this effort will address a wide range DOE applications, with an emphasis on energy related needs and possibly NW related issues. Students were involved in every aspect of this project (see Chapter 7) and based on this initial interaction may lead to identifying potential candidates for future DOE efforts. When successful, *Responsive Nanocomposites* will allow for materials that can adapt to ever changing conditions. This will revolutionize the packaging industry, materials durability, and flexibility for a single component- a tire that can adjust to the weather significantly improving safety, energy, and durability. This project united a diverse group of established experts and facilitates their interaction through student researchers to address a pre-competitive research area identified by Sandia in concurrence with industrial partners as a critical need. This project was ideally suited and found to successfully initiate students to nanotechnology and supply career guidance, working with established experts to address critical research.

The following sections are broken down into the individual attempts to generate Responsive Nanocomposites: (i) **Electrospinning and Forcespinning of Responsive nanocomposites** (Boyle), (ii) **Shaped Metal Nanoparticles for Responsive Nanocomposites** (Shelnutt), (iii) **Graphene Synthesis, Composites and Assemblies** (Lambert), (iv) **Multiphoton Deposition and 3D Micro/Nanostructuring of Active, Catalytic, and "Smart" Materials** (Brinker), (v) **Computational models for Responsive Nanocomposites** (Grest). In these sections, some details of the results achieved will be presented with appropriate papers referenced for published materials.

This page intentionally left blank

CHAPTER 2

Electrospinning and Forcespinning of Responsive Nanocomposites

Timothy J. Boyle, Thu Q. Doan, Daniel T. Yonemoto, Sarah M. Hoppe, Chris Apblett, Gregory von White II, Nelson S. Bell
Sandia National Laboratories, Advanced Materials Laboratory, 1001 University Boulevard, SE, Albuquerque, New Mexico, 87106

Palanikkumaran Muthiah, Wolfgang Sigmund
Department of Materials Science and Engineering, University of Florida, Gainesville, Florida 32611-6400, USA

Introduction

For this project, the responsive nanocomposite would be produced by combining a responsive polymer with metallic nanoparticles. As the polymer reacted to the external stimuli (i.e., heat), it was expected that the metallic nanoparticles would be 'exposed' or 'hidden'. This would alter the surface reaction to water. While a number of routes to the polymeric nanowires were considered, after evaluation of solution or pull processes, it was determined that methods that would continually produce nanowires would be critical to meet the large scale demands that these materials would eventually require. Therefore, we focused on electrospinning and forcespinning processing to generate polymeric wire matrices. Prior to synthesizing the desired responsive nanocomposite, a great deal of effort focused on generating metal nanoparticles, including gold (Au^o), silver, (Ag^o), copper (Cu^o), germanium (Ge^o), and cadmium selenide (CdSe). Once the proper system was determined, the materials were isolated, functionalized and introduced into the predetermined parameters for production of polymeric nanowires. Electrospinning and forcespinning processing were used to generate polymeric wires. Different materials (i.e., metals, metal oxides) were also investigated as alternative matrices. Precursors for these wires included metal alkoxides ($M(OR)_x$, where M = Sn, Ti, Zr, Hf), metal amide alkoxides (M = Sn), polymers, and nanoparticles (Au^o, Ag^o, CdE). This section details the precursors and nanomaterial synthesis routes used. The following details the more successful aspects of this study.

Nanoparticle Synthesis.
Several types of nanoparticles were investigated to incorporate into polymer solutions for electrospinning. The majority of these routes followed established protocols; however, new routes to nanoparticles of materials were also developed.

i. Gold dots: Au^o nanodots were synthesized using a two-phase (water-toluene) reduction of the gold salt reported by Brust *et al*. First, an aqueous solution of $HAuCl_4$ and a separate solution of tetraoctylammonium bromide (TOAB) in toluene were prepared. The TOAB solution was added to the gold solution and vigorously stirred until all of the gold was transferred into the toluene layer, as indicated by the aqueous layer changing from yellow to colorless. Next, the organic

layer was isolated and dodecanethiol was added to this layer under vigorous stirring. Then, an aqueous solution of $NaBH_4$ was added to reduce the Au^+ to Au^o metal nanoparticles. Ethanol was added to this solution and centrifuged to precipitate out and isolate the nanoparticles.

ii. Gold rods: Water dispersible Au^o rods were produced using the seeding process by White *et al*.[1] In this synthesis, a gold nanoparticle seed solution was generated by reducing an aqueous solution of $HAuCl_4$ and cetyltrimethylammonium bromide (CTAB) with $NaBH_4$.

iii. Silver dots: Monodisperse Ag^o nanoparticles were generated using the procedure for the Au^o dots,[1] but modified for silver. First, an aqueous solution of $AgNO_3$ and a separate solution of tetraoctylammonium bromide (TOAB) in chloroform were prepared. The TOAB solution was added to the silver solution and vigorously stirred for an hour to transfer the silver into the toluene layer. Next, the organic layer was isolated and dodecanethiol was added to this layer under vigorous stirring. Then, an aqueous solution of $NaBH_4$ was added to reduce the Ag^+ to Ag^o metal nanoparticles. Ethanol was added to this solution and centrifuged to precipitate out and isolate the nanoparticles.

iv. Silver cubes: Using a solution precipitation route described by Peng and Sun, hexanes dispersible Ag^o nanocubes were synthesized.[2] In this procedure, a solution of octyl ether and oleylamine was refluxed under argon. Next, a solution of $AgNO_3$ and dimethyldistearylammonium chloride was quickly injected into the flask containing the refluxing solution. This mixture was heated and stirred for one hour. The solution was cooled to room temperature and centrifuged to isolate the nanoparticles. This procedure was also repeated, but the solution was refluxed for two hours instead of one hour to observe the effect of reaction time on the morphology of the nanoparticles.

v. Cadmium Chalcogenide dots: CdE dots were prepared following the procedure previously reported.[3] In this synthesis, a solution of trioctylphosphine oxide, tetradecylphosphonic acid, and $Cd(OAc)_2$ were heated under argon. For CdS, separate solution containing trioctylphosphine, toluene, and $S(SiMe_3)_2$ was injected into the heated solution. After heating for an appropriate amount of time, the flask was placed into a boiling water bath to cool to 60 ^oC. Then, a methanol/acetone solution was injected into the flask to quench the reaction.

vi. Copper. Following the Bunge et al report,[4] CuCl was converted to copper mesityl (Cu(Mes)) using (Mes)MgBr in THF/dioxane. The resulting Cu(Mes) was isolated by filtration, dried, and used without further purification. To a 310 ^oC mixture of hexadecylamine and octadecene, Cu(Mes) dissolved in ocatadecene was added and heated for ½ h. The resulting Cu^o nanoparticles were isolated by extraction with toluene and precipitation with an alcohol.

v. Germanium. Following the literature preparative route established by Gerung et al.,[5] germanium amide was dissolved in oleylamine and stirred until all the material was completely dissolved forming a pale yellow solution. The precursor solution was rapidly injected into a 3-neck flaskcontaining octadecene heated to 300 ^oC. The temperature was regulated using an Omega positive-feedback temperature controller 9100A with 3 ^oC accuracy and was connected to a K-type thermocouple and a variable voltage regulator (Variac) heater. Upon injection, the temperature dropped to 280 ^oC and recovered to 300 ^oC within 1 min. wherein the color of the

solution changed immediately to dark purple. After reacting for 1 h, the solution was extracted twice with a 1:1 mixture of $CHCl_3/CH_3OH$ and the final Ge^o nanowires in $CHCl_3$ were precipitated by the addition of excess acetone. After centrifugation, the dark Ge^o nanowire powder can be rediluted in a variety of solvents, including $CHCl_3$, toluene, or hexanes.

vi. Nickel. A similar prepratory route was followed as reported for the Copper nanoparticles synthesis (*vide infra*), replacing CuCl with $NiCl_2$.

Materials Characterization.

Scanning Electron Microscopy (SEM). ES samples for SEM were prepared by cutting the aluminum foil or graphite sheet to fit a 5 x 9 mm stage. These sample were indivudally placed on the SEM stage using double-sided carbon tape. These samples were analyzed without further processing. All sample images were obtained using a Hitachi S-5200 Nano SEM field emitter gun scanning electron microscope (FEGSEM). For EDS acquisition, a PGT EDS detector and Spirit software were used.

Transmission Electron Microscopy (TEM). All samples were imaged using a Philips CM 30 TEM equipped with a Thermo Noran System Six Energy Dispersive X-ray Spectrometer (EDS) System operating at an accelerating voltage of 300 kV. For the ES samples, the copper TEM grid was secured at the tip of a reverse tweezer and placed in front of the collection plate. ES was performed for 10-15 mins. and the copper grid was used for TEM without further processing.

Cyclic voltammetry (CV). Electrochemical studies of the ES materials of tin were prepared by changing the working distance between the spray tip and the substrate to localize all the deposited material. Deposits were made on graphite paper (Grafoil™). All testing was conducted under an Ar atmosphere in 1M TBAP in acetonitrile against a Ag/Ag^+ reference with Pt counter electrode. Cyclic voltammetry was performed at 25 mV/sec at room temperature starting at 0.1V vs. Ag/Ag^+ (just above the Sn^0 to Sn^{2+} potential) and sweeping cathodically to look for SnO reduction to Sn^0 in the first sweep. Electrospun (ES) samples were punched with a 1cm diameter punch to have a defined area of electrode for each measurement.

iv. Beryllium dome X-ray diffraction (BeD-XRD).[6-8] BeD-XRD is a powder XRD method used to characterize air-sensitive compounds. Information pertaining to the details of the beryllium dome XRD (BeD-XRD) analyses has been previously disseminated; [6-9] hence, only a short description is presented here. All sample preparation was performed in an argon filled glovebox using a 1 cm quartz disk (zero-background plate), where the sample was pressed into the specimen cavity, leveled to the holder base using a glass slide, and the BeD cover sealed. The BeD holder was carefully loaded into the Siemens D500 diffractometer. For all scans the instrument settings were 40 kV and 30 mA with a: 0.04^o step-size, 1 sec count-time, scan range of $5\text{-}30^o$ 2θ, 1° divergence and receiving slits; the goniometer radius was 250 mm. *Note:* Due to the presence of potentially toxic Be^o, it is important that only trained personnel, wearing the appropriate personal protective equipment (i.e., rubber gloves) handle the BeD. If poor handling techniques or any other means shatter the BeD-XRD, proper safety clean-up and disposal protocols *must* be followed.

Sample Handling. BeD XRD was done on the graphite sheet and resulted in two very intense peaks indicating that our substrate was not amorphous. This has caused some difficulty in characterizing the phase of these materials. Several different routes for identification have been attempted: 1) BeD XRD was done on the material that was electrospun on substrate, however the amount of material present was not enough to obtain any XRD pattern. The substrate was the main peaks observed for each of these samples; 2) scrapping the sample off of the graphite and loading that powder onto the BeD zero background holder still resulted in too much residual graphite to get a pattern for the samples; 3) attempts to wash the sample off the graphite and use the soluble fraction for XRD. No pattern was obtained because of the low solubility of the compounds that are on the substrates or the low yield of material on the graphite does not allow enough sample to be collected. 4) The most promising option is to place a small glass slide on the graphite during ES to see if sample can be collected on the slide. This would allow BeD XRD to be done because the glass slide is amorphous and therefore will not overshadow the sample patterns.

Electrospinning.

The desired arrangement for these responsive nanocomposites for our concept of the project was to include the above nanomaterials in a responsive polymer. In order to maximize their impact, it was decided that a nanowire would be best. Several routes to nanowires were explored with electrospinning determined to be the optimal method. Electrospinning[10-16] involves the application of a high electrical field (1-5kV/cm) to a drop of solution pushed through a needle. A general setup is shown in Figure 2.1. The applied high electrical force overcomes the surface energy of the droplet and forms a Taylor cone, which through a whipping motion, forms mats of fibers that possess a high surface area to mass ratio. This method is a simple yet versatile continuous process that can produce fiber diameters in ranges from a few micrometers to 100 nanometers. In order for a continuous fiber to be formed, it is necessary to have a link from drop to drop. Typically this requires the use of a polymer; however, we have shown that simple precursors, such as $[Sn(OR)_2]$ or $[Sn(NR_2)(OR)]_2$ dissolved in polar solvents will work to generate wires.

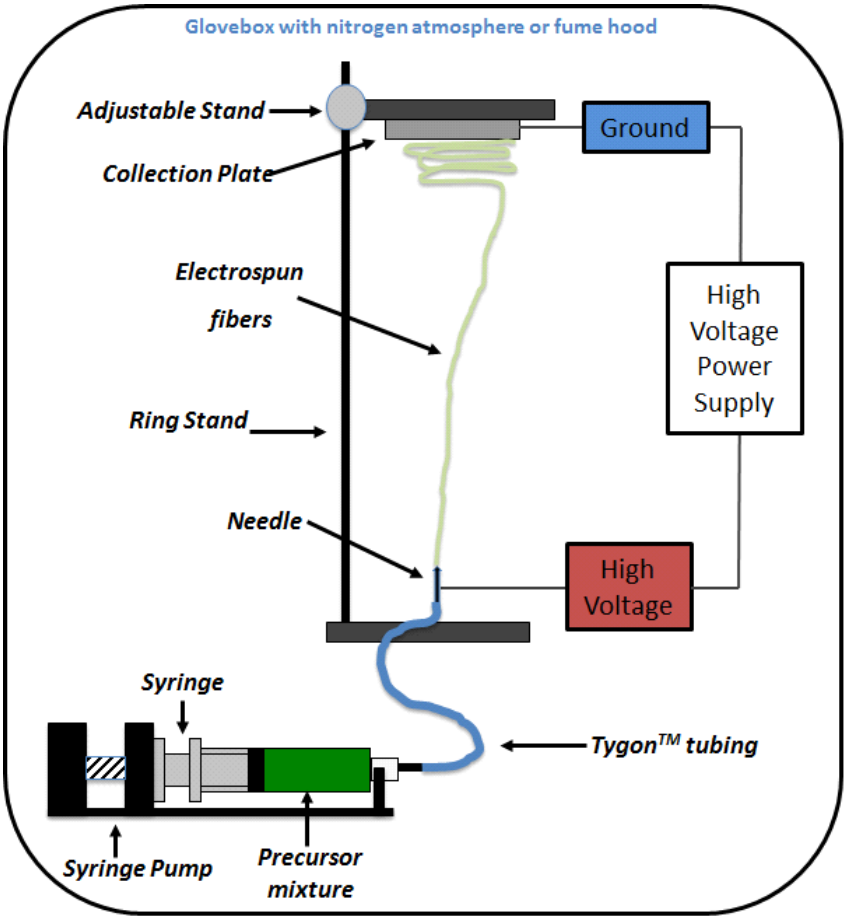

Figure 2.1. Electrospinning general setup

A. Powering Up. 1) Make up the solution in the appropriate solvent and make sure the precursor is fully dissolved (for polymer/nanoparticle solutions, sonicate the solutions for at least 5 mins), 2) wrap the collection plate in aluminum foil or clip graphite to ring stand, 3) attach the pink electrode (ground) to graphite or foil, 4) fill a syringe with the solution. Back dial out completely to allow pump to move and then place the syringe into the pump holder, 5) Attach Tygon™ tubing to syringe, 6) attach needle to the tubing with white connectors and clamp down tubing, 7) clip the black electrode to needle, 8) turn on the syringe pump (set it to 100 until you see a droplet then set it to the appropriate flow rate setting), 9) tTurn on the high voltage power source and set it to the appropriate setting. *B. Powering Down.* 1) Slowly power down the voltage, 2) turn off the power source, 3) turn off the syringe pump, 4) take down ES setup and clean up.

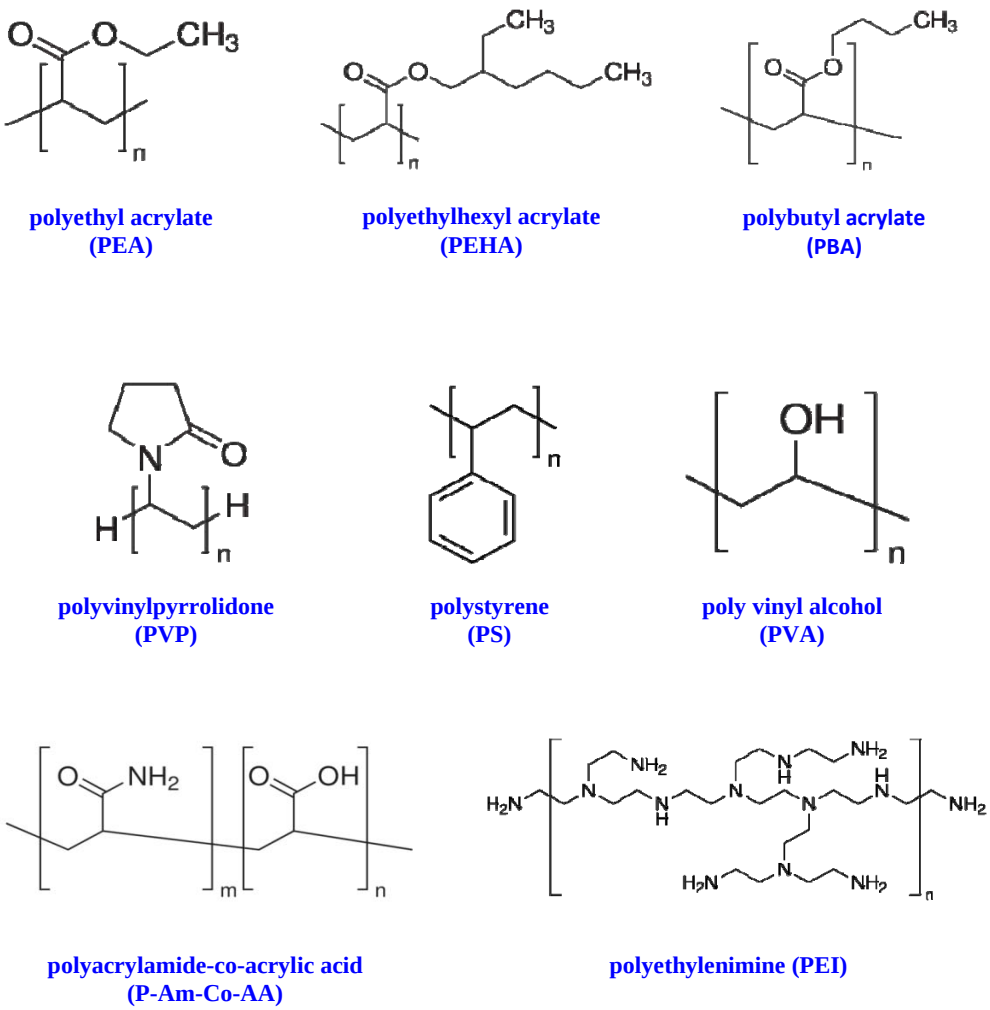

Figure 2.2. Schematic representation of polymers used for electrospinning.

Polymers. Electrospinning nanowires typically involves solutions of polymers and those that were evaluated for electrospinning in this project are shown in Figure 2.2. These polymers included polyvinylpyrrolidone (PVP), polystyrene (PS), poly vinyl alcohol (PVA), polyethyl acrylate (PEA), polybutyl acrylate (PBA), polyethylhexyl acrylate (PEHA), polyacrylamide-co-acrylic acid (P-Am-Co-AA), and polyethyleneimine (PEI). Additionally, a polystyrene/ poly(N-isopropylacrylamide) (PS/PNIPA) blend solution was also examined. ES was performed using an inverted setup (Figure 2.1) but the experimental parameters were adjusted for each material. For the polymer and polymer with nanoparticles solutions, the weight percentage of polymers ranged from 3 to 50 % in either THF, ethanol, chloroform, or water. The flow rates used ranged from 6 – 30 μL/min and the voltage setting was between 8 – 20 kV. The ES samples were spun onto either aluminum foil or graphite paper (Grafoil^{TM}). For all of the samples, the needle tip was watched to ensure no clogging occurred. The following tables show the polymer used, the conditions employed for ES, and the SEM images of the final ES material. For Table A the low solubility of the acrylate polymers (PEA and PEHA) led to materials that at best could be

described as electrosprayed. The low solubility for the polybutyl alcohol (PBA) also did not yield any material of interest.

	Table A		
	Polyethyl acrylate (PEA)	**Polyethyl hexyl acrylate (PEHA)**	**Polybutyl alcohol (PBA)**
	SEM images of electrospun (a) 50 % by weight PEA in THF and (b) neat PEA at 15 kV and 15µL/min	*SEM images of electrospun (a) 50 % by weight PEHA in THF at 15 kV and 15 µL/min, (b) 10 % by weight of PEHA in EtOH at 8kV and 15 µL/min, (c) 10 % by weight of PEHA in EtOH at 8kV and 15 µL/min*	*SEM images of electrospun (a) 50 % by weight PBA in THF*
A	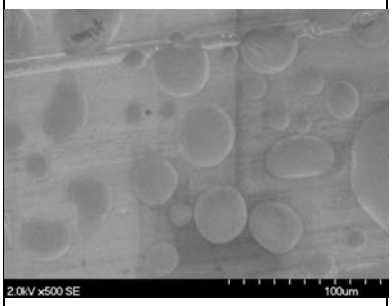	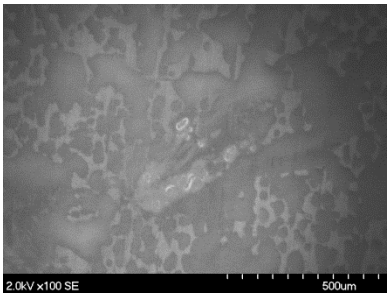	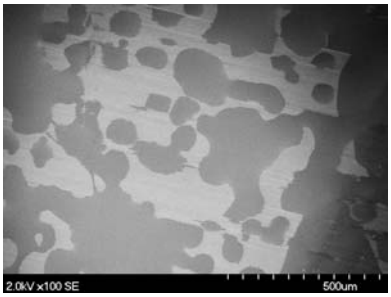
B	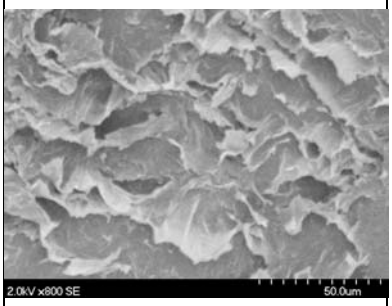	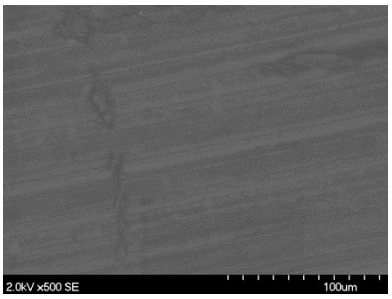	
C			

However, the efforts at the University of Florida did yield some extremely interesting materials that are detailed in the paper entitled “Thermally Tunable Wettability of Blended Vs. Crosslinked Poly(N-isopropylacrylamide) Electrospun Fiber Mats”.[15] This work reports on thermally tunable wettability of electrospun fiber mats of: polystyrene(PS)/poly(N-isopropylacrylamide) (PNIPA) blended (bl-PS/PNIPA) and crosslinked poly(N-isopropylacrylamide-co-methacrylic acid) (PNIPA-MAA) (xl-PNIPAMAA). Both the bl-PS/PNIPA and xl-PNIPAMAA fiber mats demonstrate reversibly switchable wettability, with

the bl-PS/PNIPA fiber mats approaching super-hydrophobic ≥150° and super-hydrophilic contact angle (CA) values at heating and cooling cycles, respectively. PNIPA chemistry and the Cassie-Baxter model were used to explain the mechanism behind the observed extreme wettability. Weight loss studies carried out by gravimetric method indicate that the blended PS/PNIPA and cross-linked PNIPA-MAA fiber mats are stable at extreme temperatures. This work also resulted in a patent application: "rapid response nanofiber mats" that switched between closer to superhydrophobic contact angle values to superhydrophilic characteristics in a few seconds with changes in environmental temperatures. However, these nanofiber mats have potentially been estimated to respond in micro to milli-seconds. The actual component and a schematic detailing the results are shown in Figure 2.3

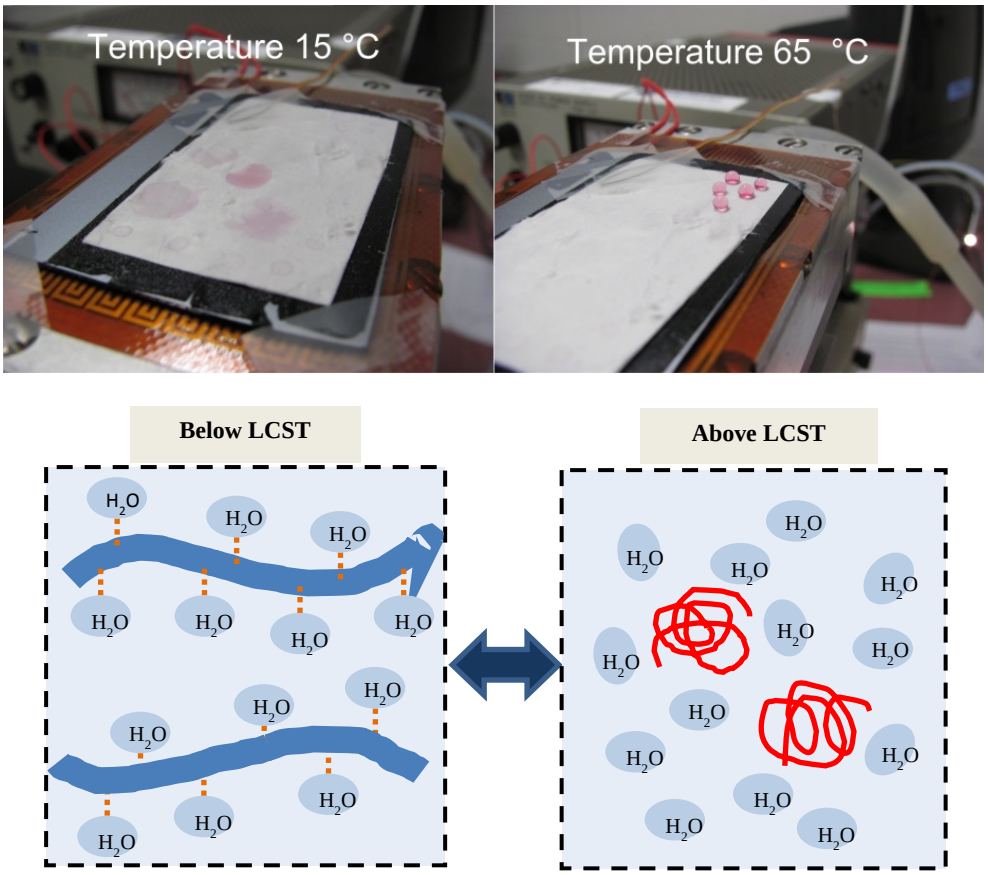

Figure 2.3 Above, the electrospun mat at the temperature shown. Below, describes the temperature dependent reversible hydrogen bonding between PNIPA and water molecules, showing the well-established mechanism schematically.

Following the UF lead, we explored the ES of acrylamide polymeric material, under slightly different conditions. Table B shows the wide variety of materials that can be achieved by simple changes in the solvent (EtOH to H_2O) and the rate at which the sample was pumped through the syringe.

	Table B		
	Polyacrylamide-co-acrylic acid (P-Am-Co-AA)	**Polyacrylamide-co-acrylic acid (P-Am-Co-AA)**	**Polyacrylamide-co-acrylic acid (P-Am-Co-AA)**
	SEM images of electrospun (a) 20 μm, (b) 10 μm, and (c) 5μm 10 % by weight P-Am-Co-AA in EtOH at 15 kV and 15 μL/min	*SEM images of electrospun 3 % by weight P-Am-Co-AA in H_2O at (a) 15 kV and 15 μL/min, (b) 20 μm and (c) 5 μm at 15 kV and 9 μL/min*	*SEM images of electrospun 3 % by weight P-Am-Co-AA in H_2O at (a) 20 kV and 6 μL/min, (b) 10 μm and (c) 2 μm at 20 kV and 9 μL/min*
A	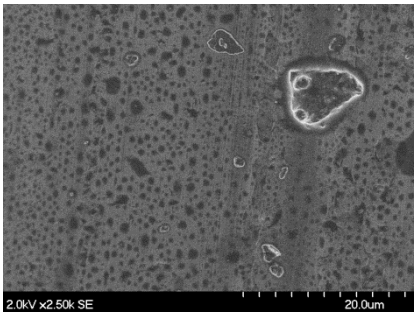	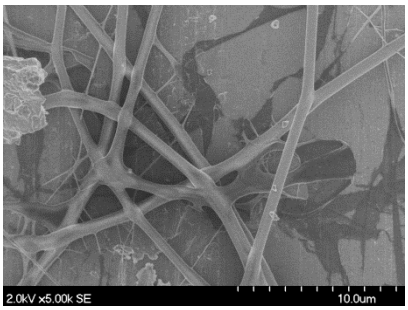	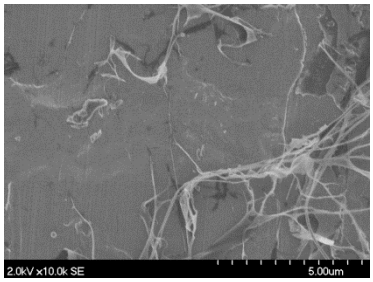
B	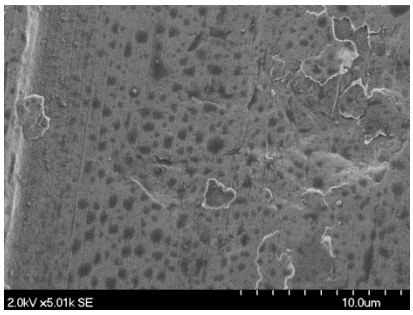	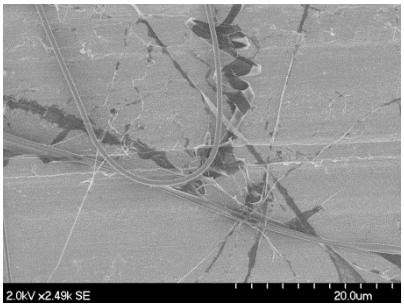	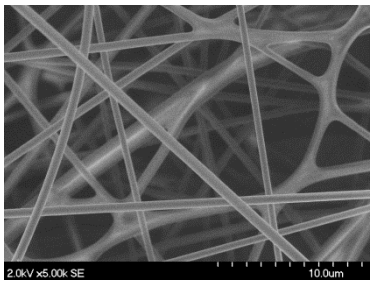
C	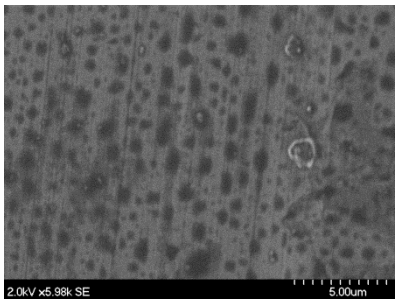	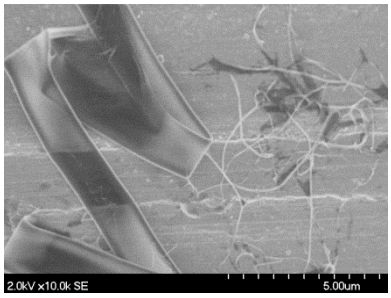	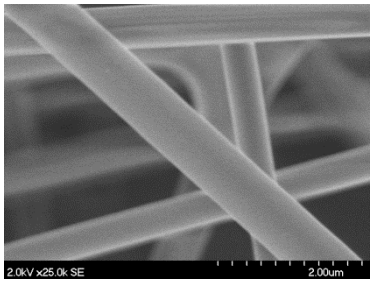

Another responsive polymer, PEI, was investigated under similar conditions. Again, the method had to be tailored to the individual polymer. The polymer was found to be reasonably soluble in the polar $CHCl_3$; however, the final materials generated were not of any utility. The results are shown in Table C.

Table C	**Polyethyleneimine (PEI)**
SEM images of electrospun 25 % by weight PEI in $CHCl_3$ at 15 kV and 30 µL/min	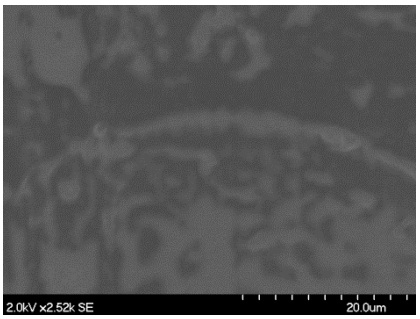

Further exploration of the ES of other polymers was undertaken using PVA, PVP, and PS (See Figure 2.2). The results of these studies are shown in Table D. It should be noted that each new sample required a unique set of parameters fine-tuned for the specific polymer investigated. This unique set of parameters involves solvent, flow rate, voltage applied, etc. As can be observed, the majority of polymers studied generated wires. While the PVA showed improved wire production, the resulting samples appear 'wet'. This was associated with the low solubility which required dilution in ethanol.

In contrast, the PVP and PS systems yielded the expected and desired mat of wires. Again, different solvent systems were required for the PVP versus the PS systems, demonstrating the tunability required for each sample system. The surface morphological variations on these fibers is interesting. For the PVP, the wires appear smooth but the PS fibers have rough edges. The samples were both processed through an identical needle tip, so this must be a result of the solvent or applied voltage. Further studies to understand and exploit this behavior is required.

	Table D		
	Polyvinyl alcohol (PVA)	**Polyvinylpyrrolidone (PVP)**	**Polystyrene (PS)**
	SEM images of electrospun fibers of 8 % by weight PVA solution in EtOH at) 15 kV, 15 µL/min (a) 10 µm and (b) 5 µm	*SEM images of electrospun fibers of 10 % by weight PVP solution in EtOH at (a) 8 kV, 30 µL/min, (b) 15 kV, 15 µL/min, and (c) 15 kV, 30 µL/min.*	*SEM images of electrospun fibers of (a) 5 % by weight PS solution in $CHCl_3$ at 15 kV and 9 µL/min, (b) 5 % by weight PS solution in $CHCl_3$ at 15 kV and 15 µL/min, and 15 % by weight PS solution in $CHCl_3$ at 15 kV and 15 µL/min (b) 5 µm and (c) 1 µm.*
A	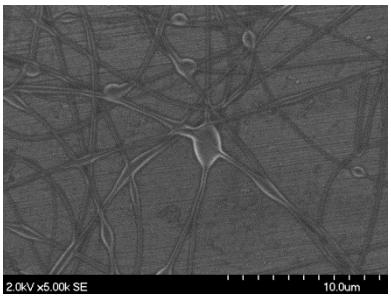	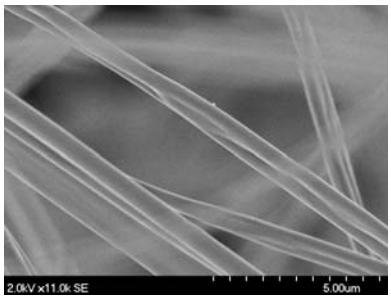	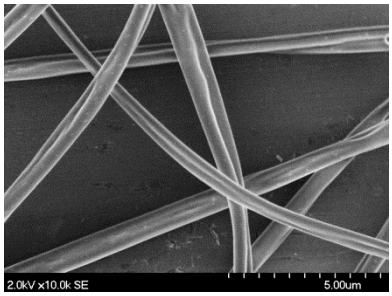
B	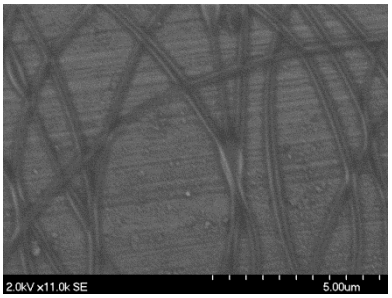	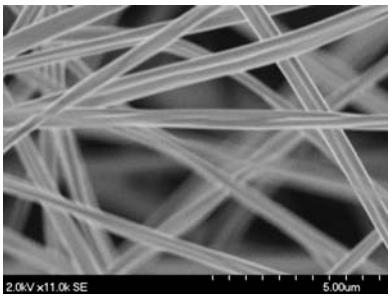	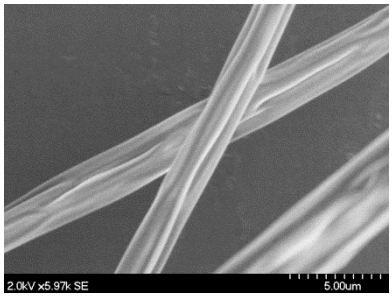
C		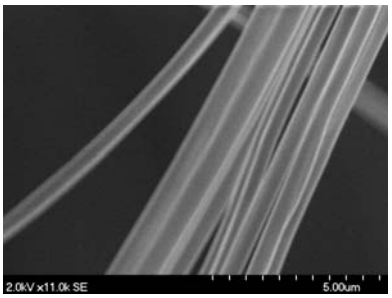	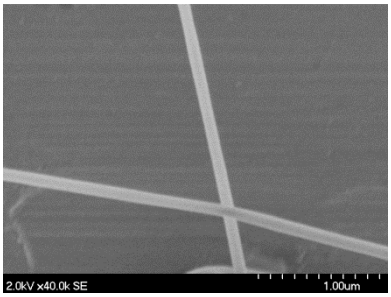

Nanocomposites. Based on the scale bar it is obvious that these polymeric materials are not in the nanoregime but that is based on the tip size of the needle and with adjustments could be easily reduced. Further, the 'nano' aspect of the Responsive Nanocomposite was originally meant to refer to the inclusion of the nanoparticles discussed previously. The inclusion of these species was undertaken and the results are shown in Table E. Due to the high quality mat of wires that were easily and reproducibly generated, the initial nanocomposite material investigated was the PVP system. PVP is NOT a responsive polymer but the first studies were

focused on proving that nanocomposites with metallic nanoparticles could be generated by this method. Table E shows the results of these studies.

	Table E		
	PVP with Au^o dots.	***PVP with Au^o rods.***	***P(Am-Co-AA) with Au^o rods.***
	SEM images of electrospun PVP in EtOH with varying concentrations of Au^o dots in toluene at 15 kV and 15 µL/min: (a) 5 % by wt. Au^o dots, (b) 10 % by wt. Au^o dots, and (c) 15 % by wt. Au^o dots	*SEM images (a) 5 µm and (b) 1 µm and (c) TEM images of electrospun PVP in EtOH with1.5 % by weight Au^o nanorods in H_2O at 15 kV and 15 µL/min.*	*SEM images of electrospun P(Am-Co-AA) with 2% by weight Au^o nanorods at (a) 15 kV and 6µL/min and (b) 20 kV and 6µL/min.*
A	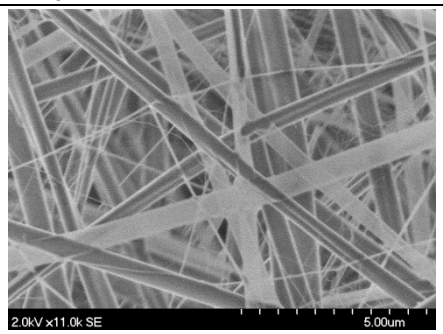	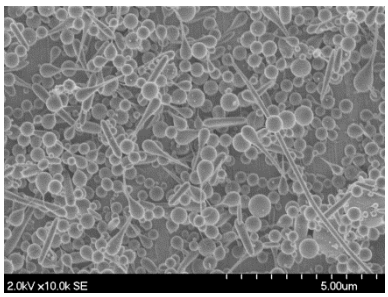	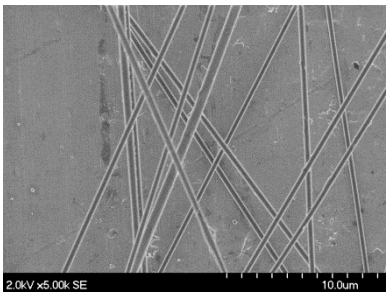
B	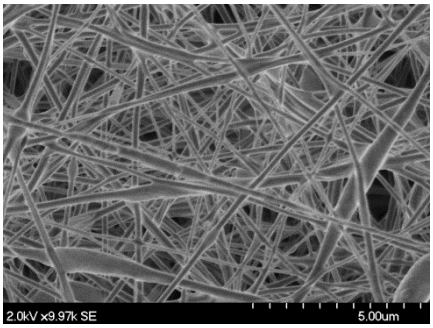	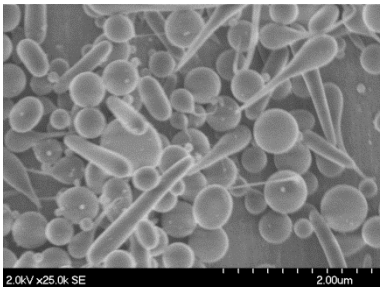	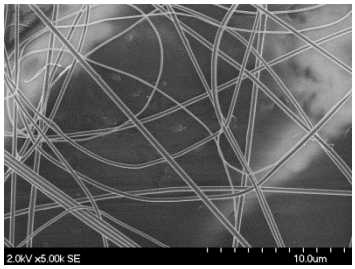
C		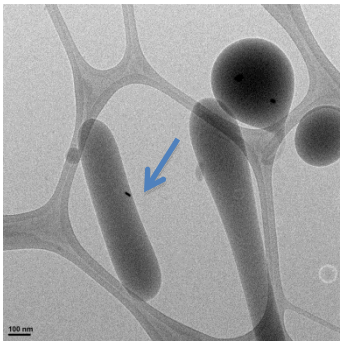	

The first nanomaterial introduced was Au^o dots. This material was selected for several reasons including availability, functionality variations available, and assumed surface differential reactivity with water. It was determined that the load levels of the nanoparticles should be kept at low levels to maintain manageable viscosities. However, nanoparticles can be observed using the higher magnification offered by TEM (see Table E row C, arrow). As can be observed, the particle are present and may be at the surface, which would be ideal for the responsive

nanocomposite which upon activating should encompass the particle. Further work with the acrylate derivatives to increase load levels are being pursued (see Table F). In particular, the functionalization of the particles may be the key to increasing the amount of particle without destroying the fluidity of the monomer precursors to the polymer. Alternative metals were also investigated with an emphasis placed on Ag^o due to similar reasons noted for Au^o.

	Table F	
	P(Am-Co-AA) with Ag^o dots.	***PVP with Ag^o dots.***
	SEM images of electrospun P(Am-Co-AA) with 25 % by weight Ag^o dots at (a) 15 kV and 6µL/min and 20 kV and 9 µL/min (b) 5 µm (c) 2 µm.	*SEM images of electrospun PVP in EtOH with varying conc.of Ag^o dots in $CHCl_3$ at 15 kV and 15 µL/min: (a) 10 % by wt. Ag^o dots and (b) 25 % by wt. Au^o dots*
A	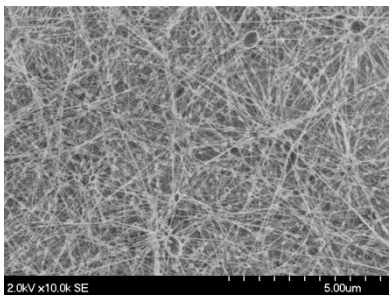	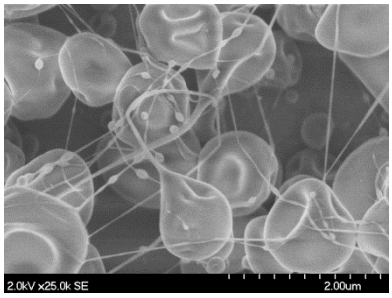
B	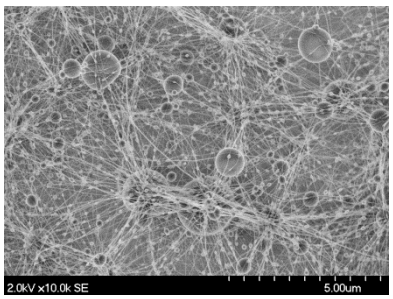	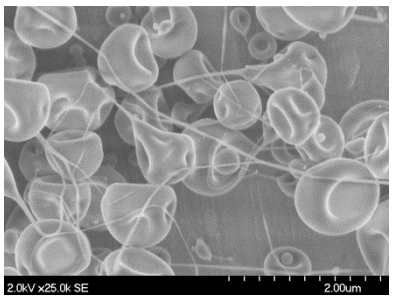
C	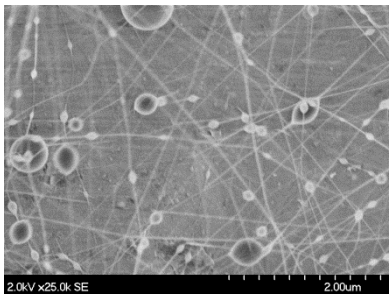	

Testing of Responsive Nanocomposites. Several samples of responsive nanocomposites were evaluated using contact angle measurements on a VCA Optima, AST Prouducts, Inc. instrument. The automated dispensing system used a 30 gauge flat tipped stainless steel needle and DI water that had a resistivity of > 18 MΩ, collected from a nanopure Milli-Q purification system (Millipore, Inc.). The observed angles are shown below in Table G for the room temperature investigations. Based on the closest comparison of samples, the loadings seem to have reduced the hydrophobicity of the polymer. Additional work is necessary to make meaningful comparisons.

Table G							
Sample Room Temperature	**Solv't**	**kV**	μL	**Min**	**Max**	ΔT Min	ΔT Max
Clean Aluminium foil	-	-	-	*97.3*	*97.7*	-	-
3 % PamAA	H_2O	15	9	*49.0*	*54.0*	*59.00*	*62.20*
3 % PAmAA	H_2O	15	15	*50.30*	*62.40*	*78.30*	*77.80*
3 % PamAA	H_2O	20	6	*46.30*	*65.20*	*53.90*	*58.90*
3 % PAmAA (45-60 min)	H_2O	20	9	*17.60*	*29.60*	*22.00*	*24.20*
3 % PamAA (3 h)	H_2O	20	9	*22.50*	*24.90*	-	-
0.5 mL AuNR 5.0 mL 3 % PAmAA	H_2O	20	9	*19.00*	*24.20*	*24.20*	*24.40*
0.5 mL AuNRs 5.0 mL 3% PAmAA	H_2O	15	6	*29.80*	*38.70*	*24.40*	*26.70*
25% Ag PAmAA	H_2O	20	9	*18.60*	*25.70*	*27.50*	*29.20*
25 % Ag PAmAA	H_2O	15	6	*22.30*	*27.30*	*22.40*	*24.40*

Further high temperature analyses were conducted to determine the effects of temperature on the hydrophobicity of the compounds. Results have shown that with the increase in temperature to 60 degrees C, the pure polymer compounds generally have an increase in their contact angles, but the increase is very slight in magnitude. As for the gold and silver functionalized compounds the contact angles seem to remain relatively unaffected noting only slight changes (at most 4 degrees). What is interesting is that the AuNR doped polymer compound spun at 15kV and 6μL/min decreased its contact angle whereas the other Au doped compounds either exhibited no change or a higher contact angle. Further investigation is necessary to determine why this anomaly occurs.

Ceramic Precursor

As an alternative to organic matrices, we became interested in generating an electrospun wire that did not utilize a polymer at any point in the process. This, if it could be made small enough, could also be the nano-aspect of the responsive nanocomposite. Literature reports have shown a polymer ceramic mixture can be processed to remove the organic component, leaving a ceramic nanowire. However, we chose to develop novel precursors that could form the wire without a polymer. In order to do this, the complex must be asymmetric in its decomposition to favor premature decomposition followed by linking, etc. Or, the compound must have built in linkages. The different systems investigated for electrospinning included: tin(II) amide/alkoxides,[16] tin(II) amides,[16] and group 4 metal alkoxides/carboxylates ($M(OR)_4$, where M = Ti, Zr, Hf).[17] The synthesis of the various precursors is discussed briefly below.

i.Tin: In order to develop the asymmetric ligated tin(II) precursors of interest, it was necessary to synthesize a suitable precursor. Due to its high solubility, low decomposition temperature, and general high chemical reactivity, $Sn(NR_2)_2$ was thought to be a suitable precursor. It was synthesized was from the metathesis of the metal halide with an alkali metal amide (eq 1). With this in hand, reaction with a series of arylalcohols was undertaken forming the hetero- (n = 1)

and homoleptic (n = 2) species (eq 2). The H-OAr reagents used included H-OC_6H_4(R)-2: R = CH_3 (H-*o*MP), $CH(CH_3)_2$ (H-*o*PP), $C(CH_3)_3$ (H-*o*BP)] or [H-$OC_6H_3(R)_2$-2,6: R = CH_3 (H-DMP), $CH(CH_3)_2$ (H-DIP), $C(CH_3)_3$ (H-DBP)]. The reaction mixtures were stirred for 12 h. For those reactions that formed a small precipitate, it was removed by centrifugation. The reaction or mother liquor was set aside, open to the glovebox atmosphere to allow the volatile fraction to slowly evaporate until crystals formed. All analyses and electrospinning were performed on the crystalline material.

$$\mathbf{SnCl_2 + 2\,LiNR_2 \rightarrow Sn(NR_2)_2 + 2LiCl} \qquad \mathbf{(1)}$$

$$\mathbf{Sn(NR_2)_2 + \mathit{n}\,H\text{-}OAr \rightarrow Sn(OAr)_{\mathit{n}}(NR_2)_{2\text{-}n} + \mathit{n}\,H\text{-}NR_2} \qquad \mathbf{(2)}$$

ii. Group 4 metals (Ti, Zr, Hf): Two series of group 4 metal alkoxides were synthesized and investigated for electrospinning. These alkoxides were either neo-pentoxide (ONep) or *tert*-butoxide (OBu^t) derivatives modified with a series of sterically varied carboxylates (H-ORc) in toluene (eq 3). The resulting $M(ORc)_n(OR)_{4-n}$, where M = Ti, Zr or Hf, OR = ONep or OBu^t, H-ORc = H-OPc (HO_2CCHMe_2), H-OBc (HO_2CCMe_3), H-ONc ($HO_2CCH_2CMe_3$), and n = 1, 2, or 4. The reaction mixtures were stirred for 12h. The reaction or mother liquor was set aside open to the glovebox atmosphere to allow the volatile fraction to slowly evaporate until crystals formed. For these reactions, the commercially available $M(OBu^t)_4$ was used and M(ONep) was synthesized from literature reactions.[17]

$$\mathbf{M(OR)_4 + \mathit{n}\,H\text{-}ORc \rightarrow M(ORc)_{\mathit{n}}(OR)_{4\text{-}\mathit{n}} + \mathit{n}\,H\text{-}NR_2} \qquad \mathbf{(3)}$$

Once isolated, the various compounds were electrospun by dissolving the precursor in a polar solvent. For tin and group 4 metals, each compound (0.200 mmol) was dissolved in 3 mL of THF to produce a 0.0667 M solution. For tin, the solution was used for ES at a flow rate of 15 μL/min and a voltage setting of 15 kV for 45-60 mins. For group 4 metals, the flow rate and voltage setting was 15 μL/min at 15 kV, 60 μL/min at 18 kV , or 30 μL/min at 20 kV. These solutions were ES for 45-60 mins. The various results for the different precursors isolated are shown below. A detailed effort is available in the literature. [16]

Once these compounds had been developed, the precursors were evaluated in the electrospinning setup shown in Figure 2.1. Using tin(II) amide $[Sn(\mu\text{-}NMe_2)_2]_2$, tin(II) amide alkoxides $[(OAr)Sn(\mu\text{-}NMe_2)]_2$ [where OAr = *o*MP (**1**), *o*PP (**2**), *o*BP (**3**), DMP (**4**), DIP (**5**), DBP (**6**)], and tin(II) alkoxides ($[Sn(\mu\text{-}OAr)_2]_\infty$ (where OAr = *o*MP (**7**), *o*PP (**8**)), dinuclear $[(OAr)Sn(\mu\text{-}OAr)]_2$ (where OAr = *o*BP (**9**), DMP (**10**) or DIP/$HNMe_2$ (**11**)), or mononuclear $[Sn(DBP)_2]$ (**12**) complexes, electrospun materials were attempted that did not employ a polymeric matrix.

The first attempt focused on the $[Sn(\mu\text{-}NMe_2)_2]_2$ with products that appeared to be electrosprayed versus the desired electrospun nanowires. However some wire-like formation can be observed in the various SEM images (see Figure 2.4).

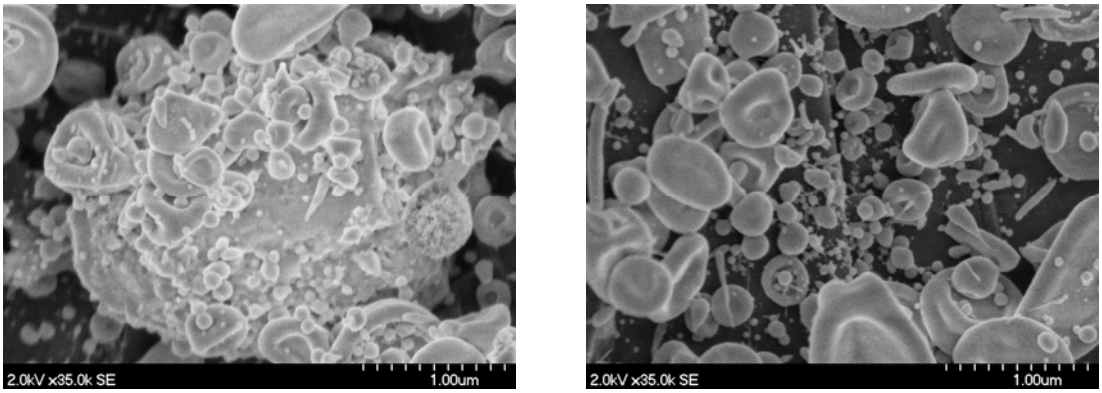

Figure 2.4 SEM images of electrospun $Sn(NMe_2)_2$ in THF

This led to a study of the novel $[(OAr)Sn(\mu\text{-}NMe_2)]_2$, $([Sn(\mu\text{-}OAr)_2]_\infty$, and $[(OAr)Sn(\mu\text{-}OAr)]_2$ precursors. From ES routes, the heteroleptic species were found to form 'tadpole-shaped' materials. Results from these experiments are show in Table H. The unusual tadpole shape is thought to be due to one of two phenomena: (i) the drop pulls away from the top without ES or (ii) the ES starts but prior to completion the drop breaks away. In contrast, the homoleptic species formed electrosprayed nanodots as can be seen in Table G. The one exception noted was for **7**, where, without use of a polymer matrix, nanowires of Sn^o, decorated with micron sized 'balls' were observed. Due to the small amount of material generated, PXRD patterns were inconclusive to the identity of the generated material; however, cyclic voltammetry on select samples was used to tentatively identify the final Sn^o (from **7**) with the other sample identified as SnO_x (from **1**).

H	Mono sub Precursor	SEM image		Di sub Precursor	SEM image
1	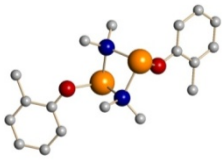	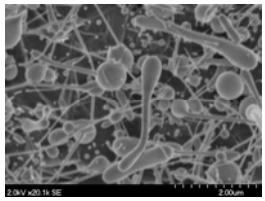	4	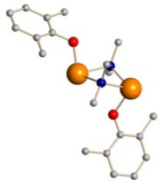	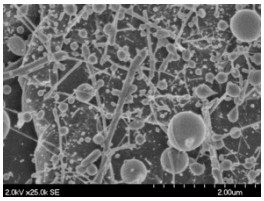
2	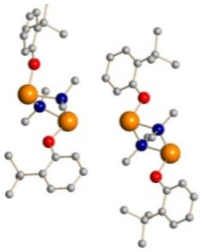	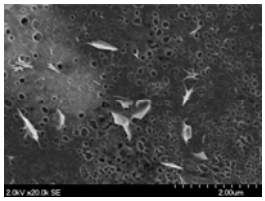	5	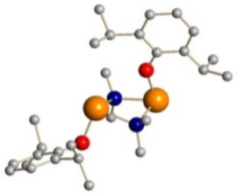	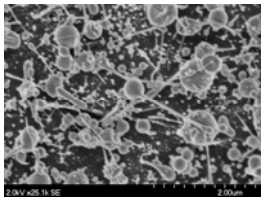
3	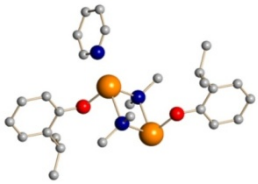	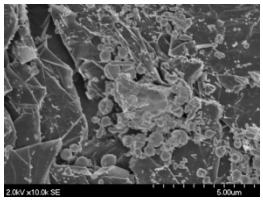	6	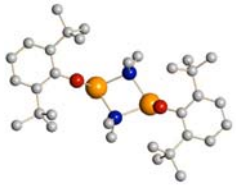	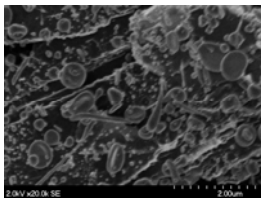

G	Mono sub Precursor	SEM image		Di sub Precursors	SEM image
7	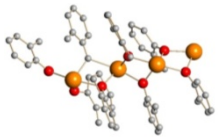	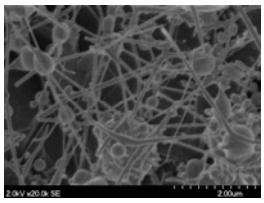	10	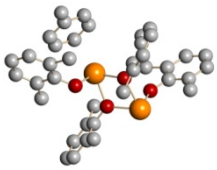	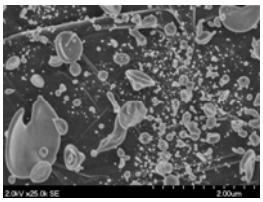
8	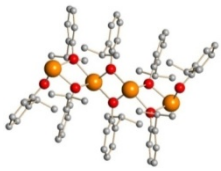	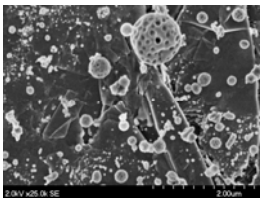	11	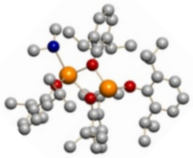	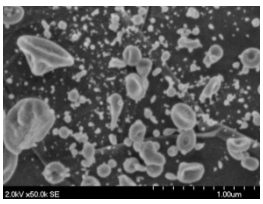
9	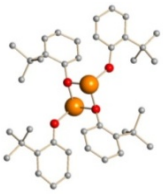	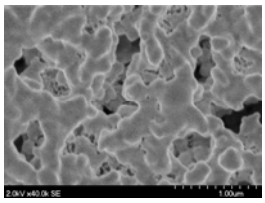	12	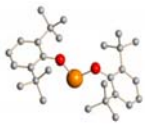	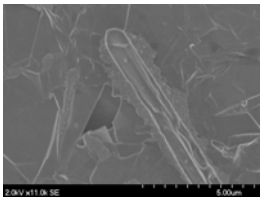

To examine the effects of changing the flow rate and voltage settings on the final material morphology, ES of $[Sn(NMe_2)(oMP)]_2$ was undertaken (see Figure 2.5). By keeping the flow rate constant and decreasing the voltage from 15 kV (Figure 2.5b) to 10 kV (Figure 2.5a), longer and thinner wires were formed. The effect of varying the flow rate was observed by increasing and decreasing this parameter. Decreasing the flow rate from 15 µL/min (Figure 2.5b) to 12 µL/min, yielded thin rods. This may be the result of the solution being pumped too slow to maintain a Taylor cone and thus primarily rods form. By increasing the flow rate to 20 µL/min nanowires with diameters of 50-80 nm were generated (Figure 2.5c).

(a)

(b)

(c)

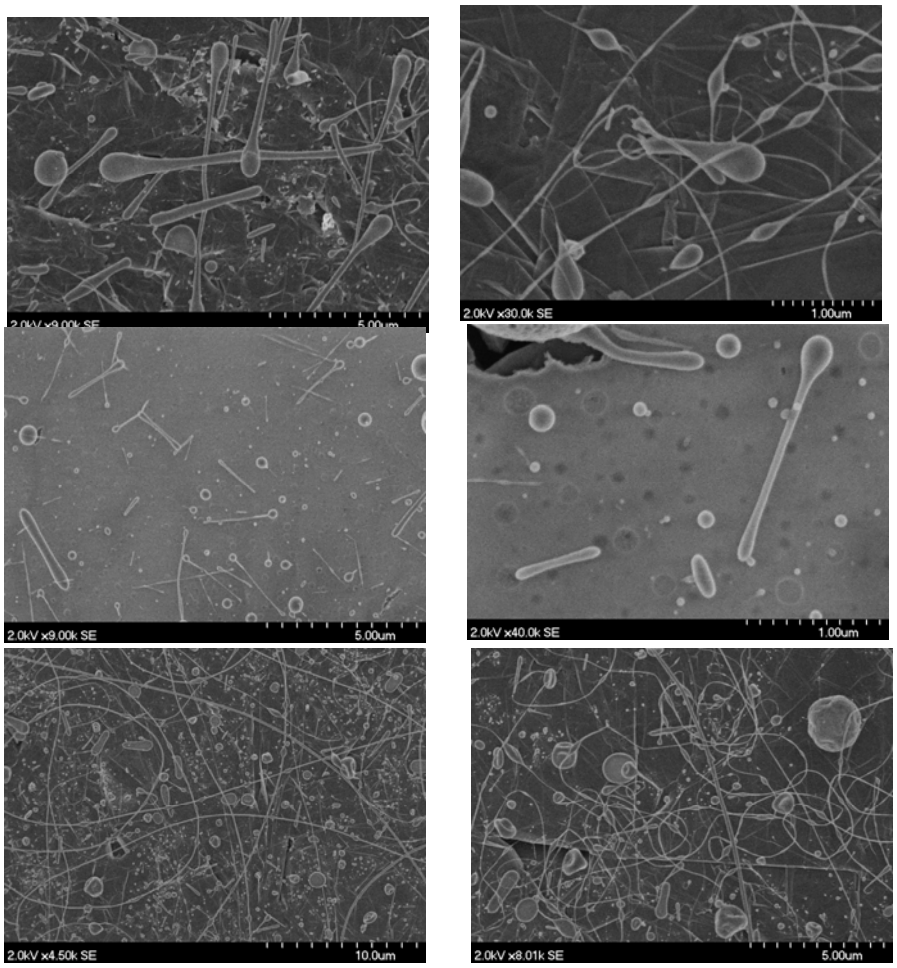

Figure 2.5. SEM images of ES of [Sn(NMe2)(oMP)]2 at (a) 10 kV and 15 µL/min, (b) 15 kV and 12 µL/min, and (c) 15 kV and 21 µL/min.

Due to too small of an amount of material generated, the identification of the nanomaterials generated and identification of the phase formed using PXRD analyses was not possible. Cyclovoltammetry (CV) electrochemical analyses were explored as a means to identify the resultant material. If SnO formed, then upon a reductive sweep, a Sn^{2+} to Sn^0 reduction peak at approximately -0.05V vs. ref will be present. If Sn^0 was present instead, then no peak will be observed upon reduction but upon an anodic sweep, an oxidation peak will be present. The cyclic

voltammogram plots for the four separate electrospun samples (2 h deposition time): (a) **1**, (b) **1** (8 h), (c) **5** , and (d) **7** are shown in Figure 2.6.

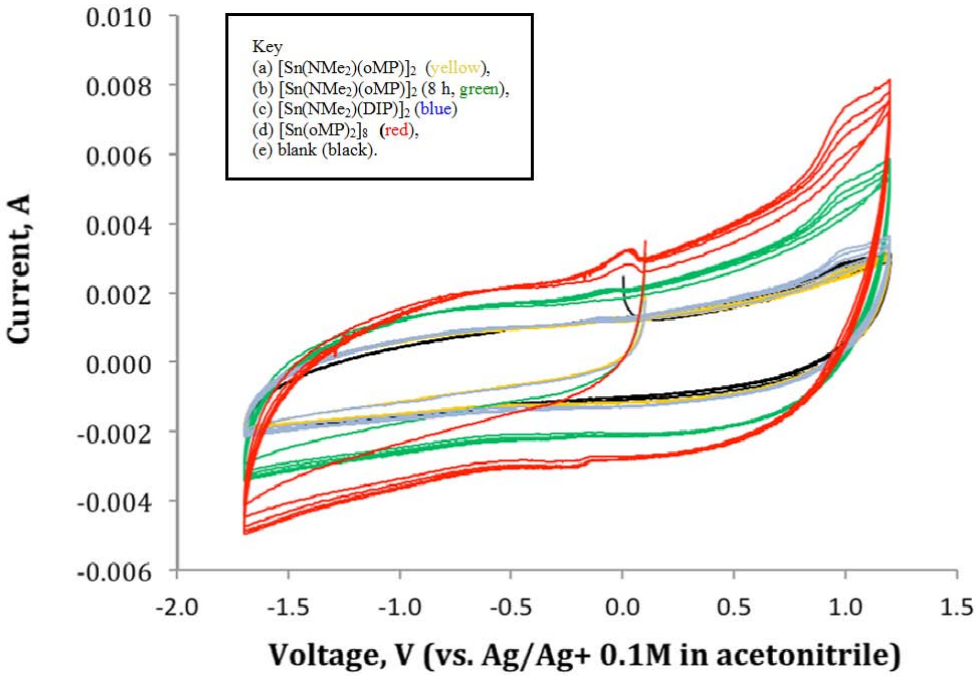

Figure 2.6. Cyclic voltammograms of electrospun wires (2h) from precursor (a) $[Sn(NMe_2)(oMP)]_2$ (yellow), (b) $[Sn(NMe_2)(oMP)]_2$ (8 h, green), (c) $[Sn(NMe_2)(DIP)]_2$ (blue) (d) $[Sn(oMP)_2]_\infty$ (red), (e) blank (black).

For the samples generated from compound **1** (8h) and **7** there was sufficient material present for electrochemical analysis. For **1** (8h) electrospun materials, no peaks were observed for the reductive sweep. This indicates the material generated was SnO. Subsequent sweeps showed similar peaks as those present for the ES material from **7**. For the **7** electrospun materials, there was no reduction peak on the first cathodic sweep, but a significant oxidation peak at approximately -50 mV (vs. ref) was noted; this is consistent with the potential of Sn^0 to Sn^{2+} oxidation.

Group 4 metal alkoxides (Ti, Zr, Hf). Early transition metal ceramic oxide materials have a number of electrochemical applications that would be useful for initiating the responsive nancomposites of interest. Again, pursuit of the polymer free materials was undertaken. Several routes were explored with an emphasis on the carboxylates (HORc) for this effort. The Group 4 metals were used due to their widespread use for a wide variety of electrical applications. The following discussion focuses on the (i) parent alkoxides, (ii) the carboxylic acid modified derivatives, and (iii) the full carboxylate species and the resulting ES materials generated therefrom.

The initial efforts for ES of ceramic nanowires focused on using just the metal alkoxide precursor. If successful, this would eliminate the need for further precursor development and

would establish a baseline to compare with any modifications. The OBu^t derivatives are oils and thus not structurally characterized; however, it is firmly established that they are sterically hindered monomers. Therefore, we did not pursue any ES efforts with these materials. The ONep derivatives are all structurally characterized (Ti, Zr, and Hf) .[17] The resulting materials generated are shown below in Figure 2.7.

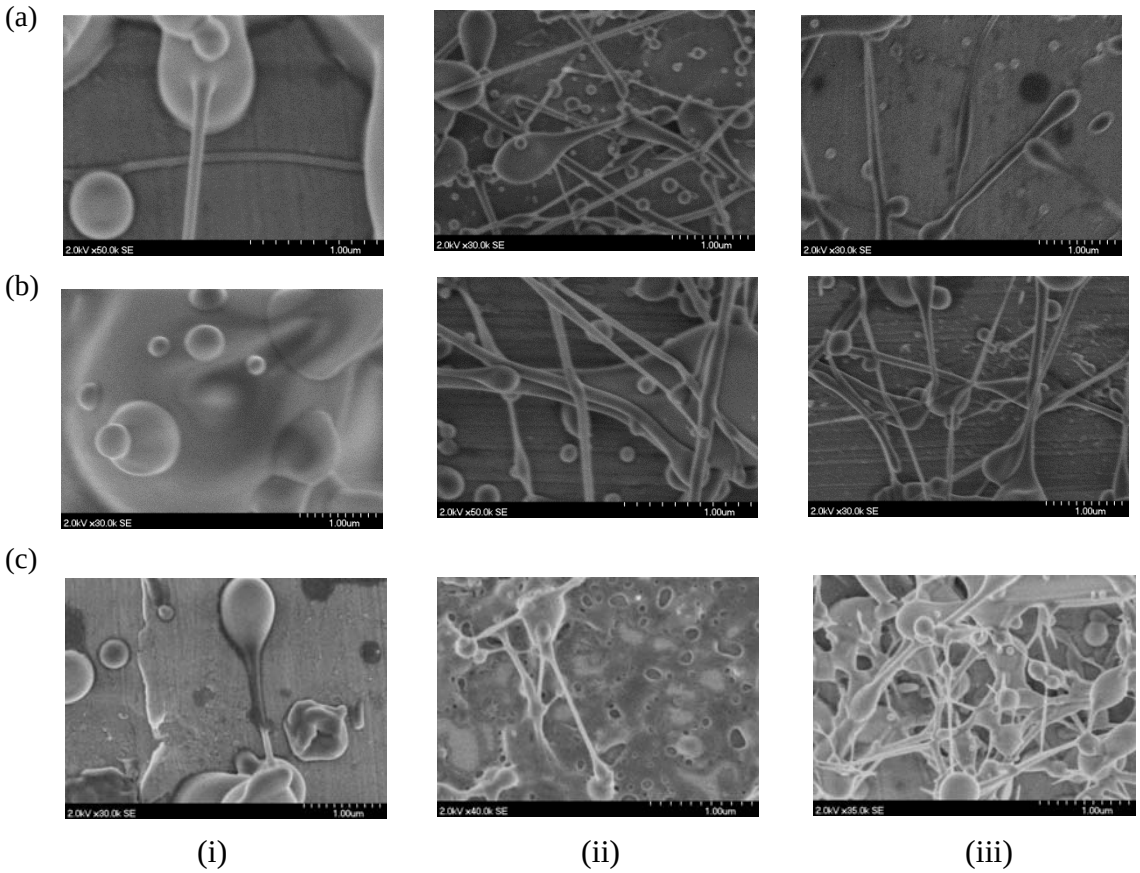

Figure 2.7. SEM images of electrospun 0.200 mmol (i) Ti, (ii) Zr, (iii) Hf neo-pentoxide in THF at (a) 15 kV, 15 µL/min, (b) 18 kV, 60 µL/min, and (c) 20 kV, 30 µL/min.

As can be observed, the heavier congeners readily form wires, with balls on them. This is not an unusual occurrence for polymeric systems that are not at high enough flow rate. Attempts to adjust either the molarity or speed rate did not yield wire like morphologies. The smaller Ti species made tadpole shaped complexes again. Due to the promising morphologies noted here, we undertook further studies using modified metal alkoxides. Since any changes made for the precursor require full characterization, the structures obtained are shown below with the results noted in the ES material.

Modification of the $M(ONep)_4$ was undertaken, focusing on the heavier elements due to their promising results obtained for the parent alkoxides. The OPc, OBc, and ONc mono substitution products for the Zr system were obtained and identified as dinuclear species. These are shown in Figure 2.8a.

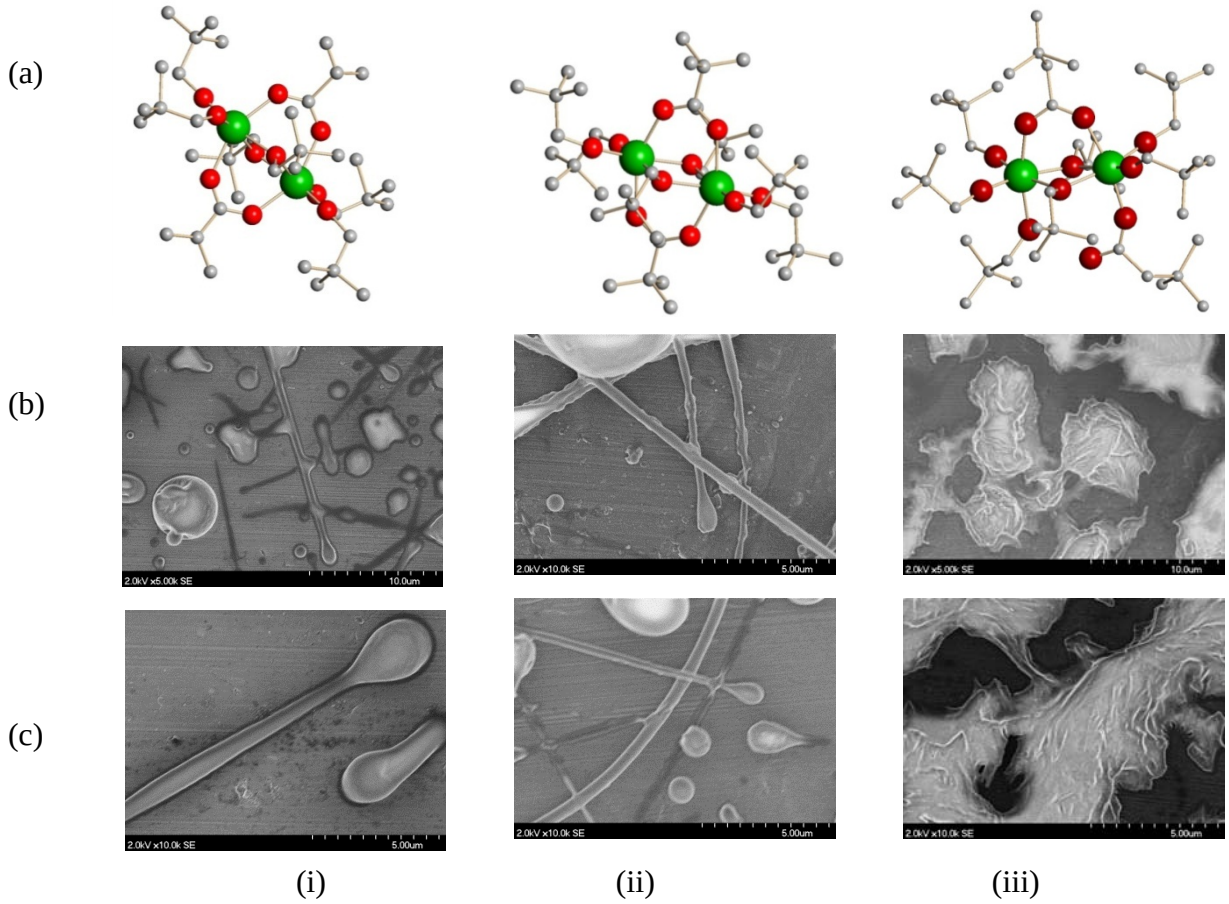

Figure 2.8. (a) Structure plot of $Zr(ONep)_3(ORc)$ (i = OPc, ii = OBc, iii =ONc) SEM images of electrospun 0.200 mmol $Zr(ONep)_3(ORc)$ in THF at (b) 10 kV, 30 µL/min, and (c) 10 kV, 60 µL/min

From the SEM images shown in Figure 2.8 b and c, it is apparent that the substitution has had a negative effect on generating wire like morphologies. The larger the sterically demanding ORc moiety, the worse the ability to ES. This is not related to solubility, since all species demonstrated the same generally high solubility. Exploration of the Hf species was undertaken as well. The initial efforts focused on the ORc modified OBu^t derivatives. Again, identification of the starting material was critical and Figure 2.9a shows the $Hf(OBu^t)_3(ORc)$ (ORc = (i) OPc, (ii) OBc) derivatives. The products isolated from the ES experiments were also not wire like morphologies. Switching to the Hf/ONep system finally, nanowire formation was noted for the ONep/OBc system(Figure 2.10). Again, droplets on the wires were observed for this system. Interestingly, the smaller OPc and larger ONc derivatives did not form wires but resembled the other failures noted for the OBu^t/ORc complexes.

(a)

(b)

(c)

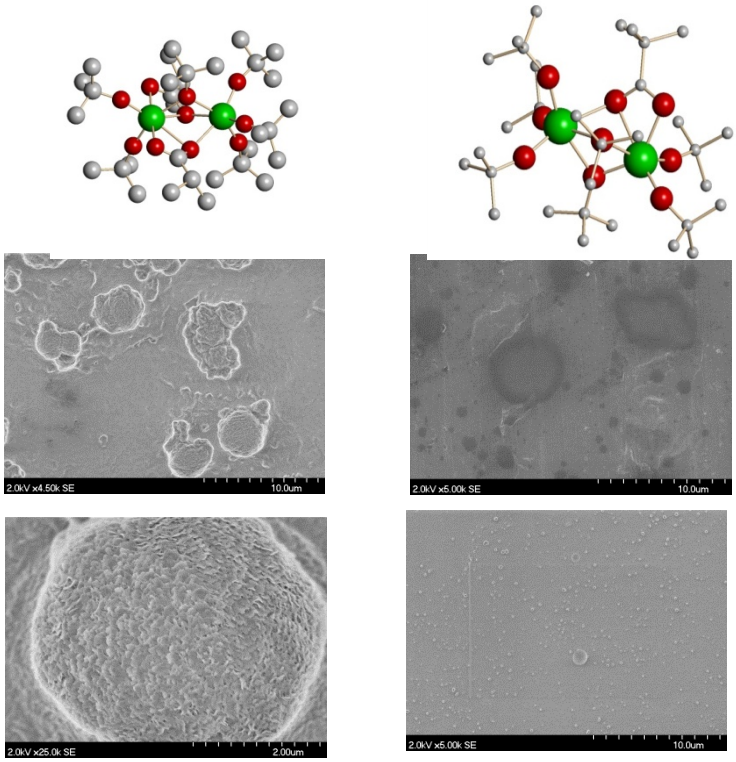

(i) **(ii)**

Figure 2.9. (a) Structure plot of $Hf(OBu^t)_3(ORc)$ (ORc = (i) OPc, (ii) OBc) SEM images of electrospun 0.200 mmol $Hf(OBu^t)_3(ORc)$ in THF at (b) 10 kV, 30 µL/min, and (c) 10 kV, 60 µL/min

(a)

(b)

(c)

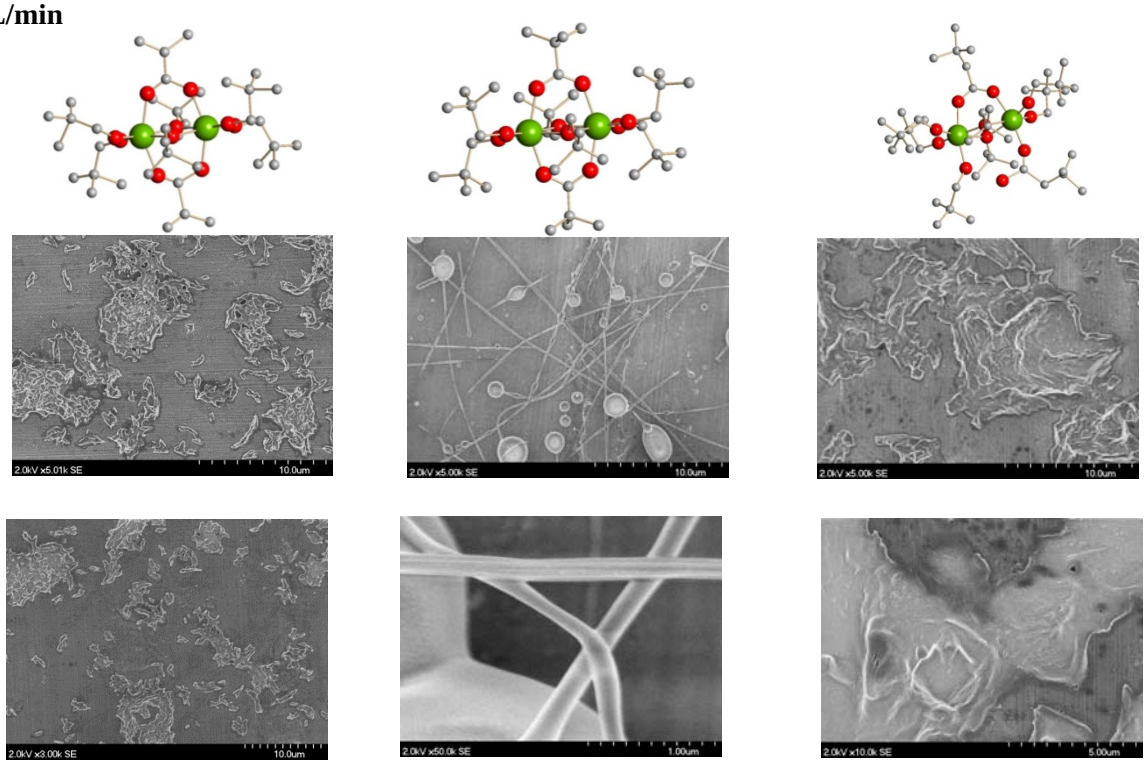

(i) **(ii)** **(iii)**

Figure 2.10. (a) Structure plot of $Hf(ONep)_3(OR)$ (ORc = OPc, OBc, ONc) SEM images of electrospun 0.200 mmol $Hf(ONep)_3(ORc)$ in THF at (b) 10 kV, 30 µL/min, and (c) 10 kV, 60 µL/min

In addition, the homoleptic ORc species were of interest. Surprisingly, little information is available on the structural properties of these compounds. Therefore, we undertook the synthesis and characterization of the $M(ORc)_4$ species. The Hf species are shown in Figure 2.11a. As can be seen, independent of the steric bulk of the pendant chain of the ORc ligand, the compounds all adopt dincuelar complexes with bridging and terminal ORc ligands available. The terminal ORc is ideal for linking to the next droplet and these were ES as before. Figure 2.11 b and c show the results of these studies. As can be seen, the OPc appears to merely electrospray the final ceramic material. However, for the larger, more sterically demanding ORc ligands, the final morphologies are wire-like. However, the OBc reveals a previously unobserved grain structure that forms the final wire. The ONc are much smoother. A great deal more work to understand why these differences occur is underway.

(a)

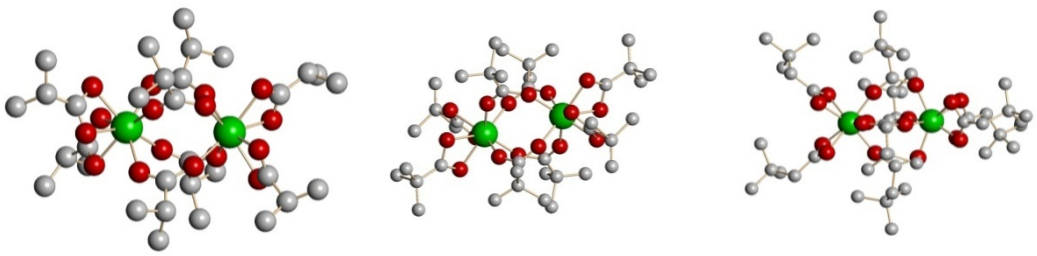

(b)

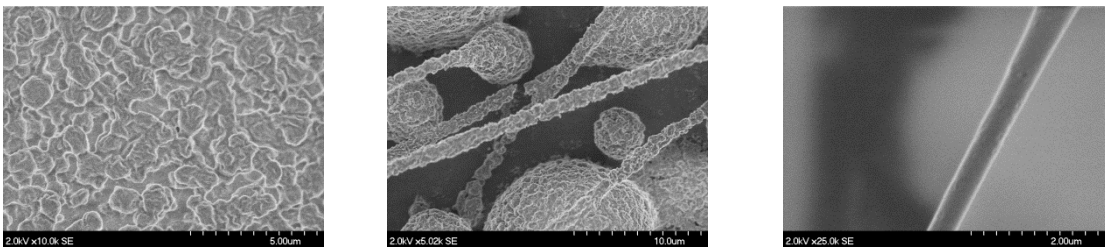

(c)

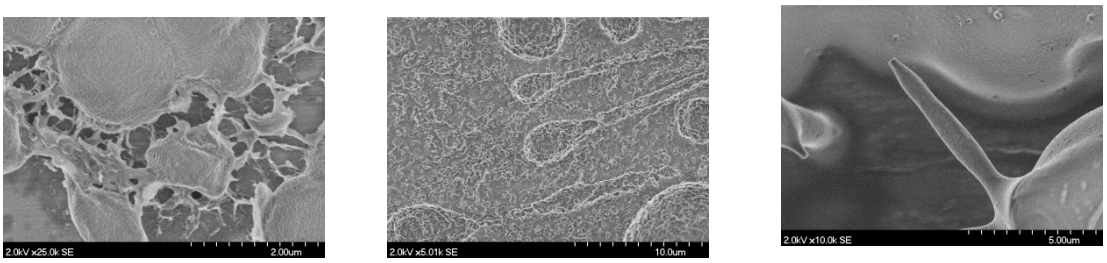

(i) (ii) (iii)

Figure 2.11. (a) Structure plot of $Hf(ORc)_4$, (ORc = OPc, ii OBc, (iii) ONc) SEM images of electrospun 0.200 mmol $Hf(ORc)_4$ in THF at (b) 10 kV, 15 µL/min, and (c) 10 kV, 60 µL/min

The homoleptic precursors have the necessary 'linker' ligands, which allow for fiber formation for the heavier congeners. The interesting grainy morphology needs to be explored and exploited for the increased surface area these fibers will impart to any system, thereby increasing the interaction with the matrix material. The following Table I lists the materials investigated and the results obtained for the various carboxylate modified species. As the matrix of experiments is completed, a clearer understanding of the precursor effect on the final morphology will be made and assistance in designing other systems without the need of a polymer will become available.

Table I	1:1	1:2	1:4
Zr –OBu^t			
OPc	NC	NC	NC
OBc	NC	NC	NC
ONc	NC	NC	NC
Zr –ONep			
OPc	Some tadpoles and droplets	NC	NC
OBc	Wires and tadpoles	NC	NC
ONc	Irregular	NC	NC
Hf–OBu^t			
OPc	NC	NC	irregular
OBc	Sprayed	NC	Wires and dots
ONc	NC	NC	Irregular some wires
Hf –ONep			
OPc	Irregular	NC	irregular
OBc	Wires and tadpoles	NC	Wires and dots
ONc	Irregular	NC	Irregular some wires

NC – ES not completed.

Forcespinning

Another method of interest for the production of ceramic wires is forcespinning. This relatively new method uses centrifugal force and air resistance to spinfibers . It works by filling a reservoir cup with the desired material followed by rotation at high speeds. A set of small holes allow the material to escape and if properly designed the material will form wires. The company 'FiberRio' has made these commercially available and SNL recently obtained it for use in another project. We have investigated the utility of this for production of nanofibers that would be more consistent with higher yields than those noted for ES.

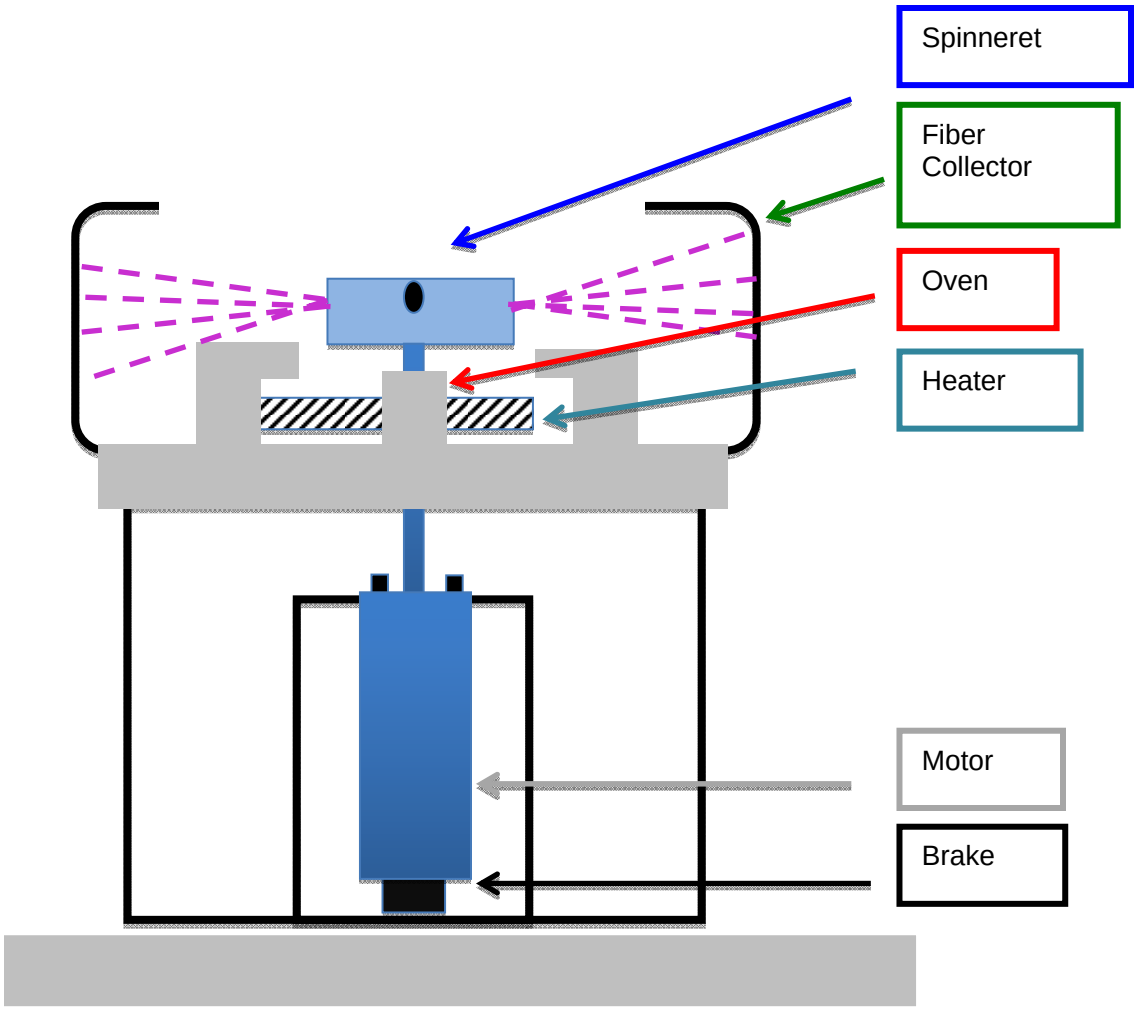

Figure 2.12. General setup for Forcespinning

Figure 2.12 shows the general setup required to forcespin. The entire setup is enclosed in a cabinet. Addition of the liquid sample to the spinneret must be done in the air, which makes dealing with air sensitive species difficult. Once introduced, the sample is spun (much like cotton-candy is made using sugar). Again, linkages from one drop to the next are required to ensure that nanowires are formed. The materials are collected on a series of wickets. Large amounts of nanowire materials can be rapidly generated using this technology.

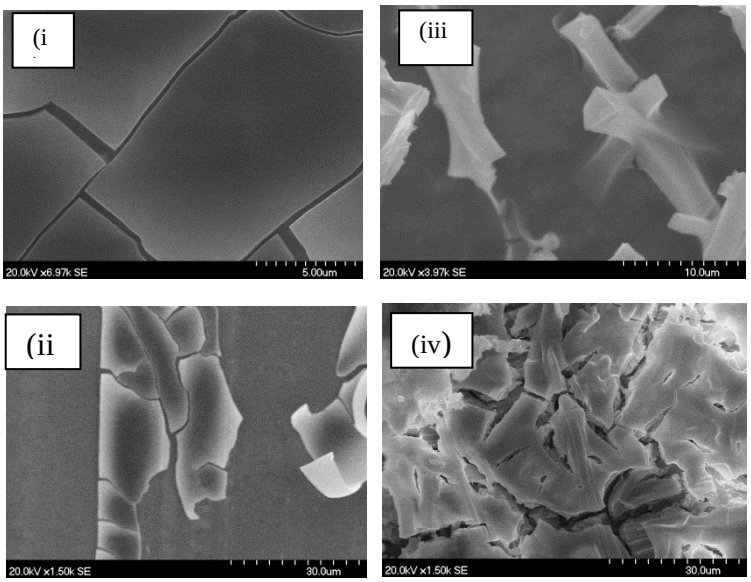

Figure 2.13. SEM images of FS samples with spin speeds (ss) ranging from 2000-7000 (i) $Zr(OBu^t)_4$ ss = 5000 (ii)$Zr(OBu^t)_4$ ss = 7000(ii) $Hf(OBu^t)_4$ ss = 3500 (iv)HfOBut ss = 2000

For this project, the Hf and Zr derivatives explored for ES were used for the FS experiments, since a number of these compounds clearly showed they were available for nanowire formation. The initial investigations focused on the $M(OBu^t)_4$ M = Zr, Hf either neat, no solvent, or in a 1M solution of hexanes. Both of these led to spraying rather than the development of wires, as shown in Figure 2.13. This was attributed to the steric bulk of the OBu^t ligand preventing the necessary linkage from drop to drop to form wires. Therefore, the previously developed ORc precursors used in ES (See Figures 2.8 -2.11) were investigated. The preliminary species studied were the $Hf(OBu^t)_n(OBc)_{4-n}$ derivatives as we had structures for each different stoichiometric ratio (1:1, 1:2, 1:4).

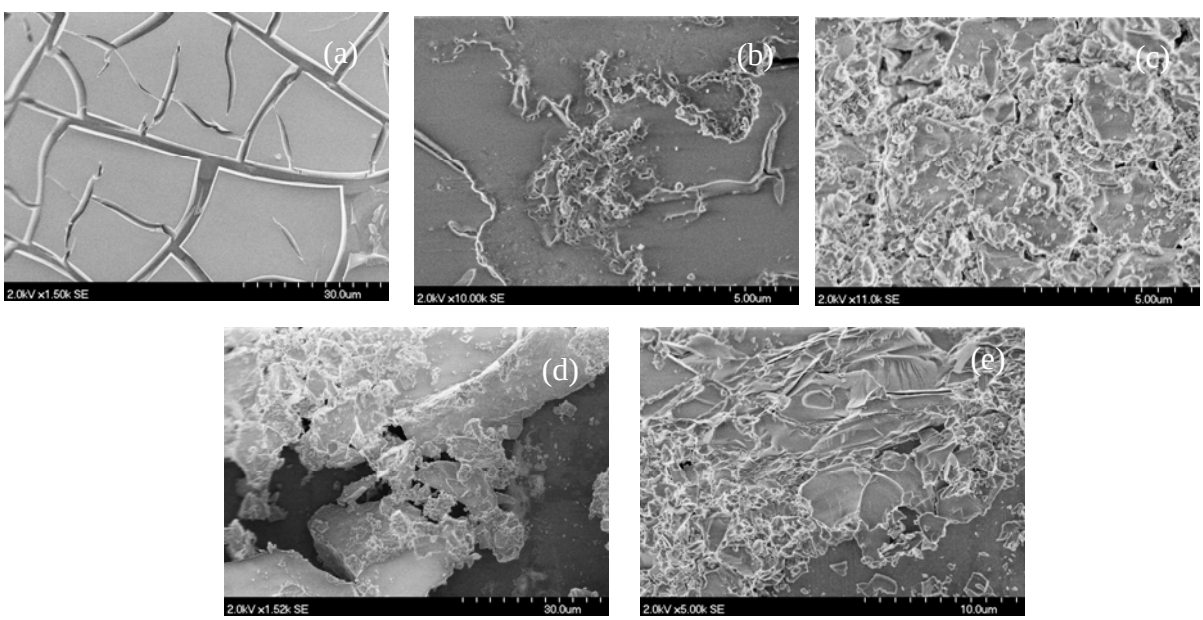

Figure 2.14. SEM images of $Hf(OBc)_n(OBut)_{n-1}$ ss = 2000 for(a) n = 1, (b)n = 2, (c) n = 3 and (d) n = 1, ss = 4000, (e) n =1, ss = 8000

Originally we attempted to use a one molar solution of the various compounds dissolved in hexanes, but these compounds were not soluble enough to produce a uniform solution necessary to avoid the clogging of the forcespinning apparatus.. As a result, these samples were evaluated at the highest possible loading, separating any excess solute through the use of a centrifuge.
After the FS of the various samples was completed, SEM images were collected to determine the effect of precursor on the final materials generated. Figure 2.14 has the various samples and spin speeds indicated for the $Hf(OBc)(OBu^t)_3$ series. As can be observed, these samples mainly sprayed, however, for the 2 and 3 substituted species, it appears there is potential for wire formation. Altered spin speeds (SS) of the 1:1 sample as shown in Figure 2.14 d and e did not improve the production of wires.

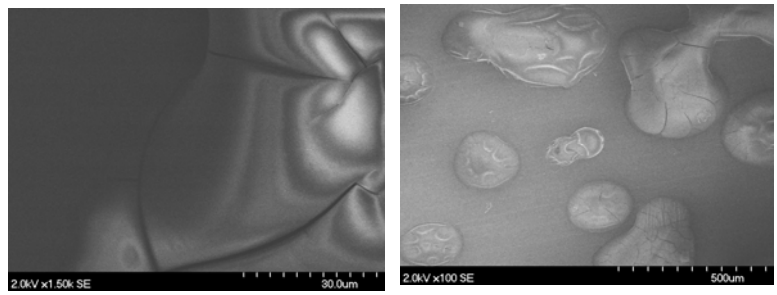

Figure 2.15. SEM images of $Hf(OBut)_3(TAP)$ ss = 2500

Alternative precursors that were oils were also investigated. The 2,4,6-tris-(dimethylamino methyl)phenol (H-TAP) demonstrated more spraying behavior versus spinning. The results are shown in Figure 2.15.

In addition, some preliminary work generating a hybrid material using a metal alkoxide and polymer were investigated. The polyacrylic acid polymer (see Figure 2.16) was mixed with a series of $Hf(OR)_4$ to generate a mixed polymer/metal alkoxide precursor. This was thought to be beneficial for generating polymeric wires that could be converted to the ceramic material after processing. Unfortunately the correct polymer loadings could not be achieved. In general, the polymer solution ended up being a colloidal suspension, which would have only clogged the needle tips of the forcespinning instrument. Thus, no FS attempts were made with this polymer. Since the hybrid materials did not work as expected, the original idea of loading polymers with nanoparticles were explored with FS processing. The forcespinning samples were run for 5 min at 3000 or at 8000 rpm, depending on the sample. The samples looked very promising and through SEM data have shown to form wires and other morphologies. SEM images of these compounds are shown below in Figure 2.17.

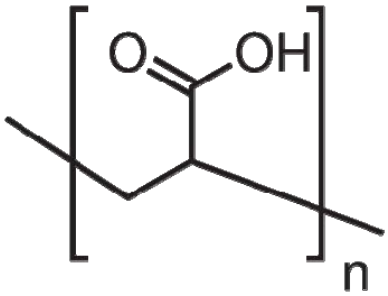

Figure 2.16. Poly(acrylic-acid) (n~450000 and 1,000,000)

(a) (b) (c)

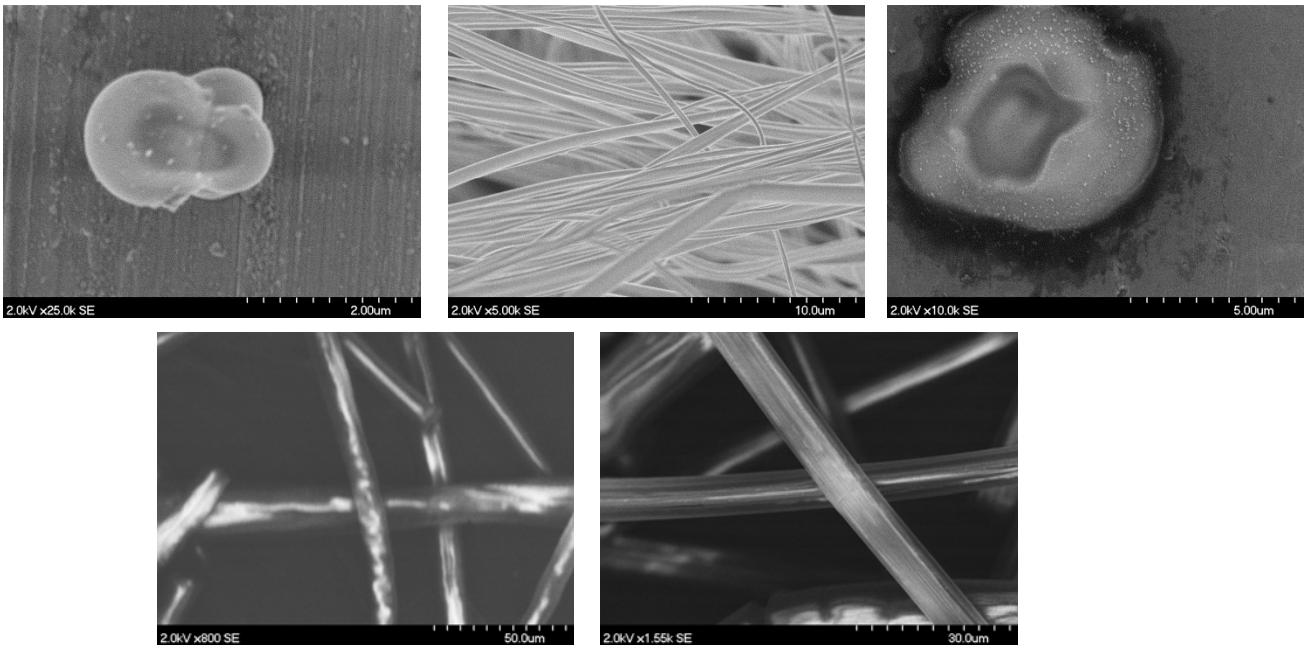

(d) (e)

Figure 2.17. (a) , 2.5 EVA 1 mL Ago NP, (b) Ago NP in PVP/THF, (c)5%PVP w/ Ago NP , (d) 14.7% wt PS, 200 uL Auo NPs , (e) 8.1% wt PS, 500 uL Auo NPs. SS = 3000 for all samples

Summary and Conclusion.

The development of Responsive Nanocomposites through electrospinning and forcespinning processing appears to be a promising avenue for production of the necessary nanowire materials. We have successfully shown that responsive polymers can be made by ES with some extreme response based on temperature.[15] These nanofiber mats exhibit fast response properties between super-hydrophobic and super-hydrophilc contact angle values that may be used in designing responsive car tires. In addition, several novel routes to nanomaterials (i.e., ceramic and metallic) have been developed. The particles have been successfully integrated into polymers, electrospun, and contact angle testing is underway to show the impact these fillers have on the final properties. Extending this concept, we have developed routes to electrospun ceramic (Group 4) and metal (Sn^0)[16] wires that do not require any polymer removal. This will allow us to expand the matrices of interest not only for this application but others as well. Extension of these concepts to forcespinning efforts has begun and shows some promise; however, significant precursor development will be necessary to generate polymer free ceramic nanowires.

References for Chapter 2:

[1] G. V. WHite; M. G. Provost; C. L. Kitches, *Int. Eng. Chem. Res.* **51** 5181 (2012).

[2] S. Peng; Y. G. Sun, *Chem. Mater.* **22** 6272 (2010).

[3] S. D. Bunge; K. M. Krueger; T. J. Boyle; M. A. Rodriguez; T. J. Headley; V. L. Colvin, *J. Mater. Chem.* **13** 1705 (2003).

[4] S. D. Bunge; T. J. Boyle; T. J. Headley, *Nano Letters* **3** 901 (2003).

[5] H. Gerung; T. J. Boyle; L. J. Tribby; S. D. Bunge; C. J. Brinker; S. M. Han, *J. Am. Chem. Soc.* **128** 5244 (2006).

[6] T. J. Boyle; L. A. M. Ottley; T. M. Alam; M. A. Rodriguez; P. Yang; S. K. McIntyre, *Polyhedron* **29** 1784 (2010).

[7] M. A. Rodriguez; T. J. Boyle; P. Yang; D. L. Harris, *Powder Diffraction* **23** 121 (2008).

[8] T. J. Boyle; L. A. M. Ottley; M. A. Rodriguez; R. M. Sewell; T. M. Alam; S. K. McIntyre, *Inorg. Chem.* **47** 10708 (2008).

[9] T. J. Boyle; P. Yang; L. A. M. Ottley; M. A. Rodriguez; T. M. Alam; S. Hoppe, *Unpublished work* (2009).

[10] C. Burger; B. S. Hsiao; B. Chu, *Annual Review of Materials Research* **36** (2006).

[11] R. Dersch; M. Graeser; A. Greiner; J. H. Wendorff Australian Journal of Chemistry, 150 (2007) 719-728.

[12] A. Greiner; J. H. Wendorff, *Angewandte Chemie-International Edition* **46** (2007).

[13] S. Ramakrishna, *An introduction to electrospinning and nanofibers*. World Scientific: Singapore ; Hackensack, NJ, 2005; p 382.

[14] D. H. Reneker; A. L. Yarin, *Polymer* **49** (2008).

[15] P. Muthiah; S. M. Hoppe; T. J. Boyle; W. Sigmund, *Macromolecular Rapid Communications* **32** 1716 (2011).

[16] T. J. Boyle; T. Q. Doan; L. M. Steele; S. M. Hoppe; K. Hawthorne; R. M. Kalinich; W. M. Sigmund, *Dalton Trans* **(in press)** (2012).

[17] T. J. Boyle; T. M. Alam; E. R. Mechenbier; B. L. Scott; J. W. Ziller, *Inorg. Chem.* **36** 3293 (1997).

This page intentionally left blank

CHAPTER 3

Shaped Metal Nanoparticles for Responsive Nanocomposites

Kathleen E. Martin, Yongming Tian, Yujiang Song, Eulalia Perreira, John A. Shelnutt

Department of Inorganic Chemistry and Nanomaterials (1815), Advanced Materials Laboratory, 1001 University Boulevard, SE, Albuquerque, New Mexico 87106

Enhanced Mobility in Organic Field-Effect Transistors (OFET) Containing Platinum Nanodendrites

A TEM image of the globular Pt nanodendrites used in this work is shown in Fig. 3.1. These dendrites were produced by autocatalytic oxidation of ascorbic acids and reduction of aqueous Pt complex at the surface of Pt seed nanoparticles produced by photocatalytic reduction of Pt complex by a Sn porphyrin catalyst. The platinum dendrites were the included in a dispersion in P3HT (0.3 %wt) in anhydrous chloroform that was the dried in air to form a nanoparticle-modified polymer film of ~60 nm thickness. Electrical measurements on the photoactive films are illustrated in Fig. 3.2 and Table 3.1. The data was determined from source/drain current *versus* gate/source voltage characteristics on 20 mm channel length, bottom contact MOSFETs (V_{ds} = -20 V).

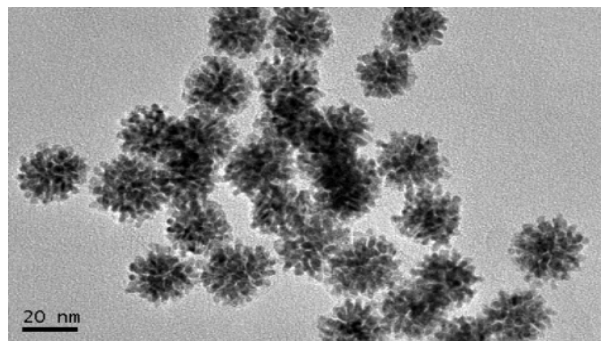

Fig. 3.1. *TEM image of platinum nanodendrites produced by photocatalytic and autocatalytic growth using ascorbic acid as reductant and visible light.*

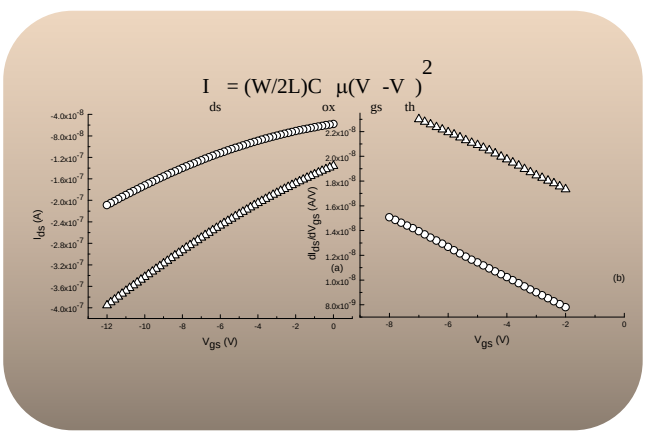

Fig. 3.2. *(a) I_{ds} versus V_{gs} plots for 20 μm channel length bottom gate/bottom contact MOSFETS made using Pt nanoparticle loaded P3HT (o) as-made, before bias stressing, and (Δ) following bias stressing (V_{gs} = + 20V, V_{ds} = 0 V)) for 120 seconds. All measurements were performed with V_{ds} = -0 V. (b) dI_{ds}/dV_{ds} versus V_{gs} data obtained from (a) by numerical differentiation.*

From these measurements we found that the Pt nanodendrites lower the threshold voltage and reduced (intrinsic) charged defect densities in the Pt dendrite-modified film (See Table 3.1). This is due to increased hole mobility. We also find that nanoparticle charging is absent in the films. XRD studies of the film show no change in P3HT crystallinity, except for slightly more disorder. The metal particles apparently serve as conductors, possibly acting simply to effectively increase the P3HT polymer chain length.

Table 3.1. *Threshold voltage and hole carrier mobility in P3HT and Pt nano-particle loaded P3HT.*

Organic Semiconductor	Threshold voltage (V)	Hole mobility ($cm^2V^{-1}s^{-1}$)
P3HT	10.2	0.0011
P3HT + 2.4% by volume Pt dendrites	4.4	0.0093

Gold Nanotriangles of Controlled Size and Gold Zn/Sn Porphyrin Clover Nanocomposites

Gold nanotriangles can be produced by photocatalytic reduction of Au(III) complexes in the presence of a capping agent. The average size of the triangular nanoplates is easily controlled by changing the concentration of photocatalyst and capping agent. Photocatalytic reduction of Au(III) proceeds by the following reaction cycle.

$SnP + h\nu \rightarrow SnP^*$

$SnP^* + TEA \rightarrow SnP^{-}\bullet + TEAox$

$SnP^{-}\bullet + Au(III) \rightarrow SnP + Au\ (II)$

The Au(II) produced in this photocycle is highly unstable in solution, and will either disproportionate or directly react with TEA or water to form Au(0). The nanoplates may grow by aggregation and fusion of smaller nanoparticles.

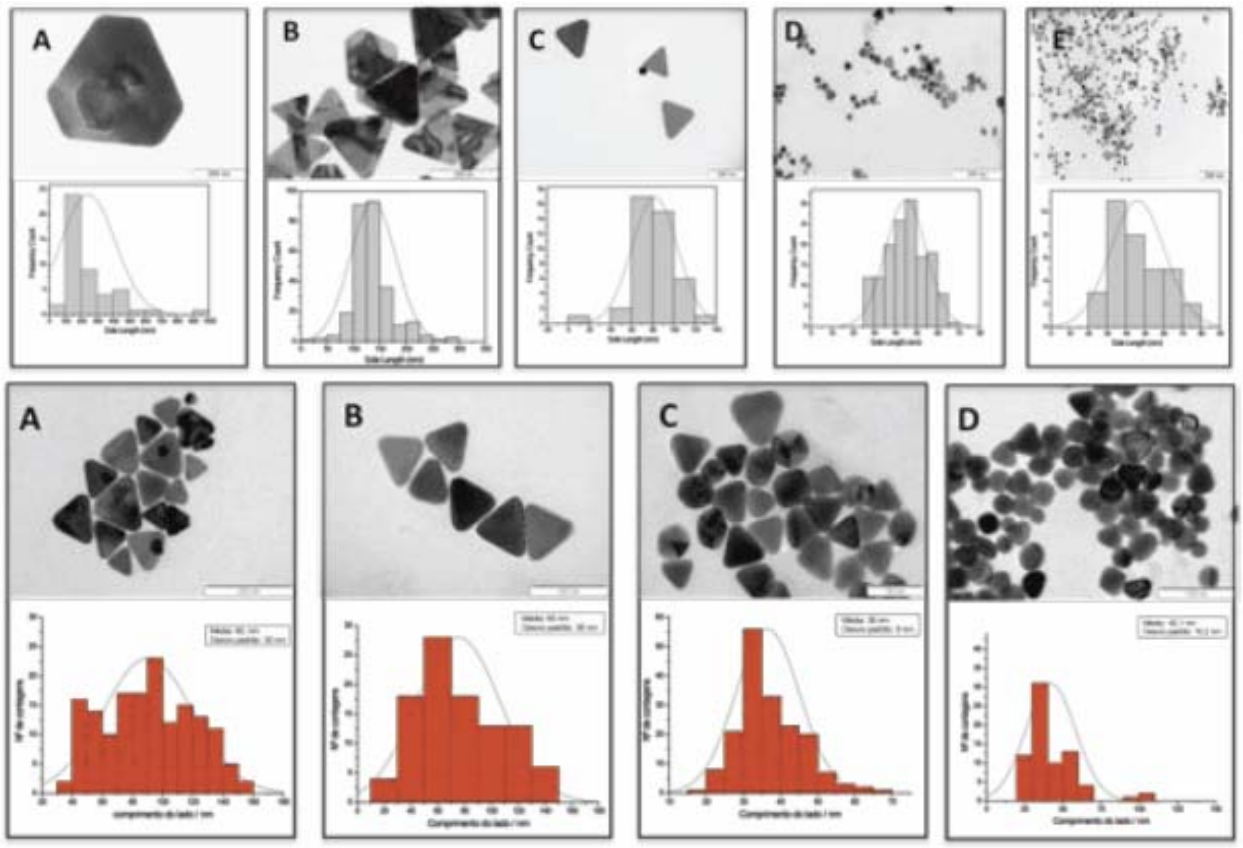

Fig. 3.3*. Gold nanotriangles produced with increasing concentrations of Sn porphyrin photocatalyst and capping agent (left to right).*

Size control of the gold triangles is obtained by the choice of photocatalyst concentration. Fig. 3.3 shows TEM images of gold nanotriangles grown with different photocatalyst concentrations. Smaller nanoplates are obtained for higher concentrations of photocatalyst and capping agent.

In a similar manner, photocatalytic reduction of gold(I) thiosulfate by self-assembled Zn/Sn porphyrin clovers-like microstructures leads to gold nanocomposites with cooperative binary ionic (CBI) solids. These structures are shown in the SEM images of Fig. 3.4 (top). Photocatalytic reduction of gold(I) thiourea by Zn/Sn porphyrin CBI clovers produces only a few large gold particles (Fig. 3.4, bottom). Neither reaction occurs in the dark (left), but the reaction proceeds rapidly in visible light (right).

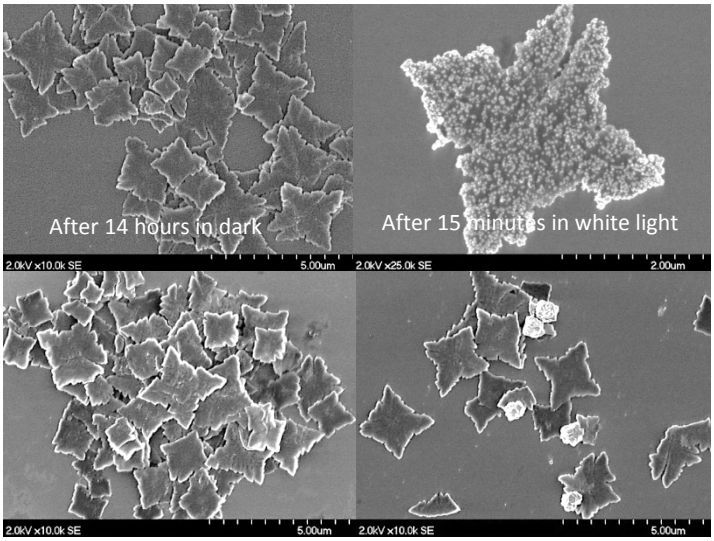

Fig. 3.4. *Photocatalytic growth of gold nanoparticles on CBI solid microclovers.*

Copper Nanotriangles of Controlled Size and Copper Nanowires

Reduction of $CuSO_4$ in the presence of CTAB using ascorbic acid as the reductant leads to the formation of copper metal nanotriangles and nanowires. These are shown in TEM images in Fig. 3.5, which also follows the development with time. The nanostructures appear to form by nanoparticle coalescence.

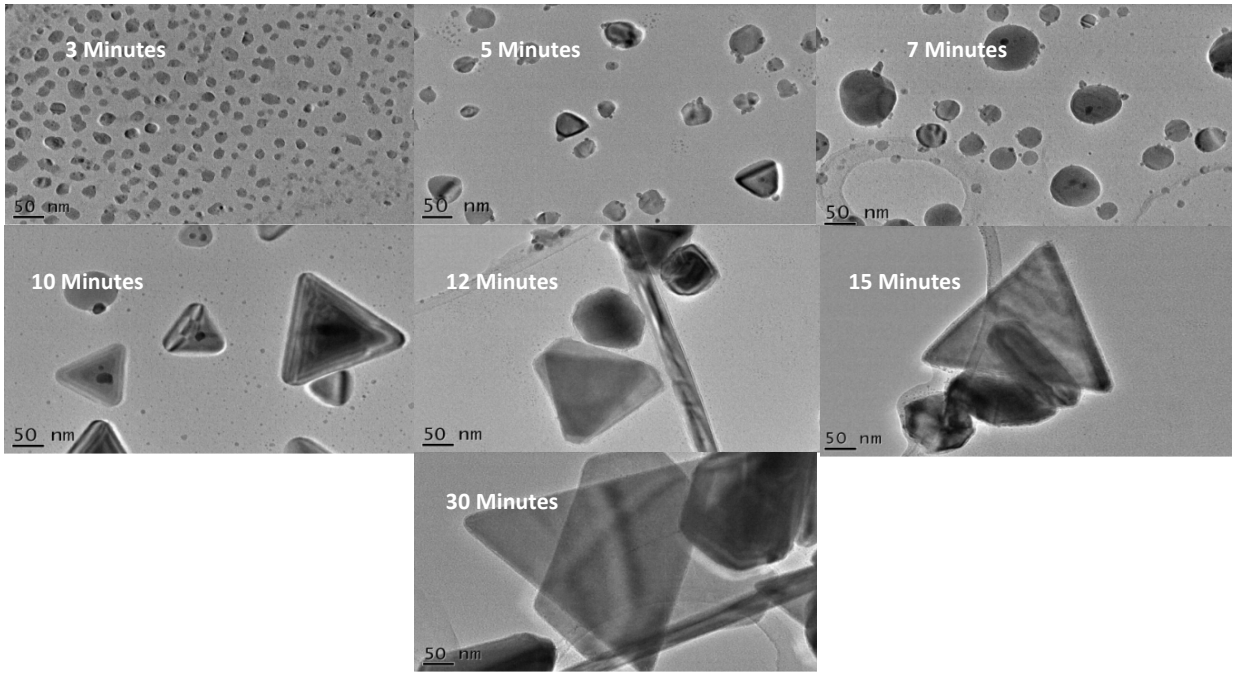

Fig. 3.5. *Chemical reduction of aqueous copper sulfate with ascorbic acid in the presence of CTAB. The nanotriangles and nanowires form within 1 hour by nanoparticle coalescence.*

When CuOAC is used instead of Cu sulfate, the product favors wire formation instead of triangles as shown in the TEM image in Fig. 3.6.

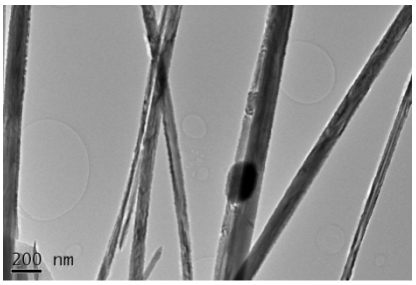

Fig. 3.6. *Chemical reduction of aqueous CuOAc with ascorbic acid in the presence of CTAB produces mainly nanowires..*

CHAPTER 4

Multiphoton Deposition and 3D Micro/Nanostructuring of Active, Catalytic, and "Smart" Materials

Bryan Kaehr, Lauren Zarzar, C. Jeffery Brinker, Joanna Aizenberg,

Introduction

The nano/microstructuring of active materials such as catalysts or responsive polymers is highly important for the development of "smart" systems that can autonomously respond, adapt to, or interact with, their environment. The development of techniques for the 3D placement and structuring of such materials on the nano and microscale is especially significant as materials systems increasingly rely on the interaction between multiple materials components to achieve desired results. We have pursued the use multiphoton lithography (MPL) as a method by which to achieve such control over materials deposition and properties in 3D. We have developed several new approaches to pattern materials previously not deposited by MPL and demonstrate how these new materials, namely responsive hydrogels and metal catalysts, can be incorporated with 3D architectures to create responsive hybrid systems.

Responsive hydrogels are crosslinked polymer networks which can be tailored to respond to environmental changes in humidity, temperature, pH, light, biomolecules, etc. based on the moieties of the monomers present in the polymer. Upon change in environmental conditions the polymer network will either swell or shrink; for instance, a pH-responsive hydrogel poly(acrylamide-*co*-acrylic acid) will be contracted when the pH is less than the pK_a of acrylic acid (4.3) and swollen when the pH is increased. Poly(*N*-isopropylacrylamide) (PNIPAAm) is a temperature responsive hydrogel which is swollen at temperatures lower than 32°C and contracted at elevated temperatures. Such hydrogels have been hailed as "smart" materials due to their reversible volume-phase transition, and highly tunable responsive properties. We demonstrate that MPL can be used to deposit such hydrogels within arrays of high-aspect-ratio structures and used as a "muscle" to actuate such structures.

We also explore how MPL can be used to deposit metals, such as platinum and palladium, within 3D microenvironments. Previously, MPL had only been used to deposit primarily silver and gold, but never platinum and palladium, so we developed the use of an iron oxalate sensitizer previously used in photography for the photoreduction and deposition of Pt and Pd. We then use these metals for site-specific catalysis of the decomposition of hydrogen peroxide and demonstrate that by controlling the 3D placement within a structure we can control the gas and fluid flow to generate a microfluidic pump.

Experimental Results

Direct Writing and Actuation of Three-Dimensionally Patterned Hydrogel Pads on Micropillar Supports[1]

For the first time we demonstrated that responsive hydrogels can be polymerized using multiphoton lithography. Using solutions consisting of monomer dissolved in ethylene glycol with Irgacure 819 as an initiator, we able to deposit pads of both temperature and pH-responsive hydrogel with 3D control with an array of high-aspect-ratio structures (Figure 4.1).

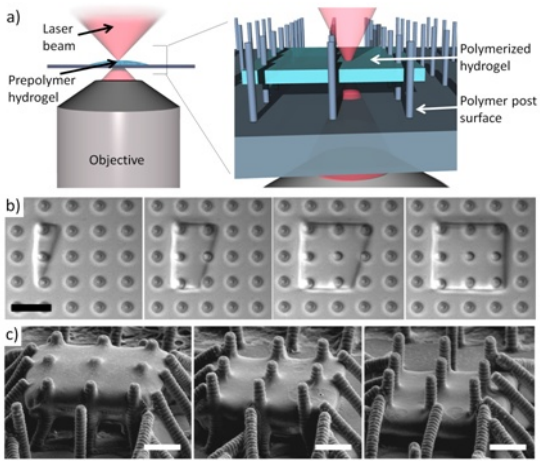

Figure 4.1. **a) Schematic showing the experimental set-up for localized synthesis of MPL hydrogels onto micropillars (height = 10 µm, pitch = 8 µm, diameter = 1.5 µm). b) Image sequence of multiphoton-induced polymerization to form a thin hydrogel structure attached to the pillars. Scale bar, 10 µm. c) SEM images show fabricated hydrogel structures placed precisely along the top, middle, and bottom of the posts. The thickness of the hydrogel pads is ~2 µm made by two passes of the scanning laser beam. Scale bars, 5 µm.**

These thin hydrogel pads, which can be placed anywhere along the lengths of the high-aspect-ratio structures, are allowed to expand significantly in the surface plane as they are not attached to the basal surface and only tethered to the structure tips; in contrast, thin surface-attached hydrogel films which are typically made by any other polymerization method which does not have 3D control, are confined in the surface plane and only allowed to expand in thickness, greatly reducing the ability for the gel to change volume. These tethered gels fabricated by MPL exhibit unique swelling properties, in which the outward lateral expansion of the gel actuates the flexible high-aspect-ratio structures (Figure 4.2).

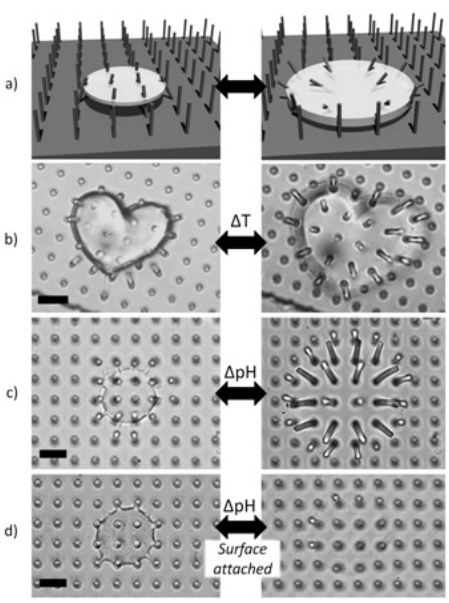

Figure 4.2. **a) Schematic showing the deflection of the flexible pillars via tip-attached hydrogel swelling. Optical microscope images of the contracted and swollen states of b) temperature-responsive hydrogel (at T>30°C and T<30°C) and c) pH-responsive hydrogel (at pH<4.25 and pH>4.25) are shown. d) pH-responsive gel under same conditions as (c) but fabricated at the base of the pillars and attached to the basal surface. Scale bars, 10 µm.**

We studied how the swelling and contracting of the gel itself, in particular a pH-responsive poly(acrylamide-*co*-acrylic acid) gel is translated to the motion of the structures. We estimate the bending angles of the structures from optical images, and plotting the bending angles of some exemplary posts versus the pH we notice that the movement correlates well with the expected volume phase transition of the gel (Figure 4.3). The greatest extent of actuation occurs at the edges of the gel, where the expansion is the greatest; this suggests a mechanism by which we can control the bending angles / actuation of structures within an expanding gel by tailoring the placement of the structure with a symmetrically swelling hydrogel. We can also calculate the force exerted by the gel using the formula below and we can plot these forces as a map (Figure 3).

$$Force = \frac{3\pi E r^4}{4h^3} * D \qquad \textbf{(1)}$$

where E is the Young's modulus of the glycidyl methacrylate-modified epoxy (1.5 GPa), r is the radius of the posts (0.75 µm), h is the height of the posts (10 µm), and D is the distance to which the tip of each post is deflected from its initial position.

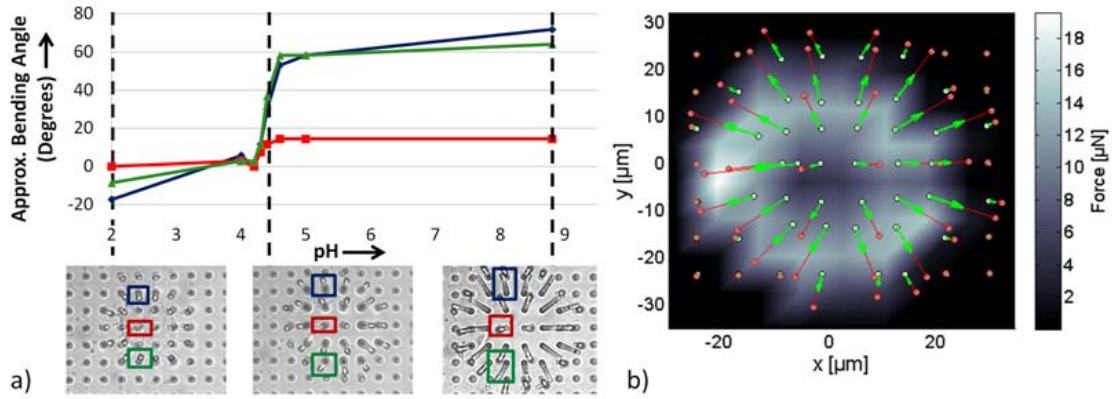

Figure 4.3. **a) Plot of approximate bending angles of pillars that support a pH-responsive hydrogel pad as a function of pH, where a negative angle represents the pillar bending inward toward the center of the gel, and a positive angle represents outwardly bending pillars. Posts near the center of the structure (red) show little change in bending. Posts near the edge of the hydrogel (blue and green) bend to very large angles (>70°). b) The displacement of the posts was used to generate a force map of the gel. White circles indicate the initial positions of the tips of the pillars when the gel is contracted, and red circles indicate the position of the tips of the pillars when the gel is swollen. Red lines connect the initial and final positions. Green arrows symbolize the amount of force normalized to the largest force experienced by a pillar in the system. The background color map visualizes the extent of the net force exerted on the pillars in different areas of the gel.**

Because we have this unique ability to control the 3D patterning of responsive hydrogels in arbitrary shapes, we demonstrated that we could deposit two different gels sequentially such that they interact at an interface (Figure 4.4). The posts sitting with pH-responsive gel to one side and temperature responsive gel to the other side can be actuated to four distinct locations depending on the four different combinations of pH and temperature.

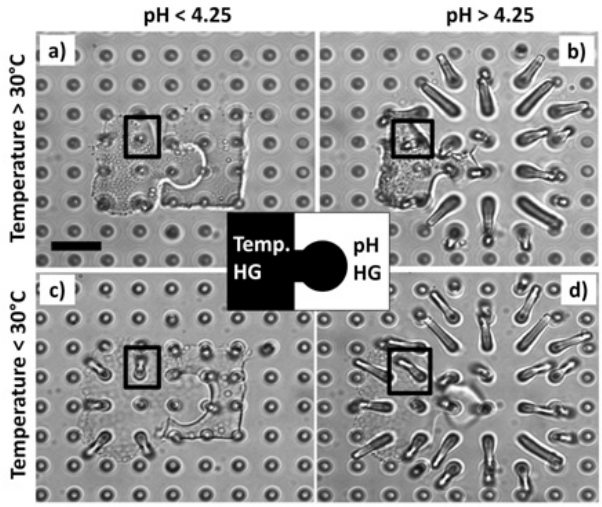

Figure 4. **A schematic image showing temperature- and pH-responsive hydrogels fabricated in close proximity as interlocking puzzle piece shapes (center). Optical microscope images at each temperature and pH combination are shown (a-d). The black outline highlights an exemplary post as it is bent at four different angles and directions depending on the combination of conditions. Scale bar, 10 μm.**

Finally, we demonstrate that this large volume change we can achieve by these tethered gels can be used to change the concentration of a dye in the gel thereby generating an optical response upon the expansion and contraction of the gel. When the gel is contracted the dye, which is polymerized into the gel network, is highly concentrated and we observe strong fluorescence intensity. When the gel is expanded the concentration of the dye is diluted and the fluorescence intensity is weaker (Figure 4.5).

Figure 4.5. **Fluorescence microscope images demonstrating fast and reversible appearance and disappearance of messages due to the change in concentration density of a rhodamine dye which was incorporated into a pH-responsive hydrogel. a) Contraction of the hydrogel in acid increases the fluorescence signal to reveal the message "word!". (See Supporting Movie 3). Scale bar, 40 μm. b) Contraction of the hydrogel in acid reveals the arrow symbol. Upper insets show DIC images of the gel. Lower insets show the fluorescence intensity profile along the length of the arrow normalized to the bit depth of the fluorescence image. Scale bar, 20 μm.**

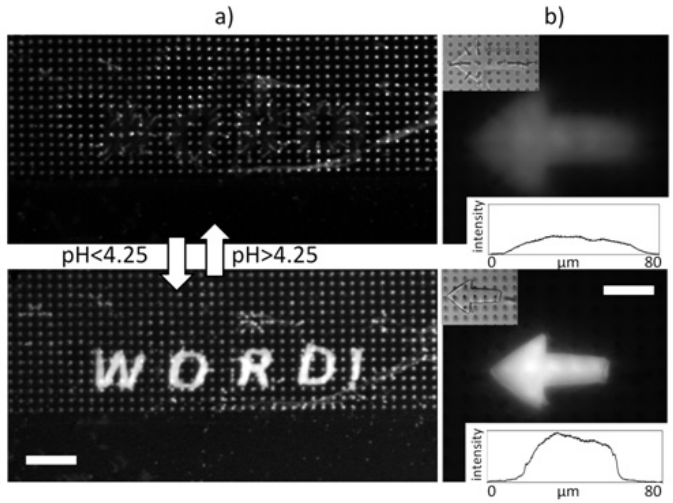

Multiphoton Lithography of Nanocrystalline Platinum and Palladium for Site-Specific Catalysis in 3D Microenvironments[2]

Integration of catalytic nanostructured platinum and palladium within 3D microscale structures or fluidic environments is important for systems ranging from micropumps to microfluidic chemical reactors and energy converters. We investigated a straightforward procedure to fabricate microscale patterns of nanocrystalline platinum and palladium using multiphoton lithography. These materials display excellent catalytic, electrical, and electrochemical properties, and we demonstrated high-resolution integration of catalysts within 3D defined microenvironments to generate directed autonomous particle and fluid transport.

For MPL of Pt and Pd, we explored the use of precursors often used in platinotype/palladiotype photographic processes first developed in the late 19th century. In one such printing method, paper (serving as the support matrix) is embedded with the ammonium salts of Pt(II) or Pd(II) and $[Fe(C_2O_4)_3]^{3-}$ and exposed to UV light inducing photochemical reduction of the iron to form a strong reducing agent which can then reduce, for instance, Pt(II) to elemental platinum following the reactions:

$$hv + 2[Fe(C_2O_4)_3]^{3-} \rightarrow Fe(C_2O_4)_2]^{2-} + C_2O_4^{2-} + 2CO_2$$

$$[PtCl_4]^{2-} + 2[Fe(C_2O_4)_2]^{2-} \rightarrow Pt\downarrow + 2[Fe(C_2O_4)_2]^{-} + 4Cl^{-}$$

To investigate MPL of Pt and Pd by adapting this photographic process, we mixed a 1:1 precursor solution comprised of 0.7 M of either of the ammonium metal salts and 1.0 M of the iron (III) oxalate and tested Pt/Pd direct-writing using a mode-locked Ti:S centered at 750 nm and focused upon a glass cover slip. Using this procedure, Pt and Pd patterns could be printed sequentially on un-modified glass with arbitrary shapes and intrinsic registration using a scanning laser, dynamic-mask based approach (Figure 6a.) Structures could be rinsed rigorously post-fabrication without any detectible delamination or degradation. Panels b and d of Figure 4.6 show energy-dispersive X-ray spectrographs (EDS) and backscatter scanning electron micrographs (SEM) respectively demonstrating the fabrication of well-defined patterns of highly pure (i.e., no iron oxides detected with EDS) Pt and Pd.

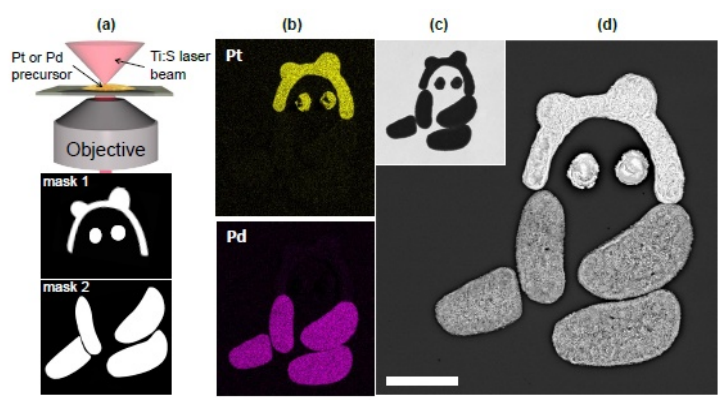

Figure 4.6. **(a) Fabrication schematic showing the two digital masks used to define Pt and Pd. (b) EDS image maps indicating regions of Pt and Pd. (c) Bright field optical micrograph. (d) Backscatter SEM. Scale bar, 20 µm.**

The Fe (III), Pt(II), and Pd(II) salts display no significant absorbance above 450 nm and excitation of the charge-transfer band of $[Fe(C_2O_4)_3]^{3-}$, which is required for its subsequent photolysis, is achieved in the range of 200-500 nm. Thus, as expected, no initial deposition was observed when 5 mW continuous wave (CW) 750 nm light was employed. High resolution SEMs (Figure 4.7) show that the metallic patterns are comprised of small metallic granules, similar to what has been reported for silver and gold. SEM cross-sectional analysis of an exemplary palladium structure revealed that the granular surface, in large part, is continuous throughout the interior of the structure down to the glass/metal interface at which point the structure appears solidified, indicating thermal melting/annealing at the interface—a consequence of heating via light absorption by the metallic pads.

We characterized the electrical properties of MPL-Pt and Pd lines written on glass substrates using an *in situ* nanoprobe technique and measured resistivity values of 4.2 ± 0.5 and 2.3 ± 0.3 (μΩ·m) for Pt and Pd respectively. Further characterization of the crystallinity and electrochemical properties of MPL-Pt was carried out using transmission electron microscopy (TEM) and cyclic voltammetry (CV). TEM analysis of the MPL-deposited Pt scraped from glass substrates showed clusters with crystallites ranging in diameter from 4 - 8 nm (Figure 4.7), and distinct crystallographic planes could be resolved in the electron diffraction pattern of crystallites located at cluster edges (Figure 4.7 inset). MPL-Pt exhibited classic platinum electrode electrochemical behavior, as shown in Figure 2, where an MPL-Pt line was used as the working electrode versus a Ag/AgCl reference electrode and a Pt coil counter electrode (Supporting Information). Cyclic voltammetry in 1.0 M H_2SO_4 resulted in characteristic hydrogen monolayer adsorption and desorption, which allowed us to estimate an electroactive surface area to geometric surface area ratio of 36.

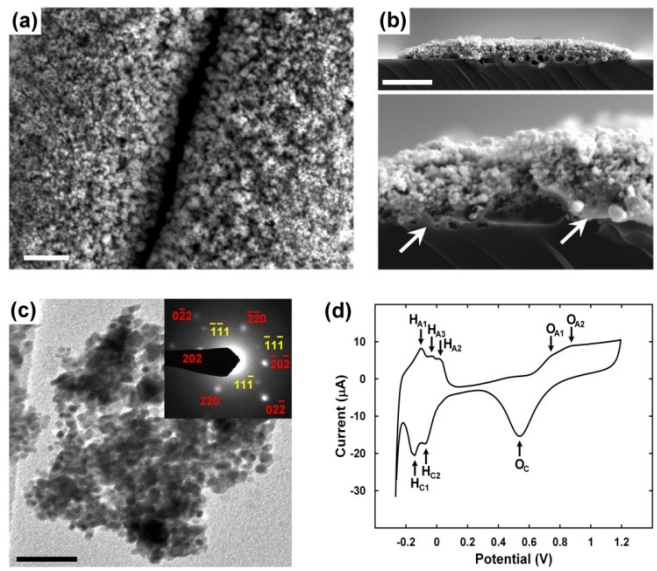

Figure 4.7. **Characterization of MPL-Pt/Pd using SEM, TEM, and CV (a) Two Pd structures separated by a ~200 nm gap. Scale bar, 1 μm. (b) Cross section of a MPL-Pd line shows that the granular structure is continuous down to the metal/glass interface, where melting/annealing of the glass (left arrow) and Pd (right arrow) is evident. Scale bar, 5 μm. (c) TEM of MPL-Pt crystallites and electron diffraction pattern obtained from the edge of a cluster (corresponding to 2 crystallites). Scale bar, 50 nm. (d) CV of an MPL-Pt working electrode in 1.0 M H_2SO_4 shows characteristic hydrogen adsorption (cathodic peaks; H_C) and desorption (anodic peaks; H_A) and formation ($O_{A1,2}$) and subsequent reduction (O_C) of an oxide layer.**

We explored Pt catalyzed decomposition of hydrogen peroxide into oxygen and water to generate directed fluid and particulate flow within 3D micro-chambers and channels. In Figure 8a, a Pt pad was patterned onto glass and then encased within a photo-crosslinked protein

chamber containing a self-crossing spiral outlet. Protein hydrogels have a number of attractive features for fabricating microenvironments, including ready diffusion across chamber walls. Addition of 1% H_2O_2 resulted in a continuous and directed flow of oxygen through the spiral as the peroxide substrate could be replenished at the catalytic site, for the most part, via diffusion across the protein hydrogel chamber walls and ceiling thereby allowing the majority of the spiral channel to maintain constant O_2 pressure.

In contrast, directing the oxygen outflow into an asymmetric channel (Figure 4.3b) resulted in a peristalsis-like effect on the channel, with the channel fluid periodically compressed and released by the oxygen bubble evolution and resultant negative pressure developed upon outflow. Pumping is illustrated by the directional transport of microspheres at relatively high velocities (60 µm/s) through the channel (Figure 4.8b). Importantly, this approach offers considerably greater flexibility versus existing techniques in the design of autonomously powered microfluidics.

Finally, we explored Pt patterning within a preformed 3D microenvironment. MPL generated protein microstructures show suitable transparency at the incident wavelength to allow Ti:S beam penetration depths of tens of microns using tight focusing (i.e. high NA objective). Nonetheless, formation of a metallic pad on the protein substrate resulted in substantial heating and deformation of the protein support. This challenge was overcome by developing a silica composite using a recently described technique, which provided sufficient mechanical reinforcement of the structural surfaces defined by the protein template to withstand the subsequent heat generated during metal deposition. Here, we designed a geometry where gas flow is forced downward, underneath the catalyst, to exit into the surrounding fluid (Figure 4.8c). Traversing the imaging plane through the structure clearly shows that the gas generated from the top chamber is directed underneath the Pt catalyst, demonstrating high resolution integration of a metallic component that is otherwise unachievable without 3D lithographic control.

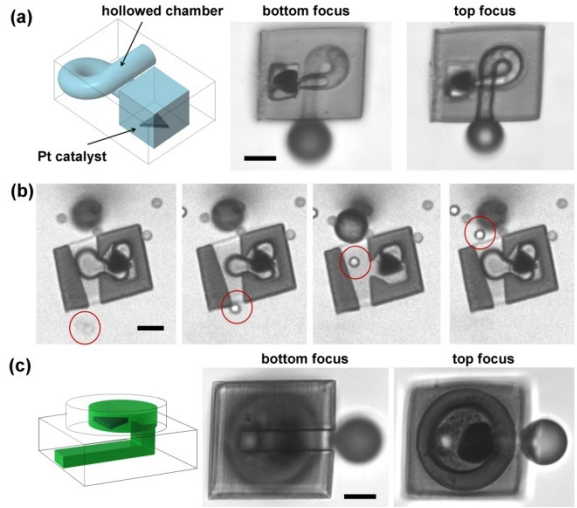

Figure 4.8. **(a) A Pt catalyst contained in a protein chamber directs gas flow through a self-crossing spiral channel into the surrounding fluid. (b) The directional outflow of gas produced at an MPL-Pt catalyst contained in a microchamber pumps a 5 µm particle (circled in red) through the asymmetric channel. (c) An MPL-Pt catalyst printed inside the upper chamber of a 3D microchamber directs gas flow downwards underneath the catalyst. Scale bars, 10 µm.**

Summary

This work has greatly expanded the set of active, catalytic, and "smart" materials that can be patterned with MPL. We have demonstrated that MPL can be used to pattern responsive hydrogels in 3D to enable actuation of high-aspect-ratio flexible microstructures. We can control the consecutive placement of multiple materials, allowing us to probe the interface between two responsive materials. We also have demonstrated that MPL can be used to deposit metals, namely Pt and Pd, which we use as catalysts. By incorporating the catalysts within 3D microenvironments we can control fluid/gas flow and generate a micropump using the Pt or Pd catalyst to site-specifically decompose hydrogen peroxide.

Specifically we achieved the following major milestones:

1) We developed protocols for MPL of responsive hydrogels, poly(acrylamide-*co*-acrylic acid) and poly(*N*-isopropylacrylamide)

2) We quantitatively studied how the responsive gel interacts with the flexible high-aspect-ratio structures to which the gel is tethered. We analyzed the bending angles and forces exerted by the gels.

3) We demonstrated that these responsive gels exhibit very large volume changes which can be used to reversible change the concentration of an active moiety, such a fluorescent dye, creating images which appear and disappear as the gel swells and shrinks

4) We developed protocols and chemistry to deposit nanocrystalline platinum and palladium

5) We studied both the crystallinity of the Pt and Pd as well as electrochemical and conductive properties.

6) We demonstrated that when the Pt or Pd catalyst is positioned strategically within a designed 3D microenvironment that we can control the gas/fluid flow from the decomposition of hydrogel peroxide. Such site specific catalysis can be used to create a micropump.

References for Chapter 4:

1. Zarzar, L. D.; Kim, P.; Kolle, M.; Brinker, C. J.; Aizenberg, J.; Kaehr, B., Direct Writing and Actuation of 3D-Patterned Hydrogel Pads on Micropillar Supports. *Angew. Chem. Int. Ed.* **2011,** *50*, 9356-9360.
2. Zarzar, L. D.; Swartzentruber, B. S.; Harper, J. C.; Dunphy, D. R.; Brinker, C. J.; Aizenberg, J.; Kaehr, B., Multiphoton Lithography of Nanocrystalline Platinum and Palladium for Site-Specific Catalysis in 3D Microenvironments. *Journal of the American Chemical Society* **2012,** *134*, 4007-4070.

This page intentionally left blank

CHAPTER 5

Graphene Synthesis, Composites and Assemblies

Part A.

Timothy N. Lambert,[1*] Carlos A. Chavez,[1] Nelson S. Bell,[2] Cody M. Washburn,[3] Michael T. Brumbach,[4] Todd M. Alam,[2] David R. Wheeler[5], Claudia C. Luhrs[6], Stephen Wakeland[6]

[1]Department of Materials, Devices and Energy Technologies, Sandia National Laboratories, PO Box 5800, Albuquerque, New Mexico, 87185
[2]Department of Electronic and Nanostructured Materials, Sandia National Laboratories, PO Box 5800, Albuquerque, New Mexico, 87185
[3]Department of Organic Materials, Sandia National Laboratories, PO Box 5800, Albuquerque, New Mexico, 87185
[4]Department of Materials Characterization, Sandia National Laboratories, PO Box 5800, Albuquerque, New Mexico, 87185
[5]Department of Biosensors and Nanomaterials, Sandia National Laboratories, PO Box 5800, Albuquerque, New Mexico, 87185
[6]Department of Mechanical Engineering, University of New Mexico, Albuquerque, New Mexico, 87131

Part B.

Jeffrey R. Potts, Prof. Rodney S. Ruoff
Department of Mechanical Engineering, University of Texas at Austin, Austin, Texas

Part A.

Motivation

Graphene, a one-atom thick 2-d monolayer of fused sp^2 carbon bonds in a honey-comb like network, has attracted a great deal of scientific interest due to its outstanding mechanical, electrical, thermal and optical properties, as well as its high theoretical surface area of 2630 m^2/g [1-4]. Graphene-based materials (graphene, graphene oxide, exfoliated graphite, chemically modified graphene, etc.) have therefore found use in a variety of applications, including in composites materials.

Here we present our work on developing responsive composites based on graphene. We first report on a 1.) new method for the synthesis of graphene using a plasma processing method and then report 2.) on work highlighting the self-assembly of photo-responsive graphene-ceramic thin films.

Accomplishments

Section 1. Synthesis of highly reduced disordered graphenes using an aerosol-through-plasma method

T. N. Lambert, C. C. Luhrs, C. A. Chavez, S. Wakefield, T. Alam, and M. Brumbach "Graphite oxide as a precursor for the synthesis of disordered graphenes using the aerosol-through-plasma method" *Carbon* **2010** *48*, 4081-4089.

C. Luhrs and **T. N. Lambert** "Graphite-based Precursors for the Synthesis of Graphenes Using the Aerosol-Through-Plasma method" US Patent Application *submitted* **2011**.

Summary:

The thermal exfoliation and reduction of graphite oxide was obtained by passing an aerosol of coarsely ground graphite oxide with no solvent through a low-power (900 W) microwave generated plasma, with argon as the carrier and plasma gas. The reduced material obtained by this aerosol-through-plasma method was characterized by powder X-ray diffraction, Raman, X-ray photoelectron and solid state ^{13}C NMR spectroscopy, transmission electron microscopy, thermo-gravimetric and elemental analysis and surface area analysis methods. These materials

consist of single to few-layers of graphene and displays high disorder, large surface areas (~ 640 m^2/g) and low (< 4%) oxygen content.

1. Introduction:

The methods for graphene synthesis/preparation have recently been reviewed [5], with a variety of preparative methods available including: chemical vapor deposition, micromechanical exfoliation, epitaxial growth by heating silicon carbide and by reduction of graphene oxide or graphite oxide. Graphite oxide (GO) is a convenient and cost effective starting material for graphene synthesis as it is readily available from graphite.[6] The preparation of graphene-like materials from GO has been achieved with a variety of synthetic methods, including: dispersion, followed by chemical reduction with hydrazine[7] or $NaBH_4$[8], electrochemical reduction,[9, 10] reduction using solvothermal[11, 12] or microwave approaches[13], TiO_2 assisted UV photo-reduction[13], ultra-low vacuum thermal methods[14] and thermal exfoliation/reduction methods, i.e. rapid thermal heating in a tube-type furnace[15, 16]. The thermal and low vacuum methods are of particular interest as no additional extraneous chemical reducing agents are required. Graphene materials with a low oxygen content (~ 9-10%) and high surface area (600-900 m^2/g) can be realized. Thermal expansion/exfoliation of GO occurs when the rate of decomposition of oxygen functionalities (epoxy and hydroxyl and carboxy) in GO is greater than the diffusion rate of the evolved gases (e.g. CO_2) that are produced. This condition results in pressures that exceed the Van der Waals forces holding the graphene sheets together.[15, 16]

Here we show that disordered graphene-like nanosheets can be produced from the rapid thermal expansion/de-oxygenation of GO using an aerosol-through-plasma (ATP) approach. For decades, plasma processing of materials on the nanoscale has been an enabling technology for various "planar" technologies. Recently, developments have provided for its use for preparing particulate structures, which can be isolated as free powders/materials[17-20]. In fact, the technology has proceeded to the point where commercial materials are now available from ATP methods. As explained recently, the ATP approach is different than plasma enhanced chemical vapor deposition (PECVD) normally used to produce carbon nanostructures, as the carbon precursor in ATP is passed directly through the plasma.[21] There are two references in the literature in which free standing graphene has been obtained by employing a microwave plasma: these efforts utilize

ethanol as the chemical precursor.[21, 22] Here, we describe our success in obtaining disordered graphene-like materials (herby termed, plasma reduced graphite oxide or PRGO) with low oxygen content from GO using the ATP process.

2. Experimental

2.1 *Synthesis*

2.1.1 *Synthesis of Graphite Oxide and plasma reduced graphite oxide (PRGO).* GO was prepared following a modified Hummers method[6, 23] using purified natural graphite (SP-1, 30 μm nominal particle size, Bay Carbon, Bay City, MI). Plasma reduced graphite oxide (PRGO) was prepared by aerosolizing coarsely ground GO (no solvent) through a low power (700 or 900 W) microwave generated plasma with argon as the carrier and plasma gas. The material was collected on the filter bed as a dark black, light and fluffy material or in an ethanol solvent trap, whereby the material was subsequently lyophilized to obtain the material as a powder. The plasma has been previously described.[17-20] For comparison, chemically reduced graphene oxide (RGO) was prepared using hydrazine hydrate at an initial graphene oxide dispersion of 0.5 mg/mL as previously described[7, 24] An exfoliated, thermally reduced graphite oxide (TRGO) sample was also prepared by rapid heating at 1150 ^{o}C, following published procedures[15, 16]

2.2 *Characterization*

2.2.1 *Powder X-ray Diffraction (PXRD).* Powders were mounted as EtOH slurries directly onto a zero background holder purchased from The Gem Dugout, State College, PA 16803 and allowed to dry. Samples were scanned at a rate of 0.02°/2 s in the 2θ range of 5−80° on a Bruker D8 Advance diffractometer in Bragg-Brentano geometry with Cu Kα radiation and a diffracted beam graphite monochromator. Phase identification was determined from the PXRD patterns using Jade 9 Software suite and the JCPDS powder diffraction files.

2.2.2 *Transmission Electron Microscopy (TEM).* PRGO was placed either 1) directly as solid powder or 2) from a dilute EtOH dispersion, onto a holey carbon type-A, 300 mesh, copper TEM grid purchased from Ted Pella, Inc., Redding, CA 96049 and allowed to dry. These were studied using a JEOL 2010 high resolution transmission electron microscope (HRTEM), operating at 200 kV accelerating voltage. Electron energy loss spectroscopy (EELS) was carried out in a

JEOL 2010F FASTEM field emission gun scanning transmission electron microscope (STEM/TEM) equipped with Gatan GIF image filtering system for energy filtered TEM and EELS analysis.

2.2.3 *Thermogravimetric Analysis.* Temperature Programmed Oxidation (TPO) analysis was executed on a Netzch STA 409 under N_2/O_2 95%/5% atmosphere, between room temperature and 800 ^{0}C. Samples were heated at a rate of 5 ^{o}C/min. Commercial graphite powder (Aldrich 99.99+%) and an amorphous carbon (produced by ATP from anthracene precursor) were used for comparison. The amorphous carbon sample was produced with the plasma torch as well, although in conditions of high flow-low residence time, starting with anthracene as the precursor. The resulting sample was analyzed by XRD and HRTEM-selected area electron diffraction (SAED) means and no long-range order for the sample was found by these techniques. HRTEM of such sample showed nanometer sized particles (data not shown).

2.2.4 *Surface area analysis.* N_2 adsorption/desorption on samples was measured using a Micrometrics ASAP 2020 or a Micrometrics Tristar 3000 sorptometer.

2.2.5 *Raman Spectroscopy.* Raman spectra were recorded using a Thermo Scientific Smart Raman DXR instrument with a DRX 633 nm laser with a high-resolution gradient from 150 cm^{-1} to 2100 cm^{-1}. Resulting data was analyzed using the Thermo Scientific Software and re-plotted for presentation purposes using Kaleidagraph software.

2.2.6 *X-ray photoelectron spectroscopy.* X-ray photoelectron spectroscopy (XPS) was performed with a Kratos Axis Ultra DLD with monochromatic Al Kα (1486.6 eV) source at 225 W, and an analyzer pass energy of 20 eV. The analyzed spot size was 300 x 700 microns and base pressures were less than 5 x 10^{-9} Torr. Charge neutralization was used for all samples. Energy normalization was performed, by setting the first primary component of the C 1s spectrum at 284.5 eV. Data were analyzed using CasaXPS software. Peaks were fit using a Shirley background and a Gaussian/Lorentzian line shape. Peak positions and FWHM for C 1s values were allowed to vary within a limited range, since identical fitting constraints could not be used to fit all spectra.

2.2.7 *Nuclear Magnetic Resonance Spectrocospy.* Solid state ^{13}C magic angle spinning (MAS) NMR spectra were obtained on a Bruker Avance 400 at 100.63 MHz, using a 4 mm broadband probe, at room temperature, spinning at 7.5 kHz for the graphene sample and 10 kHz for the GO sample. A standard direct single pulse Bloch decay pulse sequence with TPPM ^{1}H decoupling was used. The ^{13}C chemical shifts were referenced to the carbonyl resonance of a secondary glycine sample (δ = 176.0 ppm with respect to TMS).

2.2.8 *Elemental Analysis.* Elemental analyses were performed on a Perkin-Elmer 2400 CHN-S/O Elemental Analyzer.

3. Results and Discussions

3.1 *Aerosol-through-plasma treatment*

We prepared GO by oxidation of SP-1 graphite from Bay Carbon with $KMnO_4$ in a concentrated H_2SO_4 solution.[23] Isolated GO was then ground to a coarse powder with a mortar and pestle and subjected to the aerosol-through-plasma (ATP) process. A microwave atmospheric plasma torch system was used in order to promote GO sample reduction and thermal exfoliation. A basic diagram of the ATP system is shown in Figure 1. Starting from the base of the figure, the process can be described as: Dry GO sample is placed in a beaker and subject to the vibration generated by an ultrasonic bath. The GO particles are hence aerosolized with a carrier gas (e.g. argon (Ar)), and travel through an alumina tube that is connected to a quartz tube directed to the center of a plasma discharge zone produced by a microwave guide and Ar gas. The discharge zone and its surrounding area constitute the hottest part of the system (~ 2500 K). Precursor GO particles carried by the aerosol gas are subjected to high heating rates while passing through it. This rapid heating process is believed to promote the loss of oxygen functionalities and be responsible for the particles exfoliation and reduction, i.e. conversion to PRGO. Particles residence time at the discharge region is extremely short (less than 1 second), due to the gases flow rates utilized, 3.5 slpm. Particles immediately pass from the discharge area through a chimney in the afterglow region and get finally collected by a filter system (or EtOH trap as mentioned in experimental section). Unless indicated otherwise, the power in the microwave generator was 900 Watts. Given that a critical temperature of at least 550 ^{o}C is required for the thermal expansion/exfoliation of GO,[16] expansion and reduction of GO into a reduced graphene structure

with ATP is readily expected. While GO is a dense black solid material, the filter trapped PRGO appears as a black and light fluffy material (of similar appearance in nature to that obtained from rapid thermal heating of GO in a furnace/oven), Figure 5.1. Volume expansion of the material is immediately obvious; suggestive of a thermally expanded material.

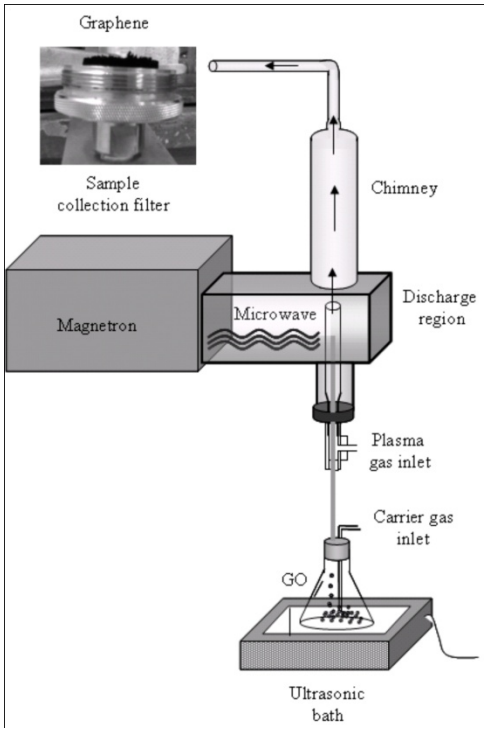

Figure 5.1. Schematic of the Microwave Atmospheric Plasma Torch system used to exfoliate and reduce GO into PRGO.

3.2 *Powder X-ray diffraction (PXRD)*

GO forms a well-ordered layered structure, as indicated by a well-defined d_{001} peak in its powder X-ray diffraction (PXRD) pattern. The exact 2θ values can range from 8-12°, depending on extent of hydration, and were determined to be ~ 2θ = 10.2^o (correlates to a basal spacing of 8.7 Å) for the GO samples prepared here, Figure 5.2. The peak at ~ 2θ = 10-12° is lacking in the PRGO sample and the peak for the PRGO is observed at 2θ = 24° indicating a basal separation of 3.70 Å, larger than that of graphite at 3.35 Å. The broadness of the (002) peak is also consistent with poor ordering along the stacking direction and indicative of a powder comprised of disordered graphene-like nanosheets. The broad/nearly inexistent 101/001 peak(s) at 2θ = 42-44° suggests poor through plane alignment also consistent with a disordered material.

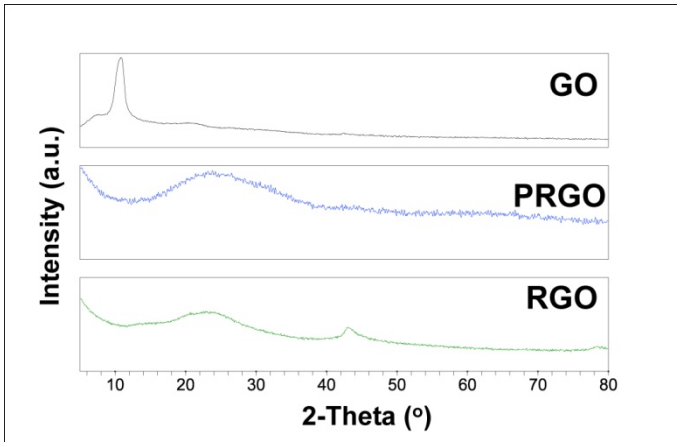

Figure 5.2. PXRD patterns for GO, PRGO, RGO.

3.3 *Raman Spectroscopy*

The chemical reduction of GO to PRGO was also confirmed with Raman spectroscopy, Figure 3. The GO as prepared here exhibits D- and G-bands at 1338 and 1603 cm^{-1} with a D/G ratio of 0.84. Upon ATP treatment, the G-band shifts from 1603 to 1595 cm^{-1}, while the D-band shifts from 1338 to 1328 cm^{-1}, Figure 5.3. A marked increase in the I_D/I_G ratio of is also observed (I_D/I_G = 1.8). In comparison, RGO as prepared here exhibits a lower I_D/I_G ratio of ~ 1.5. Shifts to lower numbers are expected upon reduction and the accompanying increase in I_D/I_G ratio for RGO has been explained by the presence of smaller but more numerous sp^2 domains in the carbon [7]. While numerous fundamental studies (e.g. molecular electronics) are pursuing defect free single sheet graphene, disordered graphene materials are likely to be more applicable in the areas of capacitors and Li-ion storage applications. For example, the Li-ion capacity of graphene-based anodes has been shown to best correlate with increasing disorder, as identified by increasing I_D/I_G ratios.[25]

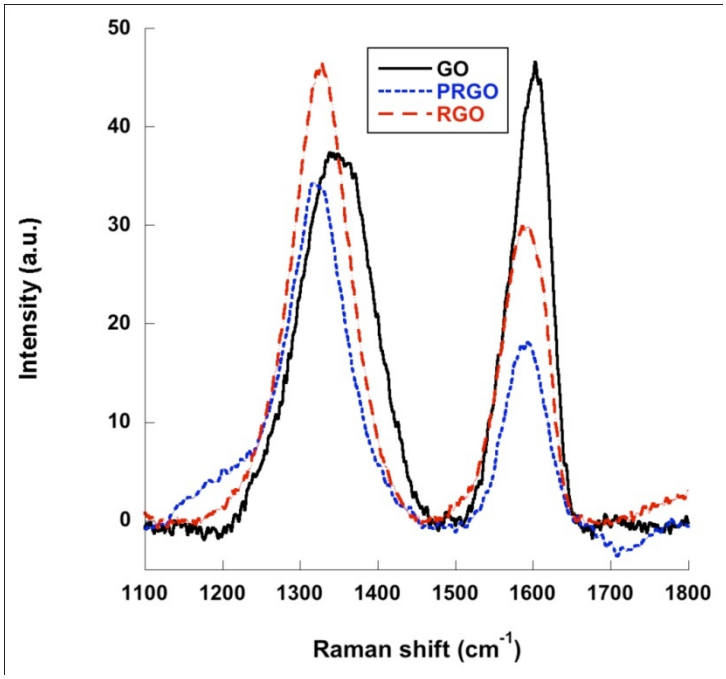

Figure 5.3. Raman spectra of GO (black), PRGO (blue) and RGO (red).

3.4 *X-ray photoelectron spectroscopy*

Survey XPS spectra (data not shown) show atomic percentages of 73% C and 25% O for the GO sample (similar to values reported in the literature),[15] and 97% C and 3% O for the PRGO sample, indicative of a highly reduced PRGO material. The C 1s and O 1s spectra, from X-ray photoelectron spectroscopy (XPS), for a GO and a PRGO sample are shown in Figure 5.4. C 1s peak fitting was performed using a common set of 5 peaks for all C 1s spectra, Figure 5.4a and 4b. Loss features (plasmon, π-π* shake-up) at high BE in the C 1s can convolute the spectra,[26, 27] so only chemical species were identified here. BE positions for the carbonaceous species can be found in the literature.[7, 27-32] For GO, C 1s fitted peak positions, [FWHM], and (peak assignments) were identified at 284.5[1.4] (C-C), 285.4[1.2] eV (C-H), 286.5[1.3] eV (C-O), 288.1[1.4] eV (C=O) and 289.7[2.0] eV (O-C=O), Figure 4a. C 1s peak fits for PRGO gave fitted components at 284.5[0.74] eV (C-C), 285.4[1.4] eV (C-H), 286.8[1.3] eV (C-O), 288.3[1.4] eV (C=O) and 290.6[2.5] eV (O-C=O and carbonate), Figure 5.4b. For PRGO samples, there was a significant narrowing of the C-C peak, and a general broadening of the peaks in the high binding energy (BE) tail of the C 1s spectra. As expected, the C-C component of the PRGO becomes very prominent, relative to the C-C component of GO, and there is a large decrease in the contributions from carbonyl components, again consistent with considerable de-oxygenation and reduction in the PRGO sample.

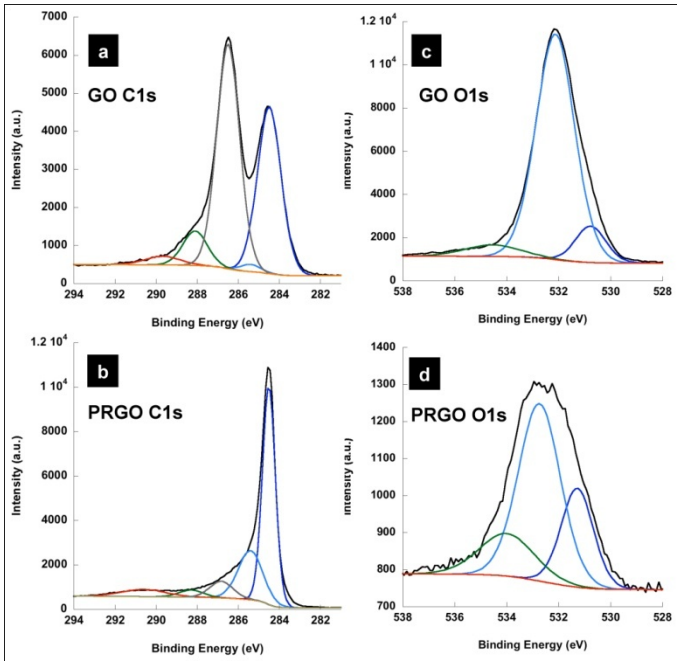

Figure 5.4. XPS spectra. C 1s spectra for a) GO and b) PRGO and O1 s spectra for c) GO and d) PRGO.

The overall oxygen signal was significantly less in the O 1s spectra for the PRGO sample, however, similar fit components could be used for both spectra. For GO, O 1s fitted peak positions, [FWHM], and (peak assignments) were identified at 530.8[1.4] eV (C=O), 532.1[1.7] eV (C-OH), and 534.6[2.5] eV (COOH), Figure 5.4c. Peak fits for PRGO gave spectral components at 531.3[1.5] eV (C=O), 532.7[1.9] eV (C-OH) and 534.0[2.5] eV (COOH), Figure 4d. Peak assignments were made following Desimoni *et al.* and references therein;[26] however, it should be noted that peak assignments given in Yang *et al.*[27] contradict these assignments, and contributions from SO_4^{2-} and/or other adventitious species are routinely neglected. Yang *et al.* give the assignments from low to high BE as (O=C-OH), (C=O), and (C-OH). Their (C-OH) peak assignment, the highest BE component they identified, is at approximately 533 eV, still consistent with our findings and other literature. The intensity ratios relative to the ratios observed in the C 1s components suggest that our peak assignments and those of Desimoni *et al.* are correct. In our work, the PRGO O 1s spectrum show a general coalescence of the distinct spectral components observed in the GO sample as the total O 1s signal decreases, i.e. the PRGO O 1s spectrum could also be fit with one broad (FWHM ~ 2.9 eV) spectral component. This shows that the surface chemical species are more uniform and less distinguishable in the reduced PRGO sample, as was also evident from the C 1s spectra.

3.5 *^{13}C MAS NMR*

The solid state ^{13}C MAS NMR spectrum of GO and PRGO are shown in Figure 5. Assignment of the GO chemical shifts is based on previously reported values.[33] GO, as prepared here, shows major resonances (with assignments) at δ = +129 (C=C, 26%), δ = +104 (C=C, 20%), +70 (C-OH, 27%) and +61 (C-O-C, 18%) ppm, with minor carbonyl resonances (C=O, ~ 7%) at +163 and +187 ppm. In the PRGO sample these multiple carbon resonances are replaced by a single very broad resonance at δ = +109 ppm (FWHM = 3910 Hz). Although this chemical shift is lower than the +112 to +118 ppm reported by others,[33] it correspond to a C=C carbon environment. The broadness of this resonance can be contributed to the high disorder within this graphene sample, along with the sample being conductive. This line width is similar to the broad line width observed for graphite samples. The reduced signal to noise results from the very small amount of PRGO sample used for the MAS NMR analysis.

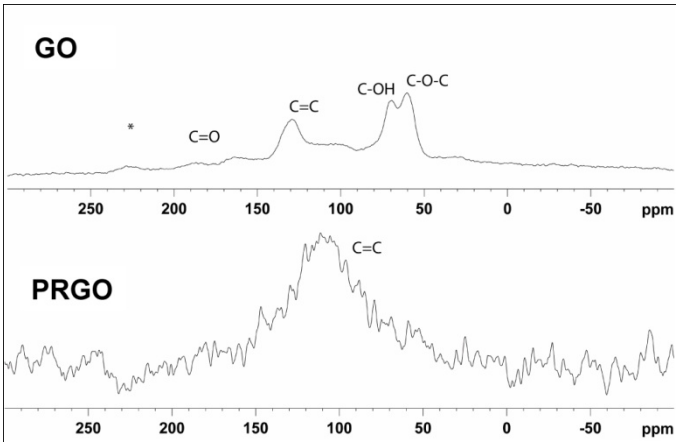

Figure 5.5. ^{13}C MAS NMR spectra of (top) GO and (bottom) PRGO, * indicates spinning sideband.

3.6 *Transmission Electron Microscopy*

A portion of this sample was dispersed in EtOH and deposited onto carbon coated for TEM analysis. Alternatively, the sample was loaded directly into the TEM grid as a solid material. TEM shows the formation of unsupported graphene with regions in which single and few layer graphene is clearly observed (noted by an arrow) and regions in which the sample presents the expected crumpled morphology for an aggregated graphene-like sample, Figure 5.6a. Ordered lattices are visible in some areas of the sample, although disordered sections were also found. Selected area electron diffraction (SAED) of the sample shows well defined spots along the [001] zone axis that confirm the existence of the graphene crystalline structure, along with blurry rings, originated by amorphous regions in the sheets, Figure 5.6b. High angular annular dark field images of the sample, Figure 5.6c, show variations in the image contrast that could be correlated to sample thickness. A large (i.e. micrometer long) sheet of graphene located in the center of the image along with crumpled sections is visible.

The crystalline structure of the nanosheets as prepared here was also confirmed by EELS (Figure 5.6d), with its spectrum exhibiting the characteristic graphitic 1s−π* and 1s−σ* peaks in the K-edge region at 285 and 292 eV, respectively.[34, 35] No peaks for hydrogen (13 eV) and oxygen (532 eV) K-edge peaks, and OH peaks (at ~ 528 eV) were observed in the spectra, indicative of minimal hydrogen, oxygen, and OH groups in the material.

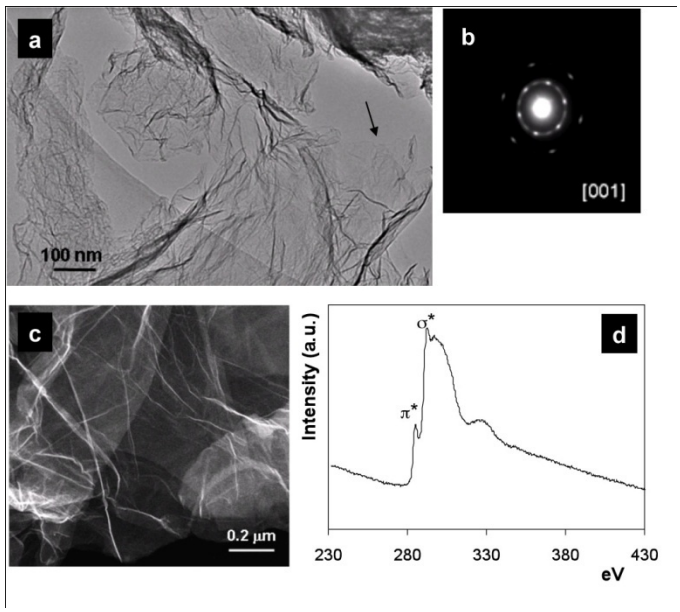

Figure 5.6. a) Bright-field TEM micrograph of PRGO, arrow indicates single/few layer area, b) SAED pattern shows crystalline graphitic nature and some amorphous features, c) STEM micrograph, d) EELs spectra showing 1s−π* (285 eV) and 1s−σ* peaks (291 eV) in the K-edge region indicating graphitic nature of the PRGO nanosheets.

3.7 *Elemental analysis*

GO, RGO, PRGO and TRGO were also analyzed for their C, H, N elemental composition, Table 1. Fully reacted GO has been reported to have 55.7% C, 2.1% H and 40.1% O,[15] as determined from micro-elemental analysis (EA). Values are similar for GO prepared here: 51.5% C, 45.9% O and 2.4% H, Table 1. The discrepancies observed here, and found in the literature,[15] for the elemental composition of GO as obtained with XPS or EA methods is likely due to the presence of water entrapped between (and on) the surface of graphene oxide sheets,[7] a hygroscopic material. Such water is likely not detected under the high vacuum and limited surface interrogation conditions of XPS. Rapid heating of GO is known to lead to exfoliation and thermal reduction.[15, 16] Such "splitting" of GO, to give a thermally reduced graphite oxide (TRGO) obtained under optimum conditions for single sheet graphene formation has been reported to yield a material with 86.4% C, 0.8% H and 11.3 %O (C/O ratio = 7.6). TRGO prepared here under similar conditions gave a material with 88.9% C, 0.46% H and 10.1% O (C/O ratio = 8.8). The PRGO prepared here, under largely un-optimized conditions, is 93.1% C, 2.2% H and 4.3% O as determined by microanalysis, with slightly higher oxygen content than

the values obtained by XPS (96.8% C and 2.6% O). Due to the hydrophobic nature of reduced graphene materials,[7] elemental composition values for PRGO from EA and XPS methods are similar. The higher percentage of H in PRGO is consistent with a more disordered/defective graphene sheet structure, consistent with our Raman and PXRD findings. Despite the fact that exfoliated single sheets of graphene were not obtained exclusively, the ATP process here provides a graphene-like material with lower oxygen content (C/O molar ratio ~ 21.5) than those obtained (C/O molar ratio ~ 8 – 9) by rapid heating in a furnace reported to date.[15] Presumably, the extreme rapid heating of the GO when subjected to the conditions of the plasma is responsible for the lower oxygen content. In comparison, RGO also typically contains 10-11% O as well as N (3.5%) when the reducing reagent hydrazine is used, Table 1.

Table 1: Elemental analysis of graphene materials[a]

Sample	C	H	O	N	C/O (EA)
Graphite	98.1	NA	1.9	-	51.6
GO	51.5	2.4	45.9	0.27	1.1
RGO	85.0	0.81	10.7	3.5	7.9
PRGO	93.1	2.2	4.3	0.31	21.6
TRGO[b]	88.9	0.46	10.1	0.58	8.8
TRGO[c]	86.4	0.8	11.3	_	7.6

[a]GO = graphite oxide, RGO = reduced graphene oxide (hydrazine method), PRGO = plasma reduced graphite oxide, TRGO = thermally reduced graphite oxide (1150 ^{o}C). Data obtained from CHN microanalysis. [b]TRGO sample prepared here @ 1150 ^{o}C via rapidly expanded furnace method.[15] [c]Atomic composition reported in literature.[15]

3.8 *Thermogravimetric analysis*

A temperature programmed oxidation (TPO) method was used to compare the graphitic nature of PRGO with both graphite and amorphous carbon (see experimental section for details) as shown in Figure 5.7. Each sample was individually heated at a rate of 5 ^{o}C/min from 50 ^{o}C to 850 ^{o}C under an atmosphere of 95% N_2/5% O_2. The oxidation curve for graphite shows an initial loss of weight, consistent with sample conversion to CO_2, at temperatures of approximately 635 ^{0}C. Graphite sample weight loss happens as a gradual process that is still underway at temperatures above 850 ^{0}C. On the other hand, amorphous carbon oxidation occurs at lower temperatures, approximately 450 ^{0}C. Amorphous particles react more readily with oxygen at moderate temperatures while graphitic products undergo similar reactions at higher temperatures due to their crystalline constituents. The PRGO sample produced by the microwave plasma method here, begins the oxidation process at the same temperature as the graphite flakes, proving the crystalline nature of the resulting PRGO sheets; however, the graphene sample loses weight at a higher rate than the graphite flake sample, in a process that is complete at 800 ^{0}C. We believe that PRGO samples react more completely with oxygen contained in the analysis atmosphere

(N_2/O_2) than graphite flakes due to more surface area being exposed, as well as the presence of edge defects in the graphene nanosheets.

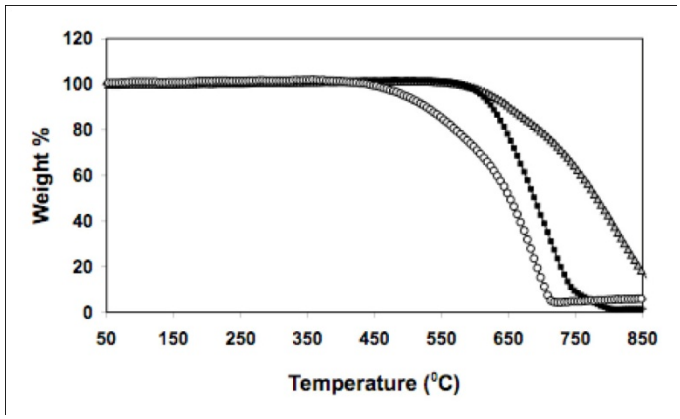

Figure 5.7. TPO plot of graphite (⑩), PRGO (⑤) and amorphous carbon (○) heated at 5 °C/min 95%/%5 N_2/O_2 analysis atmosphere.

3.9 *Surface area analysis*

In order to determine the surface area and pore sizes and volumes of PRGO, N_2 adsorption-desorption measurements along with Brunauer-Emmet-Tellet (BET) and Barrett-Joyner-Halenda (BJH) methods were used. A nitrogen adsorption-desorption isotherm for PRGO is shown in Figure 5.8.

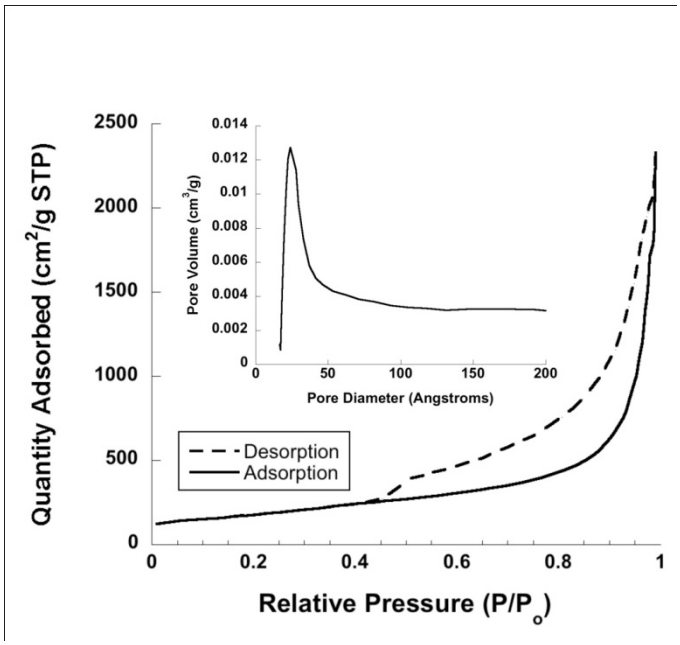

Figure 5.8. Nitrogen-sorption isotherms for PRGO and (inset) pore volume distribution plot.

While the theoretical surface area of an individual (reduced) graphene sheet is ~2600 m^2/g,[36] BET analysis revealed that PRGO prepared here (at 900W power) had surface area of 621 m^2/g, with pore sizes and volumes of 17 nm and 3.02 cm^3/g, respectively, Table 2. Collection of PRGO in an ethanol trap gave slightly higher values, Table 2. Optimized conditions by others have resulted in completely exfoliated, thermally reduced graphene-like materials that exhibit BET determined surface areas of 600 to 900 m^2/g.[15] In these studies, the BET defined surface areas were found to be dependant on the amount of water present in the GO sample heated, as water vapor retards the thermal expansion.[15] BET analysis revealed that TRGO prepared by our hands had a similar BET surface area of 631 m^2/g, with larger pore sizes and volumes of 34.3 nm and 6.05 cm^3/g, respectively, Table 2. Lower BET values can be explained by the incomplete exfoliation of the GO during reduction and expansion in the plasma or by subsequent aggregation of the graphene nanosheets. The use of a GO precursor with incomplete oxidation or high water content, and a shorter residence time in the plasma during thermal treatment are all plausible reasons for lower surface areas. Preliminary studies also indicate that a lower plasma power leads to a lower surface area. For example, conducting the reduction at a plasma power of 700W gave a PRGO material with a BET surface area of 510 m^2/g. Plasma and GO precursor optimization studies are underway and will be reported in due course.

Table 2: Surface area analysis of graphene materials[a]

Sample	BET Surface Area (m^2/g)	Pore Volume (cm^3/g)	Pore diameter (nm)
GO	39	0.247	25.5
RGO	466	0.525	3.89
PRGO[b]	621	3.02	17.0
PRGO[c]	657	4.01	18.6
PRGO[d]	510	2.32	15.9
TRGO[e]	631	6.05	34.3

[a]GO = graphite oxide, RGO = reduced graphene oxide (hydrazine method), PRGO = plasma reduced graphite oxide, TRGO = thermally reduced graphite oxide @ 1150 ^{o}C. [b]900W, collected dry on filter, [c]900W, collected in EtOH trap, [d]700W collected dry on filter, [e]Prepared @ 1150 ^{o}C following literature protocol.[15]

4. Conclusions

In summary, graphene-like materials were successfully prepared from the exfoliation/reduction of GO using an aerosol-through-plasma approach. Low power (900W) microwave plasma processing of GO gave a highly reduced, disordered (I_D/I_G = 1.8), graphene-like material with low-oxygen content (~ 4%) and high surface-areas (621-657 m^2/g) as determined by BET.

Section 2. Self-assembly of Photo-responsive Graphene-Titania films

Invited Manuscript: **T. N. Lambert**, C. A. Chavez, N. S. Bell, C. M. Washburn, D. R. Wheeler and M. T. Brumbach "Large Area Mosaic Films of Graphene-Titania: Self-Assembly at the Liquid-air Interface and Photoresponsive Behavior" *Nanoscale* **2011** *3(1)*, 188-191.

Summary:

Combining graphene, with its theoretically high surface area of ~ 2630 m^2/g, and inorganic nanomaterials makes it possible to develop new nanocomposite materials with expanded utilities. For example, coupling the desire able properties of the graphene with the well-established photo-properties of titania (TiO_x)[37] has led to enhanced photocatalyst and photovoltaic materials.[38-44] A significant challenge is in developing new synthetic routes to such materials. Routes based on solution processing are often favored due to their expected cost effectiveness and simplicity.[24] To date, TiO_x-graphene composites have been prepared by solution mixing, e.g. dispersion of nanoparticle titania with colloidal graphene oxide (GO), or by the *in situ* growth of TiO_x with GO or surfactant dispersed graphene. Chemical, thermal and photo-reduction methods have been employed to convert TiO_x-GO to TiO_x-reduced graphene oxide (TiO_x-RGO) materials. Harvesting the power of self-assembly could provide facile, chemically directed approaches to such composite materials.[45-48] Here we demonstrate a new self-assembled route to thin self-assembled films of graphene-titania and show that they are photoresponsive.

1. Introduction:

Recently we prepared a series of TiO_2-GO composites, with varying TiO_2/GO ratios, from the hydrolysis of TiF_4 in the presence of GO, and we additionally formed reduced graphene oxide (RGO) composites (i.e. TiO_2-RGO) using chemical and thermal reduction methods.[24] Under appropriate synthesis conditions, long range ordered stacks of TiO_2-GO were formed in the micron sized regime. We rationalized, that under carefully controlled conditions, we should be able to form similar self-assembled-titanium dioxide-reduced graphene oxide (SA-TiO_2-RGO) structures on the nanoscale (~ 100 nm thickness). In particular we were attracted to the "on-demand" photo-reduction of GO with TiO_2,[49] thereby forming soluble TiO_2-RGO (sol-TiO_2-RGO). We hypothesized that under the appropriate conditions, an evaporation induced type assembly[50] could be used to prepare the target SA-TiO_2-RGO films at the fluid-air interface.

Here we report that upon UV-photo-reduction of an aqueous solution of TiO_2-GO, the sol-TiO_2-RGO that is formed can form unsupported self-assembled nanosheets (~ 30-200 nm thick and up to ~ 1-2 cm^2) at the fluid-air interface under approriate evaporative conditions. These SA-TiO_2-RGO films are formed as a "mosaic assembly" of photo-reduced graphene oxide and inter-calated/graphene-bound TiO_2. Surface tension and surface wetting measurements support the formation of sheets at the liquid-air interface via an evaporative driven process aided by methanol. These mosaic films were successfully transferred to solid substrates and shown to display photocurrent generation under UV irradiation (λ_{exc} = 350 nm, 25-30 mJ cm^{-2}): e.g. SA-TiO_2-RGO films deposited onto interdigitated electrodes (IDEs) generated ~ 12-20 nA cm^{-2} of current when excited with UV radiation. Exposure of SA-TiO_2-RGO films to UV radiation, followed by exposure to deaerated silver (Ag^+) salt solutions led to to the reduction of Ag^+ on the surface of the graphene sheet, forming silver nanoparticles on the surface of the graphene film, i.e. Ag^o-SA-TiO_2-RGO films were formed. It is likely that the UV exposure caused charge transfer, resulting in storage of electrons in the graphene for subsequent silver reduction.[37, 38, 49]

2. Experimental

2.1 Synthesis

In a typical synthesis, 100 mg of 0.04 M TiO_2-GO[24] was dispersed with sonication (60 min) in 100 mL of deionized water in a 125 mL Erlenmeyer flask. The sample was exposed to a 900 W UV lamp (20 cm away) for 3-5 h while stirring. The solution turned from a brown color to a black color, with some precipitate formation, during the exposure. The reaction was transferred to centrifuge tubes and spun at 3500 rpms for 10 min. The black solution (supernatant) was placed aside. The precipitate was washed with water (50 mL) and MeOH (30 mL), and these washes were added to the original supernatant. The combined solutions (sol-TiO_2-RGO) were allowed to sit undisturbed loosely covered where upon SA-TiO_2-RGO films formed at the air-liquid interface over several days.

2.2 Characterization

2.2.1 Scanning Electron Microscopy (SEM). SA-TiO_2-RGO films were deposited on a silicon wafer and imaged using a Zeiss Supra 55VP field emitter gun scanning electron microscope

(FEGSEM). A Noran EDS detector and Noran System Six software were used for the acquisition of the EDS spectra. EDS Data was plotted using Kaleidagraph™ software.

2.2.2 X-ray photoelectron spectroscopy. X-ray photoelectron spectroscopy (XPS) was performed with a Kratos Axis Ultra DLD with monochromatic Al Kα (1486.6 eV) source at 225 W, and an analyzer pass energy of 20 eV as previously described.[51] The analyzed spot size was 300 x 700 microns and base pressures were less than 5 x 10^{-9} Torr. Charge neutralization was used for all samples. Energy normalization was performed, by setting the first primary component of the C 1s spectrum at 284.5 eV. Data were analyzed using CasaXPS software. Peaks were fit using a Shirley background and a Gaussian/Lorentzian line shape. Peak positions and FWHM for C 1s values were allowed to vary within a limited range, since identical fitting constraints could not be used to fit all spectra.

2.2.3 Raman Spectroscopy. Raman spectra were recorded using a Thermo Scientific Smart Raman DXR instrument with a DRX 633 nm laser with a high-resolution gradient from 150 cm^{-1} to 2100 cm^{-1}. Resulting data was analyzed using the Thermo Scientific Software and re-plotted for presentation purposes using Kaleidagraph software.

2.2.4 Powder X-ray Diffraction (PXRD). SA-TiO_2-RGO films were collected onto a zero background holder purchased from The Gem Dugout, State College, PA 16803 and allowed to dry. Samples were scanned at a rate of 0.02°/2 s in the 2θ range of 5−80° on a Bruker D8 Advance diffractometer in Bragg-Brentano geometry with Cu Kα radiation and a diffracted beam graphite monochromator.

2.2.5 Transmission Electron Microscopy (TEM). A SA-TiO_2-RGO film was placed directly onto a holey carbon type-A, 300 mesh, copper TEM grid purchased from Ted Pella, Inc., Redding, CA 96049 and allowed to dry. Films were studied using a JEOL 2010 high resolution transmission electron microscope (HRTEM), operating at 200 kV accelerating voltage.

2.2.6 Dynamic Light Scattering (DLS) and Zeta (ζ) Potential Measurements. DLS and zeta potential measurements were performed using a Zetasizer Nano ZS instrument from Malvern. This instrument utilizes laser Doppler velocimetry with phase analysis light scattering to calculate the particle size distribution and the zeta potential with a red laser (633 nm). ζ-

potential characterization was performed in background electrolyte of 10^{-3} M KNO_3, and titrated with HNO_3 and KOH for pH adjustment.

2.2.7 Interdigitated Electrode (IDE) Fabrication. A standard lift off technique of titanium and gold was patterned on quartz substrates. The 100 mm quartz wafers were primed and coated using AZ 4110 photoresist, which was spin coated on at 4000 rpm for 30 seconds. A 90 ºC for 30 seconds pre-bake produces a 1.1 mm thick layer. The use of a Karl Suss contact aligner with a 365 nm notch filter was used to expose the photo-resist, and the pattern was opened using a standard development recipe. An adhesion layer using 20 nm of Ti was deposited followed by the deposition of 300 nm of Au^o in a Temescal evaporator. A pitch of 10 micron establishes the 400 mm longer finger for a total edge length of 2 mm. The outside die dimensions are 4 mm by 8 mm and contain four identical channels that are 1 mm of interdigitated electrode.

2.2.8 RGO Testing Conditions. The SA-TiO_2-RGO thin film was placed orthogonal to the metallic trace that is approximately 1 mm in width. Each of the interdigitated channels is connected to form a signal and ground pin-out connection to a Kiethley 6517 electrometer with LabView interface for data acquisition. The channels were wire bonded at the chip level and connected via a circuit board for ease of handling and to minimize noise during photo-current measurements. A West Bond wedge tip bonder was utilized, with gold wire and a stage temperature of 100 ^oC for optimal bond conditions. Bonding after or prior to SA-TiO_2-RGO film deposition gave similar test results.

2.2.9 Uv excitation of thin films. A Horiba Flurolog Spectrometer was used for UV generation, which can go down to 250 nm wavelength using a xenon lamp for exposure. The lamp intensity is in a range from 25 to 30 mJ/cm^2 and varies slightly with warm up time on the power supply and wavelength of interest. The xenon lamp has a decrease in intensity as a function of deep ultra violet wavelengths due to the excitation energy from xenon gas in these wavelengths. A 30 min wait was used before exposure to the sample. The circuit board containing the sample (SA-TiO_2-RGO/IDE) was placed in the line of site to the lamp to maximize photo-current during exposure. First, incremental wavelengths at 50 nm intervals were used to determine the best excitation wavelength for exposure. This experiment started at 600 nm and finished at 250 nm, with a change in wavelength occurring at 10 min increments. The photocurrent had the most

significant change at 350 nm and this roughly coincides with the energy band gap of titanium dioxide. A noticeable shift at 250 nm, corresponding to the decay of intensity due to the xenon source, was also observed. Photocurrent measurements were then conducted with an excitation wavelength of 350 nm. All measurements were done using the fluorimeter enclosure to minimize laboratory lighting as a possible source of noise and error in the data collection. Initial change in resistance measurements were performed using a Black-Ray UV lamp that delivered long-wave (365 nm) ultra-violet light with ~ 21.7 mJ/cm^2 at a 5 cm working distance.

2.2.10 Colloidal Properties and Modeling. The method for calculating the surface parameters in the van Oss-Chaundry-Good model (VOCG). The development of the treatment is as follows. The Young equation relates the contact angle to the force balance at the drop edge for the liquid surface tension (γ_L), the solid surface energy (γ_S) and the interfacial energy between the solid and liquid (γ_{SL}).

$$\gamma_L \cos\theta = \gamma_S - \gamma_{SL} \quad (1)$$

Dupré, in turn, determined an equation to describe the work of adhesion:

$$\Delta G_{SL} = \gamma_{SL} - \gamma_S - \gamma_L \quad (2)$$

The Young-Dupré Equation results from combining these relationships.

$$-\Delta G_{SL} = \gamma_L (1 + \cos\theta) \quad (3)$$

The VOCG approach determines an expression for the free energy of interaction between the solid and liquid (ΔG_{SL}), based on the γ^{LW}, γ^+ and γ^- properties of the solid and liquid materials. The liquid parameters are tabulated as a scale based on the assumption that the electron donating and accepting properties of water are equal, and the Lifshitz-Van der Waals component of the surface tension is related to the Hamaker constant of the material. (l_0 is approximated as 1.57 Å.)

$$A_{ii} = 24\pi l_{0PVP}^2 \gamma_i^{LW} \quad (4)$$

The solid surface requires an expression for the interaction between the components of the surface energies of the liquid and solid phases (in equilibrium with the atmosphere). That expression is as follows.

$$\gamma_{SL} = \left(\sqrt{\gamma_S^{LW}} - \sqrt{\gamma_L^{LW}}\right)^2 + 2\left(\sqrt{\gamma_S^+\gamma_S^-} + \sqrt{\gamma_L^+\gamma_L^-} - \sqrt{\gamma_S^+\gamma_L^-} - \sqrt{\gamma_S^-\gamma_L^+}\right) \quad (5)$$

In this method, the contact angle is measured for each film using three liquids. One liquid is purely dispersive, and the other two have been characterized for their acid and base components.

The following equation is used with each fluid and contact angle (q) to determine the surface parameters of each film.

$$(1+\cos\theta)\gamma_L = 2(\sqrt{\gamma_S^{LW}\gamma_L^{LW}} + \sqrt{\gamma_S^{+}\gamma_L^{-}} + \sqrt{\gamma_S^{-}\gamma_L^{+}}) \quad (6)$$

The apolar liquid has no acid (+) or base (-) components, and therefore should interact only by van der Waals interactions. Using a liquid with known values of γ_L, γ_L^{LW}, γ_L^{+} and γ_L^{-} for contact angle measurements leaves three unknowns in the equation—γ_S^{LW}, γ_S^{+} and γ_S^{-}. It is therefore necessary to make contact angle measurements using three different liquids, all with known values of γ_L, γ_L^{LW}, γ_L^{+} and γ_L^{-}. The calculate values of γ_S^{LW}, γ_S^{+} and γ_S^{-} can then be used with equation 6 to determine γ_S:

$$\gamma_S = \gamma_S^{LW} + 2\sqrt{\gamma_S^{+}\gamma_S^{-}} \quad (7)$$

The obtained values of γ_S can then be used with the known values of γ_L in equation 1 to determine γ_{SL}. Solving for the apolar probe liquid (diiodomethane), gives a value for the dispersive component of the RGO films of 34.2 mJ/m^2. This value is substituted into the values for the remaining two equations. This results in values of γ_S^{+} = 0.897 mJ/m^2 and γ_S^{-} = 2.619 mJ/m^2. This material is a weak electron donor. This likely relates to the π bonding character of the reduced material. The overall surface energy properties of the material suggest that it has low polarity components overall, and the use of polar solvents for dispersion should not be promoted. The ζ-potential measured earlier should be the relevant dispersion mechanism in water, and adding MeOH to the water may lead to poorer dispersion of this material.

The surface energy parameters determined using the VOCG model can be used to determine the free energy of wetting of the surface (1) within the fluid (3) using the following relationship.

$$\Delta G_{131} = -2\left(\sqrt{\gamma_1^{D}} - \sqrt{\gamma_3^{D}}\right)^2 - 4\left(\sqrt{\gamma_1^{+}\gamma_1^{-}} + \sqrt{\gamma_3^{+}\gamma_3^{-}} - \sqrt{\gamma_1^{+}\gamma_3^{-}} - \sqrt{\gamma_3^{+}\gamma_1^{-}}\right) \quad (8)$$

Using these parameters, an energy of wetting for the films can be calculated using equation 8. This gives a value of ΔG_{131} = -59.09 mJ/m^2.

3. Results and Discussion

The solution (sol-TiO_2-RGO)[‡] obtained upon photo-reduction was examined by UV-vis spectroscopy and was found to have a λ_{max} value of 253 nm, compared to aqueous GO (sol-GO) with λ_{max} = 230 nm, consistent with an increase in overall conjugation, Figure 5.9a. Solutions left undisturbed in a loosely covered glass beaker generated numerous films at the air-liquid interface over the course of several days, Figure 5.9b and 5.9c. Leaving the solutions undisturbed for longer times yielded larger (and typically more) films. In general, two different film morphologies were present: square-like shapes and high aspect ratio rectangles, Figures 5.9b and 5.9c. If the initial resulting black solution (sol-TiO_2-RGO) was stored in a tightly sealed flask, no obvious precipitate nor film formation occurred, indicative of general collodial stability and film formation from an evaporation induced self-assembly. A MeOH wash was also found to be critical for effective film formation.

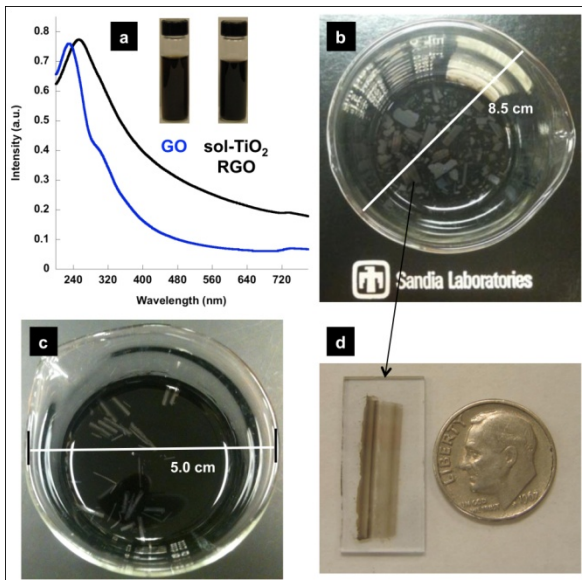

Figure 5.9. a) UV-vis spectra and picture of aqueous GO and sol-TiO_2-RGO; b) and c) SA-TiO_2-RGO thin films prepared from the UV-photo-reduction of sol-TiO_2-RGO. Two morphologies were observed: high aspect rectangles and square-like shaped films; d) A SA-TiO_2-RGO film deposited onto ITO. The striping indicates varying thickness and non-uniformity across the film in the side-to-side (short axis dimension) direction. This is a result of films "annealing" at the liquid-air interface.

In order to examine the films, they were carefully transferred to either SiO_x/Si wafers, glass or IDEs for characterization, Figures 5.9d and 5.10b. Scanning electron microscopy (SEM)

determined well-formed films ranged from ~ 30 to 200 nm in thickness, and were composed of TiO_2 nanoparticles/nanoflowers[24] and a graphene material, sandwiched together, Figure 5.10. Electron dispersive X-ray spectroscopy (EDS) confirmed the presence of Ti as expected, Figure 5.10. Films that were collected shortly after formation (within 1 day) show the development of the films as a mosaic assembly of smaller pieces of graphene and TiO_2, i.e. that is TiO_2-RGO and/or RGO sheets are randomly stacked and overlapped with TiO_2 in between sheets or stacks of sheets, Figure 5.11.

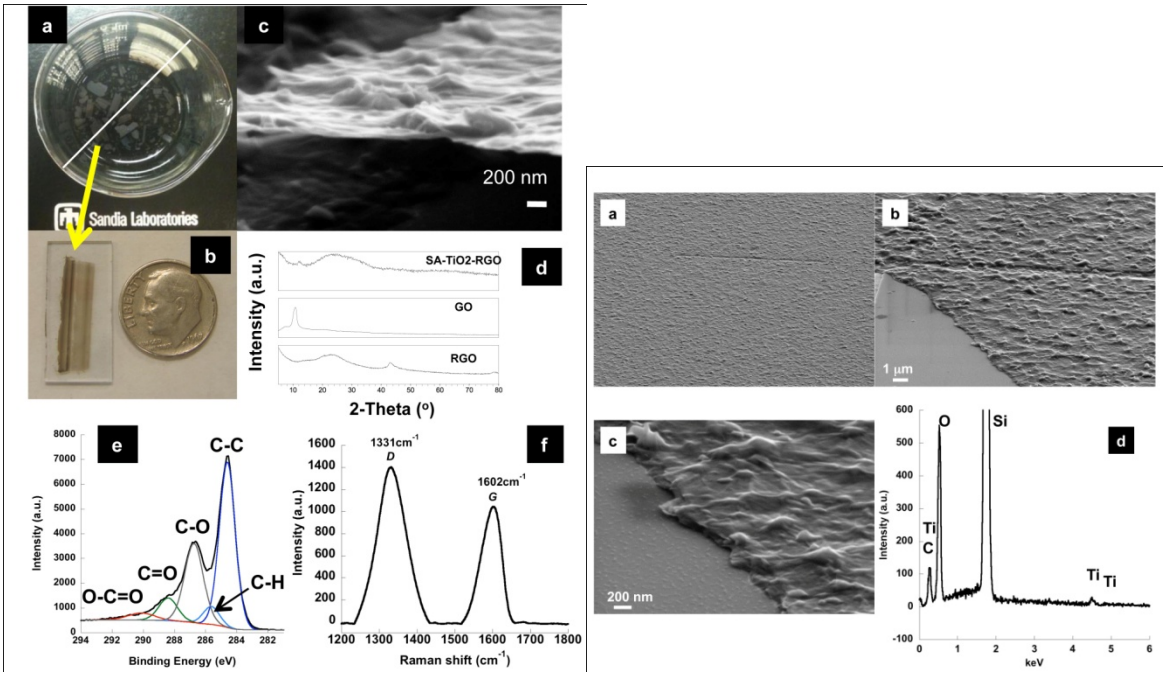

Figure 5.10. (left panel)SA-TiO_2-RGO thin films: picture a) after assembly at the air-liquid interface (white bar = 8.5 cm), b) of film collected on ITO/glass slide, U.S.A dime is shown for scale; c) SEM micrograph of exposed edge after deposition on SiO_x/Si wafer and partial delamination; d) PXRD patterns comparing SA-TiO_2-RGO, GO and RGO; e) XPS spectra indicating partial de-oxygenation; f) Raman spectra indicating reduction of the GO sheets. (right panel) Additional a)-c) SEM micrographs and d) EDS of a SA-TiO_2-RGO thin film deposited onto a SiO_x/Si wafer.

A powder X-ray diffraction (PXRD) spectra was obtained on a collection of films. SA-TiO_2-RGO displays one major broad peak at ~ $2\theta = 24^o$ (002) and a minor sharper peak at ~ $2\theta = 12^o$, Figure 5.10d. The broadness of the graphene (002) peak is consistent with short ordered domains along the stacking direction and indicative of a material comprised of disordered-like nanosheets,

while the minor peak at ~ 2θ = 12° is consistent with some GO like character. GO and RGO[51] are shown for comparison purposes. Titania is not readily observed, due to its low relative concentration in the film. The PXRD is consistent with a graphene oxide that is only partially reduced.

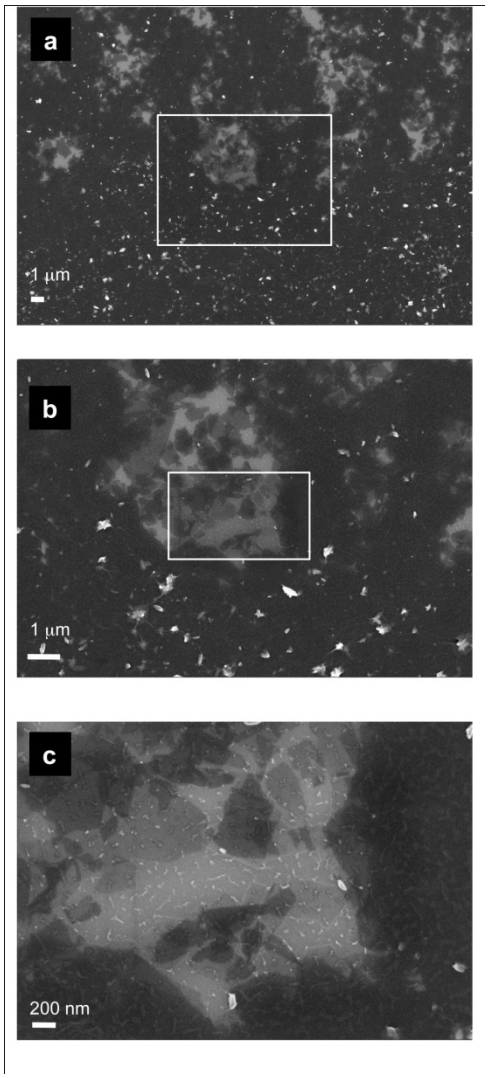

Figure 5.11. a)-c) SEM micrographs of a SA-TiO_2-RGO thin film (high aspect ratio rectangle) collected shortly after formation. Images show the film is comprised of a mosaic assembly of smaller TiO_2-RGO sheets.

X-ray photoelectron spectroscopy (XPS) was also conducted on a deposited film to determine the extent and type of oxygen functionalities present. Survey XPS spectra gave atomic percentages of 82% C and 17% O for SA-TiO_2-RGO, versus 73% C and 25% O for a GO sample. The C:O ratio (as determined by XPS analysis) of ~ 5:1 for the SA-RGO-TiO_2 film is

significantly lower than for the RGO sample obtained by chemical reduction of GO with hydrazine,[51] ca. 23:1. Quantification from XPS shows a Ti concentration of less than 1%, which can be partially attributed to the surface sensitivity of XPS as well as a low titanium content in the composite film. The XPS C 1s spectra, for SA-RGO-TiO_2 film is shown in Figure 5.10e. C 1s peak fitting was performed using a common set of 5 peaks for all C 1s spectra, following previous work.[51] For GO, C 1s fitted peak positions, [FWHM], and (peak assignments) were identified at 284.5 [1.4] eV (C-C), 285.4 [1.2] eV (C-H), 286.5 [1.3] eV (C-O), 288.1 [1.4] eV (C=O) and 289.7 [2.0] eV (O-C=O).[51] C 1s peak fits for SA-TiO_2-RGO gave fitted components at 284.5 [1.2] eV (C-C), 285.5 [1.2] eV (C-H), 286.6 [1.4] eV (C-O), 288.3 [1.4] eV (C=O) and 290.0 [2.0] eV (O-C=O and carbonate), Figure 5.10c. There is a ~ 45% reduction in the peak height, and a narrowing for the C1s (C-O) peak for SA-TiO_2-RGO (with expected corresponding increase in C-C peak), as compared to GO. In contrast, the C=O components are similar in the GO and SA-RGO-TiO_2 samples. It has been proposed that ~ 50% of the oxygen groups in GO are able to accept electrons, and that the carbonyl groups are not likely to be reduced under such mild photo-reduction conditions.[49] The XPS data presented here also supports a fairly low level (~ 32%) of de-oxygenation from photo-reduction.

When examined by Raman spectroscopy the SA-TiO_2-GO exhibited slight downfield shifts in the D- and G-bands, (1331 and 1602, respectively) along with a marked increase in the D/G ratios (I_D/I_G = 1.34) as compared to that for GO, Figure 2f. GO prepared by us exhibited D- and G-bands at 1338 and 1603 cm^{-1} with a D/G ratio of 0.84.[24, 51] Combined with the XRD and XPS data, this indicates that the graphene in the SA-TiO_2-RGO films has undergone a partial reduction, with the carboxylates (and some alcohol or epoxide functionalities) surviving the reduction process.

In order to gain some insight into the self-assembly process, zeta (ζ) potential and dynamic light scattering (DLS) measurements of sol-TiO_2-RGO prior to film formation were obtained. The development of the ζ-potential as a function of pH relates to the surface groups in the studied material. We recently demonstrated that GO and TiO_2-GO show significant ζ potentials even under highly acidic conditions (-35 to -40 mV at pH 2.5), which is sufficient for their exfoliation and dispersion in water.[24] The surface modification of GO nanosheets with TiO_2 presents little change in the development of the ζ-potential beyond a slight reduction in the strength of the measured value. The sol-TiO_2-RGO prepared here is similar in nature. ζ-

potentials for sol-TiO_2-RGO were in the range of -35 to -45 mV across the entire pH range (Figure 5.12) and this data helps to explain the general colloidal stability of sol-TiO_2-RGO observed by us, and others.[49] This wide range pH stability is also consistent with the retention of carboxylate groups during the photo-reduction. DLS data shows the average particle size in the solution to be to be ~ 250 nm in size across a wide pH range, Figure 5.12. This is generally consistent with the numerous sheets observed in the mosaic assembly SEM images, Figure 5.11.

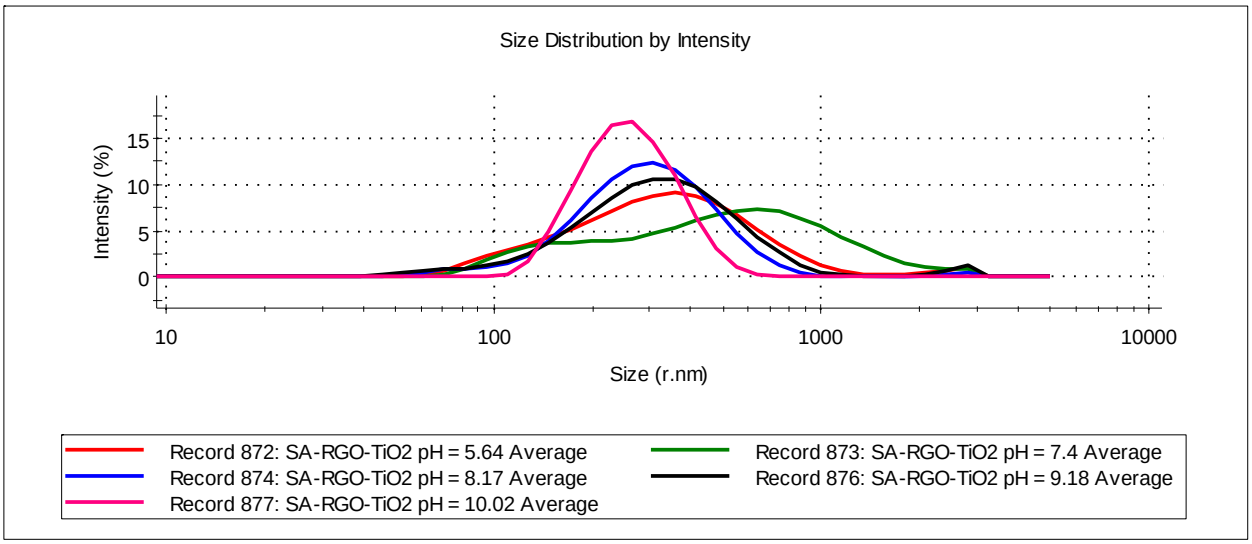

Figure 5.12. Size determination of sol-TiO_2-RGO as determined using dynamic light scattering.

Contact angle measurements using known parameter liquids (Table 3) on the SA-TiO_2-RGO films were also performed and analyzed using the surface tension component theory based on the van Oss-Chaundry-Good model (VOCG), as described in the experimental section.

Table 3. Contact Angle and Surface tension values for known liquids.

Fluid Phase	Contact Angle	Surface Tension	γ_L^{LW}	γ_L^{+}	γ_L^{-}
Diiodomethane	50.13 ± 4.90	50.8	50.8	0.01	0
Ethylene Glycol	47.46 ± 7.87	48.0	29.0	1.92	47.0
Water	81.81 ± 2.74	72.8	21.8	25.5	25.5

Briefly, the VOCG model treats a surface as composed of an apolar component related to Lifshitz-Van der Waals interactions (γ^{LW}), and the electron acceptor parameter (γ^{+}) and an electron donating parameter (γ^{-}). The treatment results in a relationship between measured contact angle of a probe liquid with the interaction components for the liquid and solid phases (see supporting information).[52] Surface energy paramaters for the SA-TiO_2-RGO film were determined to be γ_s^{LW} = 34.2 mJ/m^2, γ_s^{+} = 0.897 mJ/m^2 and γ_s^{-} = 2.619 mJ/m^2. This data indicates that the SA-TiO_2-RGO film surface has a low surface polarity component (in addition to the carboxylate groups). While the van der waals interaction is the major component of the surface energy of the SA-TiO_2-RGO, the γ_s^{-} value indicates that the surface is also a weak electron donor, consistent with the π-bonding character of a reduced graphene surface. Using these parameters, a free energy of wetting (ΔG_{131}) for the films can be calculated using Equation 1 below as ΔG_{131} = -59.09 mJ/m^2 indicating that the material is not hydrophobic (as observed).

$$\gamma_{SL} = \left(\sqrt{\gamma_S^{LW}} - \sqrt{\gamma_L^{LW}}\right)^2 + 2\left(\sqrt{\gamma_S^{+}\gamma_S^{-}} + \sqrt{\gamma_L^{+}\gamma_L^{-}} - \sqrt{\gamma_S^{+}\gamma_L^{-}} - \sqrt{\gamma_S^{-}\gamma_L^{+}}\right) \qquad (1)$$

The calculated values of γ_s^{LW}, γ_s^{+} and γ_s^{-} are used with Equation 2 below to determine total surface energy (γ_s), which is calculated to be 37.3 mJ/m^2.

$$\gamma_S = \gamma_S^{LW} + 2\sqrt{\gamma_S^{+}\gamma_S^{-}} \qquad (2)$$

These values (Table 4) show that the material is not hydrophobic and is wetted by the aqueous fluid phase. The ζ-potentials measured are the relevant dispersion mechanism and explain the colloidal stability prior to evaporation.

Table 4. Contact Angle and Wetting properties modeling of SA-TiO_2-RGO nanosheets/thin film.

Solid Phase	γ_S^{LW}	γ_S^{+}	γ_S^{-}	γ_{sv} (mJ/m^2)	ΔG_{131} (mJ/m^2)
SA-RGO-TiO_2	34.2	0.897	2.619	37.3	-59.09

The self-assembly process performed here requires the addition of both methanol and subsequent evaporation, which has several effects within the interface and in the interactions between/with the particles. Addition of methanol to water is known to lower the surface tension in a non-linear fashion.[53] For example, concentrations as low as 5 mol% methanol lower the surface tension by ~12 mN/m. Transfer of a particle or unit surface area from the fluid phase to a second phase is

energetically described by the surface energy of transfer, $\Delta W = \gamma_{13}-\gamma_{12}$. The aqueous surface tension of 72 mN/m (= γ_{12}) can therefore be lowered to 60 mN/m or less by the addition of methanol, and with a solid value γ_{13} = 37.3 mJ/m^2, the nucleation barrier to dewetting is clearly lowered significantly.[53]

The surface assembly observed here will require nucleation of a stable pore nuclei or pinhole in the growing surface sheet to dewet at the interface. Attempts to measure the contact angle with methanol over the SA-TiO_2-RGO films showed rapid spreading and the formation of Moiré fringes before evaporation. This effectively zero value for the contact angle is evidence that these films are completely wet by methanol and indicate high surface interaction of methanol with the SA-RGO-TiO_2 nanosheets. Thus there is likely a driving force for association of nanosheets with the excess concentration of methanol at the evaporating interface, leading to thin fluid layers over the nanosheets, and a lower surface tension at the interface, which increases the probability of forming a stable pinhole. Local defects leading to pinhole formation could also be promoted by the methanol due to evaporation induced local cooling or fluid transfer.[53]

The model for self-assembly therefore is proposed to relate to the nucleation of dewetted nanosheets at the interface based on the surface activity of methanol with both the solid and fluid phases. Growth of these nanosheets into macroscopic structures is a topic which will require additional study, especially with regards to understanding the origin of the two sheet/film morphologies that are observed. It is proposed that additional nanosheets are added by both growth from within the bulk of the solution, as well as lateral capillary forces resulting from the menisci of the dewetted assemblies. Such assembly behavior has been observed in a macroscopic sense, with high aspect rectangular films “annealing” on the surface to form larger films over time.

As shown in recent studies, RGO materials can store and shuttle electrons and have therefore has potential as new 2-dimensional catalyst nanomats.[54, 55] Excitation of the TiO_2 in a TiO_2-GO solution leads to the formation of an excitated state (electron-hole pair) which injects the electron into the GO structure, resulting in reduction of GO and (if in excess) charge storage. This phenomena is being exploited to develop new devices for photovoltaics, and photoelectrochemical catalysis.[38-44] Very recently, it has been demonstrated that graphene can

provide for ~ a 90% improvement in photocurrent in TiO_2-RGO photoanodes.[38] In order to demonstrate that the SA-TiO_2-RGO films prepared here could function in a similar manner, films were deposited onto an IDE and dried, Figure 5.13a.

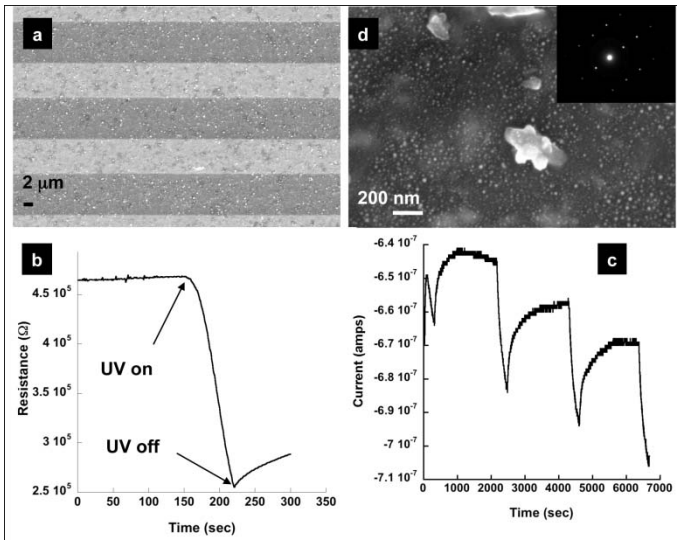

Figure 5.13. a) SEM micrograph of SA-TiO_2-RGO thin film deposited onto an IDE; Representative b) change in resistance across IDE (λ_{exc} = 365 nm), and c) photocurrent cycling (~ 0.25 cm^2 film) in air at 5 min ON and 30 min OFF intervals, with exposure to UV-radiation (λ_{exc} = 350 nm); d) SEM micrograph of ternary Ag^o-SA-TiO_2-RGO film. Smaller Ag^o nanoparticles are visible on the graphene surface. Several larger TiO_2 particles/flowers[4] are also visible. (inset) SAED pattern from TEM indexes to Silver-3C, *syn*, JCPDS (004-0783).

First, the change in resistance across the IDE device was measured while the sample was exposed to UV radiation (λ_{exc} = 365 nm, ~ 21.7 mJ cm^{-2}). Figure 5.13b shows a representative decrease in resistance of ~ 200 kΩ when a ~ 0.25 cm^2 film is exposed. This drop in resistance is attributed to 1) the genertion of an electron-hole pair in the titania, and 2) the subsequent injection/storage of electrons into the graphene structure of the SA-TiO_2-RGO sheet. XPS studies indicated that even with extended UV exposure (several hours), no additional reduction or oxidation of the graphene sheet occurred, indicating graphene stability. While oxygen is known to be a scavenger of electrons/holes that are generated in solution, the devices prepared here surprisingly function in air. The amount of photocurrent generated as measured in air was typically ~ 12-20 nA cm^{-2}. Three repetitive cycles were also performed (e.g. 5 min ON and 30 min OFF), demonstrating the stability of the film to multiple exposures, Figure 5.10c. The low

current obtained is attributed to the thin nature of the film and also its optical transparency of ~ 50%. The ratio of TiO_2 to RGO is another variable that will provide an influence over the amount of current generated. The slow return to ground state is also again surprising given that these devices are exposed to air. Some downward drift is also observed and may be due to a build-up of charge at the film/substrate interface. In essence, SA-TiO_2-RGO films are able to stabilize charge separation generated from photoexcitation. Electron transfer and storage for de-aerated colloidal TiO_2-GO solutions has been demonstrated;[49, 54] however, this stability in air is unexpected. Further studies will be required to better understand this phenomena. Utilization of this charge generation/storage is demonstrated here by the photochemical synthesis of Ag^o nanoparticles[54] on the surface of the SA-TiO_2-RGO film. Briefly, SA-TiO_2-RGO films were irradiated with a UV-lamp (365 nm, ~ 10,000 μW cm^{-2}) in air for 30 min, the lamp was then removed and 200 μL of a degassed solution of 10 mM $Ag(NO_3)$ was pipetted on top of the film. After 10 min, the solution was removed and the film rinsed with DI water and dried. SEM micrographs of the resulting film show that the surface of the SA-TiO_2-RGO film is now decorated with 10-15 nm sized nanoparticles, i.e., a Ag^o-SA-TiO_2-RGO film is formed, Figure 5d. Selected area electron diffraction (SAED) studies from Ag^o-SA-TiO_2-RGO films prepared similarly on transmission electron microscopy (TEM) grids indicate that the nanoparticles index to JCPDS No. 004-0783, Silver-3C, *syn*. The Ag^o nanoparticles are primarily located on the graphene sheet and not co-localized with the TiO_2 nanoflowers/nanoparticles, suggestive of a charge transfer process from the TiO_2 to the graphene[54] prior to reduction of Ag^+, resulting in nanoparticle growth and deposition on the graphene surface of the SA-TiO_2-RGO film. Control studies demonstrate that UV excitation is required for the Ag^+ reduction to occur. While it is possible that these films are behaving in a capacitive nature with charge build up at the interface between the film and substrate, the localization of silver nanoparticles on top of the film suggests the storage of charge in the film itself.

4. Conclusions

In summary, we have demonstrated that photo-reduction of aqueous TiO_2-GO solutions can lead to the formation of unsupported SA-TiO_2-RGO films at the air-liquid interface. Assembly occurs upon lowering of the surface tension (by adding methanol), which leads to de-wetting of the sol-TiO_2-RGO and ultimately self-assembly at the air-liquid interface. These films were shown to

generate ~ 12-20 nA cm^{-2} of current when excited by UV radiation (λ_{exc} = 350 nm, 25-30 mJ cm^{-2}). The graphene sheets could store charge for brief periods of time (in air) allowing for the synthesis of Ag^{o} nanoparticles on the graphene surface. Future studies into the self-assembly of the sheets could provide for even larger optimized structures with enhanced photocurrent and electron storage properties. Evaporative driven self-assembly is a useful tool for preparing titanium-graphene composites and is likely to be applicable to other inorganic-graphene composite and chemically modified graphene, in general.

Acknowledgements: This work was supported (in part) by the Laboratory Directed Research and Development (LDRD) program and the National Institute for Nano-Engineering at Sandia National Laboratories. Sandia is a multiprogram laboratory operated by Sandia Corporation, a Lockheed Martin Company, for the United States Department of Energy's National Nuclear Security Administration under Contract DE-AC04-94AL85000. Dr. Ping Lu and Bonnie M. McKenzie are thanked for their technical assistance with electron microscopy.

References for Chapter 5, Part A.

1. A. K. Geim and K. S. Novoselov, *Nat. Mater.*, 2007, **6**, 183-191.
2. M. I. Katsnelson, *Mater. Today*, 2007, **10**, 20-27.
3. B. Z. Jang and A. Zhamu, *J. Mater. Sci.*, 2008, **43**, 5092-5101.
4. C. N. R. Rao, K. Biswas, K. S. Subrahmanyam and A. Govindaraj, *J. Mater. Chem.*, 2009, **19**, 2457-2469.
5. S. Park and R. S. Ruoff, *Nat. Nanotechnol.*, 2009, **4**, 217-224.
6. D. R. Dreyer, S. Park, C. W. Bielawski and R. S. Ruoff, *Chem. Soc. Rev.*, 2010, **39**, 228-240.
7. S. Stankovich, D. A. Dikin, R. D. Piner, K. A. Kohlhaas, A. Kleinhammes, Y. Jia, Y. Wu, S. T. Nguyen and R. S. Ruoff, *Carbon*, 2007, **45**, 1558-1565.
8. S. Yongchao and E. T. Samulski, *Nano Letters*, 2008, **8**, 1679-1682.
9. H. L. Guo, X. F. Wang, Q. Y. Qian, F. B. Wang and X. H. Xia, *ACS Nano*, 2009, **3**, 2653-2659.
10. Y. Y. Shao, J. Wang, M. Engelhard, C. M. Wang and Y. H. Lin, *J. Mater. Chem.*, 2010, **20**, 743-748.
11. C. Nethravathi and M. Rajamathi, *Carbon*, 2008, **46**, 1994-1998.
12. Y. Zhou, Q. L. Bao, L. A. L. Tang, Y. L. Zhong and K. P. Loh, *Chem. Mat.*, 2009, **21**, 2950-2956.
13. A. V. Murugan, T. Muraliganth and A. Manthiram, *Chem. Mat.*, 2009, **21**, 5004-5006.
14. W. Lv, D. M. Tang, Y. B. He, C. H. You, Z. Q. Shi, X. C. Chen, C. M. Chen, P. X. Hou, C. Liu and Q. H. Yang, *ACS Nano*, 2009, **3**, 3730-3736.
15. H. C. Schniepp, J. L. Li, M. J. McAllister, H. Sai, M. Herrera-Alonso, D. H. Adamson, R. K. Prud'homme, R. Car, D. A. Saville and I. A. Aksay, *J. Phys. Chem. B*, 2006, **110**, 8535-8539.
16. M. J. McAllister, J. L. Li, D. H. Adamson, H. C. Schniepp, A. A. Abdala, J. Liu, M. Herrera-Alonso, D. L. Milius, R. Car, R. K. Prud'homme and I. A. Aksay, *Chemistry of Materials*, 2007, **19**, 4396-4404.
17. J. Phillips, C. C. Luhrs and M. Richard, *IEEE Trans. Plasma Sci.*, 2009, **37**, 726-739.
18. J. C. Weigle, C. C. Luhrs, C. K. Chen, W. L. Perry, J. T. Mang, M. B. Nemer, G. P. Lopez and J. Phillips, *J. Phys. Chem. B*, 2004, **108**, 18601-18607.
19. C. Luhrs, J. Phillips and P. T. Fanson, *Langmuir*, 2007, **23**, 7055-7064.
20. J. Phillips, L. Cheng, C. C. Luhrs, H. Zea, M. Courtney and C. Hanson, *Proc. Mater. Res. Soc. Symp.*, 2008, **1056E**, #HH08-42.
21. A. Dato, V. Radmilovic, Z. H. Lee, J. Phillips and M. Frenklach, *Nano Lett.*, 2008, **8**, 2012-2016.
22. A. Dato, Z. Lee, K. J. Jeon, R. Erni, V. Radmilovic, T. J. Richardson and M. Frenklach, *Chem. Commun.*, 2009, 6095-6097.
23. W. S. Hummers and R. E. Offeman, *Journal of the American Chemical Society*, 1958, **80**, 1339-1339.
24. T. N. Lambert, C. A. Chavez, B. Hernandez-Sanchez, P. Lu, N. S. Bell, A. Ambrosini, T. Friedman, T. J. Boyle, D. R. Wheeler and D. L. Huber, *J. Phys. Chem. C*, 2009, **113**, 19812-19823.

25. D. Y. Pan, S. Wang, B. Zhao, M. H. Wu, H. J. Zhang, Y. Wang and Z. Jiao, *Chem. Mat.*, 2009, **21**, 3136-3142.
26. E. Desimoni, A. M. Salvi, I. G. Casella and D. Damiano, *Surf. Interface Anal.*, 1993, **20**, 909-918.
27. D. Yang, A. Velamakanni, G. Bozoklu, S. Park, M. Stoller, R. D. Piner, S. Stankovich, I. Jung, D. A. Field, C. A. Ventrice and R. S. Ruoff, *Carbon*, 2009, **47**, 145-152.
28. N. J. Havercroft and P. M. A. Sherwood, *Surf Interface Anal*, 2000, **29**, 232-240.
29. Z. M. Wang, K. Hohsinoo, K. Shishibori, H. Kanoh and K. Ooi, *Chem. Mat.*, 2003, **15**, 2926-2935.
30. L. A. Langley, D. E. Villanueva and D. H. Fairbrother, *Chem. Mat.*, 2006, **18**, 169-178.
31. H. K. Jeong, Y. P. Lee, R. J. W. E. Lahaye, M. H. Park, K. H. An, I. J. Kim, C. W. Yang, C. Y. Park, R. S. Ruoff and Y. H. Lee, *J. Am. Chem. Soc.*, 2008, **130**, 1362-1366.
32. X. L. Li, H. L. Wang, J. T. Robinson, H. Sanchez, G. Diankov and H. J. Dai, *J. Am. Chem. Soc.*, 2009, **131**, 15939-15944.
33. W. W. Cai, R. D. Piner, F. J. Stadermann, S. Park, M. A. Shaibat, Y. Ishii, D. X. Yang, A. Velamakanni, S. J. An, M. Stoller, J. H. An, D. M. Chen and R. S. Ruoff, *Science*, 2008, **321**, 1815-1817.
34. M. Filippi and L. Calliari, *Surf. Interface Anal.*, 2006, **38**, 595-598.
35. A. Duarte-Moller, F. Espinosa-Magana, R. Martinez-Sanchez, M. Avalos-Borja, G. A. Hirata and L. Cota-Araiza, *J. Electron Spectrosc. Relat. Phenom.*, 1999, **104**, 61-66.
36. A. Peigney, C. Laurent, E. Flahaut, R. R. Bacsa and A. Rousset, *Carbon*, 2001, **39**, 507-514.
37. A. L. Linsebigler, G. Lu and J. T. Yates, *Chemical Reviews*, 1995, **95**, 735-758.
38. Y. H. Ng, I. V. Lightcap, K. Goodwin, M. Matsumura and P. V. Kamat, *The Journal of Physical Chemistry Letters*, 2010, **1**, 2222-2227.
39. Y.-B. Tang, C.-S. Lee, J. Xu, Z.-T. Liu, Z.-H. Chen, Z. He, Y.-L. Cao, G. Yuan, H. Song, L. Chen, L. Luo, H.-M. Cheng, W.-J. Zhang, I. Bello and S.-T. Lee, *ACS Nano*, 2010, **4**, 3482-3488.
40. H.-B. Yao, L.-H. Wu, C.-H. Cui, H.-Y. Fang and S.-H. Yu, *Journal of Materials Chemistry*, 2010, **20**, 5190-5195.
41. H. Zhang, X. Lv, Y. Li, Y. Wang and J. Li, *ACS Nano*, 2009, **4**, 380-386.
42. O. Akhavan and E. Ghaderi, *The Journal of Physical Chemistry C*, 2009, **113**, 20214-20220.
43. K. K. Manga, Y. Zhou, Y. L. Yan and K. P. Loh, *Adv. Funct. Mater.*, 2009, **19**, 3638-3643.
44. W. Q. Peng, Z. M. Wang, N. Yoshizawa, H. Hatori and T. Hirotsu, *Chemical Communications*, 2008, 4348-4350.
45. Z. H. Tang, J. Zhuang and X. Wang, *Langmuir*, 2010, **26**, 9045-9049.
46. Y. Zhu, W. Cai, R. D. Piner, A. Velamakanni and R. S. Ruoff, *Applied Physics Letters*, 2009, **95**, 103104-103103.
47. D. H. Wang, D. W. Choi, J. Li, Z. G. Yang, Z. M. Nie, R. Kou, D. H. Hu, C. M. Wang, L. V. Saraf, J. G. Zhang, I. A. Aksay and J. Liu, *ACS Nano*, 2009, **3**, 907-914.
48. S. Biswas and L. T. Drzal, *Nano Letters*, 2009, **9**, 167-172.
49. G. Williams, B. Seger and P. V. Kamat, *ACS Nano*, 2008, **2**, 1487-1491.
50. C. Chen, Q. H. Yang, Y. Yang, W. Lv, Y. Wen, P. X. Hou, M. Wang and H. M. Cheng, *Advanced Materials*, 2009, **21**, 3007-3011.

51. T. N. Lambert, C. C. Luhrs, C. A. Chavez, S. Wakeland, M. T. Brumbach and T. M. Alam, *Carbon*, 2010, doi: 10.1016/j.carbon.2010.1007.1015.
52. X. Ma, B. Wigington and D. Bouchard, *Langmuir*, 2010, **26**, 11886-11893.
53. G. Vazquez, E. Alvarez and J. M. Navaza, *Journal of Chemical & Engineering Data*, 1995, **40**, 611-614.
54. I. V. Lightcap, T. H. Kosel and P. V. Kamat, *Nano Letters*, 2010, **10**, 577-583.
55. P. V. Kamat, *The Journal of Physical Chemistry Letters*, 2009, **1**, 520-527.

Part B.

Research achievements funded in part by the NINE project
Jeffrey R. Potts, Prof. Rodney S. Ruoff

Motivation
Graphene is a single layer of sp^2-bonded carbon atoms with exceptional physical properties. A very promising application of graphene is as a filler material in polymer nanocomposites, as graphene can provide dramatic, multifunctional property enhancement to polymers, often at very low loadings.[1] Compared with conventional polymer composites with micron-scale fillers such as glass fiber and carbon black, graphene-based materials can offer larger property improvements at lower loadings, which can simplify processing, lower component weight in molded parts, and possibly even open up entirely new applications of polymers.

While there has recently been great progress in exploring the properties of graphene/ polymer nanocomposites, relatively little work in this field has been concerned with structure-property relationships in these materials. The goal of our research is thus to investigate the relationships between the filler structure, the morphology, and the ultimate composite properties of graphene/polymer nanocomposites.

Accomplishments
1. Microwave-exfoliated graphite oxide/polycarbonate nanocomposites
Graphene-based materials are structurally similar to pristine graphene and can be produced in bulk quantities, but contain defects such as holes or heteroatoms. One such material is microwave-exfoliated graphite oxide (MEGO), produced by microwave treatment of graphite oxide (GO). We published the first report[2] on dispersion of MEGO into a thermoplastic polymer matrix by melt processing (Figure 5.14). MEGO is a high surface area (~500 m^2/g) dry powder consisting of loosely-stacked graphene platelets in an accordion-like structure (Figure 5.15).[3] We used a twin-screw microcompounder to directly disperse MEGO into bisphenol-A polycarbonate for a model study to show that effective dispersion can be achieved without the use of solvents (Figure 5.16).

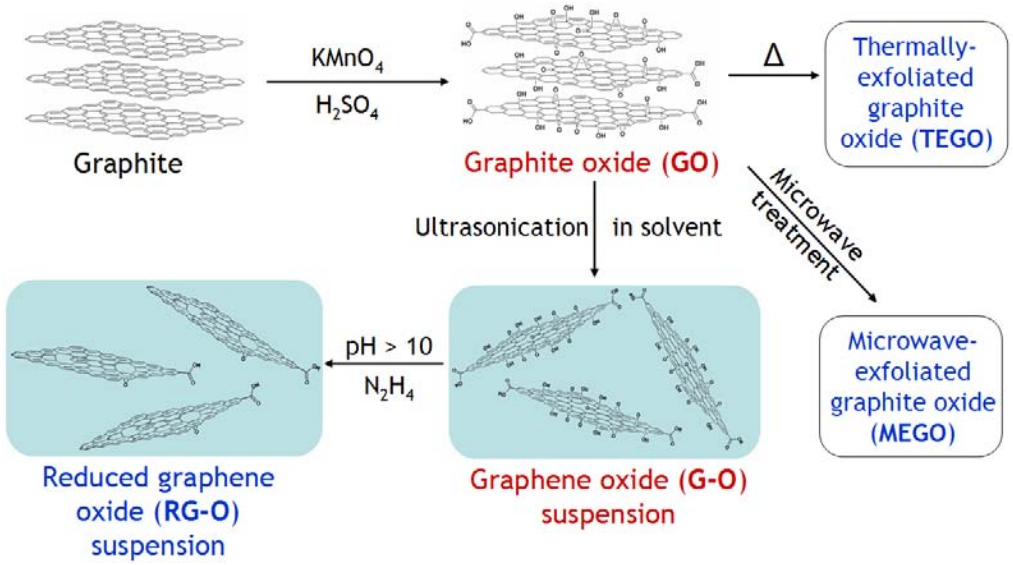

Figure 5.14. Production of graphene-based materials from graphite oxide (GO).

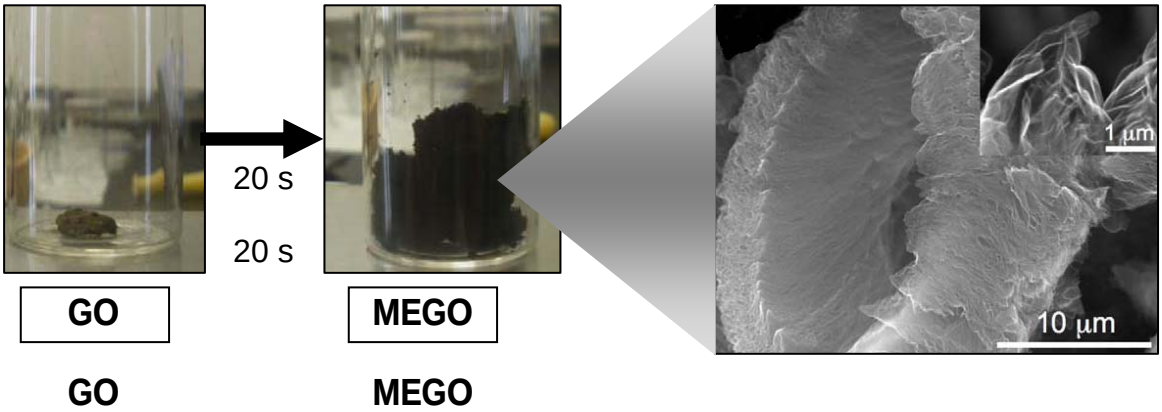

Figure 5.15. Exfoliation of graphite oxide (GO) to microwave-exfoliated graphite oxide (MEGO) by microwave treatment. Scanning electron microscope image shows the accordion-like structure of MEGO powder.

The property improvements achieved in this study were comparable to those reported in the literature on multi-walled carbon nanotube-reinforced thermoplastics. Analysis of transmission electron microscope (TEM) micrographs of 70 nm microtomed nanocomposite sections (Figure 5.17) showed a uniform dispersion of high aspect ratio platelets (average aspect ratio ~ 40). Substantial conductivity enhancement was observed above 1.3 wt% MEGO loading with connectivity percolation evident around 2.1 wt% loading. We also found that prolonged high-temperature (>200 °C) annealing further enhanced thermal and electrical conductivity properties by promoting disorientation of the dispersed platelets, enhancing their ability to form a sample-spanning network.

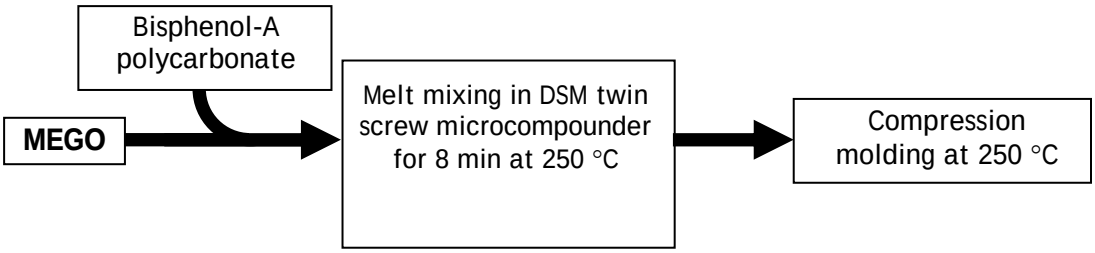

Figure 5.16. Process flow for production of MEGO/polycarbonate nanocomposites by melt processing.

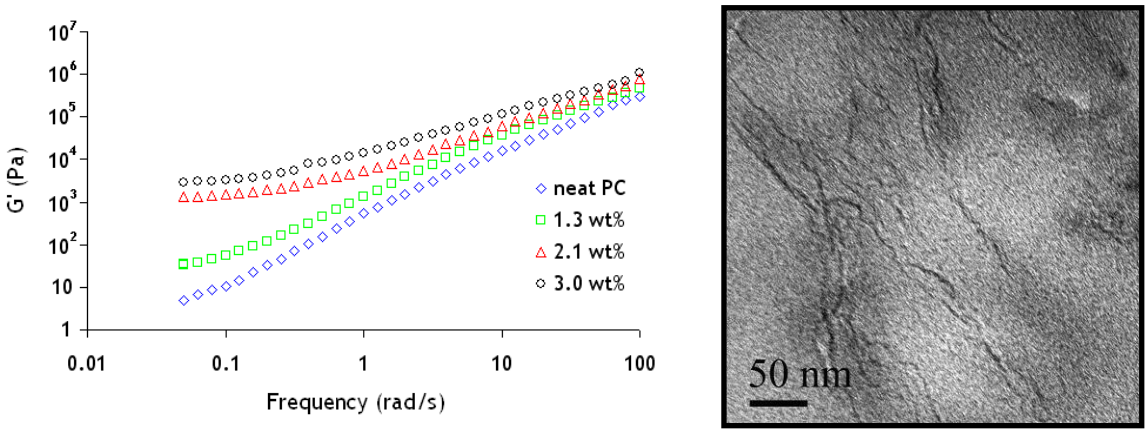

Figure 5.17. (Left) Frequency sweep of MEGO/PC nanocomposite melts showed transition to solid-like terminal behavior at 2.1 wt%, suggesting rheological percolation of MEGO platelets throughout the PC melt. (Right) Transmission electron microscope image of MEGO platelets dispersed in PC matrix showing dispersion of high aspect ratio platelets.

2. Natural rubber reinforced by graphene-based materials: structure-property relationships and filler comparisons

Working in conjunction with Goodyear Tire & Rubber Company, we investigated the dispersion of graphene-based materials into natural rubber (NR) for use in tire tread compounds. In one phase of the study,[4] we studied the relationship between processing, morphology, and properties of reduced graphene oxide/natural rubber nanocomposites. Reduced graphene oxide (RG-O) is a graphene-based material that is produced by exfoliation of GO in water into single-layer graphene oxide platelets by ultrasonic treatment, followed by chemical or thermal reduction to yield a colloidal suspension of RG-O platelets. An aqueous RG-O suspension can be mixed with aqueous NR latex and co-coagulated to form a nanocomposite (Figure 5.18). The morphology inherently created by such a procedure is continuous and "web-like" in structure, with the RG-O platelets confined to interstitial regions between latex particles (Figure 5.19). This morphology was found to be highly beneficial to electrical and thermal conductivity properties and dramatically changed the mechanical properties of the rubber. Milling or similar shear operations, commonly utilized industrially, destroy this morphology and yield a homogeneous

dispersion of RG-O platelets, resulting in properties more typical of filled rubber, but with much higher conductivity than conventional carbon black fillers (Figure 5.20).

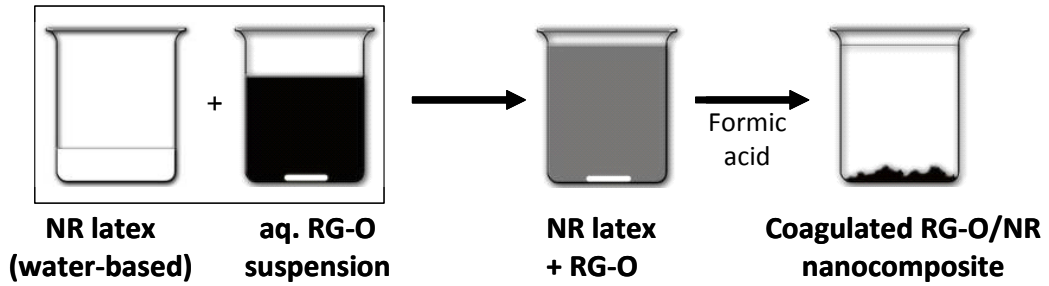

Figure 5.18. Schematic showing the latex co-coagulation procedure.

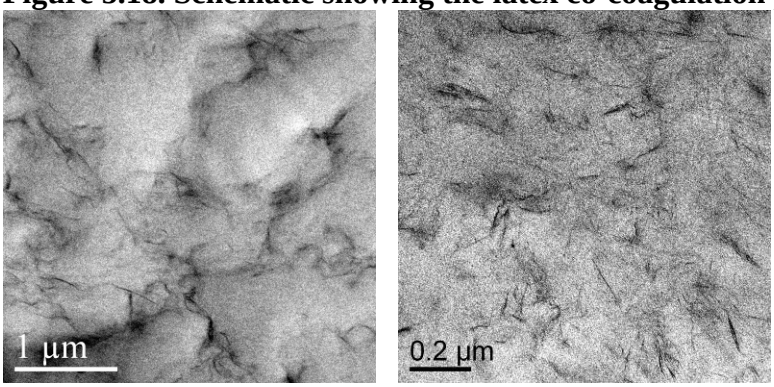

Figure 5.19. TEM micrographs of (left) un-milled and (right) milled RG-O/NR nanocomposites show the web-like, continuous network of filler formed by the co-coagulation procedure and the uniform dispersion achieved after milling this compound.

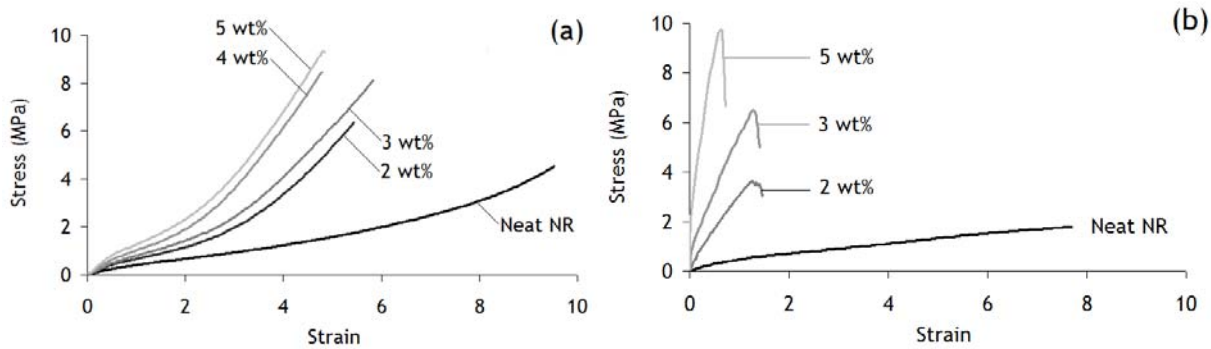

Figure 5.20. The differences in the nanocomposite morphology shown in Figure 5.19 translated to significant differences in mechanical properties. Right, stress-strain curves at various loadings of un-milled nanocomposites; left, stress-strain curves of milled nanocomposites.

In another component of our Goodyear and Sandia NINE-funded effort,[5] a comparison of various nanofillers was performed to evaluate their relative effectiveness in improving mechanical, electrical, and thermal properties. Using an identical latex co-coagulation approach as described

above, NR nanocomposites were prepared with exfoliated sodium montmorillonite (MMT), carboxylated multi-walled carbon nanotubes (MWNTs), RG-O, large-area RG-O (with nominal lateral dimensions approximately 10x larger than "conventional" RG-O), and graphene oxide (G-O) as filler. The motivation for using large-area RG-O platelets was to evaluate the effect of larger intrinsic platelet aspect ratio on property enhancement, as higher aspect ratio particles generally form percolated networks at lower loadings than isotropic particles.[6] G-O platelets were included to evaluate the effect of surface chemistry on dispersion and properties, as we had previously investigated in poly(methyl methacrylate) as a model thermoplastic matrix.[7] Samples were compared across a range of loadings and examined by TEM to evaluate dispersion (Figure 5.21). TEM analysis showed a homogeneous dispersion of filler in all cases; however, differences in the average platelet aspect ratio were evident. Of the platelet fillers, RG-O appeared to be most uniformly dispersed with the highest average aspect ratio. MWNTs were well-dispersed in the NR matrix but appeared highly bundled/entangled in regions of the cross-section.

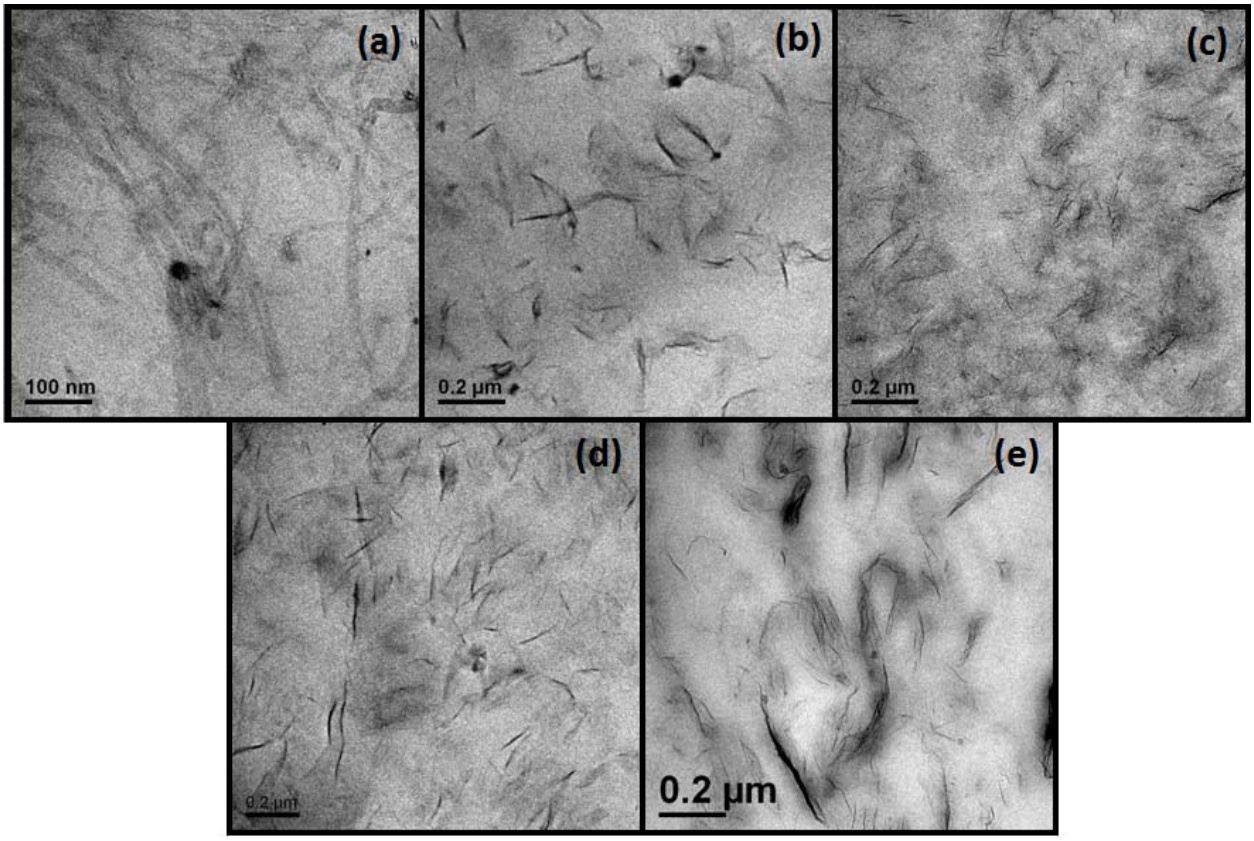

Figure 5.21 Representative TEM micrographs of the dispersion of NR-matrix nanocomposites. (a) MWNT/NR, (b) G-O/NR, (c) RG-O/NR, (d) MMT/NR, (e) large-area RG-O/NR.

Amongst the nanofillers compared in this study, the "conventional" RG-O platelets were found to provide the largest modulus and strength increases over neat NR. MWNTs provided the largest electrical and thermal conductivity enhancements of the nanofillers. Reinforcement by MMT and G-O platelets was comparable, which was expected given that both are hydrophilic

materials while NR (*cis*-polyisoprene) is hydrophobic. The storage modulus as a function of temperature (Figure 5.22) showed consistent results with stress-strain testing, indicating that RG-O platelets provide the greatest reinforcement amongst the fillers studied. Analysis of tan delta peaks (Figure 5.22) also suggested poor interfacial bonding in the G-O and MMT/NR nanocomposites, and strong interfacial adhesion between RG-O or MWNTs and NR. The use of large-area RG-O platelets was not found to be beneficial for property enhancement compared with "conventional" RG-O, perhaps due to a greater amount of re-stacking during the co-coagulation process. We speculate that the lower zeta potential of large-area RG-O platelets (-35.0 mV versus -45.5 mV for "conventional" RG-O platelets at pH 11) translated into more rapid coagulation upon addition of coagulant (dilute formic acid) thus leading to an ultimately poorer dispersion in the nanocomposite despite the larger nominal platelet aspect ratio.

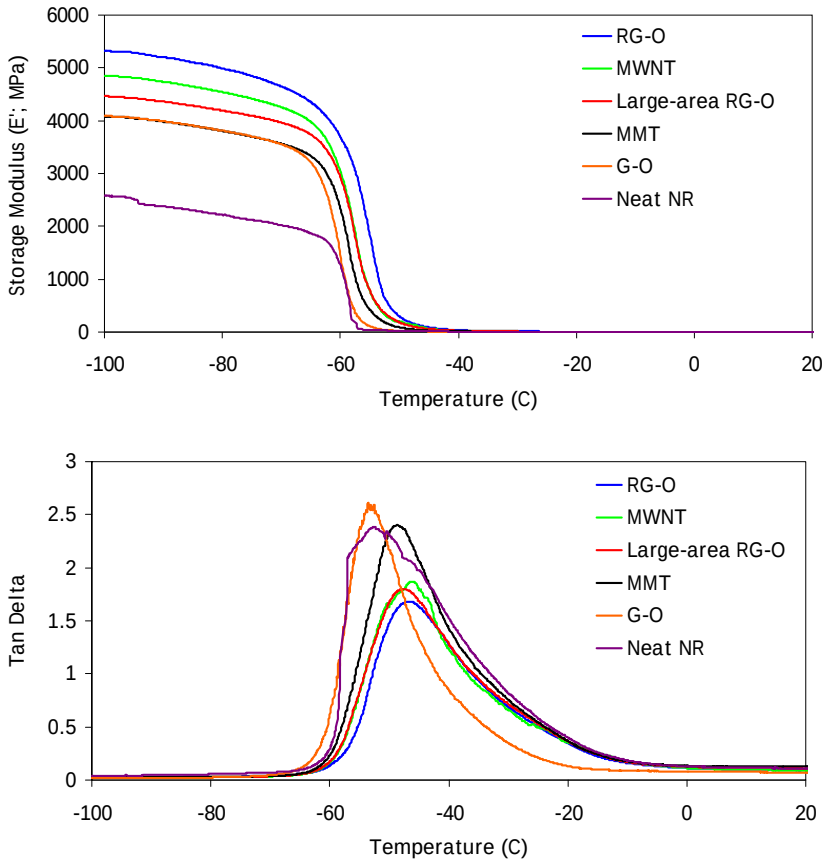

Figure 5.22. Representative dynamic mechanical analysis temperature scans of neat NR or NR matrix nanocomposites filled with various filler materials.

Finally, we have demonstrated the ability to disperse thermally-exfoliated graphite oxide (TEGO) into NR by two-roll mill processing.[8] While TEM analysis showed a good dispersion of TEGO platelets by this approach, property improvements were considerably lower than with RG-O platelets. To improve the properties further, we utilized a latex "pre-mixing" approach whereby TEGO was sonicated with NR latex in water, co-coagulated, and subsequently milled ("L-TEGO"). This processing approach yielded considerable improvements in both dispersion and properties (Figure 5.23). The stress-strain properties of the TEGO/NR nanocomposites was

compared to NR filled with carbon black (CB) as well as a commercial exfoliated graphite nanoplatelet filler produced by XG Sciences (xGnP), and it was found that TEGO provided superior reinforcement when dispersed by two-roll mill processing with even greater improvements possible with a latex "pre-mixing" step (Figure 5.24).

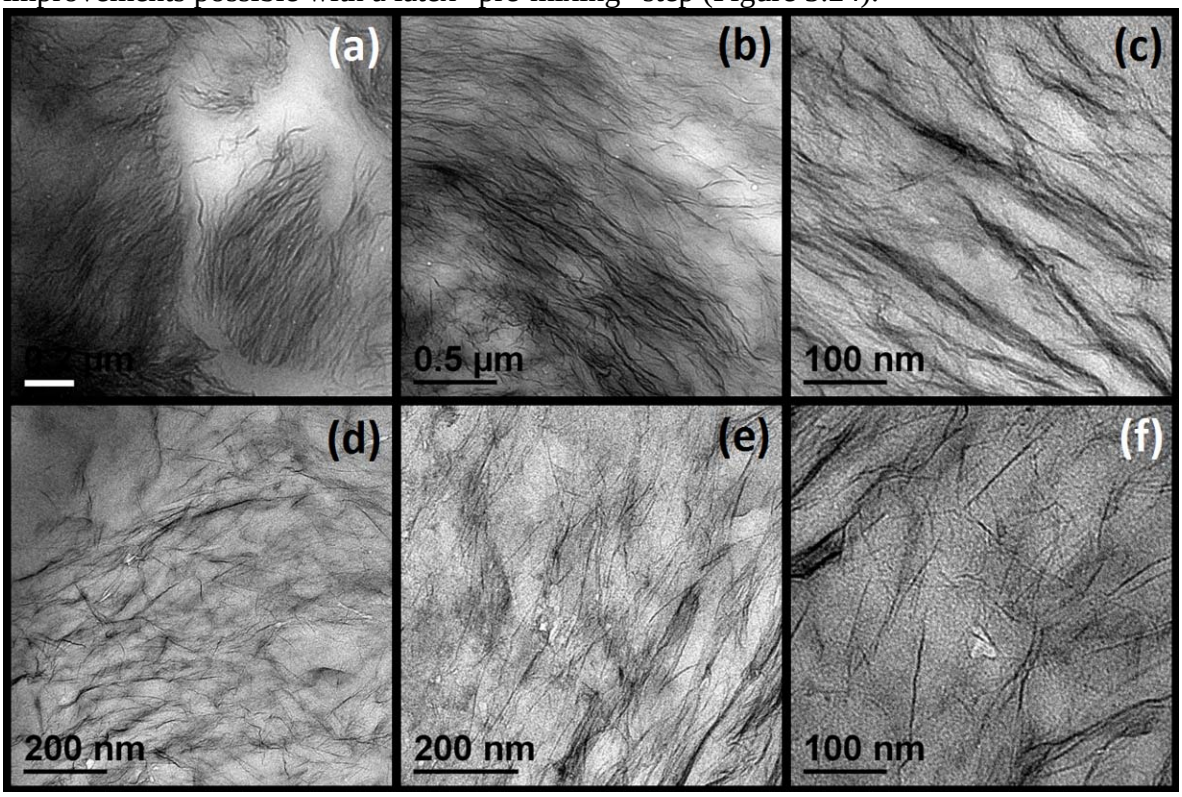

Figure 5.23. TEM micrographs of (a-c) TEGO/NR and (d-f) L-TEGO/NR nanocomposites (latex "pre-mixed" TEGO as filler). Scale bar in image (a) equal to 200 nm.

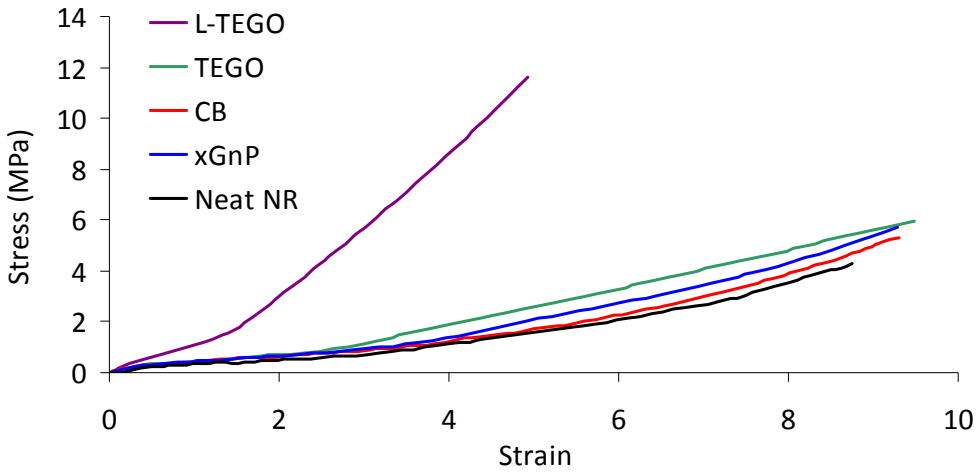

Figure 5.24. Representative stress-strain of neat NR and NR-matrix nanocomposites filled with latex pre-mixed TEGO (L-TEGO), TEGO, carbon black (CB), or exfoliated graphite nanoplatelets (xGnP).

References for Chapter 5, Part B:

1. Potts, J. R.; Dreyer, D. R.; Bielawski, C. W.; Ruoff, R. S. Graphene-based polymer nanocomposites. *Polymer* **2011,** 52, 5-25.

2. Potts, J. R.; Murali, S.; Zhu, Y.; Zhao, X.; Ruoff, R. S. Microwave-exfoliated graphite oxide/polymer composites. *Macromolecules* **2011,** 44, 6488-6495.

3. Zhu, Y. W.; Murali, S.; Stoller, M. D.; Velamakanni, A.; Piner, R. D.; Ruoff, R. S. Microwave assisted exfoliation and reduction of graphite oxide for ultracapacitors. *Carbon* **2010,** 48, (7), 2118-2122.

4. Potts, J. R.; Shankar, O.; Du, L.; Ruoff, R. S. Processing-morphology-property relationships and composite theory analysis of reduced graphene oxide/natural rubber nanocomposites. *Macromolecules* **2012**, submitted.

5. Potts, J. R.; Shankar, O.; Piner, R. D.; Du, L.; Ruoff, R. S. Effect of platelet surface chemistry and aspect ratio on the morphology and properties of graphene/nautral rubber nanocomposites. In preparation.

6. Nan, C.-W.; Shen, Y.; Ma, J. Physical Properties of Composites Near Percolation. *Annual Review of Materials Research* **2010,** 40, 131-151.

7. Potts, J. R.; Lee, S. H.; Alam, T. M.; An, J.; Stoller, M. D.; Piner, R. D.; Ruoff, R. S. Thermomechanical properties of chemically modified graphene/poly(methyl methacrylate) composites made by in situ polymerization. *Carbon* **2011**, DOI: 10.1016/j.carbon.2011.02.023.

8. Potts, J. R.; Shankar, O.; Murali, S.; Du, L.; Ruoff, R. S. Improving dispersion in thermally-exfoliated graphite oxide/natural rubber nanocomposites. In preparation.

CHAPTER 6

Computational models for Responsive Nanocomposites:

(A) Effective Interactions between Grafted Nanoparticles in a Polymer Matrix,
Dong Meng and Sanat K. Kumar, J. Matthew D. Lane and Gary S. Grest

(B) Universal Viscosity Behavior of Polymer Nanocomposites,
Jagannathan T. Kalathi, Gary S. Grest, and Sanat K. Kumar

(C) Fully atomistic simulations of the response of silica nanoparticle coatings to alkane solvents
Brandon L. Peters, J. Matthew D. Lane, Ahmed E. Ismail, and Gary S. Grest

Part A.
Effective Interactions between Grafted Nanoparticles in a Polymer Matrix

Dong Meng and Sanat K. Kumar*
Department of Chemical Engineering, Columbia University,
New York, NY 10027

J. Matthew D. Lane and Gary S. Grest
Sandia National Laboratories, Albuquerque, NM 87185

Abstract

Molecular dynamics simulations were used to delineate the separation dependent forces between two polymer-grafted nanoparticles in a polymer melt, the associated potential of mean force (PMF), and the molecular origins of these forces. The nanoparticle radius (=5, in units of the size of the chain monomers) and grafted brush length (=10) were held constant, while the grafting density and the polymer matrix length were varied systematically in a series of simulations. We first show that simulations of a single nanoparticle do not reveal any signatures of the expected autophobic dewetting of the brush with increasing polymer matrix length. In fact, density distributions of the matrix and grafted chains around a single nanoparticle appear to only depend on the grafting density but not on the matrix chain length in the regime where autophobic dewetting is expected, i.e., when the matrix chain length is equal to or longer than the graft chain length. We thus conjecture that two nanoparticle simulations might be more illuminating in these situations. Indeed, the calculated forces between two nanoparticles in a melt show that increasing the matrix chain length from 10 to 70 causes the inter-nanoparticle potential of mean force (PMF) to go from purely repulsive to attractive with a well depth greater than k_BT. These results are purely entropic in origin and arise from a competition between brush-brush repulsion and an attractive inter-nanoparticle interaction caused by matrix depletion from the inter-nanoparticle zone. The matrix-induced Asakura-Oosawa type inter-nanoparticle attraction, which dominates at intermediate nanoparticle separations especially in the case of long matrix chains, is thus implicated as the essential player in the autophobic dewetting phenomenon, which drives phase separation in these situations.

I. Introduction

It is now well accepted, both theoretically and experimentally, that the functionalization of nanoparticles (NP) with polymer brushes can enhance their miscibility in a polymer matrix.[1-20] This is particularly true if the brush and matrix are of the same chemical structure, and if the brush grafting density is high. Early simulations of single grafted nanoparticles in a polymer matrix showed that the brush density profiles varied smoothly with variations in graft density and matrix chain length.[10, 11, 21-24] Since no unusual variations were found in the density profile, it was hard to interpret this behavior as being a manifestation of any dramatic change in wetting behavior of the brush as the length of the melt chains increased. In particular there was no evidence for a phenomenon called "autophobic" dewetting which occurs when the matrix chains are much longer than the brush chains dewet it due to entropic factors. In contrast to these inconclusive results for single nanoparticles, experiments showed a clear transition to autophobic dewetting, and hence phase separation between the particles and the matrix, when the matrix chains became much longer than the brush.[2, 12, 25, 26] Another aspect to consider in this context is that nanoparticles grafted with polymer chains act akin to a block copolymer. Similar to block copolymer systems that are well known to undergo microphase separation when the covalently bonded blocks are strongly immiscible, in the case where the nanoparticle core and the chains grafted to it dislike each other energetically, and if the grafted chains are long enough, then, the core and the grated chains can be thought as the immiscible blocks on the nanoparticle "block copolymer". Depending on the volume fraction, energetic interaction and steric constraints in the system microphase separation can happen to form a range of anisotropic morphologies.[27] Adding polymer-grafted nanoparticles to a homopolymer melt is thus analogous to adding a structure forming block copolymer to a selective solvent. Understanding how these various factors, i.e., autophobic dewetting, the analogy to block copolymers and the role of the homopolymer matrix as a selective solvent, affect the nanoparticle dispersion in the matrix is a central question in this evolving field.

In previous work from our group, Kalb et al.[28] simulated a single nanoparticle with grafted chains of length 500 in a polymer melt of length 1000 as a function of the number of grafting density on the nanoparticle, Σ. Intuitively we expected that, since the matrix chains are twice as long as the grafts, we should see evidence for the autophobic dewetting between the matrix and

the nanoparticle for high enough Σ. However, we found no unequivocal evidence, partially because the interfacial width between the grafts and the matrix chains varied smoothly with grafting density. Thus, we concluded that studies of a single grafted nanoparticle cannot readily yield information on the miscibility of the grafted nanoparticle with the matrix. The current work builds on this premise and conducts studies of two nanoparticles in a polymer melt, which we assert are necessary to properly understand these miscibility issues.

Here it is relevant to point out that Smith and Bedrov[29] have also conducted molecular dynamics simulations on two polymer-grafted nanoparticles in a polymer melt. To properly sample the various separations of the nanoparticles they used umbrella sampling methods and were thus able to compute the separation dependent potential of mean force (PMF). Here we expand on this approach, but rather than use umbrella sampling, calculate the average forces between the two nanoparticles as function of their separation distance using standard NVT molecular dynamics. While this approach verifies the results derived previously by Smith and Bedrov, we are additionally able to provide a detailed analysis of the origins of the net forces between nanoparticles, and its components, e.g., the matrix contribution, the brush forces and any inter-nanoparticle interactions. We find that, for large grafting densities, the dominant contribution to the effective interactions between the two nanoparticles comes from the sum of all the interactions experienced by the brush chains. For small NP separations brush-brush repulsions dominate and the PMF is repulsive. At larger distances, this repulsion is compensated by brush-matrix interactions, which is sensitive to any depletion of matrix chains between the nanoparticles. Such depletion attraction is similar to the Asakura-Oosawa type interaction. That is when the distance between two confining surfaces is smaller than the diameter of solute macromolecules, the molecules tend to be depleted from the confined region due to the size constraint causing a drop in osmotic pressure in the region. This Asakura-Oosawa type depletion attraction[30, 31] between the nanoparticles overcomes the brush-brush repulsion when the matrix chains are long enough, i.e., in a regime where we expect that the matrix autophobically dewets the brush. For short matrix polymers, we find no attractions at any separation between the nanoparticles suggesting that this dewetting mechanism is probably not operational. These results thus unequivocally verify the notion that, in this limit, the miscibility of nanoparticles with the polymer matrix is driven by the wetting behavior of the brush-matrix interface.

In the next section we present our model for the nanoparticle and the polymer along with the simulation methodology. In Sec III, we first present results for a single nanoparticle, followed by our study of the forces between two nanoparticles as a function of increasing matrix polymer chain length and their molecular origins. We then conclude in Section IV.

II. Model and Methodology

The geometry of most of our simulations, which incorporated two nanoparticles, are sketched schematically in Figure 1a. Both brush and melt polymer chains are represented using the coarse-grained bead-spring model of Kremer and Grest.[32, 33] All monomers are chemically identical and have a mass *m* and diameter σ. The non-bonded interactions between monomers are described by the Lennard-Jones potential:

$$U_{m,m}(r) = \begin{cases} 4\varepsilon\left[\left(\frac{\sigma}{r}\right)^{12} - \left(\frac{\sigma}{r}\right)^{6}\right] & r \leq r_c \\ 0 & r > r_c \end{cases} \quad (1)$$

where ε is the pair interaction energy. For most of the simulations we take the cutoff distance to be r_c=3.0σ, though we also study the purely repulsive case $r_c=2^{1/6}\sigma$ for comparison. Bonded interactions are described using the finitely extensible nonlinear elastic (FENE) potential with a spring constant $k=30\varepsilon/\sigma^2$ and a maximum extent R_0 =1.5σ.[32, 33] Following Smith and Bedrov,[29] a nanoparticle (NP) is represented by a uniform sphere of diameter $\sigma_{NP}=5\sigma$, and we use an "expanded" Lennard-Jones potential for pair interactions between the NP and a chain monomer,[29]

$$U_{NP,m}(r) = \begin{cases} 4\varepsilon\left[\left(\frac{\sigma}{r-R_s}\right)^{12} - \left(\frac{\sigma}{r-R_s}\right)^{6}\right], & r \leq R_c \\ 0, & r > R_c \end{cases} \quad (2)$$

R_s=2σ is the "shifted" distance which ensures that $U_{NP,m}(r)$=0 when a monomer and the nanoparticle are in contact. The cutoff radius, R_c, for nanoparticle-monomer interactions is chosen to be 5σ. Since the value of the effective distance enters the potential as ($r-R_s$), for R_c=5σ, (R_c-R_s)=3σ, which is consistent with the monomer-monomer cutoff distance.

n_g chains are grafted to the surface of each nanoparticle. The first bead of each tethered chain fixed at a distance 2.5 σ away from the center of nanoparticle are evenly distributed on a spherical surface by minimizing the total interaction energy among the n_g sites that interact with each other through a purely repulsive $1/r^2$ pair potential. Two values of n_g have been used in this

study, n_g=30 and 60, respectively, which correspond to grafting densities of Σ= 0.38 and 0.76 chains/σ^2. The tethered chain length is fixed to be M_g=10 in all cases, while the degree of polymerization of the melt chain, M, is varied from 10 to 140 in a series of simulations. This allows us to study the effects of chain length ratio M/M_g on miscibility behavior.

All simulations are carried out using the LAMMPS parallel molecular dynamics (MD) package. MD simulations are performed in an orthogonal simulation box. In the single nanoparticle simulations a cubic simulation box is used with the nanoparticle fixed at the center of simulation cell. There are a total of 14000 monomers, catenated into chains, in the cell. In the two-nanoparticle simulations an orthogonal simulation box of aspect ratio 2:1:1 is used, with the nanoparticles being fixed at positions (–*D*/2, 0, 0) and (*D*/2, 0, 0), where *D* is the separation distance. These simulations contain 42000 chain monomers. The initial states of the polymer chains are created as described in Auhl *et al*.,[34] at an overall monomer density ρ_m=0.85σ^{-3} with the additional restriction that no monomers overlap the nanoparticles. Overlapping monomers in the initial states are pushed off each other using a soft potential until they are far enough apart for the LJ interaction to be switched on. In order to obtain the equilibrated simulation box dimension, a short *NPT* ensemble simulation is conducted at T=1.0ε/k_B and pressure P=0.01ϵ/σ^3. A neat polymer melt at the same temperature and pressure corresponds to a monomer density of ρ_m=0.89σ^{-3}. For the one-nanoparticle studies the simulation box has dimensions of $L\sim25.5\sigma$ and for the two-nanoparticle simulations the box has a dimension of $L\sim29\sigma$ with the actual box size varying slightly across systems.

For each set of parameter values (Σ and *M; M_g*=10 in all cases), a series of production runs are conducted in the NVT ensemble for different nanoparticle separation distances, *D*. During each NVT simulation, the Nose-Hoover equations of motion are integrated with a time step δt=0.005τ, where $\tau = \sigma(m/\epsilon)^{1/2}$. The nanoparticles are allowed to rotate about their centers of mass, but are not allowed to translate. A relaxation phase is allowed in the beginning of each NVT simulation for a run time that is three times the correlation time of the end-end vectors of matrix chains. Each production run is of length 2 x10^5 -2x10^6 τ depending on the melt chain length *M*, grafting density Σ and separation distance *D*. The runs were continued until the uncertainty of

average forces for all three components was less than $0.2\sigma/\varepsilon$. The net force on each nanoparticle, f (t, D), is directly measured every five time steps. The mean force F(D) is calculated as the time average of f (t, D). The resulting F(D) is then numerically integrated to obtain the potential of mean force.

We emphasize here that unusually long runs were necessary to properly calculate the forces, since the fluctuations are large. These fluctuations also appear to be long ranged in time, as shown in Figure 6.1b in which each point corresponds to the time average of f(t, D) on the particle fixed at (D/2, 0, 0) over $10^5\tau$. Here, the separation distance D=9σ, the grafted chain length Mg= 10, the matrix chain length M=10 and the grafting density is Σ=0.76chains/σ^2. Strong, long-lived fluctuations in the x component of the mean force are observed. The y and z components show smaller fluctuations. The data reported everywhere else correspond to averages obtained over simulation runs which are roughly 5 times longer than the blocks used in Fig. 6.1b. This lengthy averaging procedure leads to a considerable reduction in uncertainty. These long equilibration times for the interparticle forces are surprising since the relaxation times of the longest matrix chains (M=70), which we had expected to control equilibration, is $\sim 10^4\tau$. In light of this result, we conclude that the proper averaging of the forces requires, not only a proper sampling of the melt, but also of the relative orientations of the brushes on the two nanoparticles. We believe that we have to run longer than the rotational relaxation times of the nanoparticle, which is we now realize is the slowest mode in this system. Indeed, measures of the rotational autocorrelation functions for a grafted nanoparticle yield relaxation times of $\sim 10^5\tau$, consistent with these long equilibration times. We always ran long enough that the forces in the transverse directions (i.e., the y and z directions) and the uncertainty in the force in the x direction was $<0.2\varepsilon/\sigma$.

III. Results and Discussion

One-Nanoparticle simulations

Before measuring forces in multi-nanoparticle simulations, we conducted simulations on a single grafted nanoparticle in a polymer melt for each set of Σ and M values. These give us information on the brush and melt density profiles.

Figures 6.2 (a) and (b) show the radial dependence of the composition for component *i*, $\phi_i(r) \equiv \rho_i(r)/[\rho_g(r) + \rho_m(r)]$(i.e., the brush or matrix segments) at the two grafting densities Σ=0.38 and 0.76 chains/σ^2, respectively. Here $\rho_g(r)$and $\rho_m(r)$ are the number densities of brush and matrix segments at radial distance *r* from the center-of-mass of the nanoparticle. While the brush profiles are more extended at higher grafting density (Figure 6.2c), they are surprisingly insensitive to the ratio of the matrix to the grafted chain length for M/M_g>1. Thus, the brush height *h* (defined at position where $\phi_g(r) = \phi_m(r) = 0.5$) is found to be 1.3$\sigma$ for Σ=0.38 chains/σ^2 and 2.8σ for Σ=0.76chains/σ^2 for both M/M_g considered. Our results for different M values are new. However, they strongly reiterate the notion[28] that single particle simulations do not yield meaningful insights into the miscibility of grafted nanoparticles with a polymer matrix. As we shall show below, the M=70 system appears to be a situation where the matrix should autophobically dewet the brush, while the M=10 is a case where the nanoparticles are sterically stabilized by the grafted chains. The lack of dependence of the density profiles in Figure 6.2 for such changes in M directly underscores our point. We also note that our results for changes in density profiles with variations in grafting density are qualitatively consistent with previous simulations,[17] even those which employed long chains for both brushes and melts (500 and 1000 beads, respectively).[28] Specifically, we find that that the brush becomes more extended with increasing grafting density. Regardless, our findings continue to stress that we need to perform simulations for two (or more) nanoparticles to shed light on the miscibility of grafted nanoparticles with polymer melts.

Two-Nanoparticle simulations

According to our single particle simulations, as well as previous studies, the brush profiles around a single nanoparticle are insensitive to the change of ratio M/M_g when $M>M_g$. This suggests that the previously observed phase behavior of these systems[10] with multiple nanoparticles in a polymer melt must be sensitive to subtle changes of the distribution of brush and matrix segments when two (or more) particles come close. We next use two-nanoparticle simulations to show how the forces between grafted particles depend on the grafting density and ratio M/M_g. We then provide an explanation for the observed attraction on a molecular basis. Since the two nanoparticles are placed along the x axis, the y and z components of the time averaged net force should equal zero, while the x component of the net forces on the two

nanoparticles should be equal in strength but opposite in direction (Fig. 6.1). Both of these facts are verified to within the uncertainties of the simulations. Therefore, only the x component of the net force on the grafted nanoparticle placed at (D/2, 0, 0) will be reported, unless otherwise stated. The net force exerted on the grafted nanoparticle includes the force exerted on its core and the grafted brush chains by the matrix and the grafted chains on the second nanoparticle. At equilibrium, the *time averaged* net force on the grafted nanoparticle equals that exerted on the nanoparticle core. This is verified through simulations showing that the differences between the two forces, namely the forces experienced by the core versus the force experienced by the core and the grafted chains, are less than $0.001\varepsilon/\sigma$ in all cases (well within the uncertainties of the simulations). As a result, in the following, we do not distinguish the *time averaged* net force on the grafted nanoparticle and the *time averaged* net force on nanoparticle core and refer to both as the time averaged net force on the nanoparticle.

Snap shots from two NP simulations with M=70 and Σ=0.76chains/σ^2 at D=8σ and 11σ are shown in Figure 6.3. Figure 6.4 shows the time averaged net force on a nanoparticle as a function of separation distance, *D*, for five of the systems studied. When the matrix chain length is short (M=10, M/M_g=1), the net force between grafted nanoparticles is always repulsive (positive) and monotonically decays towards zero with increasing *D* for both grafting densities Σ=0.38 and 0.76 chains/σ^2. Both the range and strength of repulsion are larger at higher grafting density, presumably due to the more extended brush profiles. The force curves in these cases can be fit reasonably well by the empirical functional form $F(D) = (a/D)^b$ where a and b are the fitting parameters. We find $a = 8.64$, $b = 6.88$ for Σ=0.38 chains/σ^2 and $a = 11.13$, $b = 7.82$ for Σ=0.76 chains/σ^2. Given that $\sigma_{NP} = 5\sigma$ and the brush height $h = 1.3\sigma$ and 2.8σ for the two grafting densities, respectively, we have $a \sim \sigma_{NP} + 2h$, i.e., that the parameter *a* roughly equals the effective size of a grafted nanoparticle, while b characterizes the steepness of the variation. The conclusion that the repulsive forces between NPs are characterized by an effective diameter that is the sum of the NP diameter and the brush chain extent is in agreement with the intuitive idea that the brushes serve to sterically stabilize the particles in this limit. Here we note that other functional forms, e.g., $F(D) - (a/(D - \sigma_{NP}))^b$, might be more appropriate to describe the data – however, we do not see any dramatic improvements in the quality of the fits obtained and hence use the simplest form. Simulations at additional grafting densities and closer inter-NP

separations are apparently necessary to obtain a more analytically reliable form for the inter-NP forces.

As the matrix chain length is increased (M=70, M/M_g=7), the strength of repulsion at small *D* is reduced. At large separations, an attractive (negative) interaction force is observed. In this case, the empirical functional form $F(D) = [(\frac{a}{D})^b - (\frac{a}{D})^c] \exp(d - eD)$ is found to describe the force as a function of *D*. The repulsion term is adopted from the pure repulsive cases where the parameter a is still the effective size of a grafted particle. It is important to emphasize here that the two functional forms used to describe the forces between the particles in the two cases are empirical and that they are used to simplify the calculation of the potential of mean force (PMF) between two particles, following:

$$\Psi(D) = -\int_{\infty}^{D} F(D)\, dD. \quad (3)$$

Figure 6.5 compares the potential of mean force with the results from Smith and Bedrov's recent simulations of a similar coarse-grained system using the umbrella sampling method for the an apparently identical brush length M=10 and coverage .[29] Clearly, our results are in qualitative agreement with the previous results, with a better match being obtained for M=10 and Σ=0.38chains/σ^2. Our PMF consistently seems to be shifted toward smaller separations, as can be seen by the distance at which the potential first crosses zero with increasing *D*. We believe that these differences are due to small differences in the models used to represent the grafted nanoparticles. In our system, a smooth particle core is used with the "grafting bead" of each grafted chain fixed onto a spherical surface of radius 2.5 σ from the center of nanoparticle. Smith and Bedrov constructed a nanoparticle from 61 composite atoms with 60 of them located at 2.5σ from the core center as the tethering sites to which grafting beads are connected. Therefore, M_g=10 in Smith and Bedrov's study corresponds roughly to M_g=11 in our model, with this result suggesting that the minima in the PMF curves should be shifted by roughly one monomer size. Differences may also come from the polymer model. Smith and Bedrov[29] study a bead necklace chain (or tangent bead chain) model with a bond length fixed at σ, while FENE bonds with an equilibrium bond length of ~0.97σ are used in the current work .

Molecular Origins of the observed PMFs

The net force on a grafted nanoparticle equals the sum of the net force on its brush chains and its core, i.e.,

$$F(D) = F_{brush}(D) + F_{core}(D) \quad (4)$$

Each of these two contributions can be further separated into the forces exerted by the matrix, the brush on the other nanoparticle ("opposite" brushes) and the opposite particle core, i.e.,

$$F_i(D) = F_i^{mat}(D) + F_i^{brush2}(D) + F_i^{core2}(D) \quad (5)$$

where *i*= brush and core. Figure 6.6 shows the variation of each of these components as a function of *D* for M_g=10, M=70 at two different graft densities, namely 0.38 and 0.76 chains/σ^2, respectively. For both graft densities the forces on the particle core are much smaller compared to that on the brushes. Apparently, the core is sterically separated from its surroundings by its grafted chains leading to these small forces. For the same reason, the force on the brushes exerted by the opposite core is also small. Thus, the net force on a grafted nanoparticle comes mainly from the forces experienced by the grafted chains, primarily through their interactions with the matrix chains and the opposing brush. It seems reasonable to assume that the repulsive and attractive interactions between grafted nanoparticles must then be due to the unbalanced density distribution of matrix and opposite brush segments around the nanoparticle.

In the two-nanoparticle system, the density distribution is a two dimensional function of x and r, where r is the distance of a spatial point to the origin, which is at the center of the line joining the centers of the two nanoparticles (Fig. 6.1a). We define the quantity

$$\Delta\rho(r) = \frac{1}{D-\sigma_{NP}} \int_{\frac{(D-\sigma_{NP})}{2}}^{\frac{(\sigma_{NP}-D)}{2}} [\rho(r,x) - \rho(r,D-x)]\,dx \quad (6)$$

to characterize the density difference on the two sides (<D/2 and >D/2) of the nanoparticle placed at x=D/2. Figure 6.1a shows schematically that the integral in Eq. (6) corresponds to integrating densities on the surfaces of the two cylinders and then subtracting the right side contribution from the left side. Plotting $\Delta\rho(r)$ as a function of *r* then allows us to understand how this density "imbalance" on the two sides of the sphere increases as a function of distance from the center-line For an isolated nanoparticle $\Delta\rho(r) = 0$ as the distribution of segments in this case is spherically symmetric.

Figure 6.7(a) compares such density differences for two systems M=10 and M=70 with Σ=0.76 chains/σ^2 at D=9, 10 and 11σ. We first consider the density contribution from the brush on the opposite particle. Since the opposite brush is only present on the <D/2 side of the right hand sphere, the second term on the right side of Eq. (6) is always zero. Thus, intuitively, we expect $\Delta\rho_{brush2}(r) > 0$ for all r as shown in Figure 6.7(a). $\Delta\rho_{brush2}(r)$ shows a maximum value in the vicinity of $r \approx \sigma$. For a given graft density, the $\Delta\rho_{brush2}(r = 0)$ increases with decreasing *D*, and seems to be insensitive to the change in matrix chain length M.

Figure 6.7(a) also shows that $\Delta\rho_{matrix}(r) < 0$ for all r indicating that the matrix segments are depleted on the <D/2 side. This is the origin of the Asakura-Oosawa type depletion attraction between the particles, with this effect being in competition with the brush-induced repulsion between the particles. The degree of depletion in $\Delta\rho_{matrix}(r)$ is shown to increase with the matrix chain length M for r<5σ while for r>5σ the results for the different matrix chain lengths seem to overlap. Since the bare NP diameter is 5σ, we conjecture that such depletion effects are only sensitively dependent on grafting density, M and M_g for r<5σ. For r>5σ, the depletion is solely due to the trivial excluded volume effect that matrix segments are replaced by the opposite brush segments on the <D/2 side.

The third part of Figure 6.7(a), shows the total density difference $\Delta\rho_{brush2}(r) + \Delta\rho_{matrix}(r)$ plotted *vs. r* for three different *D* values and *M*=10 and 70, respectively. First of all note that the y-axis scale is smaller in this figure. By analogy to Figure 6.6, this finding suggests that the NP's behavior is affected by two relatively large but opposing factors – increase in contacts with the opposite brush (repulsive) and a depletion of matrix chains (Asakura-Osawa type attractive forces). We first focus on *M*=10, where the inter-NP forces are repulsive everywhere (Figures 6.4 and 6.5). For *D*=9σ, the net increase from the brush density dominates the behavior. At larger *D* (=10σ and 11σ), the density differences still appear to be essentially positive at all r. Note that there seems to be a small region between 4σ and 5σ in the third part of Fig 6.6a where this quantity is slightly negative, but these numbers are within simulation uncertainties. We thus conclude that the force results observed for *M*=10 appear to be completely dominated by the increase in brush density between the NPs. We now consider *M*=70. For all *D*, increasing the matrix chain length reduces the short-ranged brush induced increase in density, and a net

depletion of segments at larger r. For D=9σ, this medium-ranged depletion apparently does not control inter-NP forces, which are smaller relative to the M=10 case, but still repulsive (Figures 6.4 and 6.5). For larger D, especially for $D = 11\sigma$, it is clear that there is a net depletion of segments for all r. Since the inter-nanoparticle force is attractive over this range of D values (Fig. 6.4), we conclude that the matrix depletion effect is the molecular cause of these medium ranged inter-NP attractions.

These points are even clearer when we plot $\Delta\rho_{brush1}(r) + \Delta\rho_{brush2}(r) + \Delta\rho_{matrix}(r)$ as function of r. At very small r this quantity is negative for both M. However, for the smaller M, this quantity essentially goes to 0 for all large r values, strongly suggesting that the overall system incompressibility dominates behavior. The results at the larger M value show a medium ranged negative value implying that there is an overall (small) depletion of segments between the nanoparticles. We suggest that this small, matrix-driven depletion effect is the root cause of the attractive forces between the nanoparticles.

Qualitatively similar behavior in the density differences are also observed at Σ=0.38 chains/σ^2 (Figure 6.7(b)). Compared to the higher grafting density, all the depletion effects seem to be smaller in magnitude although still of the same spatial range. Apparently, the system incompressibility dominates more than at the higher grafting density due to the lesser number of constraints that are imposed due to the lower graft density.

We also performed a few simulations using purely repulsive pair potentials for a matrix chain length M=140 and Σ=0.76 chains/σ^2 . This is compared to results obtained from the same physical situation except that the attractive interactions were retained in the LJ potential. The same type of effective inter-NP attractions are observed in both cases (not shown) and the density differences in the two cases are very similar as shown in Figure 6.8. This conclusively illustrates that for the present model the effective inter-nanoparticle attraction has an entropic origin as implied above.

IV. **Conclusions**

We have used molecular dynamics simulations to calculate the forces and hence the potentials of mean force between two polymer-grafted nanoparticles in a polymer melt. We first show that simulations of a single nanoparticle do not shed new light on the origins of phase behavior in these systems. The density distributions around single nanoparticles appear to only depend on grafting density, but not on the matrix chain length, especially when the matrix chain length is equal to or longer than the graft chain length. This result is particularly powerful since we expect to see signs of autophobic dewetting between the brush and matrix chains in this regime of matrix chain length, a point that is completely not captured. In contrast to these findings, the potential of mean force between two nanoparticles, which are in good agreement with the previous findings of Smith and Bedrov,[29] show strong variations with changes in the matrix chain length. We show that increasing the matrix chain length from 10 to 70 causes the inter-nanoparticle potential of mean force to go from repulsive everywhere to attractive at intermediate separations with a well depth on the order of k_BT. These results are purely entropic in origin, and arise from a competition between brush-brush repulsion and an attractive inter-nanoparticle interaction caused by matrix depletion from the inter-nanoparticle zone. While the brush repulsion always "wins" at short separation, the matrix induced Asakura-Oosawa type inter-nanoparticle attraction dominates for intermediate separation and long matrix chain length matrices.[13, 15, 30, 31, 35]

Our results clearly suggest that going from one nanoparticle to two nanoparticles lead to new physics that shed light on this very interesting miscibility question. Looking forward, it is apparent that simulations of three, and more, nanoparticles would be very interesting – however, preliminary simulations on a three nanoparticle system, in the same spirit as the two NP calculations presented in this paper, shed very little new light. Rather, the uncertainties in inter-nanoparticle interactions were so large, even after very long simulations, that we conclude that the current approach cannot be reliably extended even to this case. The simulations of systems with a larger number of nanoparticles, and their associated phase behavior, thus remain an open but fascinating area of research.

Figures and Captions

Figure 6.1: Schematic showing the geometry of the system studied. The center of mass of the two nanoparticle cores are located at (–D/2, 0, 0) and (D/2, 0, 0). In this case the density distribution is a two-dimensional function of x and r. The shaded region in the figure indicates the cylindrical geometry under study in Eq. 6. The integral in Eq. 6 corresponds to a calculation on the surface of the cylinder on the left minus the analogous calculation on the right. (b) Evolution of the "block" average of the measured forces with simulation time. The time block used in calculating the averages is $10^5\tau$.

Figure 6.2: Comparison of composition profiles of brush and matrix segments for a single nanoparticle with a brush of length M_g=10. Data are shown for M=10 and M=70, respectively, at (a) Σ=0.38 chains/σ^2, (b) Σ=0.76 chains/σ^2. (c) Compares the data for to M=70 at two different coverages.

Figure 6.3: Snapshots of two grafted nanoparticles in polymer matrix at two separation distances (a) D=11σ and (b) D=8σ. Here, the grafted chain length M_g=10, the matrix chain length M=70 and the grafting density Σ=0.76 chains/σ^2. The matrix chains are not displayed in the plot for clarity.

Figure 6.4: The net force F on the grafted nanoparticle located at (D/2, 0, 0) as a function of particle separation distance D. The dotted lines are only a guide to the eye, while the solid lines show the fits to the two cases discussed in the text. See text for details on the functional forms that are used in the fitting.

Figure 6.5: Potential of mean force between two grafted nanoparticle in two cases, Σ=0.38 chains/σ^2 and M=10 shown in solid black lines; Σ=0.76 chains/σ^2 and M=70 shown in solid red lines. The dotted lines show the potential of mean force obtained for the corresponding cases in reference. [29]

Figure 6.6: Variation of force components exerted on the grafted nanoparticle located at (D/2, 0, 0) with particle separation distance D at M=70 and (a) Σ=0.38 chains/σ^2 and (b) Σ=0.76 chains/σ^2. The force components are: force on the brush chains due to the opposite nanoparticle

core (solid line and triangle); due to brushes on the opposite nanoparticle (solid line and square); due to matrix polymers (solid line and circle); force on nanoparticle core due to brushes on the opposite nanoparticle (dashed line and open square); due to matrix polymers (dashed line and open circle).

Figure 6.7: Segmental density differences (defined by Eq. (6)) for opposite brush segments, matrix segments and total density difference (i.e., opposite brush and matrix) as functions of the radial distance r on the < D/2 side and >D/2 side of the grafted nanoparticle located at (D/2, 0, 0) for three D values, in units of σ. Here (a) Σ=0.76 chains/σ^2 and (b) Σ=0.38 chains/σ^2. Part (a) also has an additional plot corresponding to the sum of the density differences of the opposite brush, the same brush and the matrix.

Figure 6.8: Comparison of the total segmental density differences on the < D/2 side and >D/2 side of the grafted nanoparticle located at (D/2, 0, 0) at M=140, Σ=0.76 chains/σ^2 between a pure repulsive system shown in dashed lines and open symbols, and a LJ system shown in solid lines and solid symbols.

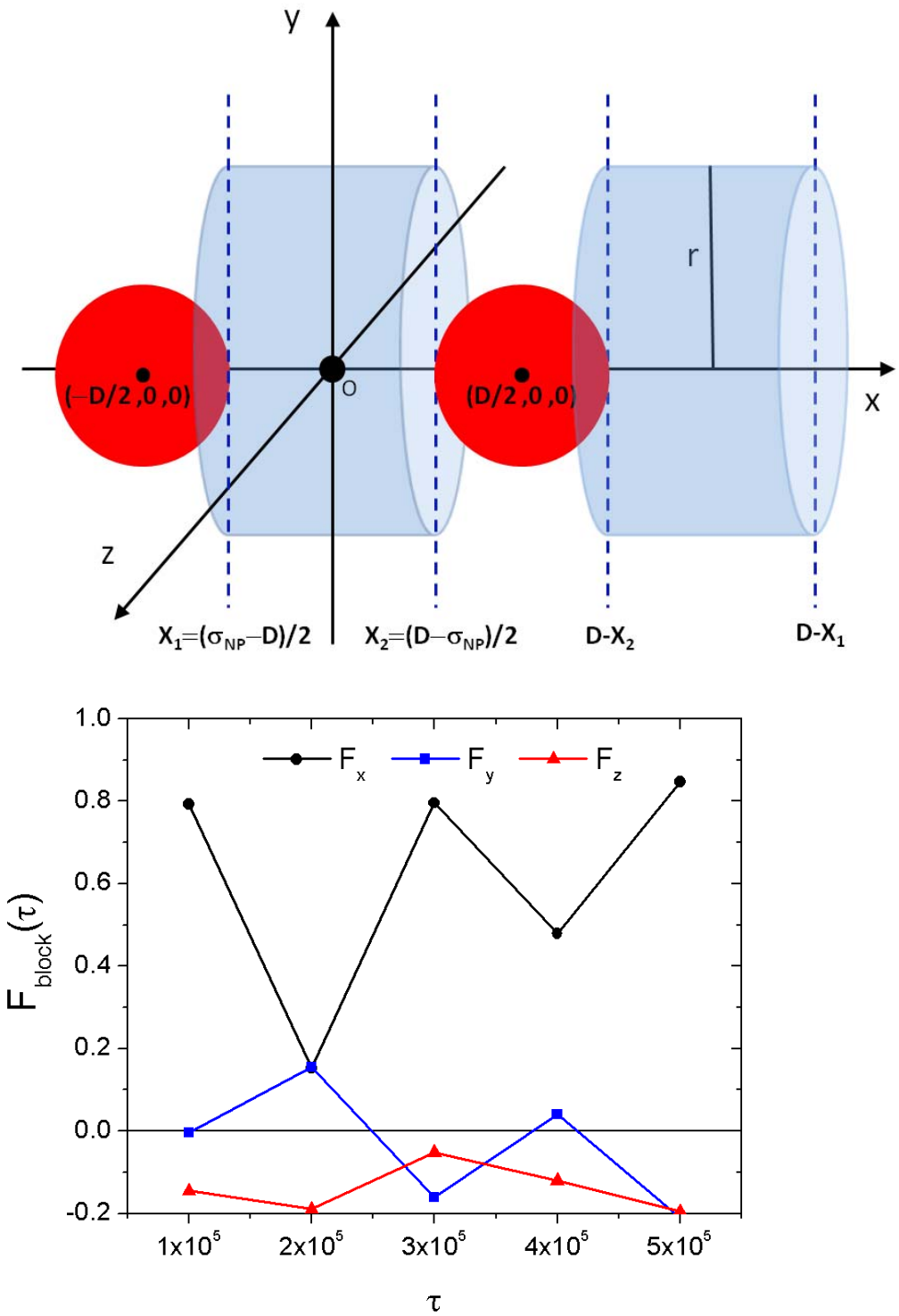
y
r
(−D/2 ,0 ,0)
O
(D/2 ,0 ,0)
x
z
X1=(σNP−D)/2
X2=(D−σNP)/2
D-X2
D-X1
Fx
Fy
Fz
Fblock(τ)
1.0
0.8
0.6
0.4
0.2
0.0
-0.2
1x10^5
2x10^5
3x10^5
4x10^5
5x10^5
τ

Figure 6.1

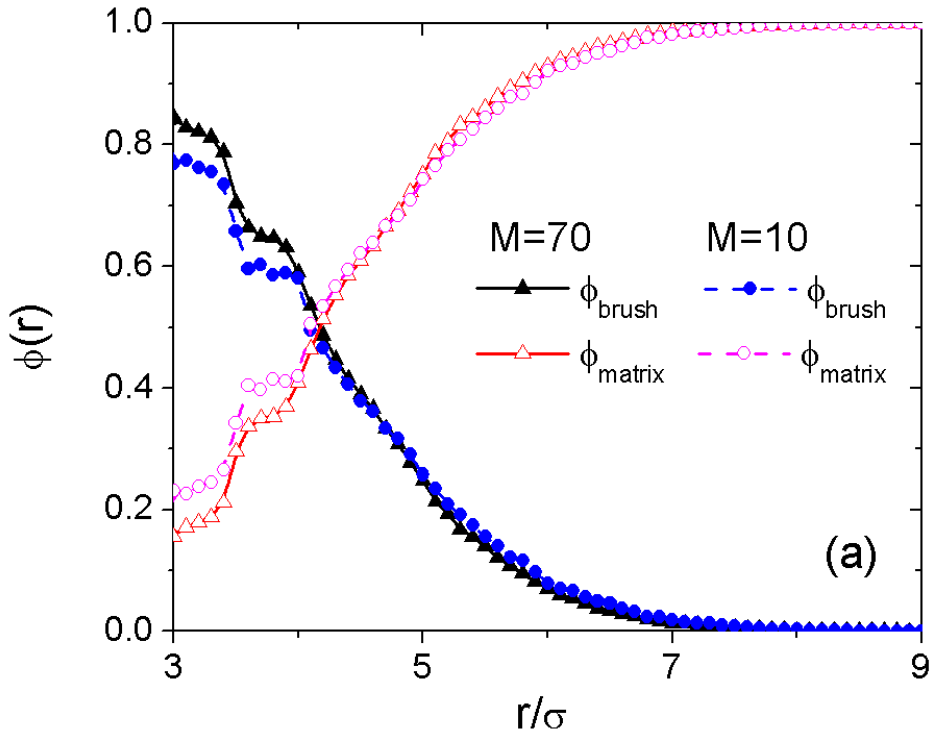
1.0
0.8
0.6
0.4
0.2
0.0
3
5
7
9
r/σ
ϕ(r)
M=70
M=10
ϕbrush
ϕbrush
ϕmatrix
ϕmatrix
(a)

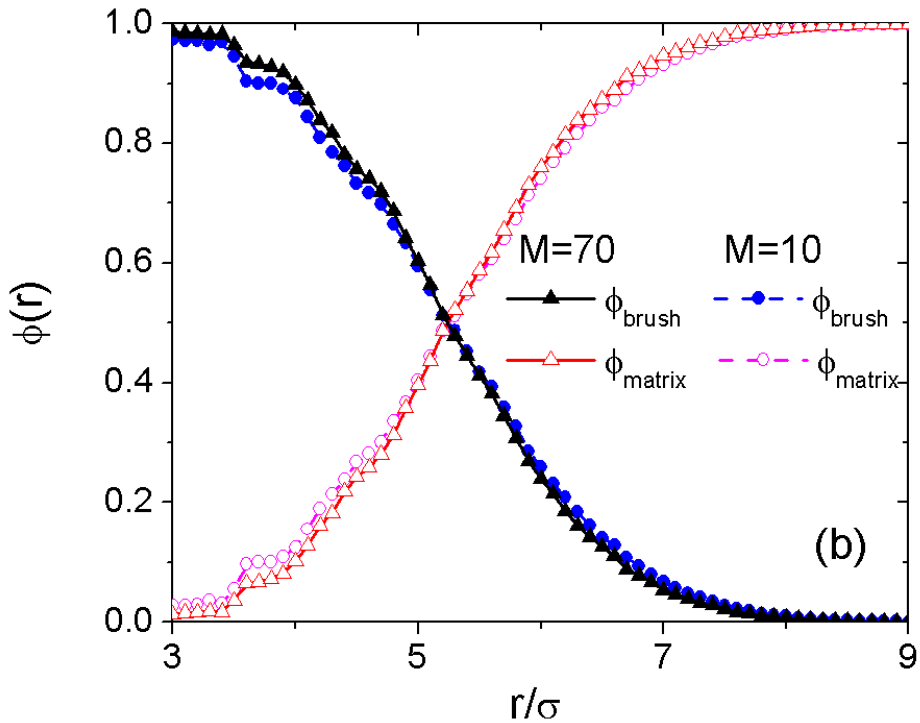
1.0
0.8
0.6
0.4
0.2
0.0
3
5
7
9
r/σ
ϕ(r)
M=70
M=10
ϕbrush
ϕbrush
ϕmatrix
ϕmatrix
(b)

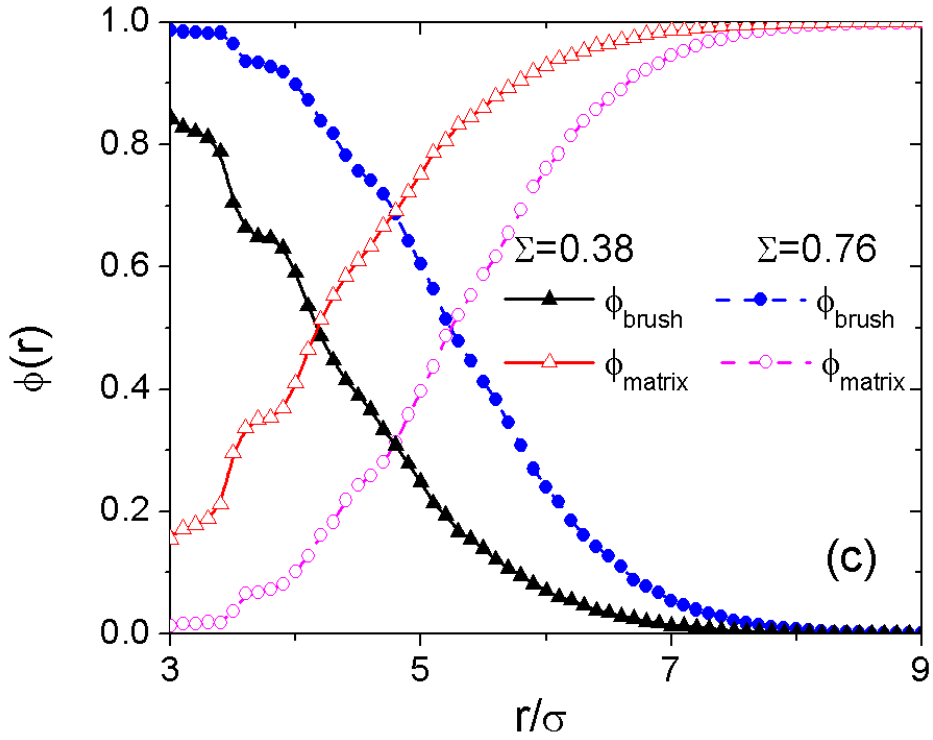
1.0
0.8
0.6
0.4
0.2
0.0
3
5
7
9
r/σ
ϕ(r)
Σ=0.38
Σ=0.76
ϕbrush
ϕbrush
ϕmatrix
ϕmatrix
(c)

Figure 6.2

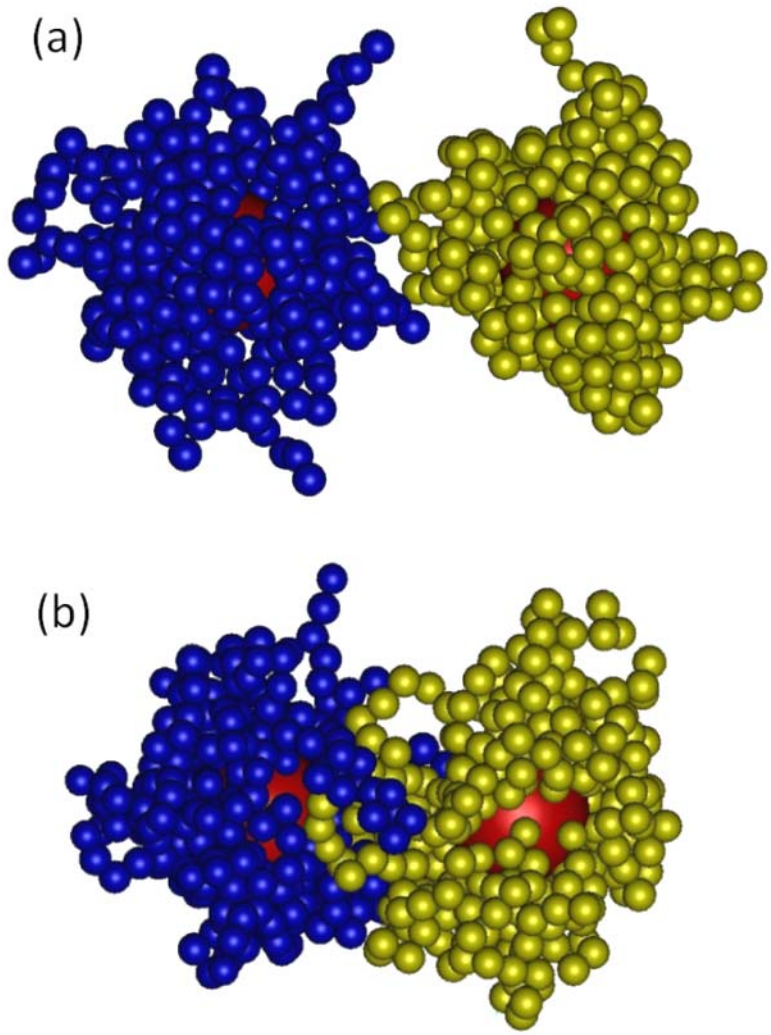

Figure 6.3

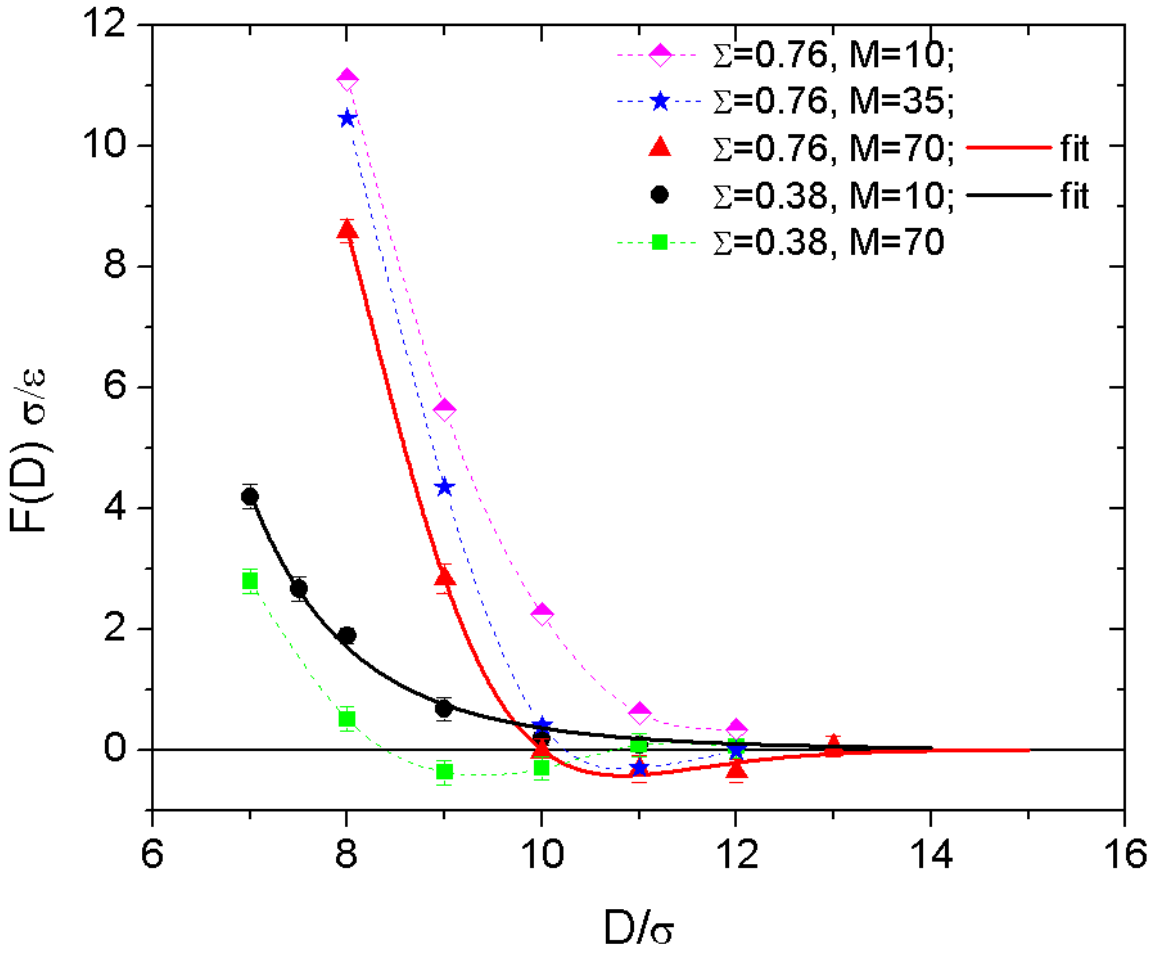
Σ=0.76, M=10;
Σ=0.76, M=35;
Σ=0.76, M=70;
fit
Σ=0.38, M=10;
fit
Σ=0.38, M=70
F(D) σ/ε
D/σ
12
10
8
6
4
2
0
6
8
10
12
14
16

Figure 6.4

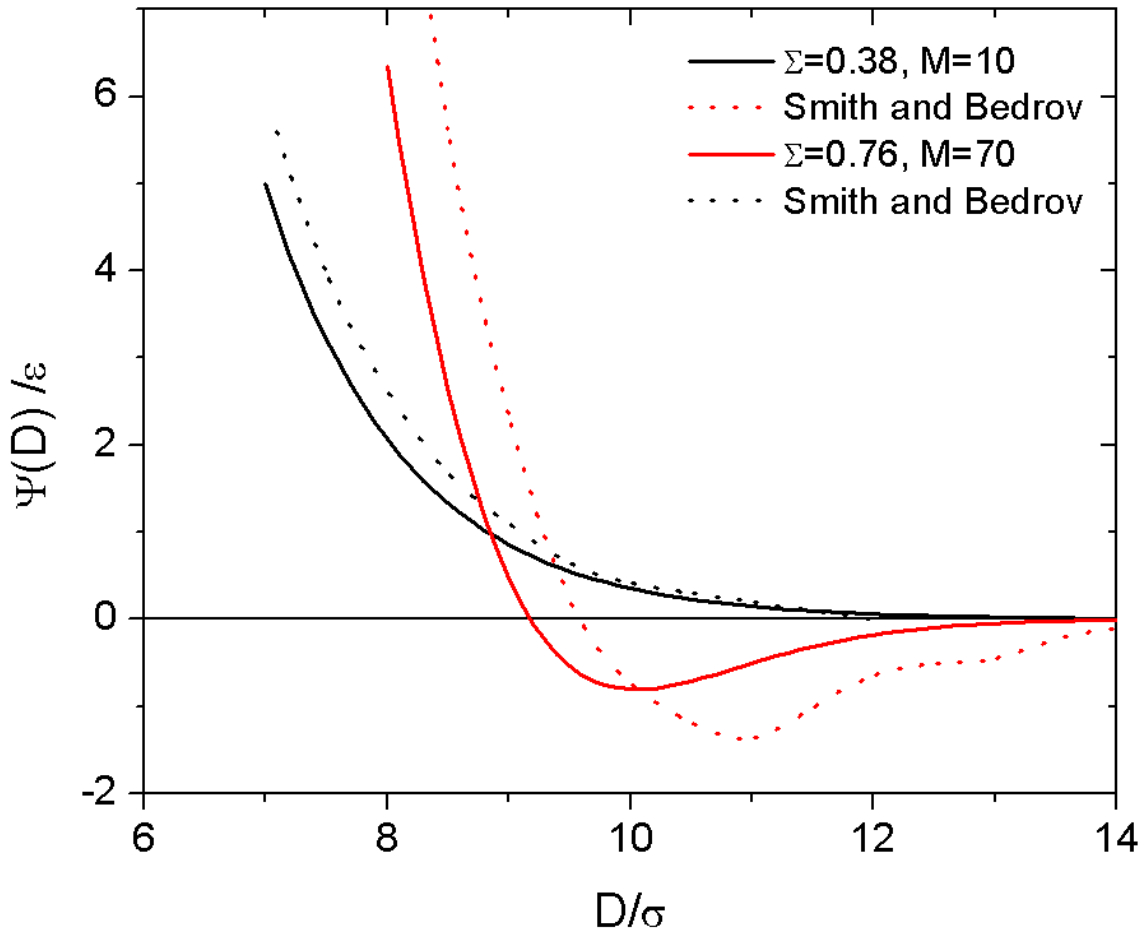
Σ=0.38, M=10
Smith and Bedrov
Σ=0.76, M=70
Smith and Bedrov
Ψ(D) /ε
D/σ
6
4
2
0
-2
6
8
10
12
14

Figure 6.5

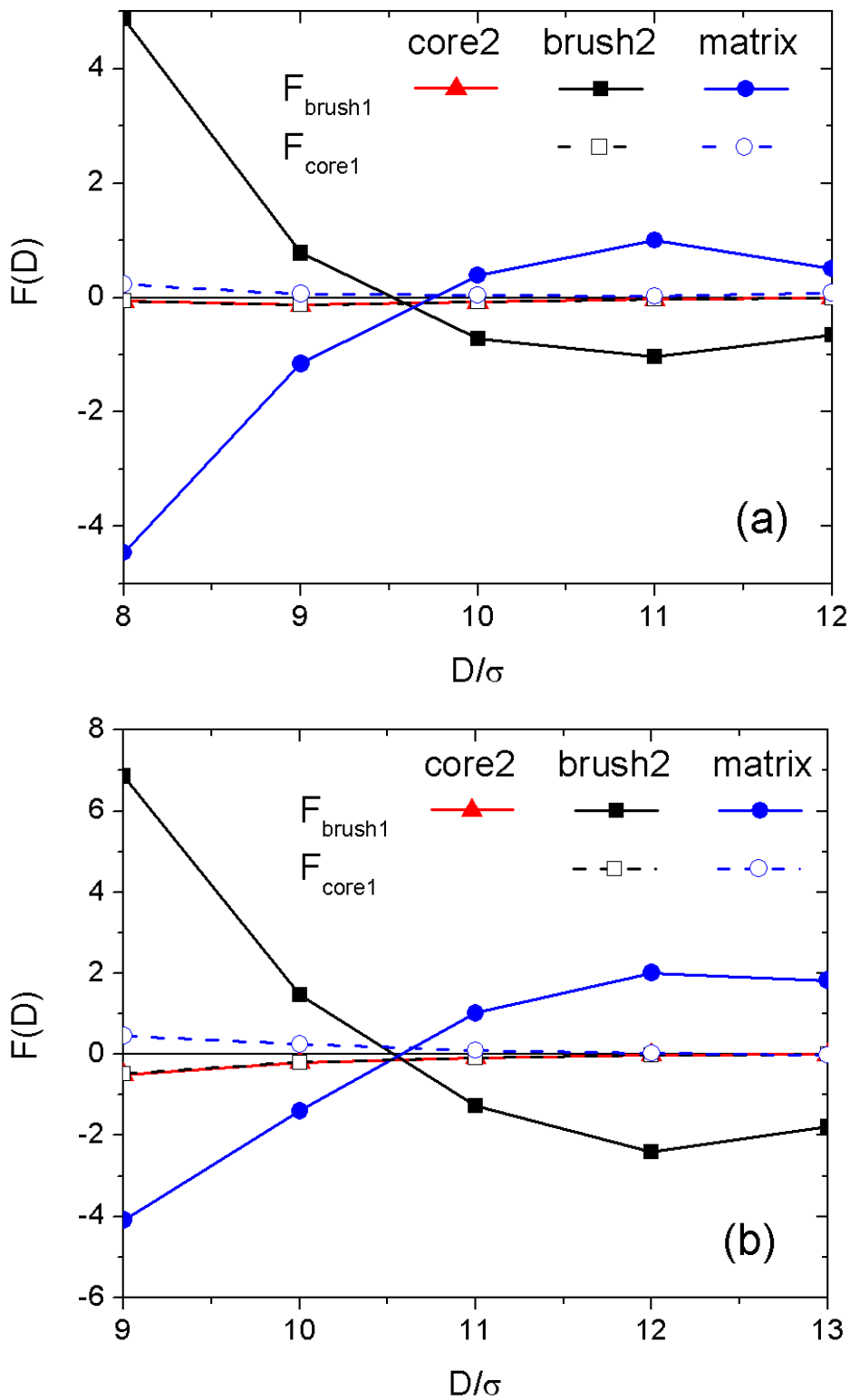

Figure 6.6

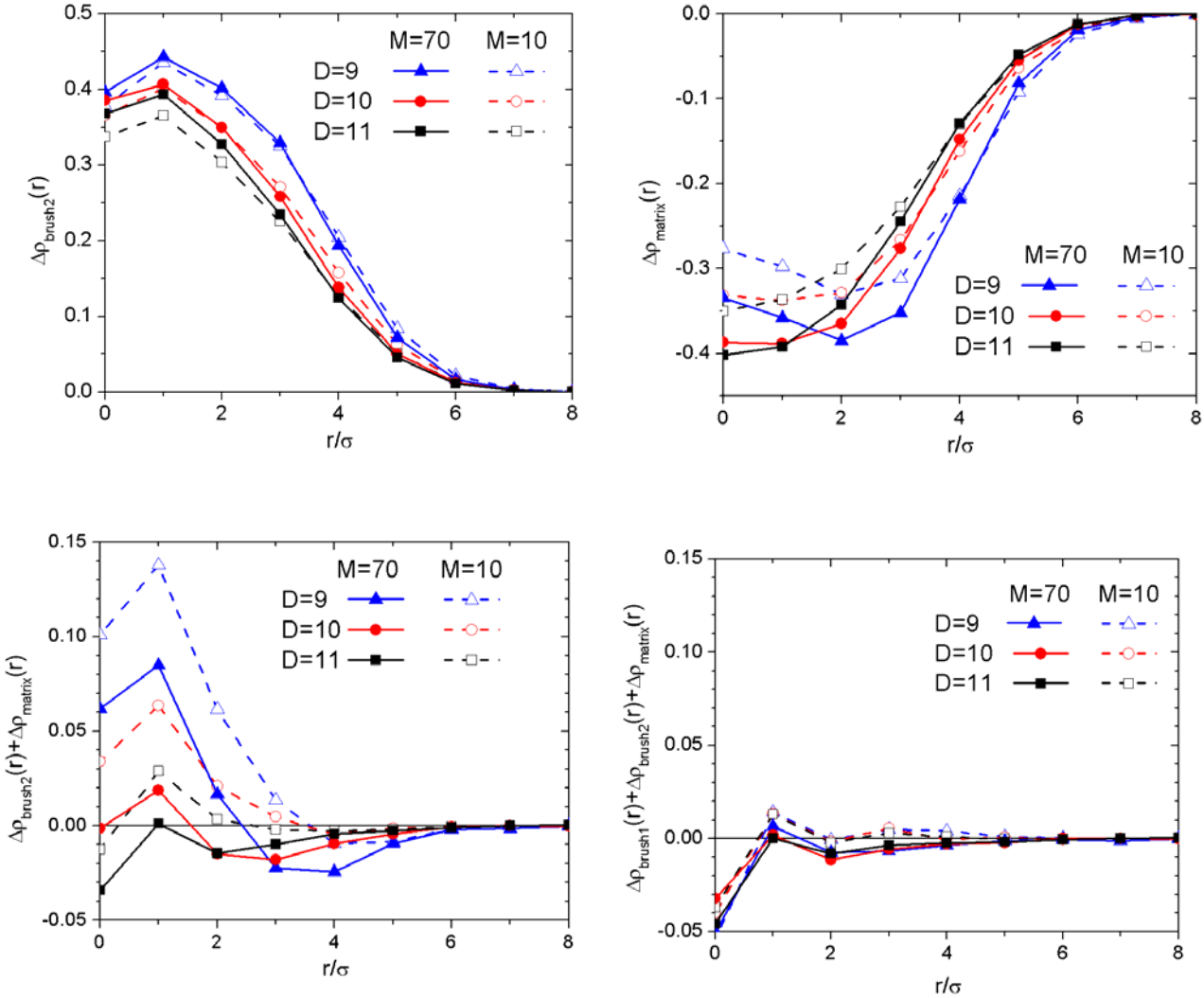
M=70
M=10
D=9
D=10
D=11
$\Delta\rho_{brush2}(r)$
$\Delta\rho_{matrix}(r)$
$\Delta\rho_{brush2}(r)+\Delta\rho_{matrix}(r)$
$\Delta\rho_{brush1}(r)+\Delta\rho_{brush2}(r)+\Delta\rho_{matrix}(r)$
r/σ

Figure 6.7a

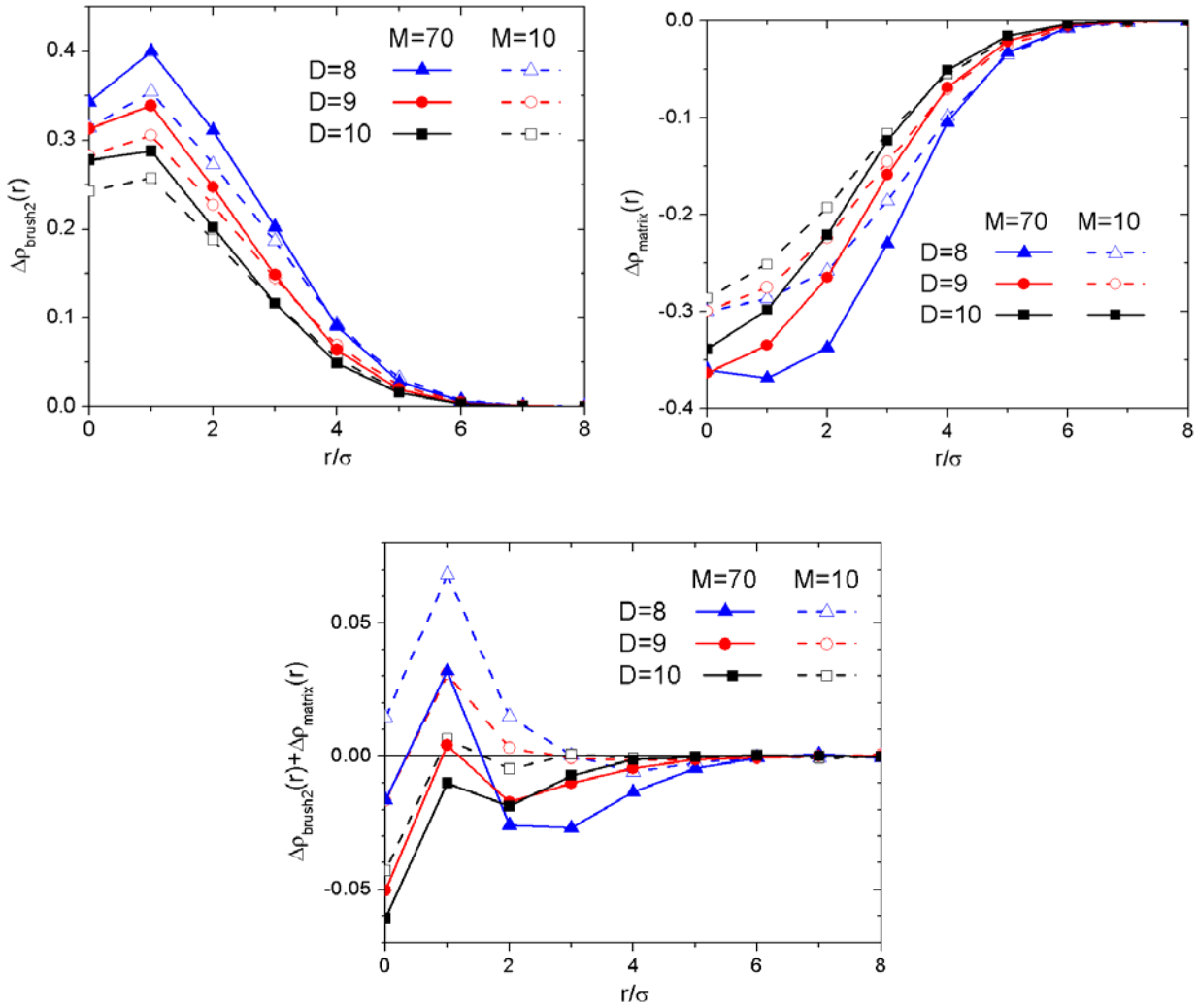
M=70
M=10
D=8
D=9
D=10
$\Delta\rho_{brush2}(r)$
r/σ
$\Delta\rho_{matrix}(r)$
$\Delta\rho_{brush2}(r)+\Delta\rho_{matrix}(r)$

Figure 6.7b

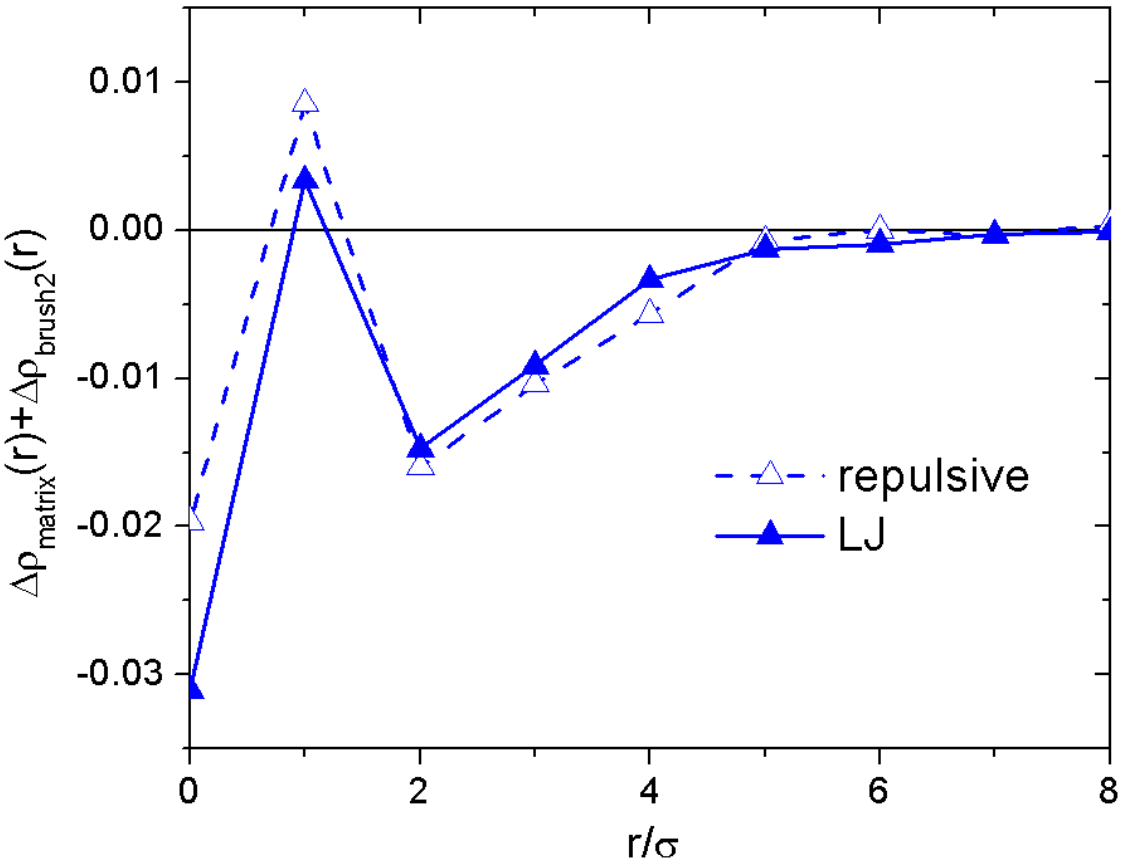
0.01
0.00
-0.01
-0.02
-0.03
0
2
4
6
8
r/σ
Δρmatrix(r)+Δρbrush2(r)
repulsive
LJ

Figure 6.8

References for Chapter 6, Part A.

1. I. Borukhov and L. Leibler, *Macromolecules*, 2002, **35**, 5171-5182.
2. D. L. Green and J. Mewis, *Langmuir*, 2006, **22**, 9546-9553.
3. M. W. Matsen and J. M. Gardiner, *J Chem Phys*, 2001, **115**, 2794-2804.
4. L. Meli, A. Arceo and P. F. Green, *Soft Matter*, 2009, **5**, 533-537.
5. T. Morinaga, K. Ohno, Y. Tsujii and T. Fukuda, *European Polymer Journal*, 2007, **43**, 243-248.
6. T. Morinaga, K. Ohno, Y. Tsujii and T. Fukuda, *Macromolecules*, 2008, **41**, 3620-3626.
7. K. Ohno, T. Morinaga, K. Koh, Y. Tsujii and T. Fukuda, *Macromolecules*, 2005, **38**, 2137-2142.
8. J. Pyun, S. J. Jia, T. Kowalewski, G. D. Patterson and K. Matyjaszewski, *Macromolecules*, 2003, **36**, 5094-5104.
9. D. A. Savin, J. Pyun, G. D. Patterson, T. Kowalewski and K. Matyjaszewski, *J Polym Sci Pol Phys*, 2002, **40**, 2667-2676.
10. X. R. Wang, V. J. Foltz, M. Rackaitis and G. G. A. Bohm, *Polymer*, 2008, **49**, 5683-5691.
11. J. J. Xu, F. Qiu, H. D. Zhang and Y. L. Yang, *J Polym Sci Pol Phys*, 2006, **44**, 2811-2820.
12. L. Yezek, W. Schartl, Y. M. Chen, K. Gohr and M. Schmidt, *Macromolecules*, 2003, **36**, 4226-4235.
13. A. Jayaraman and K. S. Schweizer, *Macromolecules*, 2008, **41**, 9430-9438.
14. A. Jayaraman and K. S. Schweizer, *J Chem Phys*, 2008, **128**, 164904.
15. A. Jayaraman and K. S. Schweizer, *Macromolecules*, 2009, **42**, 8423-8434.
16. R. S. Hoy and G. S. Grest, *Macromolecules*, 2007, **40**, 8389-8395.
17. J. Klos and T. Pakula, *Macromolecules*, 2004, **37**, 8145-8151.
18. R. C. Ball, J. F. Marko, S. T. Milner and T. A. Witten, *Macromolecules*, 1991, **24**, 693-703.
19. D. Dukes, Y. Li, S. Lewis, B. Benicewicz, L. Schadler and S. K. Kumar, *Macromolecules*, **43**, 1564-1570.
20. K. Hur, R. G. Hennig, F. A. Escobedo and U. Wiesner, *J Chem Phys*, 2010, **133**.
21. S. E. Harton and S. K. Kumar, *J Polym Sci Pol Phys*, 2008, **46**, 351-358.
22. A. Striolo, *Nanotechnology*, 2008, **19**.
23. C. Xu, K. Ohno, V. Ladmiral and R. J. Composto, *Polymer*, 2008, **49**, 3568-3577.
24. J. Kalb, D. Dukes, S. K. Kumar, R. S. Hoy and G. S. Grest, *Soft Matter*, 2011, **7**, 1418-1425.
25. K. Gohr, T. Pakula, K. Tsutsumi and W. Schartl, *Macromolecules*, 1999, **32**, 7156-7165.
26. K. Gohr and W. Schartl, *Macromolecules*, 2000, **33**, 2129-2135.
27. P. Akcora, H. Liu, S. K. Kumar, J. Moll, Y. Li, B. C. Benicewicz, L. S. Schadler, D. Acehin, A. Z. Panagiotopoulos, V. Pryamitsyn, V. Ganesan, J. Ilavsky, P. Thiyagarajan, R. H. Colby and J. F. Douglas, *Nat Mater*, 2009, **8**, 354-359.
28. J. Kalb, D. Dukes, S. K. Kumar, R. S. Hoy and G. S. Grest, *Soft Matter*, **7**, 1418-1425.
29. G. D. Smith and D. Bedrov, *Langmuir*, 2009, **25**, 11239-11243.
30. S. Asakura and F. Oosawa, *J Chem Phys*, 1954, **22**, 1255-1256.
31. S. Asakura and F. Oosawa, *Journal of Polymer Science*, 1958, **33**, 183-192.
32. G. S. Grest and K. Kremer, *Phys Rev A*, 1986, **33**, 3628-3631.

33. K. Kremer, G. S. Grest and I. Carmesin, *Phys Rev Lett*, 1988, **61**, 566-569.
34. R. Auhl, R. Everaers, G. S. Grest, K. Kremer and S. J. Plimpton, *J Chem Phys*, 2003, **119**, 12718-12728.
35. J. B. Hooper and K. S. Schweizer, *Macromolecules*, 2006, **39**, 5133-5142.

Part B.
Universal Viscosity Behavior of Polymer Nanocomposites

Jagannathan T. Kalathi,[1] Gary S. Grest,[2] and Sanat K. Kumar[1, *]

[1]Department of Chemical Engineering, Columbia University, New York, NY 10027, USA
[2]Sandia National Laboratories, Albuquerque, New Mexico 87185, USA
(Dated: May 20, 2012)

Adding a low molecular weight plasticizer typically reduces the viscosity of a polymer melt. In contrast, spherical nanoparticles (NP), which can reinforce a polymer's solid-state properties, can either increase or decrease the melt's viscosity. While knowledge of the flow behavior of a polymer nanocomposite is crucial to its processability, there is no universal organizing principle that can explain the experimentally observed complex dependence of a filled polymer's viscosity on filler size and NP-polymer interactions. Our non-equilibrium molecular dynamics simulations show that small spherical NPs act akin to plasticizers and serve to reduce the melt's viscosity. This effect can be overcome by making the chain-NP interactions attractive or by making the NPs bigger. Crucially, our simulations allow us to systematically organize the viscosity data of filled polymer melts over a broad range of systems studied, thus providing a strong basis from which to predict the flow behavior of this commercially important class of materials.

It is well accepted that micrometer sized spherical fillers increase the viscosity of a polymer melt from its pure value, η_p, to a value, η, predicted by the Einstein-Batchelor law: $\frac{\eta}{\eta_p} = 1 + 2.5\phi_{NP} + 6.2\phi_{NP}^2$ .., where ϕ_{NP} is the NP volume fraction [1-3]. However, for spherical fillers in the 5-10 nm size range, the viscosity can be reduced or increased relative to the pure polymer even when the NPs are chemically identical to the polymer matrix [4, 5]. In a similar vein, it has been found that dilute concentrations of ~1nm diameter POSS fillers can reduce or increase the viscosity of a chemically dissimilar polymer matrix, depending on the polymer chain length, the miscibility state of the nanocomposite and the interactions at the POSS-polymer interface [6]. While there have been extensive simulations on the rheology of nanocomposites [7-12], most have focused on the importance of polymer-NP interactions on viscosity. Indeed, it has been found that weak interactions at this interface yield a viscosity reduction, while an attractive interface increases viscosity, in good agreement with experiments [13, 14]. The complicated, and poorly understood dependence of the η on NP size and chain size,

and its interplay with the interactions at the polymer-NP interface, are the central issues we study here.

We represent a polymer chain using the Kremer-Grest bead-spring model [15]. Inter and intra-chain interactions between monomers are described by a standard Lenard-Jones (LJ) potential $V(r) = 4\varepsilon\left[\left(\frac{\sigma}{r}\right)^{12} - \left(\frac{\sigma}{r}\right)^{6}\right]$ truncated at $r_c = 2.5\sigma$, where σ is the monomer size, and ε is the energy scale. Adjacent monomers on a chain are bonded by a FENE potential [15]. Three adjacent monomers on a chain experience a bending potential, $V(\theta) = k_\theta[1 + cos\theta]$, with $k_\theta = 0.75\varepsilon$. Adding this bending potential increases the polymer's characteristic ratio, C_∞, from 1.76 to ≈2.2 [16], while reducing its entanglement chain length N_e from 70 to 45 [17]. We consider three different linear melts, comprised of chains of length N=40 (unentangled), N=100 (transition region) and N=400 (entangled), so as to examine the experimentally postulated role of entanglements [5]. Two NP models are employed. "Smooth" spherical NPs of diameter σ_{NP} consist of a uniform distribution of monomer-sized spheres interacting through LJ interactions. The total interaction between a pair of NPs is determined by integrating over all the interacting LJ atoms in the two NPs [18]. The well depth of the effective pair potential between two NPs is thus governed by a Hamaker energy prefactor, A [18]. The NP mass is proportional to its volume, $m = \rho V_{np}$, with a number density of LJ particles $\rho\sigma^3$=1.0. Following this, for NP-NP interactions, $A_{nn} = 4\pi^2\varepsilon = 39.48\varepsilon$ [18]. We employed a cut-off distance $r_c = \sigma_{NP}$ so that NP-NP interactions are purely repulsive. While a corresponding analysis for NP-polymer interactions would lead to $A_{np} = 24\pi\varepsilon \approx 72\varepsilon$, we find that NP-polymer mixtures with this A_{np} are immiscible. Rather, larger A_{np} have to be used to achieve miscibility. We therefore employ $A_{np} = 100\varepsilon$ to represent "athermal" interactions between NP and polymer monomers (see Fig. 2 below for more justification) and $A_{np} = 400\varepsilon$ for favorable attractions. Both NP-chain potentials use a cut-off distance $r_c = \frac{\sigma_{NP}}{2} + 4\sigma$. In the "rough" NP model, a collection of LJ atoms, each equivalent to a chain monomer, are held together in an FCC crystal lattice. The polymer-NP interaction is attractive and the well depth of the potential, ε_{np}, is varied in a series of simulations. For all particles with $\sigma_{NP} \geq 3\sigma$ the potential is truncated at $r_c = \frac{\sigma_{NP}}{2} + \sigma$, while we use $r_c = 2.5\sigma$ for smaller particles. The interaction between atoms in one NP with atoms in all other NPs is purely repulsive with $r_c = \sigma$. The NP's are spatially well dispersed under all

conditions studied. We simulated 500 chains of length N=40,100, and 400 for the neat melts, while filled systems consisted of 500-1033 chains for N=400 and 500-2000 chains for N=40 and 100. The NP volume fraction $\phi_{NP} = \frac{\sigma_{np}^3 N_{np}}{(\sigma_{np}^3 N_{np} + \sigma^3 N N_p)}$ is set to its desired value, where N_{np} and N_p are the number of NP and chains, respectively.

Both neat and filled melts of N=100 and 400 are prepared and equilibrated following the double-bridging procedure [16]. The N=40 melt is equilibrated by running at constant pressure ($P^* = 0$) to get the appropriate density, and then at constant volume long enough that the chains move their own size. The temperature was $T^* = \frac{kT}{\varepsilon} = 1$, and the pressure $P^* = 0$. The equilibrated systems are then sheared at constant volume at a shear strain rate, $\dot{\gamma}$, and non-equilibrium trajectories generated by integrating the SLLOD equations of motion [19] with the parallel molecular dynamics LAMMPS code [20]. We used a time step of δt=0.005 or 0.01 τ, where $\tau = \sqrt{m\sigma^2/\varepsilon}$. The components of the pressure tensor are stored over runs which are at least 10 $\dot{\gamma}^{-1}$ in length [21]. From the resulting data, we verified that the diagonal components of the stress tensor were equal to zero (within simulation uncertainty) in all cases and so we continue to mimic the $P^* = 0$ conditions relevant to experiment. The shear viscosity is calculated using $\eta = -\frac{\langle P_{xz} \rangle}{\dot{\gamma}}$, where $\langle P_{xz} \rangle$ is the ensemble averaged *xz*-component of the pressure tensor along the flow and gradient directions of the shear, respectively. At high $\dot{\gamma}$, the time dependent viscosity reaches a plateau after an initial overshoot. This plateau value is used to estimate the shear viscosity. For low $\dot{\gamma}$, particularly for N=40 and 100, this overshoot is almost absent.

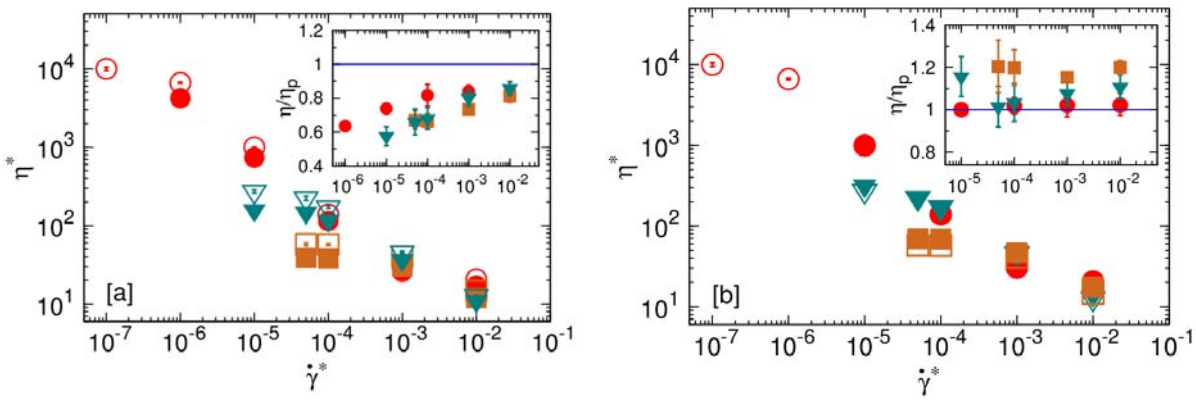

Figure 6.9: Reduced shear viscosity, $\eta^* = \frac{\eta\sigma^3}{\varepsilon\tau}$ *vs.* reduced strain rate $\dot{\gamma}^* = \dot{\gamma}\tau$. Neat and NP-filled melts are represented by open and closed symbols, respectively, at a fixed $\phi_{NP} = 0.11$ for N=40 ( ), N=100 (▼), and N=400 (●). (a) $\sigma_{NP} = 1\sigma$ (b) $\sigma_{NP} = 10\sigma$. Inset shows the ratio of the filled to neat melt viscosity as a function of $\dot{\gamma}^*$.

All three neat melts exhibit shear thinning (Fig. 6.9). The N=100 data reach their zero-shear plateau for $\dot{\gamma}^* \approx 10^{-5}$, while the N=400 melt does not attain a plateau even for $\dot{\gamma}^* = 10^{-6}$. We conjecture that increasing N by a factor of 4 in the entangled regime leads to an increase in relaxation time of ~64. We cannot access $\dot{\gamma}^* < 10^{-6}$ where this plateau should emerge. (At the lowest $\dot{\gamma}^* = 10^{-7}$, we need 75 days on 216 processing cores on the Cray XE6 Hopper at NERSC to get an estimate of the viscosity. Reliable estimates need runs that are 10 times longer! Such runs are thus almost infeasible at this time.)

Figure 6.9 also presents results for two different sized rough NPs at a particle loading of $\phi_{NP} = 0.11$. To mimic the experiments [4, 5], where the particles are energetically neutral *vis-a-vis* the polymer, we choose the energy of interaction between the NP and polymer segments to be equal to the polymer-polymer interactions, namely, $\varepsilon_{NP} = \varepsilon$. The insets show that the ratio of viscosity of the filled system to the neat melt as a function of $\dot{\gamma}^*$. For N=40 and N=100, and especially for the larger particle size, this viscosity ratio is essentially unchanged when we go from the zero shear limit well into the shear thinning regime. The key point learned from these shorter chain results is that, even though we do not access the zero shear limit in the N= 400 simulations, we can still draw meaningful conclusions regarding the effect of the NPs on the zero shear melt viscosity. The viscosity of melts filled with $\sigma_{NP} = 1\sigma$ particles is 30-40% lower than the neat melt, with a weak N dependence [Fig. 6.9(a)]. The η of the entangled melt is

not significantly affected by $\sigma_{NP} = 10\sigma$ NPs for both N=400 and N=100 while it increases by 25% for N=40 (Fig. 6.9(b)).

Figures 6.10(a) and (b) show the effect of particle size on the melt's viscosity at a NP loading $\phi_{NP} = 0.11$ for N=40 and 400, respectively, for different interaction strengths. We see that a rough NP with $\varepsilon_{np} = \varepsilon$ behaves akin to a smooth NP with A_{np}=100ε- as argued above, this A_{np} value corresponds to an athermal nanocomposite. Apparently, particle smoothness does not qualitatively alter the conclusions drawn. For N=40 [Fig. 6.10(a)] and $\varepsilon_{np} = \varepsilon$ (neutral NPs) the filled melt's viscosity, η, is lower than that of the pure melt, η_p, for $\sigma_{NP} \lesssim 5\sigma$. We recover the neat melt's viscosity when the particles become as large as 5σ. The results for the longer chains (N=100 and 400) are qualitatively consistent with these conclusions, except that the crossover to viscosity ratios greater than 1 occurs for $\sigma_{NP} > 8$ and 10 σ, respectively.

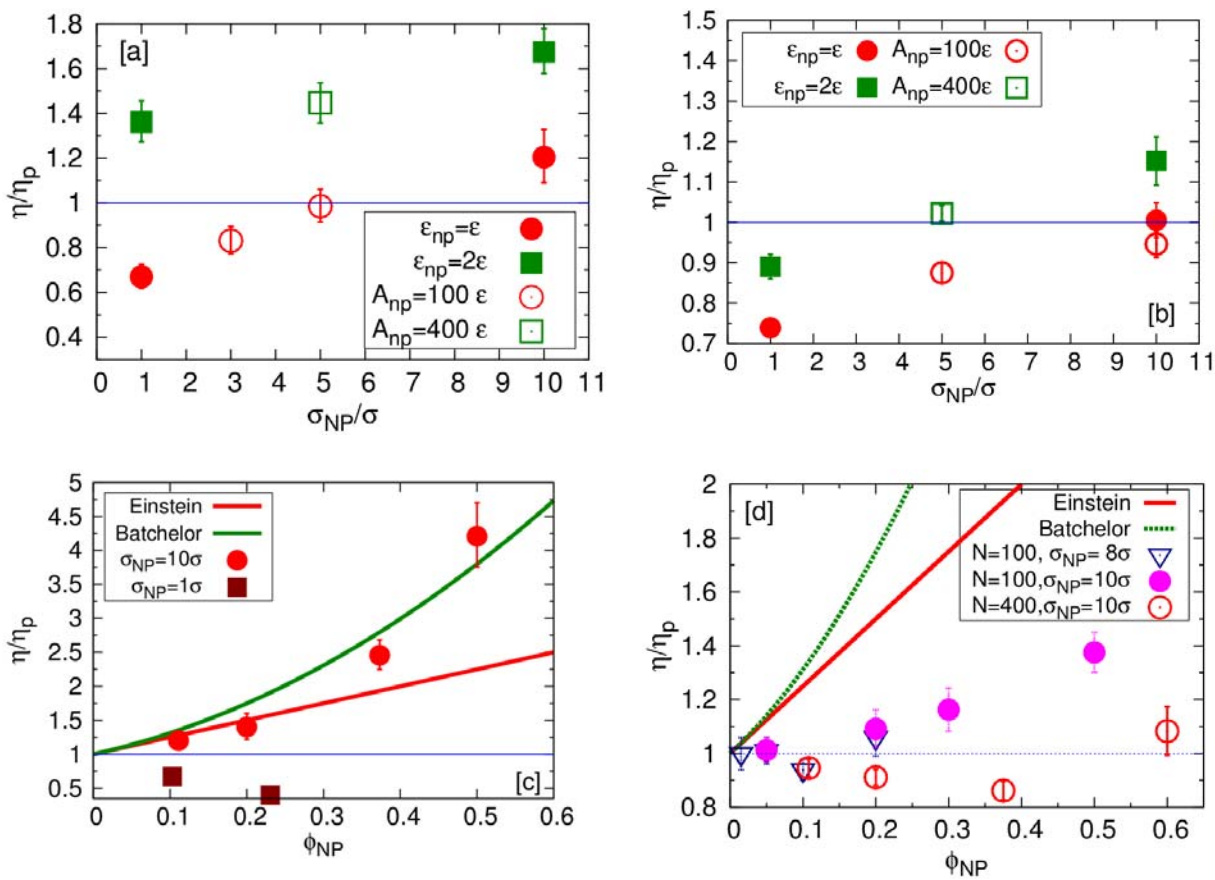

Figure 6.10: Effect of NP size and type of interaction between the NP and polymer on shear viscosity for (a) N=40, $\dot{\gamma}^* \to 0$; (b) N=400, $\dot{\gamma}^* = 10^{-5}$ for ϕ_{NP}= 0.11. Dependence of viscosity on loading of neutral NP for (c) N=40 with (σ_{NP} = 10σ and 1σ) as $\dot{\gamma}^* \to 0$; (d)

N=100 with (σ_{NP} = 8 and 10σ) as $\dot{\gamma}^* \to 0$ and N=400 with (σ_{NP} = 10σ) at $\dot{\gamma}^* = 10^{-5}$. In all the plots the closed symbols correspond to rough NP, while the open symbols to smooth NP. In (c) and (d), we show the Einstein and Batchelor predictions.

The viscosity becomes larger that the athermal case if the NP-polymer interactions become more favorable ($\varepsilon_{NP} = 2\varepsilon$) [Figs. 6.10(a) and 6.10(b)]. In the case of N=40 the viscosity is larger than the neat melt, independent of particle size! In contrast, for N=400 we still get viscosity reductions for small enough particles. We propose that, at these higher interaction strengths, the polymers bind strongly to the NPs; chain mobility is restricted, thus leading to higher η. These findings are consistent with previous simulations that studied the role of NP-polymer interactions on flow behavior.

Figure 6.10(c) and (d) show the dependence of η on ϕ_{NP} for the melts filled with neutral NPs. Figure 6.10(c), for the unentangled melt, shows a monotonic increase of viscosity with particle loading for $\sigma_{NP} = 10\sigma$. This result is qualitatively consistent with the Batchelor law. In contrast, for $\sigma_{NP} = 1\sigma$, the viscosity decreases with increasing ϕ_{NP}. Similarly, Fig. 6.10d shows a monotonic increase of η with ϕ_{NP} for $\sigma_{NP} = 10\sigma$ in N=100 melts. For $\sigma_{NP} = 8\sigma$ in N=100 and $\sigma_{NP} = 10\sigma$ in N=400, on the other hand, the viscosity initially drops with increasing NP loading, and then it increases beyond the pure melt value for large enough NP loading. This last trend has been observed experimentally [6].

We now examine the molecular origins of these results. We start with the ansatz that the viscosity of an entangled melt follows: $\eta = \eta_0 N(1 + N/N_e)^2$ [2], where η_0 is the viscosity of a monomer fluid, and N_e is the molecular weight between entanglements. (For unentangled polymers the last term drops out.) The addition of NP to a polymer melt can either change η_0 (e.g., through boundary conditions, flow effects or by altering the "free volume") or N_e. We now examine the relative importance of these factors.

Riggleman et al. [22] showed that the presence of "neutral" NPs reduces N_e from 62.3 (pure melt) to 56.4 (N=500, $\sigma_{NP} = 5\sigma$, φ_{NP}=0.15). The NPs were frozen in these primitive path analysis (PPA) runs, thus making the chains bend and appear more entangled. We followed [16] to estimate N_e in the N=400 melt filled with smooth NP at ϕ_{NP} = 0.11. In contrast to [22] the NPs are allowed to move during the reduction of the bond lengths, yielding more reliable estimates of N_e.

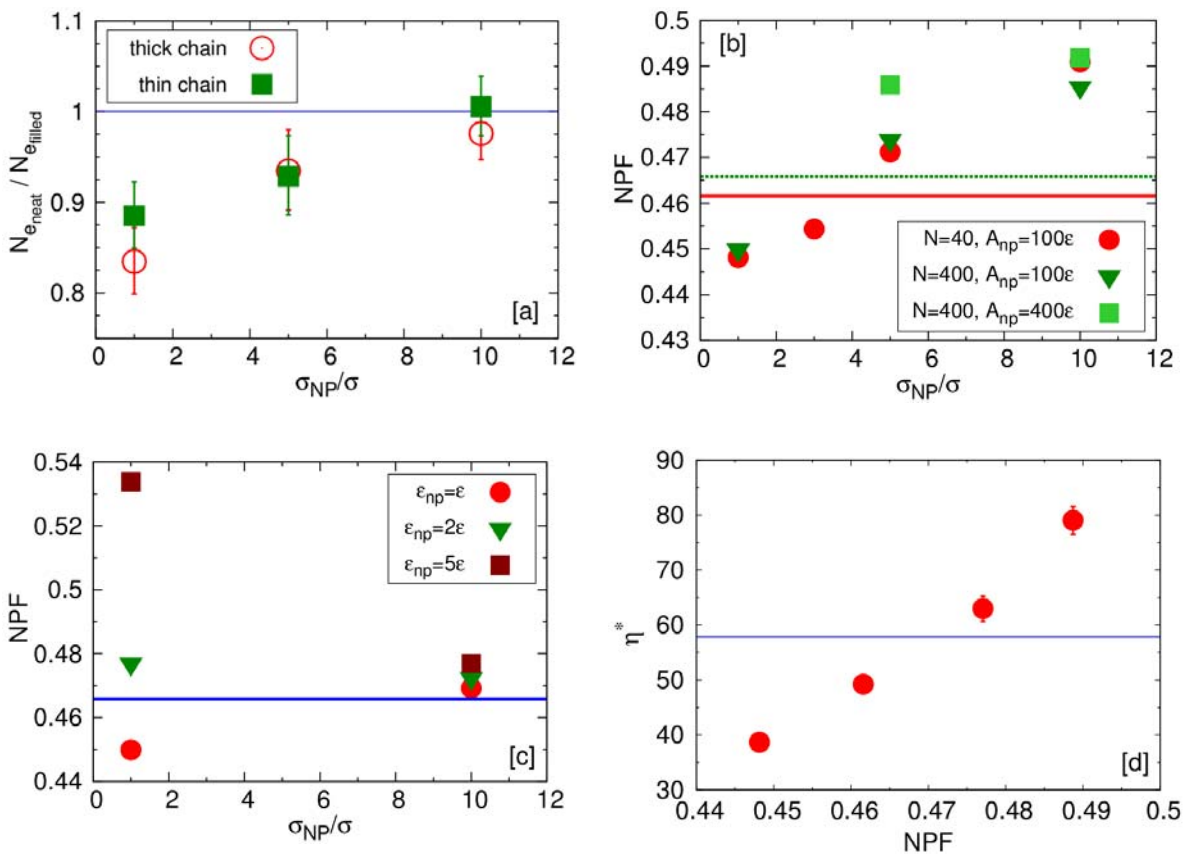

Figure 6.11: (a) Effect of σ_{NP} on N_e for N=400 melts filled with smooth NPs with A_{np}=100 ε and $\phi_{NP} = 0.11$. (b) Net packing fraction, NPF, as a function of smooth NP size for $\phi_{NP} = 0.11$. The lines represent the pure melts; (c) Effect of NP-polymer bead interaction strength on NPF for N=400 melts and rough NPs. $\phi_{NP} = 0.11$. Line represents the pure melt. (d) Dependence of η on NPF for the N=40 melt with neutral $\sigma_{NP} = 1\sigma$ NPs. Line is the pure melt.

Figure 6.11a plots (N/N_e), normalized by its value in the pure melt. Both thick chain (N=400) and thin chain PPA yield quantitatively equivalent trends. (Seven beads are inserted between adjacent monomers of the thick chain to make it a thin chain [23], while conserving the chain length). The N_e increases significantly when particle size decreases, which means that the average number of entanglements per chain decreases (Fig. 6.11a). This finding is consistent with the notion that these small NPs act akin to plasticizers. The ratio increases with NP size, and recovers to a value of unity for $\sigma_{NP} = 10\sigma$. Tuteja et al. [5] found that N_e is unaffected by the

addition of NP for $\sigma_{NP} \gtrsim 5$ nm. On assuming a Kuhn length of 1nm, we also find that N_e is practically equal to its bulk value for these NP sizes (Fig. 6.11) [5]. However, we shall show below that small departures of this ratio from unity can still have profound effects on viscosity changes.

Next we consider free volume effects [4, 5]. Since we simulate at $P^* = 0$, the density must change on adding NPs. Fig. 6.11(b) quantifies this idea by plotting the net packing fraction, defined as $NPF = \frac{\pi(N_{NP}\sigma_{NP}^3 + N_P\sigma^3)}{6V}$, as a function of NP size at $\phi_{NP} = 0.11$. Note that (1-NPF) represents the "unoccupied" or "free volume" in the system. As anticipated, adding weakly interacting, small NPs causes a strong drop in the NPF. The NPF, however, increases monotonically with NP size and recovers to its neat melt value for $\sigma_{NP} \sim 5\sigma$. Fig. 6.11(c) shows that the effect of NP-polymer interactions on NPF is more pronounced for small σ_{NP} (also Fig. 6.11(b) for $\sigma_{NP} = 5\sigma$).

In addition to equation-of-state effects, Ganesan et al. [11] presented a continuum model that does not explicitly use free volume effects, but rather includes hydrodynamic effects and wall slip. To understand the relative importance of flow *vs.* equation-of-state effects in determining η_0, we examined the filled unentangled N=40 melt's viscosity as a function of NPF [Fig. 6.11(d)]. At the lowest NPF ($\approx$ 0.45), which corresponds to P^*=0 for the filled system, the $\eta^* \approx$38. When NPF=0.46, which is equal to the NPF of the neat melt, we find $\eta^* \approx$50. Since $\eta^* \approx$57 for the pure melt, it follows that roughly 2/3 of the viscosity drop on the addition of NP to an unentangled melt is due to equation-of-state effects, while 1/3 to other flow factors.

We now assess the relative role of entanglement vs. changes in η_0 in determining the role of NP size on η. We first consider athermal systems with $\sigma_{NP} = 5\sigma$. For N=40, Fig. 6.10a shows that

$\eta/\eta_p \approx 1$, and thus it follows that η_0 is unaffected going from a pure melt to the filled state for this chain length. Since the density does not change significantly in going from N=40 to N=400 (Fig. 6.11b) we can thus predict that $\eta/\eta_p = (1 + N/N_{e,filled})^2/(1 + N/N_{e,neat})^2 \approx 0.87$ for the longer chains, in excellent agreement with the experiments. ($N_{e,neat}$ is the entanglement length in the pure melt, while $N_{e,filled}$ is the filled melt value.) For all $\sigma_{NP} \gtrsim 10$ the entanglement spacing in the filled melt is identical to the neat melt, and thus any viscosity changes are driven by changes in η_0. In contrast, for smaller NPs both entanglement and changes in η_0 play a role in the viscosity changes. We therefore conclude that changes in entanglements, density and flow factors can play an important role in determining the viscosity of filled melts, with the balance of these factors being system specific.

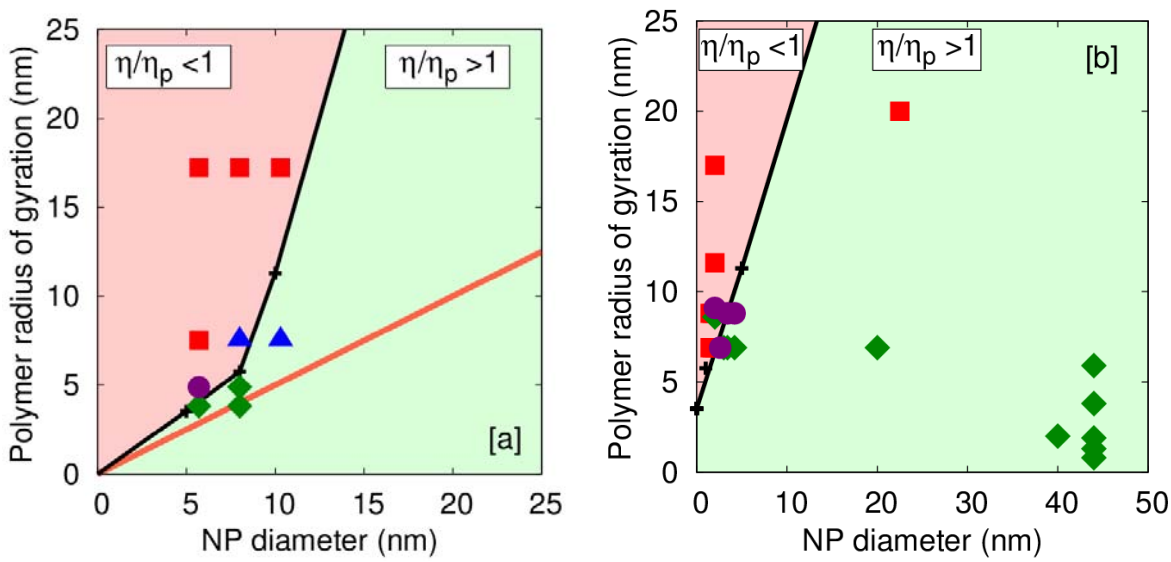

Figure 6.12: Polymer radius of gyration versus NP diameter. The experimental data are plotted in the same manner in both figures: ( ) $\eta/\eta_p < 1$ at low NP loading, and ( ) $\eta/\eta_p > 1$. (●) corresponds to $\eta/\eta_p \approx 1$, and (▲) is where η shows an initial increase of viscosity as a function of NP loading followed by a decrease. (a) "Phase" diagram of melts filled with athermal NPs. Experimental data is from [5]. Systems above the orange line should be miscible. The black line is extrapolated from our simulations separating regions where the filled melt viscosity is lower than that of the neat melt (upper-left region) from more "normal" behavior (below and to the right of the blue line). (b) Corresponding plot

for "thermal" NP/polymer systems. Only the viscosity line is shown. Data are from [6, 14, 24-28].

We now place our results in the context of the unexplained experimental trends for the viscosity of filled polymers [4-6, 14, 24-28]. We organize the experimental data by plotting the NP diameter *vs.* chain radius of gyration, R_g in Fig. 6.12. The simulations presented in Fig. 6.12a are for energetically neutral systems ($\varepsilon_{np} = \varepsilon$), which we believe to be germane to the experiments where the NP and the melts have the same chemical structure [4, 5]. Fig. 6.12b then focuses on NPs with chemical structures different from the melt [14, 24-27]. In Fig. 6.12a the "solubility" line, derived from [29], separates regions of NP-polymer miscibility from those where the polymers and NP are immiscible. All the experimental systems are in the miscible region. A second line, extrapolated from our simulations, separates the region where the η of the nanocomposites is smaller than the pure melts from the region where the viscosity is larger than the melt ("viscosity" line). (A Kuhn length of 1nm was used to convert the simulation results into the same scale as the experiments.) We first note that the slope of the viscosity line is quite different for short chains and long chains. In the short chain limit, apparently, the viscosity crossover occurs when the NP size becomes comparable to the size of the chain. For large R_g, however, the line is nearly vertical, suggesting that the chain size is no longer the controlling variable. Rather, the root-mean-squared end-to-end distance for an entanglement strand ($= \sqrt{2.2 \times 45} \approx 10\sigma$), which we take as a proxy for the entanglement mesh size, seems to define the crossover. Our findings on the importance of entanglements is consistent with many conjectures in the current literature [2-6, 11]. This "viscosity" line satisfactorily explains most of the experimental trends for the athermal nanocomposites. The data sets corresponding to the highest molecular weight melt (≈393kDa) and the next one with molecular weight ≈75kDa filled with the 25kDa NPs fall above the viscosity line [8]. Thus, we expect the viscosity of the nanocomposites, η, to fall below the pure melts, η_p, for low NP loadings as is indeed found experimentally. (At high enough NP loading this trend will reverse, as has been seen experimentally for POSS particles.) Below the viscosity line we expect that the viscosities of the filled melts should be larger than the neat melts. Consistent with this idea, the 19kDa melt and one data point for the 31kDa melt yield viscosities larger than the pure melt. The second 31kDa point has a viscosity that is nearly equal to the melt – this point lies practically on top of the viscosity line. There are, finally, two points corresponding to chains of molecular weight ~75kDa

mixed with the two larger NPs that show more complicated behavior (blue triangles). In these cases, the viscosity initially increases on adding NPs. However, with increased NP loading the viscosity decreases below that of the neat melt. We do not capture this behavior with our current models, and speculate that particle softness or polydispersity effects (in the NP or polymer size) could play important roles.

Fig. 6.12b shows the viscosity behavior of polymers filled with inorganic nanoparticles [6, 14, 24-28]. First note that, in agreement with assertions of Nusser et al. [6], the miscibility of polymer chains with these NPs plays a critical role – indeed, the experimental points on the bottom right of this figure would be immiscible if the systems were athermal. Miscibility requires the presence of favorable interactions between the NP and the chains. While we expect that there are system-to-system variations, we draw inspiration from the recent work of Hooper and Schweizer, who suggested that miscibility is only attained over a narrow range of attraction values between the NPs and the chains [30]. We therefore characterize the miscible blends through the ansatz that $\sigma_{np} = 2\sigma$. Justification for this assumption comes from the fact that the viscosity line derived in this manner serves to reliably separate experimental systems with increased vs. reduced viscosity relative to the melt, with one exception (Fig. 6.12b) which corresponds to a high molecular weight, highly polydisperse polypropylene melt filled with $\approx$20 nm diameter particles [28]. We do not extend our simulations to capture this situation, and defer this exercise to future work.

The important point that emerges is that the addition of NPs that are smaller than the chains (and apparently the entanglement spacing for long chains) serves to reduce the melt's viscosity. This effect is opposed by favorable energetic interactions at the NP-polymer interface. While Figs. 6.12 are able to organize a relatively comprehensive set of available experimental data, there might be some refinement necessary for the line in Fig. 6.12b. We expect that, not all systems can be defined by a single energetic interaction parameter between the NP and the chains, and hence we might end up having a "band" of demarcation rather than a simple "line". Regardless, we believe that Figs. 6.12 embody a first cut at a "universal" behavior for this class of problems, and provide us with a basis to quantitatively understand the flow behavior of these systems.

References for Chapter 6, Part B.

[1]. T. Kataoka, T. Kitano, M. Sasahara, K. Nishijima. "VISCOSITY OF PARTICLE FILLED POLYMER MELTS". Rheologica Acta v. 17, pp. 149-55, 1978

[2]. U. Yamamoto, K. S. Schweizer. "Theory of nanoparticle diffusion in unentangled and entangled polymer melts". Journal of Chemical Physics v. 135, pp. 224902, 2011.

[3]. L. H. Cai, S. Panyukov, M. Rubinstein. "Mobility of Nonsticky Nanoparticles in Polymer Liquids". Macromolecules v. 44, pp. 7853-63, 2011

[4]. M. E. Mackay, T. T. Dao, A. Tuteja, D. L. Ho, B. Van Horn, H. C. Kim, C. J. Hawker. "Nanoscale effects leading to non-Einstein-like decrease in viscosity". Nature Materials v. 2, pp. 762-66, 2003

[5]. A. Tuteja, M. E. Mackay, C. J. Hawker, B. Van Horn. "Effect of ideal, organic nanoparticles on the flow properties of linear polymers: Non-Einstein-like behavior". Macromolecules v. 38, pp. 8000-11, 2005

[6]. K. Nusser, G. J. Schneider, W. Pyckhout-Hintzen, D. Richter. "Viscosity Decrease and Reinforcement in Polymer-Silsesquioxane Composites". Macromolecules v. 44, pp. 7820-30, 2011

[7]. G. D. Smith, D. Bedrov, L. W. Li, O. Byutner. "A molecular dynamics simulation study of the viscoelastic properties of polymer nanocomposites". Journal of Chemical Physics v. 117, pp. 9478-89, 2002

[8]. F. W. Starr, J. F. Douglas, S. C. Glotzer. "Origin of particle clustering in a simulated polymer nanocomposite and its impact on rheology". Journal of Chemical Physics v. 119, pp. 1777-88, 2003

[9]. M. Vladkov, J. L. Barrat. "Linear and nonlinear viscoelasticity of a model unentangled polymer melt: Molecular dynamics and rouse modes analysis". Macromolecular Theory and Simulations v. 15, pp. 252-62, 2006

[10]. S. Sen, J. D. Thomin, S. K. Kumar, P. Keblinski. "Molecular underpinnings of the mechanical reinforcement in polymer nanocomposites". Macromolecules v. 40, pp. 4059-67, 2007

[11]. V. Ganesan, V. Pryamitsyn, M. Surve, B. Narayanan. "Noncontinuum effects in nanoparticle dynamics in polymers". Journal of Chemical Physics v. 124, pp. 2006

[12]. M. Wang, R. J. Hill. "Anomalous bulk viscosity of polymer-nanocomposite melts". Soft Matter v. 5, pp. 3940-53, 2009

[13]. B. J. Anderson, C. F. Zukoski. "Rheology and Microstructure of Polymer Nanocomposite Melts: Variation of Polymer Segment-Surface Interaction". Langmuir v. 26, pp. 8709-20, 2010

[14]. S. Y. Kim, C. F. Zukoski. "Super- and sub-Einstein intrinsic viscosities of spherical nanoparticles in concentrated low molecular weight polymer solutions". Soft Matter v. 8, pp. 1801-10, 2012

[15]. K. Kremer, G. S. Grest, I. Carmesin. "Crossover from Rouse to Reptation Dynamics - a Molecular-Dynamics Simulation". Physical Review Letters v. 61, pp. 566-69, 1988

[16]. R. Auhl, R. Everaers, G. S. Grest, K. Kremer, S. J. Plimpton. "Equilibration of long chain polymer melts in computer simulations". Journal of Chemical Physics v. 119, pp. 12718-28, 2003

[17]. R. Everaers, S. K. Sukumaran, G. S. Grest, C. Svaneborg, A. Sivasubramanian, K. Kremer. "Rheology and microscopic topology of entangled polymeric liquids". Science v. 303, pp. 823-26, 2004

[18]. P. J. in't Veld, S. J. Plimpton, G. S. Grest. "Accurate and efficient methods for modeling colloidal mixtures in an explicit solvent using molecular dynamics". Computer Physics Communications v. 179, pp. 320-29, 2008

[19]. M. E. Tuckerman, C. J. Mundy, S. Balasubramanian, M. L. Klein. "Modified nonequilibrium molecular dynamics for fluid flows with energy conservation". Journal of Chemical Physics v. 106, pp. 5615-21, 1997

[20]. S. Plimpton. "FAST PARALLEL ALGORITHMS FOR SHORT-RANGE MOLECULAR-DYNAMICS". Journal of Computational Physics v. 117, pp. 1-19, 1995

[21]. W. B. Lee, K. Kremer. "Entangled Polymer Melts: Relation between Plateau Modulus and Stress Autocorrelation Function". Macromolecules v. 42, pp. 6270-76, 2009

[22]. R. A. Riggleman, G. Toepperwein, G. J. Papakonstantopoulos, J. L. Barrat, J. J. de Pablo. "Entanglement network in nanoparticle reinforced polymers". Journal of Chemical Physics v. 130, pp. 2009

[23]. R. S. Hoy, G. S. Grest. "Entanglements of an end-grafted polymer brush in a polymeric matrix". Macromolecules v. 40, pp. 8389-95, 2007

[24]. B. J. Anderson, C. F. Zukoski. "Rheology and Microstructure of Entangled Polymer Nanocomposite Melts". Macromolecules v. 42, pp. 8370-84, 2009

[25]. G. V. Gordon, R. G. Schmidt, M. Quintero, N. J. Benton, T. Cosgrove, V. J. Krukonis, K. Williams, P. M. Wetmore. "Impact of Polymer Molecular Weight on the Dynamics of Poly(dimethylsiloxane)-Polysilicate Nanocomposites". Macromolecules v. 43, pp. 10132-42, 2010

[26]. R. S. Ndong, W. B. Russel. "Rheology of surface-modified titania nanoparticles dispersed in PDMS melts: The significance of the power law". Journal of Rheology v. 56, pp. 27-43, 2012

[27]. R. G. Schmidt, G. V. Gordon, C. A. Dreiss, T. Cosgrove, V. J. Krukonis, K. Williams, P. M. Wetmore. "A Critical Size Ratio for Viscosity Reduction in Poly(dimethylsiloxane)-Polysilicate Nanocomposites". Macromolecules v. 43, pp. 10143-51, 2010

[28]. S. Jain, J. G. P. Goossens, G. W. M. Peters, M. van Duin, P. J. Lemstra. "Strong decrease in viscosity of nanoparticle-filled polymer melts through selective adsorption". Soft Matter v. 4, pp. 1848-54, 2008

[29]. M. E. Mackay, A. Tuteja, P. M. Duxbury, C. J. Hawker, B. Van Horn, Z. B. Guan, G. H. Chen, R. S. Krishnan. "General strategies for nanoparticle dispersion". Science v. 311, pp. 1740-43, 2006

[30]. J. B. Hooper, K. S. Schweizer. "Theory of phase separation in polymer nanocomposites". Macromolecules v. 39, pp. 5133-42, 2006

Part C.

Fully atomistic simulations of the response of silica nanoparticle coatings to alkane solvents

Brandon L. Peters,[1] J. Matthew D. Lane,[2] Ahmed E. Ismail,[3] and Gary S. Grest[2]

[1]Department of Chemical and Biological Engineering, University of Wisconsin, Madison, Wisconsin 53706, USA

[2]Sandia National Laboratories, Albuquerque, New Mexico 87185, USA

[3]Faculty of Mechanical Engineering, RWTH Aachen University, D-52056 Aachen, Germany

Abstract
Molecular dynamics simulations are used to study the effect of passivating ligands of varying lengths grafted to a nanoparticle and placed in various alkane solvents. Average height and density profiles for methyl-terminated alkoxylsilane ligands ($-O-Si(OH)_2(CH_2)_nCH_3$, with n=9, 17 and 35) attached to a 5 nm diameter amorphous silica nanoparticle for coverages between 1.0 and 3.0 chains/nm^2 are presented for explicitly modeled, short-chain hydrocarbon solvents and for implicit good and poor solvents. Three linear solvents, $C_{10}H_{22}$ (decane), $C_{24}H_{50}$, and $C_{48}H_{96}$, and a branched solvent, squalene, were studied. It was found that the implicit poor solvents induced a coating structure that most closely resembled the explicit decane solvent, while the good solvent showed coating structures which were far more extended than found in the explicit solvents tested. Coatings equilibrated in explicit solvents were more compact in longer chain solvents due to autophobic response. The coating density profiles changed significantly as the chain length of the solvent was increased from decane to $C_{24}H_{50}$, while there was less difference between $C_{24}H_{50}$ and $C_{48}H_{98}$ for all coatings. The response of coatings in squalene was not significantly different from the linear chain of equal mass. Significant interpenetration of the solvent chains with the brush coating was only observed for the shortest grafted chains in decane. In all cases the methyl terminal group was not confined to the coating edge, but was found throughout the coating thickness from the core to the outer-most shell. Increasing the temperature from 300 K to 500 K increased the average brush height, but the dependence was weak.

I. Introduction

While adding nanoparticles to a polymer matrix can significantly improve the thermal, mechanical and optical properties of the resulting composite, dispersing nanoparticles in a polymer matrix has proven challenging.[1,2] Bare nanoparticles tend strongly toward phase separation and aggregation.[1-5] One way to overcome this problem is to coat the nanoparticles with chains of the same chemical structure as that of the matrix; then, if the attached ligands is long enough, the nanoparticles can be readily dispersed in the matrix.[2,4-9] However when the

chain length of the attached chains is too short, a phenomenon known as "autophobic" dewetting occurs and the nanoparticles again phase separate from the melt. This dewetting occurs because, as first discussed by de Gennes,[10] for end-grafted polymer chains on a flat surface in contact with a polymer melt, there is an entropic penalty for the melt chains to mix with short grafted chains.[11] The same effect occurs for chains grafted to a nanoparticle.[6]

To obtain a better understanding of the parameters that control the dispersion of nanoparticles in a polymer matrix, a number of experimental studies of phase separation have been carried out.[1-5,7-9] These studies show that as the chain length of the polymer melt increases, the average height of the attached ligands, commonly referred to as a polymer brush, steadily decreases, reaching a limiting value for long polymer matrix chains. Similar results have been observed in numerical simulations for coarse-grained bead-spring models of grafted chains on a nanoparticle in a matrix of chemically similar chains.[12-15] However, except for two recent studies of the potential of mean force between grafted nanoparticles in a polymer,[15,16] these studies do not address the issue of what controls the phase separation. Due to limitations on computer time, most of these previous studies have modeled grafted nanoparticles in an explicit-atom simulation of a realistic polymer to explore the dependence of the brush density profile on the relative chain length of the grafted and matrix chains and on the grafting density. Here we present explicit-atom simulation results for alkane chains grafted on a nanoparticle in an alkane solvent of increasing chain length. All of our simulations are in the regime where the chain length of the attached ligands and chain length of the solvent are comparable in size to that of the nanoparticles. As a result the standard scaling approaches for either star polymers or flat substrates do not apply.[17-19]

Since the first reported atomistic simulations of passivated gold nanocrystallites by Luedtke and Landman,[20] there have been a number of computational studies of surface functionalized nanoparticles. Most of these studies have used united atom models,[20-34] in which the $-CH_2-$ and $-CH_3$ groups are treated as individual entities, although recently there have been a few simulations in which all atoms are included explicitly.[35-42] In most of these studies, due to computer limitations, the solvent was treated implicitly.[20-31] Recent simulations have shown that including the solvent explicitly has a significant effect on the density profile of the ligands, the force between the nanoparticles, and their aggregation.[15-16] In most previous simulations which included explicit solvents, only small molecular solvents such as water, ethane, hexane and decane have been studied.[29-38] Most previous studies have been on passivated gold nanoparticles, with the chain length of the ligands varying from butane to octadecane. However recently Ndoro et al[41,42] have simulated a silica nanoparticle embedded in a melt of 20-monomer atactic polystyrene chains using a fully atomistic model. They have also developed a coarse-grained model based on these simulations and extended the studies to a range of grafted and melt chain lengths.[43] Longer ligand and solvent chains have only been studied using coarse-grained bead-spring models.[12,15,16,40,44,45] We have performed explicit-atom simulations of alkane-coated amorphous silica nanoparticles with ligands varying in length from 10 to 36 carbons in three linear solvents—decane, $C_{24}H_{50}$, and $C_{48}H_{96}$—and in a branched solvent, squalene ($C_{30}H_{50}$). Squalene has a 24-carbon backbone with six methyl side groups and six double bonds and, unlike its linear counterpart n-tetracosane ($C_{24}H_{50}$), is liquid at room temperature. As the chain length of the solvent increases, the density profile for the attached ligands smoothly collapses as the solvent chains demix entropically from the attached ligands. We compare our results to

simulations in implicit good and poor solvents and show that treating the solvent implicitly does not capture the effect of increasing the length of the solvent chain.

In the next section, details of the model and methodology are presented. In Sec. III we compare the density profile for the ligands for varying ligand chain length in the four explicit-atom solvents and compare the results to simulations in a good or poor implicit solvent. We show that the methyl end groups can be found throughout the profile. We then present results for the effect of varying the graphing density. In Sec. IV we briefly summarize our main findings.

II. Model and Methodology

We modeled 5 nm diameter rigid amorphous silica nanoparticles, coated with methyl-terminated alkoxylsilane -O-Si$(OH)_2(CH2)_nCH_3$ ligands, in hydrocarbon solvents. Chains of length n = 9, 17 and 35 were chemisorbed with trisilanol groups. An example is shown in Fig. 6.13 for the three values of *n* in the shortest chain solvent studied, decane. The grafting density was varied between 1.0 and 3.0 chains/nm^2. This gives 80-240 ligand chains for a 5 nm diameter nanoparticle. In what follows, most of the results presented are for a full-coverage density of 3.0 chains/nm^2.

All molecular dynamics simulations (MD) were performed using the LAMMPS classical MD code.[46] All of the simulations used the all-atom Optimized Potentials for Liquid Simulations (OPLS-AA) developed by Jorgensen and co-workers[47,48] for all interactions. Nonbonded interactions consisted of a sum of standard 12–6 Lennard-Jones (LJ) and electrostatic potentials, with nearest and next-nearest neighbor pairs excluded, and interactions reduced by a factor of 1/2 for 1-4 neighbor pairs. All LJ interactions were cut off at r_c=10 Å; a switching radius of 10 Å was also used as a limit for electrostatic interactions using the particle-particle particle-mesh (PPPM) algorithm.[49] The precision of the PPPM algorithm was set to 1 part in 10^4. The OPLS-AA potential also includes harmonic bond and angle terms and torsional interactions. Details of the interaction parameters can be found in refs. 47 and 48. The equations of motion were integrated using a velocity Verlet algorithm with time step δt = 1 fs. A Langevin thermostat with a 100 fs damping constant was used to regulate the system temperature.[50]

The nanoparticle core was cut from bulk amorphous silica and then annealed to produce a surface -OH concentration consistent with experimental values.[51] The bulk silica was generated from a melt-quench process similar to the method of Lorenz et al.[52] The ligands were then attached randomly to the surface oxygens at the desired coverage and equilibrated in an implicit solvent for 1-2 ns. The nanoparticle core was treated as a rigid body.

The hydrocarbon solvents were created by equilibrating, at a pressure of 1 atm, four solvents consisting of 12,800 decane ($C_{10}H_{22}$) chains or 6400 squalene chains at 300K, and 5400 tetracosane ($C_{24}H_{50}$) chains or 2700 $C_{48}H_{98}$ chains at 400K. The higher temperature was necessary for the latter two chain lengths to be above their melting points. A void in the center of each solvent was created by inserting a soft-repulsive spherical pseudoparticle indenter into the solvent.[46] The indenter was grown slowly from radius zero to a size capable of accommodating each coated nanoparticle. The overall system dimensions were allowed to expand at constant pressure through the void growth. When the desired size was reached, the pseudoparticle was

removed, leaving the void space. The process is illustrated in Figure 6.14. The system was further equilibrated for 1 ns before the nanoparticle and solvent were merged. Any overlaps were removed using a displacement-limiting integrator (nve/limit in LAMMPS) to prevent large repulsive forces.[46]

The combined system was equilibrated for 1 ns in the constant pressure and temperature (*NPT*) ensemble, after which the system was run between 2-8 ns in the constant volume and energy (*NVE)* ensemble with a Langevin thermostat. Results for higher temperatures were obtained by raising the temperature for these initial states. All of the results presented here are for P=1 atm except for the $C_{24}H_{50}$ and $C_{48}H_{98}$ solvents at T=500K, which were heated from the T=400K systems under constant volume rather than constant pressure constraints in order to avoid phase separation.

In a number of previous simulations,[20-30] the solvent was treated implicitly; to compare our explicit solvent results, we also carried out simulations in both poor and good implicit solvents. For the poor solvent, all the interactions between atoms were the same as for the explicit atom simulations with r_c = 10 Å. This corresponds to a poor solvent over the range of temperatures studied. To model a good solvent, all non-bonded interactions were truncated at the LJ potential minimum ($r_c = 2^{1/6}\,\sigma_{ij}$), producing a purely repulsive van der Waals force.

III. Results

The radial density of the ligand coating the nanoparticle is known to depend on the chain length of the solvent, which can lead to autophobic dewetting as the chain length of the solvent increases. The effect of increasing the chain length of the solvent from 10 to 48 carbons is illustrated by simulation snapshots in Fig. 6.15a,b for $-O-Si(OH)_2(CH_2)_{35}CH_3$ ligands at a coverage of 3.0 chains/nm^2 at 400K. The radial density of the brush $\rho_b(r)$ is shown in Fig. 6.16 for these two systems as well as for $C_{24}H_{50}$. For comparison, in Figs. 6.15 and 6.16 results for an implicit poor and good solvent are also shown. As seen in Fig. 6.16, the density profile becomes more compact and phase separates from the solvent as the chain length of the solvent increases, in agreement with previous work on coarse-grained bead spring models.[12-16] The coating response for the implicit poor solvent is intermediate to the response seen in the four explicit solvents, and most closely agrees with the response in decane. The implicit good solvent the density profile is significantly more extended than any of the explicit solvents studied.

A quantitative comparison of the difference in brush height as a function of solvent chain length can be directly obtained from the average brush height <h>, given by

$$\langle h \rangle = \frac{\int_R^\infty (r-R)\,\rho_b(r)\,r^2\,dr}{\int_R^\infty \rho_b(r)\,r^2\,dr} \qquad (1)$$

where R=2.5nm is the nanoparticle radius. For the case of grafted chain length n=35 at T=400K, the average <h>= 14.6, 13.2 and 12.8 Å for decane, $C_{24}H_{50}$, and $C_{48}H_{98}$, respectively, compared to 13.8 and 18.9 Å for the implicit poor and good solvents. As expected, there is a large decrease in the average height as the chain length of the solvent increases from 10 to 24, while there is essentially no difference as the chain length of the solvent increases from 24 to 48. The data also

show that while implicit solvent simulations are computationally much less costly than explicit-atom simulations, they do not capture the subtle interactions between the ligands and solvent, particularly the autophobic dewetting as chain length increases.[6]

Density profiles for both the alkoxylsilane ligands and solvent chains are shown in Fig. 6.17 for n=17 and 35 for the four solvents studied at 400K. The shape of both profiles changes significantly as the chain length of the solvent is increased from $C_{10}H_{22}$ (decane) to $C_{24}H_{50}$, while there is less difference between $C_{24}H_{50}$ and $C_{48}H_{98}$. The results for squalene and $C_{24}H_{50}$ are very similar even though squalene, which has the same chain length, has six additional $-CH_3$ side groups. Only for decane is there any significant interpenetration of the solvent chains into the brush coating. Results for the average brush height <h> for all the cases shown in Fig. 6.17 along with those for n=9 are given in Table I.

Table I. Average height <h> (Å) for coverage 3.0 chains/nm^2. The error bars are ± 0.2Å. n is the grafted chain length in $(-O-Si(OH)_2(CH_2)_nCH_3$.

	$C_{10}H_{22}$	$C_{24}H_{50}$	$C_{48}H_{98}$	Squalene	Implicit Poor	Implicit Good
n=9						
300K	8.8	8.7	8.6	8.5		
n=17						
300K	11.3	-	-	10.7		
400K	11.9	11.3	11.2	11.3		
n=35						
300K	13.4	-	-	12.6	13.6	18.3
400K	14.6	13.2	12.8	13.0	13.8	18.9
500K	14.7	-	13.7	14.7	14.1	19.0

The effect of varying the temperature in the experimentally accessible range of 300K to 500K is illustrated in Fig. 6.18. Except for some minimal expansion of the brush at 500K, due largely to the reduction in solvent density, temperature has little effect on the profiles. For example, the average brush height <h> increases from 13.4 Å to 14.7 Å for decane and from 12.6 Å to 14.7 Å for squalene as the temperature is increased from 300K to 500K. The relative increase in real solvents, however, is still substantially larger than that observed in the implicit solvents over the same temperature range: <h> increases from 13.6 Å to only 14.1 Å for the implicit poor solvent and from 18.3 Å to 19.0 Å for the implicit good solvent as the temperature is increased from 300K to 500K.

The density profile for the terminal carbons is shown in Fig. 6.19. The most striking feature of these profiles is that the terminal carbons are not concentrated in the region near the interface, but are instead distributed throughout the brush. This is consistent with previous results on polymers attached to a flat substrate. Figure 6.19a compares results for the four real solvents: Independent of the length of the solvent chains, the probabilities of finding terminal carbons near the surface of the silica nanoparticle are comparable. The broader distribution for the terminal

carbon in decane is simply due to the larger extent of the brush in decane. As seen in Figs. 6.19b,c the effect of temperature on the distribution of the terminal carbons, as for the overall density profiles, is minimal.

The effect of varying the surface coverage is shown in Fig. 6.20 for $-O-Si(OH)_2(CH_2)_{35}CH_3$ in decane and $C_{24}H_{48}$ at 400K. Near the surface of the silica nanoparticle the density profiles overlap for both solvents as neither solvent penetrates all the way to the core of the nanoparticle even for the lowest coverage. This results in density profiles that overlap near the surface of the nanoparticle and only for larger radii *r* does the local repulsion of the ligands have a strong enough effect to extend the brush for higher coverages. The average brush height <h> is found to be 11.3, 13.9, and 14.6 for decane and 8.2, 11.8, and 13.2 Å for $C_{24}H_{48}$ for coverages of 1.0, 2.0 and 3.0 chains/nm^2 respectively.

IV. Conclusions

We have performed simulations of alkylsilane-coated silica nanoparticles in both real and implicit solvents to observe the effects of the ligand and solvent chain length on the structure of the coating and solution outside of the nanoparticle. Our results show that the brush heights of the ligands attached to the nanoparticle are altered by solvent length for grafted chains longer than n=9. For all coating chain lengths and temperatures, the average brush height is as large as or larger in $C_{10}H_{22}$ than in any of the other solvents considered. Of particular interest is the wide distribution of positions for the chain ends relative to the particle surface; conformations ranging from chain ends lying near the particle surface to nearly fully extended chains have been observed under all conditions. In addition, comparison with implicit solvents indicates that the use of an implicit solvent does not capture the changes introduced by solvent length and temperature relative to what is observed for the “real” solvents.

Future work on these systems can proceed on several fronts. Simulation of assemblies of nanoparticles will require the development of coarse-grained potentials of mean force which can efficiently describe the interactions between two (or more) particles in solution. Further research will also be needed to study the “solvation” process of nanoparticles in solvents as a function of the chain length of the solvent.

Acknowledgement
Financial support from the National Institute for Nano Engineering at Sandia is gratefully acknowledged. This research used resources obtained through the Advanced Scientific Computing Research (ASCR) Leadership Computing Challenge (ALCC) at the National Energy Research Scientific Computing Center (NERSC), which is supported by the Office of Science of the United States Department of Energy under Contract No. DE-AC02-05CH11231. This work was performed, in part, at the Center for Integrated Nanotechnologies, a U.S. Department of Energy, Office of Basic Energy Sciences user facility. Sandia National Laboratories is a multi-program laboratory managed and operated by Sandia Corporation, a wholly owned subsidiary of Lockheed Martin Corporation, for the U.S. Department of Energy's National Nuclear Security Administration under contract DE-AC04-94AL85000.

References for Chapter 6, Part C.

(1) Mackay, M. E.; Tuteja, A.; Duxbury, P.; Hawker, C. J.; Van Horn, B.; Guan, Z. B.; Chen, G. H.; Krishnan, R.S.; Science 2006, 311, 1740–1743.
(2) Akcora, P.; Liu, H.; Kumar, S.; Moll, J.; Li, Y.; Benicewicz, B.; Schadler, L. S.; Acehin, D.; Panagiotopoulos, A. Z.; Pryamitsyn, V.; Ilavsky, J.; Thiyagarajan, P.; Colby R. H.; Douglas, J. Nat. Mater. 2009, 8, 354–359.
(3) Corbierre, M. K.; Cameron, N. S.; Sutton, M.; Laariri, K.; Lennox, R. B.; Langmuir 2005, 21, 6063–6072.
(4) Winey, K. I.; Vaia, R. A., MRS Bull. 2007, 32, 314-319.
(5) Krishnamoorti, R. MRS Bull. 2007, 32, 341–347.
(6) Hasegawa, R; Aoki, Y.; Doi, M. Macromolecules 1996, 29, 6656–6662.
(7) Yezek, L.; Schartl, W.; Chen,Y. M.; Gohr, K.; Schmidt, M. Macromolecules 2003, 36, 4226–4235.
(8) Green, D. L.; Mewis, J. Langmuir 2006, 22, 9546–9553.
(9) Chevigny, C.; Dalmas, F.; Di Cola, E.; Gigmes, D.; Bertin, D; Boué, F.; Jestin, J. Macromolecules 2011, 44, 122-133
(10) de Gennes, P.-G. Macromolecules 1980, 13, 1069-1075.
(11) Aubouy, M.; Fredrickson, G. H.; Pincus, P.; Raphaël, E. Macromolecules 1995, 28, 2979-2981.
(12) Kalb, J.; Dukes, D.; Kumar, S. K.; Hoy, R. S.; Grest, G. S. Soft Matter 2011, 7, 1418-1425.
(13) Goyal, S.; Escobedo, F. A. J. Chem. Phys. 2011, 135, 184902.
(14) Shen, J.; Liu, J.; Gao, Y.; Cao, D.; Zhang, L. Langmuir 2011, 27, 15213-15222
(15) Meng, D.; Kumar, S. K.; Lane, J. M. D.; Grest, G. S. Soft Matter 2012, 8, 5002-5010.
(16) Smith G. D.; Bedrov, D. Langmuir 2009, 25, 11239–11243.
(17) Daoud, M.; Cotton, J. P., J. Phys., 1982, 43, 531–538.
(18) Milner, S. T.; Witten T. A.; Cates, M. E., Macromolecules, 1988, 21, 2610–2619.
(19) Wijmans, C. M.; Zulina, E. B., Macromolecules, 1993, 26, 7214–7224.
(20) Luedtke, W. D.; Landman, U. J. Phys. Chem. B 1998, 102, 6566–6572.
(21) Tay, K.; Bresme, F. Mol. Simul. 2005, 31, 515–526.
(22) Henz, B. J.; Hawa, T.; Zachariah, M. R. Langmuir 2008, 24, 773-783.
(23) Henz, B. J.; Chung, P. W.; Andzelm, J. W.; Chantawansri, T. L.; Lenhart, J. L.; Beyer, F. L. Langmuir 2011, 27, 7836–7842.
(24) Rapino, S.; Zerbetto, F. *Small* 2007, 3, 386-388.
(25) Ghorai, P. K.; Glotzer, S. C. *J. Phys. Chem. C* 2007, 111 , 15857–15862.
(26) Singh, C.; Pradip K. Ghorai, P. K.; Horsch, M. A.; Jackson, A. M.; Larson, R. G.; Stellacci, F.; and Glotzer, S. C. *Phys. Rev. Lett*. 2007, 99, 226106.
(27) Schapotschnikow, P.; Vlugt, T. J. H. *J. Chem. Phys*. 2009, 131, 124705.
(28) Kaushik, A. P.; Clancy, P. J. Chem. Phys. 2012, 136, 114702.
(29) Pool, R.; Schapotschnikow, P.; Vlugt, T. J. H. *J. Phys. Chem. C*, 2007, 111, 10201–10212.
(30) Schapotschnikow, P.; Pool, R.; Vlugt, T. J. H. *Nano Lett.* 2008, 8, 2930–2934.
(31) Lal, M; Plummer, M.; Richmond, N. J.; Smith, W. J. Phys. Chem. B, 2004, 108, 6052–6061
(32) Patel, N.; Egorov, S. A. J. Chem. Phys. 2007, 126, 054706.
(33) Tay, K. A.; Bresme, F. *J. Am. Chem. Soc.* 2006, 128, 14166–14175.
(34) Bresme, F.; Oettel, M. *J. Phys.: Condens. Matter* 2007, 19, 413101.

(35) Lane, J. M. D.; Ismail, A. E.; Chandross,M.; Lorenz, C. D..; Grest, G. S. *Phys. Rev. E* 2009, 79, 050501.
(36) Yang, A.-C. ; Weng, C.-I *J. Phys. Chem. C* 2010, 114, 8697–8709.
(37) Yang, A.-C. ; Weng, C.-I; Chen, T.-C. *J. Chem. Phys.* 2011, 135, 034101.
(38) Lane, J. M. D.; Grest, G. S. *Phys. Rev. Lett*. 2010, 104, 235501.
(39) Kaushik, A. P.; Clancy, P. J. Chem. Phys. 2012, 136, 114702.
(40) Lin, J.-Q. Lin; Zhang, H.-W.; Chen, Z; Zheng, Y.-G.; Zhang, Z.-Q.; Ye, H.-F. J Phys. Chem. C 2011, 115, 18991–18998
(41) Ndoro, T. V. M.; Voyiatzis, E.; Ghanbari, A.; Theodorou, D. N.; Böhm, M. C.; Müller-Plathe, F. Macromolecules 2011, 44, 2316–2327
(42) Ndoro, T. V. M.; Bo hm, M. C.; Mu ller-Plathe. F. Macromolecules 2012, 45, 171-179.
(43) Ghanbari, A.; Ndoro, T. V. M.; Leroy, F.; Rahimi, M.; Bo hm, M. C.; Mu ller-Plathe. F. Macromolecules 2012, 45, 572−584.
(44) Verso, F. L.; Egorov, S. A.; Milchev, A.; Binder, K. *J. Chem. Phys*. 2010, 133, 184901.
(45) Verso, F. L.; Yelash, L.; Egorov, S. A.; Binder, K. Soft Matter 2010, 8, 4185-4196.
(46) Plimpton, S. J. J. Comput. Phys. 1995, 117, 1-19; website: lammps.sandia.gov
(47) Jorgensen, W. L.; Maxwell, D. S.; TiradoRives, J. J. Am. Chem. Soc. 118, 11 225 (1996).
(48) Watkins, E. K.; Jorgensen, W. L. J. Phys. Chem. A 105, 4118 (2001).
(49) Hockney, R.W.; Eastwood, J.W. Computer Simulation Using Particles (Adam Hilger-IOP, Bristol, 1988).
(50) Grest, G. S.; Kremer, K. Phys. Rev. A 1986, 33,3628-3631.
(51) Maitra, P.; Ding, J.; Huang, H.; Wunder, S. L. Langmuir 2003, 19, 8994-9004.
(52) Lorenz, C. D.; Webb III, E. B.; Stevens, M. J.; Chandross, M.; Grest, G. S. Tribol. Lett. 2005, 19, 93-99.

Figures:

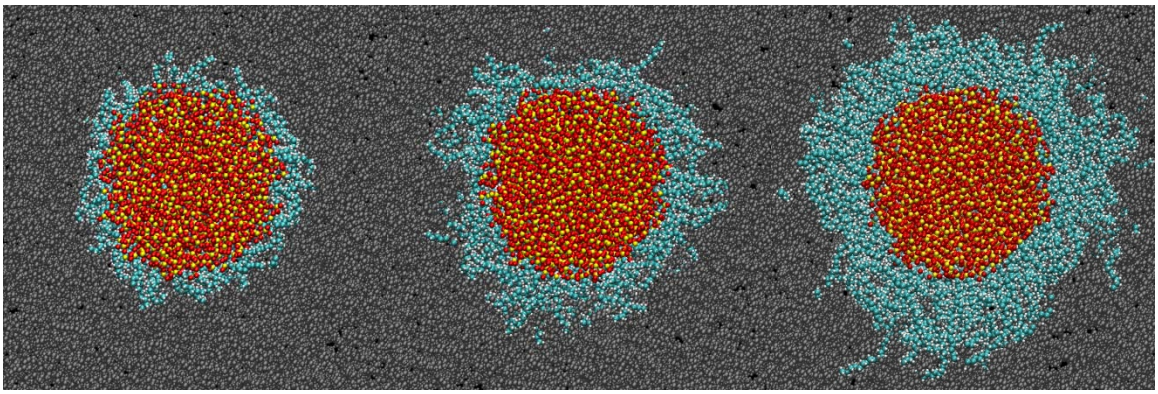

Figure 6.13. Snapshots of cross section of equilibrated 5nm diameter amorphous silica nanoparticles with alkoxylsilane -O-Si(OH)$_2$(CH$_2$)$_n$CH$_3$ ligands attached at a coverage 3.0 chains/nm^{2}at 300K in decane (from left to right) for n=9, 17 and 35 in decane.

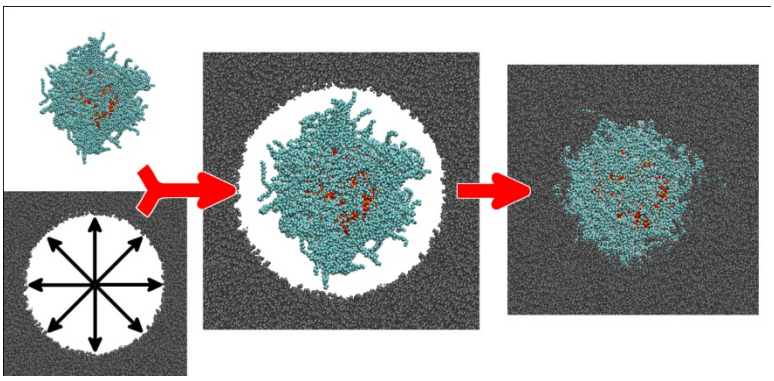

Figure 6.14. Illustration of procedure used to build the nanoparticle/solvent system. An alkoxylsilane -O-Si$(OH)_2(CH_2)_nCH_3$ amorphous silica nanoparticle is equilibrated in an implicit poor solvent (left), then merged with neat solvent which has been equilibrated with a hole large enough to accommodate the nanoparticle (center) and then equilibrated at constant pressure (right).

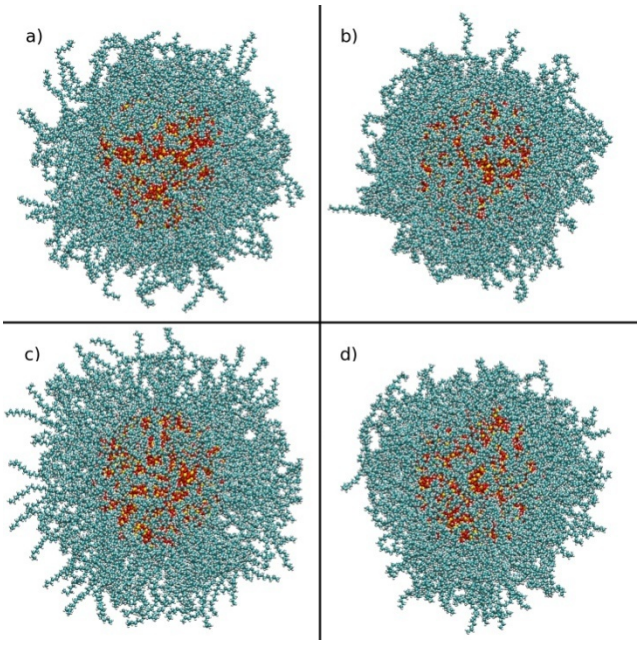

Figure 6.15. Snapshots of an equilibrated 5 nm diameter amorphous silica nanoparticle with alkoxylsilane -O-Si(OH)2(CH2)35CH3 ligands attached at a coverage 3.0 chains/nm2at 400K in a) decane and b) C48H98 (solvents not shown for clarity) compared to those in an implicit c) good and d) poor solvent.

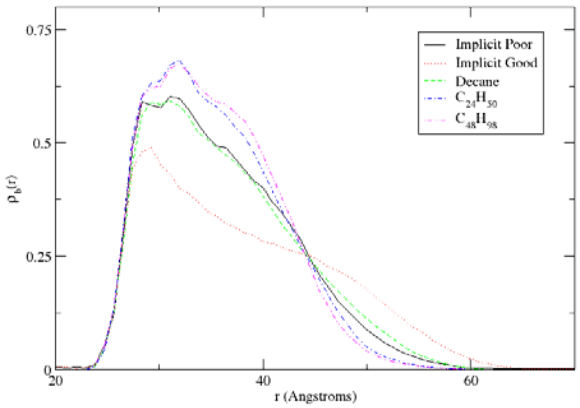

Figure 6.16. Mass density profiles (in g/cm^3) for the -O-Si(OH)$_2$(CH$_2$)$_{35}$CH$_3$ ligands for 5 nm nanoparticle in decane, $C_{24}H_{50}$, and $C_{48}H_{98}$ and implicit poor and good solvent. Coverage is 3.0 chains/nm^2.

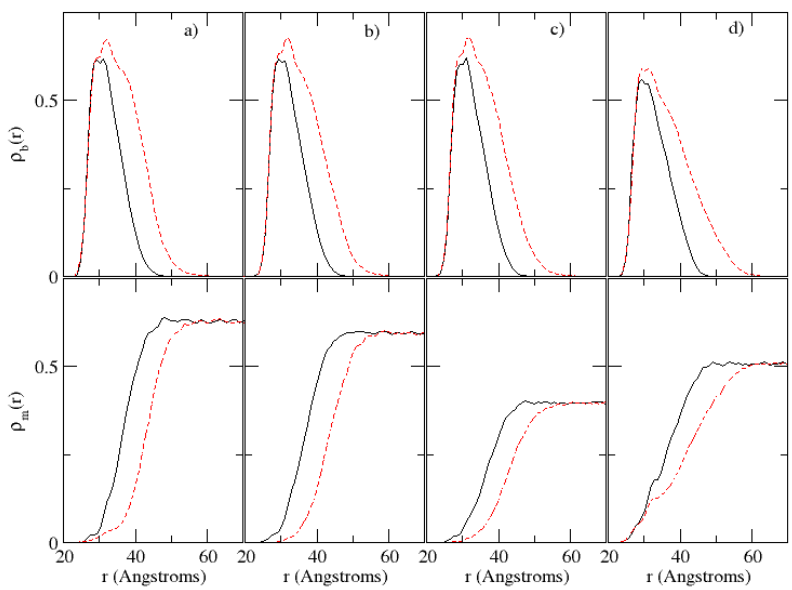

Figure 6.17. Mass density profiles (in g/cm^3) of the alkoxylsilane ligands and the solvent at 400 K for -O-Si(OH)$_2$(CH$_2$)$_{17}$CH$_3$ (dashed red line) and -O-Si(OH)$_2$(CH$_2$)$_{35}$CH$_3$ (solid black line) in $C_{48}H_{98}$ (a), $C_{24}H_{50}$ (b), squalene (c), and decane (d) solvents. The monomer densities are plotted top and the solvent monomer densities are plotted below. Results are for coverages of 3.0 chains/nm^2.

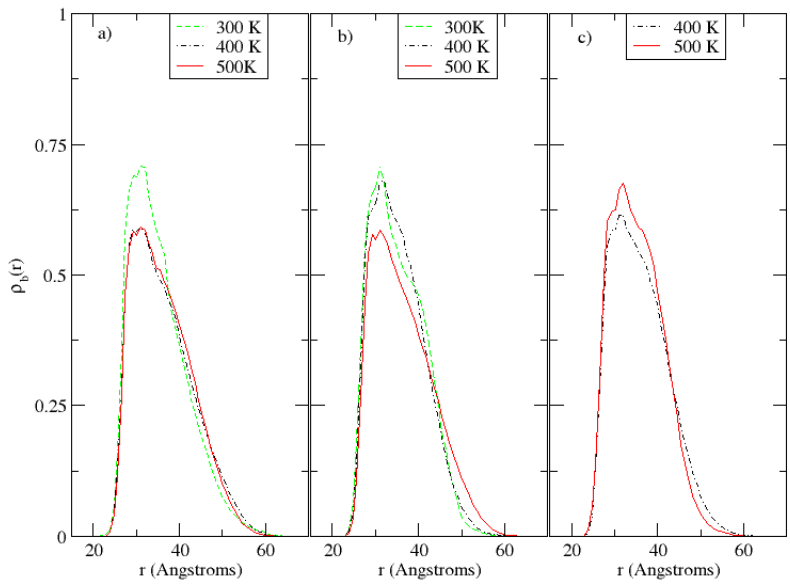

Figure 6.18. Mass density profiles (in g/cm^3) for -O-Si(OH)$_2$(CH$_2$)$_{35}$CH$_3$ at different temperatures for three solvents: a) decane for 300 K, 400 K, and 500 K, b) squalene for 300 K, 400 K, and 500 K and c) C$_{48}$H$_{98}$ for 400K and 500K. Results are for coverage 3.0 chains/nm^2.

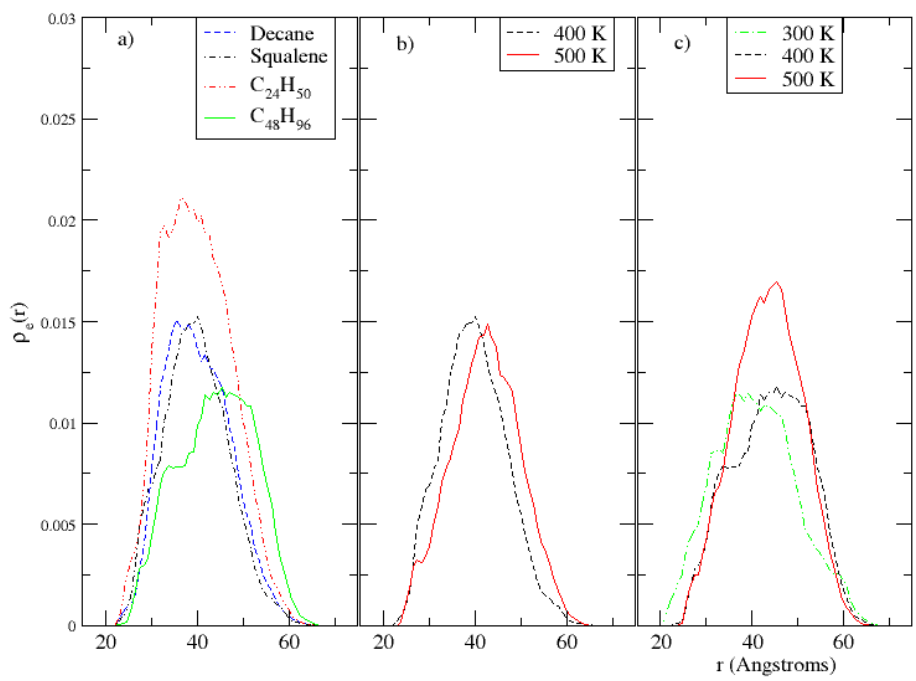

Figure 6.19. Density of carbon atoms in methyl CH$_3$ terminal groups for -O-Si(OH)$_2$(CH$_2$)$_{35}$CH$_3$ in a) four different solvents at 400 K and for b) C$_{48}$H$_{98}$ and c) decane at different temperatures. Results are for coverage 3.0 chains/nm^2.

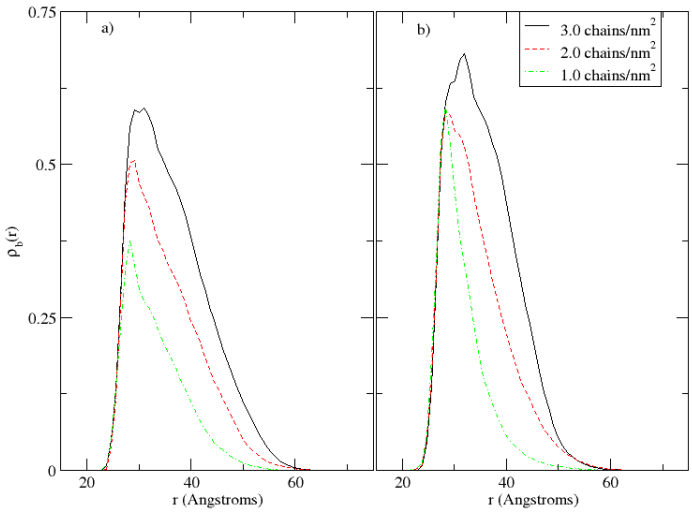

Figure 6.20. Density profiles for -O-Si(OH)$_2$(CH$_2$)$_{35}$CH$_3$ at 400K in a) decane and b) C$_{24}$H$_{50}$ for coverages 1.0, 2.0 and 3.0 chains/nm^2.

CHAPTER 7

Personnel Impact

Timothy J. Boyle

The National Institute for Nano-Engineering (NINE) was setup as collaboration between government, university, and industrial entities to involve students in large scale multi-disciplinary research projects focused on developing nano-enabled solutions to important national problems. One result of this, besides solving complex national problems, was to develop the next generation of innovative leaders in the nanotechnoloby field for the U.S. This was an attempt to address the growing concern of loss of students in the pipeline for America's science and engineering careeres. The America COMPETES Act, signed in August 2007, provides a national strategy to address this concern. NINE is intended to be the model of a novel partnership between universities and companies throughout the nation and the Department of Energy (DOE), with Sandia National Laboratories (Albuquerque, NM) as the host lab for NINE.

The following Tables 1 and 2 list the industrial partners and their interest in Responsive Nanocomposites and the students involved in this effort, respectively. Of note is the high number of students enrolled in science programs at a variety of schools across the nation. Also, the high degree of involvement from academic and industrial partners. Generally, this project allowed for a number of students to pursue their advanced degree in nanotechnology.

Table 1. Persons and Companies involved in process

Contact	Company	Interest
Mike Poldneff	GoodYear	Tires that could adjust to weather changes
Surrendra	GoodYear	
Carl Pulford	GoodYear	
Mark Disko	ExxonMobil	Deep well materials that could change upon condition changes
Rebecca Locker	ExxonMobil	
Andy Tsou	ExxonMobil	
Mike Garner	Intel	Water diodes for packing of chips.
Rahul Manepalli	Intel	

Table 2. Students enrolled in the NINE program

Principal Investigator	Mentor	Affiliation	Student	Result
Boyle	Boyle	UNM	**Thu Doan**	UIUC grad school
	Boyle	UNM	**Andrew Velasquez**	UNM/Chem
	Boyle	UNM	**Callie Hamlin**	High school
	Boyle	UNM	**Derek Wichhart**	SNL/UNM/Engineering
	Boyle	UNM	**Alia Saad**	UNM
	Boyle	UNM	**Sarah Hoppe**	BS Chem UNM
	Boyle	UNM	**Chelsea Lockhart**	UNM
	Boyle	UNM	**Michael Neville**	UNM/Chemistry
	Boyle	UNM	**Daniel Yonemoto**	UNM/Chemistry
	Sigmund	U Florida	**PK Muthiah**	UF Ph. D. granted
	Ruoff	UT-Autsin	**Jeff Potts**	UT Ph. D. granted
	Li	U Washington	**Jeremy Barker**	UW/Engineering
	Farellel	Holy Cross	**Taylor Huta**	Holy Cross/ Med School
	Farellel	Holy Cross	**Courtney Downs**	HolyCross/Chem
Shelnutt	Medforth	UNM	**Kathleene Martin**	UNM/Chem
	Wiesner	Cornell	**Rachel Dorin**	
Brinker	Aizenberg	Harvard	**Lauren Zarzar**	Harvard grad school
Lambert	Lambert	UNM	**Carlos Chavez**	LSU grad school
	Lambert	UNM	**Danae Davis**	UNM grad school
Grest	Kumar	Columbia	**Dong Meng**	Post-Doc Columbia
	Perahia	Clemson	**Sabina Maskey**	Clemson grad school
	De Pablo	Wisconsin	**Brandon Peters**	WI grad school

DISTRIBUTION

1	MS1349	Timothy J. Boyle	1815
1	MS1349	C. Jeffrey Brinker	1815
1	MS1303	Gary Grest	1131
1	MS0734	Tim Lambert	6124
1	MS1349	Bryan Kaehr	1815
1	MS1349	William F. Hammetter	1815
1	MS0888	Regan W. Stinnett	1823
1	MS0899	Technical Library	9536 (electronic copy)

Sandia National Laboratories